Title
ANGULAR DISTRIBUTION AND ATOMIC EFFECTS IN CONDENSED PHASE PHOTOELECTRON SPECTROSCOPY

Author
Davis, R.F.

Publication Date
1981-11-01

Peer reviewed

LBL-13511

Lawrence Berkeley Laboratory
UNIVERSITY OF CALIFORNIA

Materials & Molecular Research Division

ANGULAR DISTRIBUTION AND ATOMIC EFFECTS IN CONDENSED PHASE PHOTOELECTRON SPECTROSCOPY

Richard Francis Davis
(Ph.D. thesis)

November 1981

Prepared for the U.S. Department of Energy under Contract W-7405-ENG-48

ANGULAR DISTRIBUTION AND ATOMIC EFFECTS IN CONDENSED PHASE PHOTOELECTRON SPECTROSCOPY

Richard Francis Davis

Ph.D. Thesis

Materials and Molecular Research Division
Lawrence Berkeley Laboratory

and

Department of Chemistry
University of California
Berkeley, California 94720

November 1981

This work was supported by the Director, Office of Energy Research, Office of Basic Energy Sciences, Chemical Sciences Division of the U.S. Department of Energy under Contract No. W-7405-ENG-48. It was performed in part at the Stanford Synchrotron Radiation Laboratory, which is supported by the NSF through the Division of Materials Research.

ANGULAR DISTRIBUTION AND ATOMIC EFFECTS IN CONDENSED PHASE PHOTOELECTRON SPECTROSCOPY

Contents

ANGULAR DISTRIBUTION AND ATOMIC EFFECTS IN CONDENSED PHASE PHOTOELECTRON SPECTROSCOPY

Richard Francis Davis

Materials and Molecular Research Division
Lawrence Berkeley Laboratory

and

Department of Chemistry
University of California
Berkeley, California 94720

ABSTRACT

A general concept of condensed phase photoelectron spectroscopy is that angular distribution and atomic effects in the photoemission intensity are determined by different mechanisms, the former being determined largely by ordering phenomena such as crystal momentum conservation and photoelectron diffraction while the latter are manifested in the total (angle-integrated) cross section. In this work, the physics of the photoemission process is investigated in several very different experiments to elucidate the mechanisms of, and correlation between, atomic and angular distribution effects. In the first chapter, which serves as an introduction to the underlying concepts of condensed-phase photoemission, theoretical models are discussed and the connection between the two effects is clearly established. The

remainder of this thesis, which describes experiments utilizing both angle-resolved and angle-integrated photoemission in conjunction with synchrotron radiation in the energy range 6 eV $\leq h\nu \leq$ 360 eV and laboratory sources, is divided into three parts.

In Part I, angular distribution effects arising from crystal momentum conservation in valence band (VB) structure studies are probed for the following single-crystalline faces: Cu(S)-[3(111)x(100)], Pt(100)-(5x1), Cr(100)-c(2x2), and Cr(110). In these studies, the technique of angle-resolved normal photoemission (ARNP), in conjunction with synchrotron radiation in the range 6 eV $\leq h\nu \leq$ 34 eV, is utilized to determine detailed VB dispersion relations, $E(\vec{k})$, along $\vec{k}_\perp$ from the $h\nu$ dependence of VB-peak-structure energy positions in electron energy distribution curves (EDCs). Emphasis is placed on the critical evaluation of the direct-transition model (DTM) in the interpretation of ARNP data for metals, with considerable attention focused on the nature of photoelectron dispersion relations, competing processes which give rise to non-DTM features in the EDCs, and the influence of the surface on EDCs. In general, it is found that the DTM, in conjunction with a quasi-free-electron final-state dispersion relation, is quite successful in the determination of $E(\vec{k}_\perp)$ from ARNP data.

In Part II, atomic effects in the total cross section are probed in two experiments designed to <u>minimize</u> angular distribution effects: (1) samarium clusters, via intensity measurements of valence- and core-level photoemission peaks (at $h\nu$ = 60 eV and 1486.6 eV), are

shown to exhibit a particle-size-dependent electronic configuration, and (2) VB photoemission from CO-Pd (with 40 eV $\leq h\nu \leq$ 220 eV) is shown to display a dramatic adsorbate-molecular-orbital sensitivity enhancement near $h\nu$ = 130 eV arising from a Cooper minimum in the substrate VB (4d) cross section.

Part III is devoted to (localized) angular distribution effects which do not originate from bulk crystallographic order. Rather, they are analogous to well-known atomic and molecular asymmetry effects in the gas phase. In the first set of experiments, condensed-phase photoelectron asymmetry arising from the $\vec{A}\cdot\vec{P}$ interaction in randomly-oriented Pt, Ag, and Se-Pt systems is found to show atomic behavior similar to that expected for free atoms, as observed in angle- and energy-dependence measurements of photoemission intensity for core and valence levels in the range 40 eV $\leq h\nu \leq$ 252 eV. The second group of experiments is devoted to studies of C(1s) shape resonance phenomena in CO overlayers on Ni(111) and Ni(001) (300 eV $\leq h\nu \leq$ 360 eV). At the resonance maximum ($h\nu$ = 311 eV) each system exhibits an angular distribution of C(1s) intensity peaked nearly along the CO molecular axis. In both sets of experiments in Part III, significant deviations from gas-phase expectations are observed, but an important result is nonetheless established: the traditional notion that atomic and angular distribution effects in photoemission have different origins is not correct. Gas-phase angular distribution effects in modified form are present in the condensed phase.

I. INTRODUCTION

The goal of this thesis has been to investigate two aspects of condensed phase photoelectron spectroscopy (PES) that are traditionally separated mechanistically:[1] (1) angular distribution and (2) atomic effects. The emphasis has not been on the solution of any practical problems through the utilization of PES, nor is the main theme the discovery and characterization of new phenomena with PES, although it will be shown that the latter has been achieved in at least three new experiments. Rather, the general approach taken has been to investigate the physics of the photoemission process in several vastly different experiments. A special goal has been to elucidate the correlation between atomic and angular distribution effects. With a fortuitous choice of experimental conditions, atomic (total cross section) effects can be ignored in angular distribution experiments with ordered systems (Part I of this work--valence band structure studies), and angular effects can be rendered unimportant in atomic effect measurements where a total cross section is probed[2] (Part II). However, additional angular distribution effects have been found that do not originate from bulk crystallographic order (Part III of this thesis). Rather, they are analogous to gas phase atomic[3] and molecular[4] photoelectron asymmetry effects. The atomic effect, heretofore completely unnoticed (or unmentioned), is observable in randomly oriented condensed phase systems, and the molecular effect arises as a consequence of molecular adsorbate alignment.

There are subtle differences between the angular distribution effects in Parts I and III. Those in Part I arise from linear (k-space) momentum conserving transitions in itinerant states--sharp in real space because they are really k-space distributions. In Part III, the effects arise from (localized) angular momentum conservation, reflecting the symmetry properties of orbitals--broader real space angular distributions, although somewhat sharper in the molecular case because the orbitals are aligned.

Individual results are discussed separately in each chapter, but one central conclusion is stressed here: atomic and angular effects are strictly non-separable in condensed phase photoemission because the well-known gas phase angular distribution effect[3] is present in modified form in the condensed phase--the condensed phase atomic effect has an anisotropic angular distribution and is therefore generally not a simple measure of total cross section unless all angles are included. It will be shown that atomic effects can be very strong functions of the angle between $\vec{A}$ (radiation vector potential) and $\vec{p}$ (photoelectron momentum vector). They have usually been missed in condensed-phase studies because (1) intensities were not measured, and/or (2) the correct polarization experiments were not performed. The fact that atomic and angular distribution effects usually are separated is probably a matter of relative importance of order-induced and atomiclike angular distribution effects; i.e., although it really depends on the particular experiment, condensed-phase effects that have no atomic analogues (i.e., crystal momentum conservation[5] and

orbital orientation[6]) usually dominate the angular distribution with sharp and intense structures. In this case, the angular part of the photoemission matrix element derived from atomic photoexcitation can be ignored because it is a slowly varying function of angle by comparison, and is not always readily observable in ordered systems. However, if condensed phase ordering effects are small, the atomic analogue can appear as the dominant effect in the angular distribution. The traditional condensed-phase atomic effect[2]--total cross section--can still be measured in many systems, but great care must be taken in the experimental arrangement.

The remainder of this chapter is organized as follows: In Section A general aspects of a condensed-phase photoemission experiment are discussed, with particular emphasis on the nature of atomic effect and angular distribution measurements and their separability. In Section B, a brief overview of the theory of angle-resolved photoemission will be given. Aspects which have implications for atomic and angular distribution effects will be stressed, especially those which are related to bulk valence band structure measurements in Part I. Section C contains a <u>brief</u> experimental description (most details are found in the individual chapters), and Section D is a summary of the diverse experiments described in the remaining chapters of this thesis.

A. General Background

Throughout this chapter, a one-electron view of the energetics in the photoemission process will be taken. In the present and later chapters, it will become increasingly clear that there exist important many-body effects that perturb photoemission in the condensed phase. Nevertheless, the relaxation energy (for example) is ignored, especially because the focus of much of this discussion is on valence band structure. In this work, "condensed phase" refers to the bulk and surface regions of poly- and single-crystalline solids, adsorbate-substrate systems, and supported metal clusters. The range of systems is quite diverse, reflecting the broad scope of this thesis: Cu(211), Pt(100), Cr(100), Cr(110), small clusters of Sm supported on carbon, CO-Pd, Pt, Se-Pt, Ag, CO-Ni(001), and CO-Ni(111).

A condensed-phase photoemission experiment can be characterized by both (scalar) energy- and (vector) momentum-related properties. There are three parts to the photoemission event, each with its associated scalar and vector quantities: photon, system, and photoelectron. Perhaps the most exciting aspect of photoemission is that the measurement of the photoelectron's scalar and vector quantities gives direct information about the associated system quantities. The energy relationship between the three parts is simple. The photon has an energy $h\nu$, the system has initial state energies E_i (in later parts of this chapter, the subscript "n" is used), and the photoelectron (kinetic) energy is E_f. In the one-electron approximation, these are always related by a conservation condition

$$E_i + h\nu = E_f \quad , \tag{1}$$

where E_i and E_f have a suitable energy reference. There are many vector quantities, and there is no analogous general relationship between them, although momentum conservation must always be satisfied, leading to another conservation equation. The important vectors depend on the experimental conditions, but the following are usually considered: The photon is characterized by its vector potential $\vec{A}$ (Ref. 7), and in some cases the propagation wave vector $\vec{k}_{h\nu}$ is important; the system has an associated coordinate system $(\vec{x}, \vec{y}, \vec{z})$ that might consist simply of a single vector such as the surface normal $\vec{n}$ or an adsorbate molecular axis $\vec{M}$, or it might contain a full crystallographic coordinate scheme and the bound electron crystal momentum wave vectors $\vec{k}_i$; and the outgoing photoelectron is described by its external momentum vector $\vec{p}$ and/or its internal crystal momentum wave vector $\vec{k}_f$.

A general spherical coordinate scheme for these vector quantities is depicted in Fig. 1. The axes $(\vec{x}, \vec{y}, \vec{z})$ refer to the coordinates of the system such that $\vec{z}$ and $\vec{n}$ are parallel. Thus, the angles (θ,ϕ) for $\vec{A}$ and $\vec{p}$ are canonically referenced to the $\vec{x}$ and $\vec{z}$ axes as shown in Fig. 1. There is an additional angle, α (between $\vec{A}$ and $\vec{p}$), that is important in angular distribution studies. It can be derived from the (θ,ϕ) angles via the relation

$$\cos\alpha = \cos\theta_A \cos\theta_p + \sin\theta_A \sin\theta_p \cos(\phi_p - \phi_A) \quad . \tag{2}$$

This general coordinate scheme is quite useful and it will be referred to quite frequently.

Atomic effects[2] traditionally refer to phenomena that are manifested in the total photoemission cross section $\sigma_{fi}(E_f)$ of a particular initial state i to a final state f, but not in its angular properties, the latter being either averaged over or deemed unimportant. Thus, the physical view in this case is that the local atomic environment[8] dominates the photoemission event with a photocurrent $I(E_f)$ reflecting atomiclike behavior in $\sigma_{fi}(E_f)$. An atomic effect measurement can usually be achieved by integrating over $\vec{p}$ (angle-integrated PES), employing disordered (or polycrystalline) systems, using unpolarized radiation, probing core levels with x-ray photoemission, or all of the above. The advent of synchrotron radiation as a source of photons has facilitated the measurement of $\sigma_{fi}(E_f)$ [or $\sigma_{fi}(h\nu)$] in a number of interesting atomic-effect experiments with different materials.[8-12] Additionally, atomiclike resonances in $\sigma_{fi}(E_f)$ have been found in several systems.[13-16] The magnitude of $\sigma_{fi}(E_f)$ gives much insight into atomic properties, and measurement of its energy dependence is critical in this regard (see Chapter VI). In the overwhelmingly large field of analytical x-ray photoemission[17] (usually referred to with Siegbahn's acronym ESCA[18]), photoelectron energy distribution curves (EDCs) routinely reveal the elemental composition of materials by virtue of the atomic or localized nature of core-level photoemission.

Angular distribution studies refer to experiments where the vector properties of photoemission are probed.[19] This can be done (i.e., with synchrotron radiation) in conjunction with energy-dependence measurements. The major experimental requirement is that the technique of angle-resolved photoemission (ARP) be employed. Vectors such as $\vec{A}$, $\vec{k}_{h\nu}$, $\vec{n}$, $\vec{M}$, and $\vec{k}_i$ can be present in any PES experiment, but ARP is necessary to measure a well-defined $\vec{p}$ vector. In ARP, $\vec{p}$ is defined by utilizing an electron analyzer with a known, small ($\pm$ 2 to 5°) angular acceptance. It is not always necessary that the angles (θ_p,ϕ_p) be variable in an angle-resolved experiment, but it is naturally more informative to be able to change the orientation of $\vec{p}$. Photoemission can be conceptualized as a three step process:[20] (1) photoexcitation, (2) electron transport to, and (3) escape from the surface. There are numerous examples where ARP has been successfully employed to probe the effect of all three steps.[21] Here, the discussion is concerned with the first step, because it is the only one where atomic effects occur. It would otherwise be ridiculous to ignore the fact that the second and third steps can have large effects on the angular distribution even if the first step is atomiclike.[22-26] A prime example is core-level photoelectron diffraction.[22-25] Thus, we in effect equate photoemission cross section with photoexcitation cross section even though this is not rigorously correct. Actually, it will be shown in the next section that the effect of step three can be ignored if the internal angular distribution of photoelectrons is considered.

There is a particularly insightful, qualitative argument for the validity of separating atomic (i.e., total intensity) and angular properties in photoemission. In an ordered material (single- or polycrystalline) the potential $V(\vec{r})$ has the periodicity of the crystal lattice. Consider the photoexcitation matrix element (M_{fi}) between an initial state i and a final state f, where i and f are both eigenstates of the ground-state one-electron Hamiltonian $\mathcal{H}$ (in several chapters, it will be shown that this is at best only approximate[27]): $M_{fi} \propto \langle f|\vec{A}\cdot\vec{P}|i\rangle$. In this formulation, the $\vec{P}\cdot\vec{A}$ term in the interaction Hamiltonian $\mathcal{H}'$ is, as usual, ignored, because it mainly introduces additional surface terms to M_{fi}. It is straightforward to show that[28-30]

$$\langle f|\vec{A}\cdot\vec{P}|i\rangle = \langle f|[\mathcal{H},\vec{A}\cdot\vec{P}]|i\rangle(E_f - E_i)^{-1}$$

$$= i\hbar(E_f - E_i)^{-1}\,\vec{A}\cdot\langle f|\vec{\nabla}V|i\rangle \quad , \tag{3}$$

where V is the potential part of $\mathcal{H}$. The latter form of M_{fi} indicates that its magnitude is proportional to the gradient of $V(\vec{r})$. Think of $V(\vec{r})$ as a muffin-tin potential; $\vec{\nabla}V(\vec{r})$ is largest in the ion-core region and is rather small outside the atomic sphere. Thus, the atomic part of $V(\vec{r})$ is responsible for the finite cross section $\sigma_{fi} \propto |M_{fi}|^2$. In this atomic picture, the photoexcitation is essentially localized at the atom, giving rise to a total atomic photoyield. On the other hand, condensed phase angular distribution effects in this photoyield, which

depend highly on the physics of momentum conservation, transport phenomena, and escape processes, should arise from the part of the potential (thus, the wave function) external to the core[30] (this is really just another way of saying that a free electron cannot absorb a photon). Therefore, if disorder is induced by the methods discussed above, atomiclike photoemission is the only remainder. An obvious manifestation is that core-level spectra are generally viewed as atomiclike, because there is minimal amplitude in the initial-state wave function outside the core. The important (and obvious?) but subtle point that has been left out is that the atomic-core photo-excitation process described here could also have an angular effect in the condensed phase that does not depend on alignment of atoms. This is why atomic and angular distribution effects are nonseparable. Also, it can be asked: If the atomic core is responsible for the photoyield, is the final-state wave function approximated very well by a plane wave?[30] It is sometimes standard practice to do so.

B. Internal Photoemission

In the ensuing discussion, the photoemission process is analyzed internally. In this way, many of the important aspects of PES and angular distributions can be rationalized. This is simply a way of considering only the first of the three steps. It should, however, be kept in mind that the form of the measured external angular distribution can be quite different from the internal distribution because of transport and surface effects. Such perturbing effects will be

considered later in this section. The only other requirements imposed are (1) lattice periodicity so that band states exist, and (2) the one-electron approximation holds. Sections B.1 through B.3 apply mainly to valence band structure. In Section B.4, the breakdown or smearing of $\vec{k}$-conservation will be considered, with part of the emphasis on recovery of traditional atomic effects in the photoemission cross section.

1. The General Form of the Angular Distribution: $\vec{k}$-Conservation in Valence Bands.

Consider the internal photoemission intensity I in a particular final state of energy E_f and crystal momentum $\vec{k}_f$ excited by photons with energy $h\nu$. Most theoretical formulations of the intensity (and there are many[20,22,28-37]) start with an expression of Fermi's Golden Rule:

$$I_{h\nu}(E_f,\vec{k}_f) \propto \sum_{\vec{k}_i}^{BZ} \sum_{n}^{occ.} |\langle E_f,\vec{k}_f|(\vec{A}\cdot\vec{p} + \vec{p}\cdot\vec{A})|E_n,\vec{k}_i\rangle|^2 \times \delta[E_f(\vec{k}_f) - E_n(\vec{k}_i) - h\nu] \quad . \tag{4}$$

The sum is taken over all occupied energy levels (occ.) at each $\vec{k}_i$ point in the first Brillouin zone (BZ), and the delta function expresses the energy conservation condition, Eq. (1). Let us concentrate on the photoemission matrix element $|M_{fi}|^2 \propto |\langle E_f,\vec{k}_f|(\vec{A}\cdot\vec{p} + \vec{p}\cdot\vec{A})|E_n,\vec{k}_i\rangle|^2$. As usual, the surface-field

term $\vec{P}\cdot\vec{A}$ can be ignored,[38] especially because we are dealing with internal emission for now. The spatial part of the vector potential is $\vec{A} \propto \hat{\varepsilon}\ \exp(i\vec{k}_{h\nu}\cdot\vec{r})$. For simplicity, the wave vector $\vec{k}_{h\nu}$ is also ignored (it has a negligible effect on spectra for photon energies below about 200 eV anyway[39]). However, the incorporation of $\vec{k}_{h\nu}$ into $|M_{fi}|^2$ will be investigated later. The final state is taken to be a plane wave $|E_f,\vec{k}_f\rangle = \exp(i\vec{k}_f\cdot\vec{r})$. This has been the subject of controversy in recent years[30-32,37,40-51] and is discussed in considerable detail later in this section and in several additional chapters (especially II and IV) of this thesis. The initial states must be of the Bloch form: $\psi_{n\vec{k}}(\vec{r}) = U_{n\vec{k}}(\vec{r})\ \exp(i\vec{k}\cdot\vec{r})$, where $U(\vec{r})$ has the periodicity of the lattice (the plane-wave final state satisfies this also, with $U = 1$ as in the so-called "empty-lattice" approximation). The connection between Eq. (4) and atomiclike photoemission will be readily apparent later if a tight binding or Wannier Bloch form is assumed for the initial state:

$$|E_n,\vec{k}_i\rangle = \sum_s \phi_{n,s}(\vec{r} - \vec{R}_s)\ \exp(i\vec{k}_i\cdot\vec{R}_s) \quad ; \tag{5}$$

where the sum is over lattice points with vectors $\vec{R}_s$, and $\phi_{n,s}$ is a Wannier or tight-binding function centered at $\vec{R}_s$. Using these initial- and final-state wave functions, $|M_{fi}|^2$ becomes:[32]

$$|M_{fi}|^2 \propto \cos^2\alpha_f\,|\Phi_n(\vec{k}_f)|^2\,\Big|\sum_s \exp[i(\vec{k}_i - \vec{k}_f)\cdot\vec{R}_s]\Big|^2 \quad , \tag{6}$$

where $\alpha_f = \angle(\vec{A},\vec{k}_f)$ ($\neq \alpha$ in Section A) and $\Phi_n(\vec{k}_f)$ is the Fourier transform or momentum representation of $\phi_n(\vec{r})$ evaluated at $\vec{k}_f$. It has been assumed that Φ is site-independent. Additionally,[32] the term

$$\left| \sum_s \exp[i(\vec{k}_i - \vec{k}_f) \cdot \vec{R}_s] \right|^2 = \sum_{s,t} \exp[i(\vec{k}_i - \vec{k}_f) \cdot (\vec{R}_s - \vec{R}_t)] \quad (7)$$

reflects, via Bloch's theorem, the alignment of orbitals (ϕ) in the solid state. Since $\vec{k}$ is a "good" quantum number, the ϕ_s's are in spatial phase coherence with each other via the factor $\exp(i\vec{k}_i \cdot \vec{r})$. Consider them to be a series of coherent electron guns. In photoexcitation, the photon does not change the phase ($\vec{k}_{h\nu} \sim 0$), so the excited electrons must not only be coherent <u>in</u> the final state [$\exp(i\vec{k}_f \cdot \vec{r})$] but also <u>with</u> the initial state. Phase is only conserved modulo $\exp(i\vec{G} \cdot \vec{r})$; i.e., $\vec{k}$ is conserved modulo $\vec{G}$, where $\vec{G}$ is a reciprocal lattice vector, giving rise to the condition $\vec{k}_i - \vec{k}_f = \vec{G}$. Consider this another way: the momentum mismatch created in photoexcitation is compensated by the entire crystal lattice (that is, if no other momentum transfer takes place), which is quantized in $\vec{G}$ vectors. Finally, a third view: Eq. (7) is similar to the Bragg scattering condition found in x-ray diffraction. The sum over lattice vectors is negligible unless $\vec{k}_i - \vec{k}_f = \vec{G}$, i.e.,

$$\sum_{s,t} \exp[i(\vec{k}_i - \vec{k}_f) \cdot (\vec{R}_s - \vec{R}_t)] = \sum_{\vec{G}} \delta(\vec{k}_i - \vec{k}_f - \vec{G}) \quad . \quad (8)$$

Equation (8) is the crystal momentum conservation counterpart to the energy conservation condition [Eq. (1)] for a system with lattice periodicity. It represents a direct interband transition requirement because the photoexcitation $\vec{k}_i \rightarrow \vec{k}_f = \vec{k}_i - \vec{G}$ occurs at a single point ($\vec{k}_i$) in the reduced zone scheme.

Substitution of Eqs. (6), (7), and (8) into (4) gives for the angle-resolved intensity:

$$I_{h\nu}(E_f,\vec{k}_f) \propto \sum_{\vec{k}_i}^{BZ} \sum_{n}^{occ.} \sum_{\vec{G}} \cos^2\alpha_f \; |\Phi_n(\vec{k}_f)|^2 \; \delta(\vec{k}_i - \vec{k}_f - \vec{G}) \times \delta[E_f(\vec{k}_f) - E_n(\vec{k}_i) - h\nu] \quad . \tag{9}$$

The momentum conservation delta function in Eq. (9) leads to a tremendous reduction in the number of allowed $\vec{k}_i$ states--only a few terms, if any, survive. This gives rise to a large anisotropy in the angular distribution of a particular initial state, because the electron propagation direction is strictly confined by its group velocity vector:

$$\vec{v}_n(\vec{k}) = \hbar^{-1}\vec{\nabla}_{\vec{k}} E_n(\vec{k}) \quad , \tag{10}$$

and for a free-electron-like band, $\vec{v}_n(\vec{k})$ is parallel to $\vec{k}$. Thus, with a final-state wave vector $\vec{k}_f = \vec{k}_i - \vec{G}$, the photoelectron propagates in the $\vec{k}_f$ direction. Therefore, at the particular final-state energy

(E_f) the angular distribution will contain intensity at only a few angles, as governed by the two delta functions in Eq. (9). As the internal "analyzer" is rotated to select different $\vec{k}_f$ values, the angular distribution contains delta-function-shaped peaks, i.e., spikes, modulated in amplitude by the factors $\cos^2\alpha_f$ and $|\Phi_n(\vec{k}_f)|^2$.

The "sharpness" of $\vec{k}$-conserving direct transitions can be comprehended by considering that the initial- and final-state wave functions extend spatially throughout the crystal.[52] Thus, the transitions are delta functions in k-space. It would appear that measurement of E_f and $\vec{k}_f$ by virtue of peak position in the EDC and orientation of the electron analyzer in an ARP experiment gives $E_n = E_f - h\nu$ and $\vec{k}_i = \vec{k}_f + \vec{G}$ directly, representing a powerful method for the empirical determination of $E_n(\vec{k})$ relations. While the true external experimental situation is not so simple and the peaks are not actually delta functions in angle (see Section B.4 and Chapters II-IV), the direct-transition requirement can still be utilized to "map" band structures if the photoelectron dispersion relation $E_f(\vec{k}_f)$ is known. This will become more apparent in the next two sections (Sections B.2 and B.3), where diagrammatic demonstrations of direct-transition angular distributions will be presented. There are several additional features concerning Eq. (9) to discuss, first.

The photoemission intensity is modulated by the terms $\cos^2\alpha_f$ and $|\Phi_n(\vec{k}_f)|^2$ in Eq. (9). The $\Phi_n(\vec{k}_f)$ term generally has an angular dependence in k-space which behaves like that of $\phi_n(\vec{r})$ in r-space, because the Fourier transformation does not alter the angular parts of

the wave function in either the real or momentum representations.[31,44] This is the basis for the d-orbital-directed x-ray photoemission effect discovered by McFeely, et al.[6] We comment on it here because orbital-directed photoemission is an atomic effect to the extent that it is derived from orbital characteristics and not band-structure effects. However, it is not the type of atomic angular distribution effect discussed before; i.e., it is orientation-related, with no gas-phase analogue because the angular parts of Φ are averaged over in the latter. Specifically, if $Y_n(\theta_{\vec{r}},\phi_{\vec{r}})$ is the angular part of $\phi_n(\vec{r}) = R_n(r)Y_n(\theta_{\vec{r}},\phi_{\vec{r}})$ and $\Phi_n(\vec{k}) = P_n(k)Y_n(\theta_{\vec{k}},\phi_{\vec{k}})$, then $|\Phi_n(\vec{k})|^2 \propto |P_n(k)|^2$ in a randomly ordered system, where R_n and P_n are the radial parts of the real and momentum representation wave functions, respectively.

The polarization-dependence term, $\cos^2\alpha_f$, is interesting because it suggests that the angular distribution is proportional to $\vec{A}\cdot\vec{k}_f$, having no intensity for $\vec{A} \perp \vec{k}_f$. This is a simple consequence of the plane-wave approximation (PWA) for the final state.[32] It was pointed out above that the finite cross section comes from the atomic core.[30,42] It is well known that the PWA yields incorrect angular distributions for free atoms.[53] What, then, of the condensed phase? If it cannot yield correct atomic angular distributions, how can the PWA be expected to give the correct condensed-phase angular distribution [as in Eq. (9)]? There are ordered condensed-phase systems which yield significant intensity in the $\vec{A} \perp \vec{k}_f$ geometry at low photon energies.[41] Additionally, the PWA does not accurately predict relative EDC peak intensities

in ARP spectra.[44] However, the PWA is generally found to be a good approximation to the photoelectron wave function as far as propagation direction, band structure, and energy position of EDC peak structures are concerned in metals: it yields empirical valence band dispersion relations that agree well with theory.[54] There are at least three plausible reasons for this: (1) As mentioned before, the atomic part of the PES process mainly yields the total cross section in ordered systems for which the angular distribution is dominated by the sharp direct-transition resonances. The atomic part contributes a background that varies more slowly with angle and is thus rendered unimportant regardless of its validity. (2) It is apparent from this discussion that phase-coherence relationships are the important determining factors for the photoelectron propagation direction and band eigenstate. The plane wave has all the important characteristics of a phase factor. (3) The effective pseudopotential for photoelectron band states should be weak in d-band metals,[30] and the coefficients in the pseudo-wave-function-plane-wave expansion should become smaller with increasing $|\vec{G}|$ and E_f, except for the leading term ($|\vec{G}| = 0$).

The last point should be discussed in more detail. Smith, et al.[19,41] explained the presence of intensity in the $\vec{A} \perp \vec{k}_f$ geometry by taking the final state to be an expansion in plane waves rather than a single plane wave; i.e.,

$$|E_f,\vec{k}_f\rangle = \sum_{\vec{G}'} C_{\vec{G}'}(\vec{k}_f)\, \exp[i(\vec{k}_f - \vec{G}') \cdot \vec{r}] \quad , \tag{11}$$

along with an initial state $|E_n,\vec{k}_i\rangle$ given by Eq. (5), yielding for the angle-dependent matrix element magnitude:

$$|M_{fi}|^2 \propto |\sum_{\vec{G}} \sum_{\vec{G}'} [\vec{A}\cdot(\vec{k}_f - \vec{G}')]\, C_{\vec{G}'}(\vec{k}_f)\, \Phi_n(\vec{k}_f - \vec{G}') \times \delta(\vec{k}_i - \vec{k}_f + \vec{G}' - \vec{G})|^2 \quad . \tag{12}$$

The form of Eq. (12) indicates that the polarization dependence now contains an additional factor: $\vec{A}\cdot\vec{G}'$. Therefore, photoemission intensity can occur at any emission angle, so long as there exists a $\vec{G}' \not\perp \vec{A}$ to supply the momentum transfer. But this is the whole point. Crystal momentum transfer in the various $\vec{k}_f - \vec{G}'$ channels is governed by the coefficients $C_{\vec{G}'}(\vec{k}_f)$, which, in turn are generated in the plane-wave expansion by an effective pseudopotential

$$V(\vec{r}) = \sum_{\vec{G}'} V_{\vec{G}'} \exp(i\vec{G}'\cdot\vec{r}) \tag{13}$$

via first order perturbation theory, yielding for the C's:

$$C_{\vec{G}'}(\vec{k}_f) \propto V_{\vec{G}'}(|\vec{k}_f|^2 - |\vec{k}_f - \vec{G}'|^2)^{-1} \quad ; \quad |\vec{G}'| \neq 0 \quad . \tag{14}$$

The series in Eq. (13) converges rapidly in metals, and relatively few

$V_{\vec{G}'}$ terms should be important at any energy E_f. Furthermore, inspection of the terms in the right-hand side of Eq. (14) indicates that $C_{\vec{G}'}(\vec{k}_f)$ decreases with increasing $|\vec{G}'|$ and $|\vec{k}_f|$. Therefore, except at low E_f (near threshold), only the leading term (with $|\vec{G}'| = 0$) of the sum over $\vec{G}'$ in Eq. (12) survives with any appreciable amplitude, giving rise exactly to the expression in Eq. (9) for intensity with the plane-wave final state if the small terms are ignored, even though the total intensity may need to include many more terms. The conclusion, then, concerning the photoemission final state is that the PWA is totally acceptable in explaining EDC peak structures and their energy dispersion characteristics because the leading term in Eq. (12) dominates at most energies.[50,51] Therefore, a single plane-wavelike photoelectron dispersion relation, with only one $\vec{G}$ vector component (the one involved in the direct transition) from the sum in Eq. (9), should be sufficient to explain the origin of all dispersive initial-state peak structures in ARP EDCs, even though a prediction of the total intensity might require many $\vec{G}'$ vector components of the sum in Eq. (12). This is consistent with the experimentally observed result that photoemission yield from Cu(110) in the $\vec{A} \perp \vec{k}_f$ geometry is attenuated by a factor of ca. 100 relative to a geometry with $\alpha_f = 27°$, at $h\nu \geq 40$ eV (Ref. 46). It is also consistent with the results discussed in Chapters II through IV for the range 6 eV $\leq h\nu \leq$ 34 eV. Together with the direct (Chapter II) and indirect (Chapters III and IV) demonstration that photoelectron bands show dispersion through

bulk one-electron conduction band gaps, this gives us a pretty clear picture of final-state band structure in metals.

2. Mahan Cones and Valence Band Angular Distributions.

Mahan[29] was the first to demonstrate theoretically that photoelectron angular anisotropy in single crystals of free-electron-like metals is significant and has the form of conical distributions. These distributions represent a direct consequence of momentum and energy conservation. In the spirit of this early work,[29] we shall consider the direct-transition process involving free-electron-like bands to illustrate some of the important features of the direct-transition process. Since the crystal momentum vector is conserved [Eq. (8)], we resort to k-space. The first BZ of the face-centered cubic (FCC) lattice is shown in Fig. 2, in which an irreducible (1/48)th wedge is the region bound by the dashed and solid lines. The high symmetry points are indicated by their respective point group labels. A portion of the extended-zone plane that cuts through $\Gamma\Lambda LUSX\Delta\Gamma$ [the $(01\bar{1})$ plane] is shown in Fig. 3. Some of the reciprocal lattice points are indicated by their respective k-space coordinates, and the first BZ is enclosed by the six-sided polygon. Also shown is a circle indicating a constant energy contour for $\vec{k}$ states in the first BZ with $E_n(\vec{k}) = E_i$; the vector shown represents one of the $\vec{k}$'s. All $\vec{k}$ vectors ending on the circle correspond to occupied states with energy E_i. The circular shape of the contour is the result of imposing the nearly-free-electron (NFE) approximation to the valence band

structure; i.e., $E_n(\vec{k}) = \hbar^2|\vec{k}|^2/2m$ (m is the electron mass, and the inner potential is assumed to be zero for simplicity). Generally, the process to be described here is valid for valence bands in transition metals if (1) distortions in the sphericity of $E_n(\vec{k}) = E_i$ that are produced by the crystal potential are accounted for, and (2) it is noted that the photoemission final state must be a plane wave in vacuum.

In Fig. 4, the same k-space region is shown as in Fig. 3, except that now there are constant energy surfaces centered at the $(\bar{1}\bar{1}\bar{1})$ and $(\bar{2}00)$ lattice points. These surfaces are both otherwise the same, with $E_{n'}(\vec{k}') = \hbar^2|\vec{k}'|^2/2m^* = E_i + h\nu = E_f$. Consider the sphere centered about $(\bar{1}\bar{1}\bar{1})$. The inset in the lower left corner shows (a) the intersection of the two contours $E_n(\vec{k})$ and $E_{n'}(\vec{k}')$, (b) a dashed line corresponding to the contour $E_{n'}(\vec{k}') - E_n(\vec{k}) = h\nu$, and (c) the vectors $\vec{k} = \vec{k}_i$, $\vec{G} = \vec{G}_{\bar{1}\bar{1}\bar{1}}$, and $\vec{k}_f = \vec{k}_i - \vec{G}_{\bar{1}\bar{1}\bar{1}}$. The point of intersection of the three energy contours in the $(01\bar{1})$ plane corresponds to the equalities $E_f = E_i + h\nu$ and $\vec{k}_f = \vec{k}_i - \vec{G}_{\bar{1}\bar{1}\bar{1}}$, or $E_i + h\nu = \hbar^2|\vec{k}_i - \vec{G}_{\bar{1}\bar{1}\bar{1}}|^2/2m^*$. This is just the direct-transition condition, where energy and momentum conservation conditions [Eqs. (1) and (8), respectively] are simultaneously satisfied. According to Eq. (10), the photoelectron corresponding to this interband transition is traveling in the $\vec{k}_f = \vec{k}_i - \vec{G}_{\bar{1}\bar{1}\bar{1}}$ direction. There are two such directions indicated, but it is not difficult to generalize to the three-dimensional case: the angular distribution of photoelectrons is conical in shape, centered about the $\vec{G}$ vector involved in the direct transition,[20,29] with the photoelectron wave vectors ending at a plane corresponding to

the contour $E_{n'}(\vec{k}') - E_n(\vec{k}) = h\nu$. At the energy E_f, there are no internal direct-transition photoelectrons at other angles corresponding to momentum transfer with $\vec{G}_{\bar{1}\bar{1}\bar{1}}$. However, $\vec{G}_{\bar{2}00}$ is shown in Fig. 4 to also satisfy the conservation conditions, with $\hbar^2|\vec{k}_j - \vec{G}_{\bar{2}00}|^2/2m^* = E_i + h\nu$. Thus, there is an additional cone of photoemitted electrons at E_f centered about $\vec{G}_{\bar{2}00}$.

Employing NFE initial and final states, Mahan[29] obtained for the photoemission matrix element:

$$|\langle E_f,\vec{k}_f|\vec{A}\cdot\vec{P}|E_n,\vec{k}_i\rangle|^2 \propto \sum_{\vec{G}}(\vec{A}\cdot\vec{G})^2\, V_{\vec{G}}^2\, \delta(\vec{k}_i - \vec{k}_f - \vec{G}) \quad , \qquad (15)$$

where the V_G's are the Fourier components of the crystal potential [Eq. (13)]. Equation (15) illustrates that the relative strengths of the $\vec{G}_{\bar{1}\bar{1}\bar{1}}$ and $\vec{G}_{\bar{2}00}$ transitions in Fig. 4 depend not only on $\angle(\vec{A},\vec{G})$, but also on the magnitudes of $V_{\bar{1}\bar{1}\bar{1}}$ and $V_{\bar{2}00}$. It should not be necessary to consider very many higher $\vec{G}$ transitions at a given E_f because either the initial- and final-state energy contours will not overlap [Eq. (1) will not be satisfied], or the associated $V_{\vec{G}}$ will be negligible for the same reason as discussed in Section B.1: Equation (13) should converge rapidly with increasing $|\vec{G}|$. What should now be clear is that the shape and orientation of the photoelectron cone directly leads to the initial-state bands $E_n(\vec{k})$ if the energy E_f is measured concurrently with the angular distribution. Of course, the cones are still internal, but the next section will

demonstrate that the external cones lead to information--empirical determination of $E_n(\vec{k})$--about the valence bands if the normal emission geometry is chosen.

Incidently, Eq. (15) differs from Eqs. (6), (7), and (8) in two respects: (1) a sum over $V_{\vec{G}}$ has replaced $\Phi_n(\vec{k}_f)$, and (2) $\vec{A}\cdot\vec{G}$ replaces $\vec{A}\cdot\vec{k}_f$. The first modification reflects the nature of the NFE and tight-binding initial states. Of the two choices, the tight-binding function is preferable for d-band metals. Although the NFE approach works well for the final states, it is a poor approximation for the bound d bands.[20,55] The second difference gives a somewhat different polarization dependence for emission angles that are not oriented along the $\vec{G}$ vector involved in the transition. However, this is <u>not</u> the same polarization dependence as in Eq. (12). There, the expression predicts finite intensity for s-polarization of the radiation (i.e., $\vec{A}$ orthogonal to the plane of incidence) and the normal emission geometry [where $\theta_{\vec{k}_f} = \angle(\vec{k}_f,\vec{n}) = 0°$], whereas Mahan's expression generally does not. In Section B.3, it will be shown quite simply that normal emission direct-transition intensity from low-index faces usually arises only from transitions involving $\vec{G} \parallel \vec{k}_f$ in the Mahan-cone model expressed by Eq. (15). Therefore, if $\alpha_f = 90°$ and $\theta_{\vec{k}_f} = 0°$, then $\vec{A}\cdot\vec{G} = \vec{A}\cdot\vec{k}_f = 0$. In Section B.1, it was mentioned that a plane-wave final state always gives rise to a $\cos^2\alpha_f$ dependence in the angular distribution, and that this is also true for free atoms (and molecules). But, Mahan employed a plane-wave final state also. The reason that the $\cos^2\alpha_f$ dependence is not found in Eq. (15) is that the

matrix element was calculated in the form of the operator shown on the right hand side of Eq. (3) to include the effect of a real (pseudo) crystal potential. In so doing, the plane-wave final state was orthogonalized (OPW) to the initial state. This is a requirement for the transformation in Eq. (3). The OPW final state gives the different polarization dependence to the angular distribution in Eq. (15), just as it does for molecules in the gas phase. In fact, an OPW gives the correct form of the angular distribution for photoemission from randomly oriented gas-phase systems, unlike the unorthogonalized plane wave.[56]

Mahan[29] noted that the various transitions like $\vec{k}_i \rightarrow \vec{k}_i - \vec{G}$ allowed by Eq. (15) are not the only possible ones; i.e., electrons can be emitted in other directions. He termed the first type, with $\vec{k}_f = \vec{k}_i - \vec{G}$, primary cones because they should be the most intense transitions and are truly conical in shape with the cone center at $\vec{G}$. The second type, with $\vec{k}_i \rightarrow \vec{k}_i - \vec{G} - \vec{G}'$ are called secondary cones, and are not conical because they are obtained by adding the same $\vec{G}'$ to each $\vec{k}_f$ in a conical distribution. They come about because the crystal potential causes the true final state $|E_f,\vec{k}_f\rangle$ to be a full Bloch sum of plane waves in a form identical to Eq. (11), giving intensity to the $\vec{k}_f - \vec{G}'$ channels. The matrix element for this looks like Eq. (12), if Φ_n and $\vec{A}\cdot(\vec{k}_f - \vec{G}')$ are replaced by $V_{\vec{G}}$ and $\vec{A}\cdot\vec{G}$, respectively. Secondary Mahan cones are not expected to yield peak structures in ARP EDCs for the same reasons, discussed in Section B.1, that the plane-wave final state is valid. The $C_{\vec{G}'}$'s are all small

except for the leading coefficient with $|\vec{G}'| = 0$; in the limit of neglecting all other $C_{\vec{G}'}$ terms, the matrix element in Eq. (15) is once again obtained. Secondary Mahan cones are not expected to yield direct-transition peak structures in ARP EDCs. In the limit of a NFE model for the initial states, the secondary cones essentially give the same effect as the sum over $\vec{G}'$ vectors in Eq. (12); the physics is the same. To repeat the important observation noted before: Experience has shown that in nearly every system studied, and for all results discussed in this thesis, the plane-wavelike final state yields the correct interpretation of all major direct-transition features in ARP valence band spectra, even though the single PWA can yield incorrect EDC peak intensities.[54] This is evidenced by (1) the absence of secondary-cone-derived peaks in the spectra and (2) agreement of derived $E_n(\vec{k})$ relations with bulk band theory. As long as an experimental band structure study is concerned mainly with peak positions and not intensities,[49] there is no problem with the PWA. Finally, d-band metals have constant energy contours different from those in Figs. 3 and 4, but Mahan's original primary-cone direct transition model for NFE metals carries over quite well to the d-band metals. Work reported in this thesis and elsewhere demonstrates this.[57]

3. The Normal Emission Geometry for Valence Band Structure Studies.

In this section, the external angular distribution is discussed, because it ties in directly with Sections B.1 and B.2, and must be measured in an actual ARP experiment to determine band structure

properties. A major perturbation of the direct-transition angular distribution is the surface. Consider a NFE direct-transition photoelectron propagating internally in a state $|E_f,\vec{k}_f\rangle = |E_f^v,\vec{k}_{f_\parallel},\vec{k}_{f_\perp}\rangle$, where the energy reference is the vacuum level; $\vec{k}_{f_\parallel}$ and $\vec{k}_{f_\perp}$ refer to the surface parallel and perpendicular components of the internal final-state crystal momentum wave vector, respectively. At the surface-vacuum interface, only $\vec{k}_{f_\parallel}$ is conserved as the electron is matched to a running plane wave in the vacuum--the electron suffers from refraction which <u>changes</u> its propagation direction.[46,58] Additionally, the surface acts as a source of crystal momentum; $\vec{k}_{f_\parallel}$ is only conserved modulo a surface reciprocal lattice vector $\vec{G}_\parallel$. Thus, we have the following relationships:

$$E_f^v(\vec{k}_f) = (\hbar^2|\vec{k}_f|^2/2m^*) + V_0^v = |\vec{p}|^2/2m_e \quad , \tag{16a}$$

$$\vec{p}_\parallel = \hbar(\vec{k}_{f_\parallel} + \vec{G}_\parallel) \quad , \tag{16b}$$

and

$$|\vec{p}_\perp| = (2m_eE_f^v - |\vec{p}_\parallel|^2)^{1/2} \quad , \tag{16c}$$

where $\vec{p}$ is the <u>external</u> photoelectron momentum vector (as in Section A), V_0^v is the inner potential, and m^*, m_e are effective and free-electron masses, respectively. Refraction effects can be quite large when E_f^v and V_0^v are of the same order of magnitude.[46] <u>Surface umklapp scattering</u>, which corresponds to $|\vec{G}_\parallel| > 0$ in Eq. (16b), is

generally not an important effect unless the surface has a superlattice[59] (see Chapters III and IV).

Refraction adds an indeterminacy to the relationship between the internal and external angular distributions. It is critical, however, that this be overcome because the relationship between $\vec{p}$ and $\vec{k}_f$ must be understood for the external distributions to yield information about $E_n(\vec{k}_i)$ inside the crystal. There are various ways to overcome this problem in an ARP experiment. Two of the most useful approaches are: (1) to employ high-enough photon energies that $E_f >> |V_0^v|$, and (2) to select $\vec{p} \parallel \vec{n}$ in the experiment. In this thesis work, the latter method, termed angle-resolved normal photoemission (ARNP), has been utilized in band structure studies. At normal emission, $|\vec{p}_{\parallel}| = 0$ so that in the absence of surface umklapp scattering, Eq. (16b) becomes $|\vec{k}_{f_{\parallel}}| = 0$. Thus, the angular relationships are: $\theta_{\vec{p}} = \theta_{\vec{k}_f} = 0°$, or $\vec{p} \parallel \vec{k}_f$. Additionally, we know from the discussion about photoemission final-state band structure that the free-electron-like approximation holds; i.e., a dispersion relation like that shown in Eq. (16a) should yield an accurate final-state band structure, with m* and V_0^v as variables to be somehow determined. With this model, ARNP-EDC peak energy positions (E_f) yield $\vec{k}_f$ directly. Therefore, $(\vec{k}_i - \vec{G})$ is known, assuming that the peak is derived from a direct transition. If $\vec{G}$ can be determined, then $\vec{k}_i$ is also known, giving $E_n(\vec{k}_i)$ directly. The problem is actually easier than it sounds from these statements, as illustrated by the NFE primary Mahan cone diagrams in Fig. 5 for normal emission from an FCC(111) face. From the "cones" for the two different

photon energies $h\nu_1$ and $h\nu_2$, it is clear that $\vec{G}_{\bar{1}\bar{1}\bar{1}}$ gives rise to primary Mahan cone electrons propagating in the [111] crystallographic direction that were excited from initial states along the same direction in the first BZ. There is a general result for normal emission from low index faces like (100) and (111): the primary cones reduce to lines with $\vec{G}$, $\vec{k}_i$, and $\vec{k}_f$ all parallel to $\vec{n}$. This is always true because the only $\vec{G}$ vectors which can yield $\vec{k}_f \parallel \vec{n}$ for (100) and (111) faces are collinear with $\vec{n}$ and the Γ point in the first BZ. These are the only $\vec{G}$'s for which the initial- and final-state constant energy contours can intersect. Therefore, $\vec{G}$ is always known, and $\vec{k}_i$ is always along $\vec{k}_\perp$. If tunable radiation is used in conjunction with ARNP so that the size of the final-state contour can be varied, the relations $E_n(\vec{k}_i)$ can be determined for the Λ[FCC(111)] and Δ[FCC(100)] lines. This is also the case for the corresponding body-centered-cubic (BCC) low-index faces, i.e., BCC(110) and BCC(100), along Σ and Δ, respectively.

It is not always true that $\vec{G} \parallel \vec{n}$ for FCC(110) and higher-index faces like (211) (see Chapter II); i.e., $\vec{k}_i$ is not always along $\vec{k}_\perp$. In fact, for Cu(211), $\vec{G}$'s along $\vec{n}$ can not be utilized below $h\nu \approx 170$ eV. However, an amazingly simple construction in k-space shows that $\vec{G}$ is always unique and determinate under the conditions that (1) the normal emission geometry is employed, and (2) only primary cones give rise to photoelectrons along $\vec{n}$. This is illustrated for FCC(011) and FCC(211) in Fig. 6. Again, a region of the $(01\bar{1})$ plane in reciprocal space is shown along with the first BZ (shaded portion). Solid and dashed

lines are shown parallel to [211] and [011], respectively, in Fig. 6. Only reciprocal lattice points on one of the lines can give rise to normal emission in the respective [211] or [011] directions. Furthermore, only one inequivalent final-state contour intersects the first zone at any given $h\nu$. Therefore, $\vec{G}$ and $\vec{k}_i$ can always be determined. It cannot be overemphasized that the model described here represents a powerful method for the determination of $E_n(\vec{k}_i)$ relations in crystals.

In an actual ARNP experiment, it is most convenient to use the Fermi energy (E_F) as the reference level. In this way, the empirical dispersion relations can be directly compared with theoretical band structure calculations. The flow diagram below summarizes the procedure outlined above for the utilization of ARNP to empirically determine valence band structure in metals:

$$\begin{array}{ccccc} \text{measure } E_f & \xrightarrow{E_F} & E_f^F & \xrightarrow{\text{final-state model}} & \vec{k}_f, \vec{G} \\ & - h\nu \downarrow & & & \downarrow \text{DTM} \\ & E_n^F & \longrightarrow & E_n^F(\vec{k}_i) & \longleftarrow \vec{k}_i \end{array} \qquad (17)$$

In Eq. (17), E_f refers to the location of a peak in the EDC, E_f^F and E_n^F are energies referenced to E_F, and DTM stands for the direct-transition model with $\vec{k}$-conservation.

4. Effective Relaxation of $\vec{k}$-Conservation and Recovery of Atomic Effects.

The direct-transition process has a dominant influence on the angular distribution of photoemission from initial states with energy-band dispersion; i.e., phase coherence amongst the constituent atomic centers dictates the propagation direction of photoelectrons. However, the ideal mechanism suggested by Eq. (9) is never quite realized in any experiment. Atoms vibrate at finite temperatures, photoelectrons and associated holes have finite lifetimes, valence bands are not usually free-electron-like in d-band metals, the surface can influence the photoemission process, electron analyzers are limited by finite angular and energy windows, and no condensed phase system exhibits perfect order. In Part I of this thesis, it will be demonstrated that some of these effects are important and observable in the form of apparent $\vec{k}$-conservation breakdown and other complications in the valence bands of ordered metals, but perhaps surprisingly, valence band $E_n(\vec{k})$ relations can still be determined from ARNP data in the ultraviolet-photoelectron-spectroscopy or UPS energy region ($h\nu \lesssim 40$ eV) because direct transitions are still present and usually dominate the EDCs. It is the purpose of the present subsection to briefly consider some of the perturbing factors on the angular distribution model already discussed, and especially to point out that they generally give rise to a more atomiclike or localized PES process.

Seven mechanisms will be considered by which the $\vec{k}$-conservation delta function in Eq. (9) becomes a less-constrained term. The first

five effects are intrinsic because they alter the form of the photoemission cross section directly, while the latter two are extrinsic as they arise from experimental conditions that effectively simulate a breakdown of $\vec{k}$-conservation by integrating Eq. (9) over $\vec{k}_f$.

(1) Other linear momenta. If the interaction Hamiltonian is modified so as to contain creation operators for other elementary excitations simultaneous to the photoexcitation event,[60] and if the effect of the photon wave vector $\vec{k}_{h\nu}$ is included, then the delta function in Eq. (8) would take on a form like

$$\sum_{\vec{G}} \delta(\vec{k}_i - \vec{k}_f - \vec{G} + \vec{k}_{h\nu} + \sum_a \vec{q}_a) \quad , \tag{18}$$

where the sum over $\vec{q}_a$ includes all other excitations, usually phonons. The effect of phonon excitation, which is both temperature- and $h\nu$-dependent, has been discussed by several groups[39b,61-63] and will not be detailed here (Chapter IV contains more discussion). Generally, its effect on valence band EDCs is not nearly as severe in the UPS region as it is at x-ray photoemission energies. One of its most salient features is that a momentum conservation condition still exists via the delta function in Eq. (18), but the transitions are no longer direct because $\vec{G}$ is not the only momentum transfer. For a given final state $|E_f,\vec{k}_f\rangle$, more initial states can be selected in the sum over $\vec{k}_i$ [Eq. (9)] that satisfy the momentum requirement. This is, in effect, a BZ-averaging process to the extent that the sum over $\vec{q}_a$ connects many

initial states with the single final state. In the limit of complete zone-averaging, where there always exists a $\vec{q}_a$ such that any $\vec{k}_i$ can be excited to $\vec{k}_f$, Eq. (9) reduces to

$$I_{h\nu}(E_f,\vec{k}_f) \propto \cos^2\alpha_f \sum_n^{occ.} |\Phi_n(\vec{k}_f)|^2 \sum_{\vec{k}_i}^{BZ} \delta[E_f(\vec{k}_f) - E_n(\vec{k}_i) - h\nu] \quad . \quad (19)$$

Equation (19) is the expression for total-density-of-states (TDOS) photoemission; the ARP spectrum reflects the angle-independent density of initial states modulated by the factor $\cos^2\alpha_f \ |\Phi_n(\vec{k}_f)|^2$. Fortunately, this situation is approached only with x-rays or systems that have low Debye-Waller factors[39b] (see discussion in Chapter IV). However, UPS spectra always contain a background structure that probably arises in part from indirect transitions. Finally, the effect of $\vec{k}_{h\nu}$ in Eq. (18) is different from $\vec{q}_a$ because the photon wave vector is always well-defined. Therefore, it does not produce zone-averaging. In fact, in the XPS regime, where its magnitude is not negligible, $\vec{k}_{h\nu}$ can be easily accounted for in the analysis of "direct transitions."[39b,43] The incorporation of $\vec{k}_{h\nu}$ in Eq. (18) can be likened philosophically to the indirect-gap process in a semiconductor at very low temperatures, where a single phonon might account for all of the indirect transitions.

(2) Narrow-band states. Initial-state bands that show little energy dispersion with $\vec{k}_i$ have small group velocities $[|\vec{\nabla}_{\vec{k}} E_n(\vec{k}_i)| \sim 0$, see Eq. (10)]. These are the "narrow-band" states.

The velocity may be small enough that the photohole cannot delocalize throughout the band on the time-scale of the PES process ($\sim 10^{-16}$ sec), in which case the spatial phase coherence condition discussed in Section B.1 does not exist: $\vec{k}_i$ is not a "good" quantum number. This situation especially corresponds to core-level bands, for which the one-electron band velocity is negligible and the outgoing photoelectron interacts with a hole that is essentially localized. The sum over $\vec{k}_i$ in the angular distribution expression can then be performed directly on the phase factor in Eq. (7), yielding[32]

$$I_{h\nu}(E_f,\vec{k}_f)_n \propto \cos^2\alpha_f \; |\Phi_n(\vec{k}_f)|^2 \; \delta(E_f - E_n - h\nu) \quad , \tag{20}$$

where the subscript n now refers to a single initial state. Equation (20) is of the atomic form. If there is no angular dependence in $|\Phi_n(\vec{k}_f)|^2$, the angular distribution will be simply governed by the polarization term $\vec{A}\cdot\vec{k}_f$. Note that this is a slowly varying function of $\vec{k}_f$, unlike the sharp $\vec{k}$-conserving transitions encountered before. Incidently, Eq. (20) would also have resulted from an initial state taken to be a localized atomic orbital[20] (or linear combination, thereof) centered at $\vec{R}_s$, with no phase factor to reflect a $\vec{k}_i$ quantum number: $|E_n\rangle = \phi_n(\vec{r} - \vec{R}_s)$. Also, we generally do not consider the final-state bands, which are free-electron-like, to suffer from narrow-band effects. It might appear that flat d bands in the valence shell of many transition metals would experience this "localization" problem

in addition to core levels. However, even d-band electrons have a finite velocity, and the problem becomes twofold: the hole velocity and lifetime must be considered together. Evidently, based on the size of Part I and the quantity of other recent work, hole lifetimes and group velocities for the d bands are large enough that direct transitions are usually observed. Lifetime effects will be taken up next.

(3) Final-state lifetime broadening. This effect is usually termed momentum broadening because the strict $\vec{k}$-conservation selection rule is relaxed along $\vec{k}_\perp$, thereby increasing the region of $\vec{k}_\perp$ that can give rise to transitions over that allowed by a delta function.[58,59,64] The finite lifetime of the outgoing photoelectron, $\tau_e(E_f)$, places a severe restriction on the spatial extent of the final state: the wave function is confined to a region near the surface, resulting in a loss of phase coherence along $\vec{k}_{f_\perp}$ and thus $\vec{k}_{i_\perp}$. We can easily see how a concomitant "smearing" of the $\vec{k}$-conservation selection rule leads to a lifetime broadened initial-state energy distribution analogously to other types of spectroscopy. The Lorentzian broadening factor is characterized by an energy-dependent "inverse lifetime" half-width, $\Sigma_e(E_f) = \hbar[2\tau_e(E_f)]^{-1}$, for the resulting energy-broadened distribution of photoemitted electrons in a particular final state. Thus, the total final- or initial-state crystal momentum uncertainty is[64]

$$\Delta\vec{k}_\perp = 2(\partial\vec{k}_f/\partial E)\ \Sigma_e(E_f) = 2\Sigma_e(E_f)[\hbar\vec{v}_e(\vec{k}_{f_\perp})]^{-1} \quad . \tag{21}$$

This is related to the broadening in the initial-state energy distribution along $\vec{k}_\perp$ via the hole velocity, giving for the total photoelectron lifetime-induced energy broadening factor

$$\Delta E_n(\vec{k}_\perp) = 2(|\vec{v}_{h_\perp}|/|\vec{v}_{e_\perp}|)\,\Sigma_e(E_f) \quad , \tag{22}$$

where $\vec{v}_{h_\perp}$ and $\vec{v}_{e_\perp}$ are hole and photoelectron group velocities, respectively, along the surface normal. The energy broadening is obviously largest when the photoelectron velocity along the normal is smallest. Another way to view momentum broadening[37,45,58,65] is to consider the inelastic scattering length $\lambda(E_f,\vec{k}_f) = \tau_e(E_f)|\vec{v}_e(\vec{k}_f)|$ to be the spatial restriction factor.[66] Then, $\Delta\vec{k}_\perp$ and λ are simply related by the momentum representation of the uncertainty principle: $\Delta\vec{k}_\perp = [\lambda(E_f)\cos\theta_{\vec{k}_f}]^{-1}$. The form of the energy dependence of $\lambda(E_f)$ is the so-called "universal curve" of electron scattering lengths, shown in Fig. 7 (see, also, Chapter VI), with a minimum in the 50-250 eV region. "Universal" is actually nothing more than a statement of the fact that Σ_e is relatively invariant from one material to another.[64] In early ARP work, $\Delta\vec{k}_\perp$ for typical resonance lamp energies (e.g., He I and He II in Fig. 7) was considered to be so large that the resulting initial-state energy distribution curves were characterized by a <u>complete</u> smearing of $\vec{k}_\perp$; i.e., the EDCs were thought to reflect only the one-dimensional DOS (ODDOS) along $\vec{k}_\perp$ (Ref. 67). This seemed to be a reasonable assumption, because it was presumed that most of the photoemission signal came from the first

layer of atoms ($\lambda \sim 5$ Å), thereby rendering the concept of Bloch's theorem for electrons meaningless along $\vec{k}_\perp$ (Ref. 58). However, many experiments have since shown that the notion of a complete smearing along $\vec{k}_\perp$ is ridiculous for most systems, even at energies near the minimum scattering length.[57] Typical values of $\Delta\vec{k}_\perp$ are usually only several percent of a BZ dimension in the UPS energy region.[45] In several UPS experiments, values for Σ_e have been determined empirically from the energy broadening of ARP-EDC-direct-transition features.[59] The results, Σ_e typically 1 to 5 eV, support the idea that $\Delta\vec{k}_\perp$ is a much smaller perturbation than originally thought. It should be noted, however, that the extent to which the ODDOS plays a role in determining some of the valence band EDC peak structures is still under question.[68] In some systems (see Chapters III and IV) it is clear that both direct-transition and ODDOS mechanisms give rise to features in the EDCs, but certainly not all features are derived from the ODDOS as the early work indicated! Perhaps the former misconception concerning the ODDOS is related to the final-state band structure. It is credible that particular one-electron conduction bands which are non-free-electron-like have small enough group velocities that unphysically large $\Delta\vec{k}_\perp$'s [Eq. (21)] are yielded. It is rather amusing, however, that the reason that this is a fallacious notion may be the lifetime itself, because a current perception is that the finite lifetime is partially responsible for the success of the plane-wave approximation for its dispersion relation. This latter conjecture is reasonable because the bulk band structure calculations, which generally

give many non-plane-wavelike conduction bands, do not account for lifetime effects which in turn essentially reduce the influence of the crystal potential on the photoemission final state.[50,51,69] The work presented in Part I, particularly in Chapter II, represents strong evidence for this notion.

(4) Initial-state lifetime broadening. This effect has already been mentioned in reference to the direct-transition process in d-band metals. Unlike that of the photoelectron, the lifetime $\tau_h(E_n,\vec{k}_i)$ of the hole can vary widely from material to material because it is much more strongly influenced by the crystal potential and the detailed band structure.[64,70] It is therefore intrinsically a more complicated effect. Generally, there is an initial-state energy dependence for τ_h; phase-space arguments suggest that it varies inversely with $(E_n^F)^2$ (Ref. 64), but absolute values of $\Sigma_h = (\hbar/2\tau_h)$ are typically an order of magnitude lower than Σ_e for Cu d bands.[59,71] However, Σ_h can be quite large in open d-shell systems because the larger d-electron mobility in these metals accounts for much of the finite lifetime.[72] Again, we can derive a simple expression for the initial-state-lifetime-induced $\vec{k}$ broadening which reflects a loss of phase coherence in the valence band: $\Delta\vec{k}_i = 2\Sigma_h(E_n)/\hbar\vec{v}_h$. Obviously, the effect of a large Σ_h can be counterbalanced by a large group velocity. Fortunately, open d-shell metals generally have larger d-band velocities than closed shells, as evidenced by the general trend of 3d-band narrowing as one progresses from Sc to Zn.[73]

(5) Random orientation of atomic species. At first glance, this appears to be a trivial effect: if the condensed phase system does not possess lattice periodicity, then Bloch's theorem does not apply even in principle; the $\vec{k}$-conservation delta function drops out of Eq. (9) and the resulting expression for the angular distribution looks like Eq. (20), except that $\Phi(\vec{k}_f)$ is replaced by $\Phi(k_f)$. The effect is not actually this simple, as will be discussed in more detail below after the extrinsic effects are introduced.

(6) Random orientation of crystallites. Within the microcrystal structure of the polycrystalline sample, $\vec{k}$-conservation can still be important, but if the arrangement of crystallites is truly random, then there is effectively an integration of Eq. (9) over all final-state directions with a retainment of the $\cos^2\alpha_f$ factor. The angular distribution expression would have a form similar to[32]

$$I_{h\nu}(E_f,\vec{k}_f) \propto \cos^2\alpha_f \sum_n |\Phi_n(k_f)|^2 \sum_{\vec{k}}^{BZ} \delta[E_f(\vec{k}) - E_n(\vec{k}) - h\nu] \quad , \qquad (23)$$

where $|\Phi|^2$ and $\cos^2\alpha_f$ are assumed to be constants of integration over $\vec{k}_f$ orientations. The sum over $\vec{k}$ in Eq. (23) reflects a "density of direct transitions," usually referred to as the joint density of states (JDOS).[74] It has no angular dependence, though it may have an energy dependence (E_f). The only angular dependence comes from $\cos^2\alpha_f$, reflecting the preferential excitation of photoelectrons oriented along $\vec{A}$. Again, $\cos^2\alpha_f$ is always the result for a plane-wave final state.

(7) Angle-integrated photoemission (AIP). Equation (9) is again integrated over $\vec{k}_f$, yielding Eq. (23) except that the angular factor $\cos^2\alpha_f$ is lost in the integration. In a true angle-integrated PES experiment, $\vec{k}_f$ is not defined and there obviously cannot be an angular distribution; the intensity measurement yields a true cross section if it is integrated over the appropriate range of E_f. Partial angle-integration is, of course, always obtained even in an angle-resolved photoemission experiment, but this is a different matter. One strives to achieve total angular integration of EDC intensity with AIP, while with ARP the goal is to select finite but small cones of solid angle. The effect of partial angle-integration in ARP is usually included in model calculations of valence-band spectra,[75] but it is vague in its relationship to the much more detailed band-by-band analysis of spectral features presented in Part I.

An important feature of these effects for which either intrinsic or extrinsic partial or total relaxation of $\vec{k}$-conservation is induced is that the angular distribution tends to become dominated by the expression $\cos^2\alpha_f \Sigma_{(n)}|\Phi_n(\vec{k}_f)|^2$ x DOS (or x JDOS); i.e., the atomic part governs at the expense of crystal momentum. If the system is disordered, then we have $\cos^2\alpha_f \Sigma_{(n)}|\Phi_n(k_f)|^2 = \cos^2\alpha_f \Sigma_{(n)}|\Phi_n(h\nu)|^2$. Further, if AIP is employed, then the expression is simply $\Sigma_{(n)}|\Phi_n(h\nu)|^2$. Only the atomic part of the matrix element remains (of course, the details of an actual calculation of this matrix element have not been discussed). It is possible, in this case, to study atomic effects in the condensed phase if the $h\nu$ dependence of

$|\Phi_n(h\nu)|^2$ is probed (Chapter VI). Another method, however, is to measure $|\Phi(h\nu)|^2$ at a fixed photon energy with some other parameter of the system as a variable (Chapter V).

Let us return to the problem of a disordered condensed phase system, for here we know that Bloch's theorem is invalid. The angular distribution has the form $\cos^2\alpha_f\ |\Phi(k_f)|^2$. As a direct consequence of the plane-wave final state, the only angular factor in this expression is $\vec{A}\cdot\vec{k}_f$ (Ref. 53). According to Yang's theorem,[76] however, the general form of the photoelectron angular distribution from a randomly oriented system excited by a vector potential $\vec{A}$, via a dipole process, is

$$I(E_f,\vec{k}_f) = [\sigma(E_f)/4\pi][1 + \beta(E_f)\ P_2(\cos\alpha_f)] \quad . \tag{24}$$

Here, $\sigma(E_f)$ is the angle-averaged cross section ($\sim |\Phi|^2$) and P_2 is the second Legendre polynomial $P_2(x) = (3x^2 - 1)/2$. The asymmetry parameter, $\beta(E_f)$, has the limits $-1 \leq \beta(E_f) \leq 2$, as required to insure that the intensity (I) is nonnegative. It is now well known that this expression applies to gaseous systems;[3,53b] what about the disordered condensed phase? The simple $\cos^2\alpha_f$ dependence of the angular distribution for a plane-wave final state implies that $\beta = 2$, independent of energy; a plane wave always gives this result. Atomic final states are generally not plane-wavelike; $\beta(E_f)$ typically goes through dramatic oscillations with energy that may cover its entire range. In Chapter VII, it will be shown that under conditions for which Eq. (24) applies, the condensed phase angular distribution of a particular photoemission

transition (1) does indeed have the form of Eq. (24), (2) is energy dependent, and (3) has an energy dependence of $\beta(E_f)$ that is qualitatively similar to analogous gaseous systems. This is the condensed phase "atomiclike" angular distribution effect mentioned at the outset of this chapter. One of its interesting consequences concerns the final state: the latter cannot be a simple plane wave. Based on the discussion already, this comes as no surprise. The PWA works for direct transitions because they have sharply peaked Mahan-cone angular distributions. Shevchik, et al.,[30,42] suggested that the true final state ought to have the atomic form (which is not plane-wavelike) near the core because the PWA gives the wrong atomic angular distribution, and a more plane-wavelike form outside the core, where Bloch's theorem takes over. However, if the final state is purely atomiclike near the core, then it might be expected that a purely atomiclike angular distribution is yielded in condensed phase experiments with a randomly oriented system. Unfortunately, this is not the case. In Chapter VII, it will be shown that the value of the photoelectron asymmetry parameter β tends to be closer to 2 than atomic theory suggests, implying that the true final state is neither purely atomiclike nor plane-wavelike. Obviously, there are nonlocal interactions even in the disordered condensed phase system. The results of Chapter VII suggest that the relatively rapid transition from atomiclike to plane-wavelike final states, as the photoelectron propagates away from the hole, does not occur simply as a consequence of Bloch's theorem.

There are many important features of PES that have not been discussed in this simple but far-reaching introduction. Some will be dealt with as they arise in the course of this thesis. The reader is also referred to the reviews listed at the end of this chapter.

C. Experimental Summary

Each chapter is a fully contained unit. Therefore, there is some overlap in their content, such as with references, introduction, and experimental sections. Regarding the experimental sections, they are generally more complete than one usually finds in journal articles, but the exhaustive description of experimental procedures and instrumentation common to many theses is not found here. This is mainly because there are several excellent reviews of instrumentation and ultra-high vacuum (UHV) procedures utilized in condensed phase photoemission,[19,77] and the Ph.D. theses of S. D. Kevan,[78] P. S. Wehner,[79] G. Apai,[80] D. R. Denley,[81] S. P. Kowalczyk,[82] M. G. White,[83] and D. J. Trevor[84] contain ample descriptions of experimental solid-state electron spectroscopy,[78-82] synchrotron radiation in general[83] and specific VUV beam lines,[78-81,83,84] and x-ray photoelectron spectroscopy.[82] Sample preparation and characterization procedures are described separately in each chapter of this thesis. Only a few details concerning photoemission are discussed below.

A conventional photoemission experiment requires (in addition to the sample or system) a source of photons and an electron energy analyzer. Three different electron analyzers were employed in these

studies. The first was a double-pass cylindrical mirror analyzer[79,85] (CMA) with a hemispherical retarding grid (Physical Electronics Model PHI 15-255G). This CMA is not an angle-integrating detector, i.e., it does not accept electrons over the full 2π sr emanating from the sample. Rather, it analyzes an (azimuthal) cone of electrons centered about its symmetry axis, with a cone half-angle of 42.3° and a polar angular acceptance of ±6° along any azimuth. However, this is close enough to "angle-integrating" for many purposes, and this analyzer was utilized as such in atomic effect studies (Chapter VI). It was also utilized for ARNP studies of valence band structure (Chapters III and IV) for which case the analyzer was modified by placing an aperture on the front, yielding an acceptance cone of about 10 msr (1 msr = 10^{-3} sr).

It is important in many ARP studies to be able to vary the angles (θ_p,ϕ_p) at will. This is obviously the only way to obtain a full angular distribution measurement of emitted photoelectrons. However, the CMA is not particularly well-suited in this regard. While it performs its duties in ARNP studies admirably, the CMA is heavy and cumbersome; not easily rotated internally while under vacuum. This can be partially circumvented by employing several samples with different azimuthal orientations (if they are single crystalline) and by rocking the sample about an axis orthogonal to $\vec{n}$ (see Fig. 1), thereby achieving variability of both θ_p and ϕ_p. However, there are problems with this procedure. There is the obvious problem of characterizing several different samples in the same experiment. Then, there

is the problem with θ_A; it is also changed as θ_p is varied. As indicated by Eqs. (4), (9), and (20), and (23), this changes the angular distribution two ways simultaneously: (1) a new $|\vec{k}_f\rangle$ state is analyzed with (2) a different $\vec{A}\cdot\vec{P}$ operator--not a very useful way to measure the angular distribution. [This points out a problem inherent with condensed-phase ARP that does not exist in the gas phase. In condensed-phase experiments, all three parts (see Section A) can contain vectorial alignment, even with a randomly oriented sample. In the gas phase, only $\vec{A}$ and $\vec{p}$ are aligned with polarized light.] The azimuthal angle (ϕ_p) problem can be alleviated by utilizing a rotatable sample manipulator. Additionally, G. J. Lapeyre and co-workers[19,41] partially circumvented these problems by employing an angle-resolving aperture that is internally rotatable in the second stage of the CMA. This type of mechanism is now commercially available with newer CMA models. However, there is still an obvious restriction on the spatial extent of detectable photoelectron trajectories. Therefore, a 180° hemispherical sector energy analyzer with independent two-circle rotation was designed and constructed at Lawrence Berkeley Laboratory. Most of the "think work" and "hard labor" in this regard was performed by Dr. S. D. Kevan in collaboration with mechanical and electrical engineers and technicians (others assisted in different ways, especially with the construction of various associated UHV hardware and surface/adsorbate analysis instrumentation), and the premier source of information about this ARP instrument is contained within his Ph.D. thesis.[78,86] Briefly, the detection system consists of two

stainless steel Einzel lenses, a stainless steel 5.40-cm mean radius hemispherical analyzer, and a microchannel plate imaging detector assembly. The analyzer has an angular acceptance cone of about 9 msr and is continuously rotatable inside its associated vacuum chamber by ±180° in the horizontal plane and by ca. 90° in the vertical plane, thereby covering a full 2π sr, or the entire lower half-space of photoelectron trajectories originating at the sample. This detection system, in conjunction with a rotatable sample manipulator, allowed the relative orientations of vectors $\vec{A}$, $\vec{p}$, $\vec{n}$, and the crystallographic axes to be independently varied in experiments described in Chapters II, VII, and VIII.

The third analyzer system, utilized in experiments discussed in Chapter V, was a specially modified Hewlett-Packard Model HP 5950A electron spectrometer[82,87] which employs a (unpolarized) monochromatized Al Kα ($h\nu$ = 1486.6 eV) x-ray radiation source in conjunction with a 15.87-cm mean radius hemispherical analyzer. This analyzer is inherently angle-resolving because the dispersion compensation lens system has an electron angular acceptance cone of about 15 msr, but the experiments (with randomly oriented Sm metal clusters) were not designed to take advantage of this feature.

Other than those in Chapter V, all experiments were performed at the Stanford Synchrotron Radiation Laboratory (SSRL), using the electron storage ring SPEAR as the source of photons. There are excellent and extensive reviews of the properties of synchrotron radiation.[88-91] Briefly, the radiation is highly polarized ($\geq$ 75

percent) in the horizontal plane, highly collimated, and continuous from the near infrared to its cutoff energy (which is dependent upon the electron beam energy), typically in the x-ray region ($h\nu > 1$ keV). An appropriate monochromator and associated optics enables a selected portion of the energy spectrum to be utilized with a reasonable degree of resolution and with a higher degree of polarization (> 95 percent). In these studies, photons were utilized from beam lines I-1 (4° line) (in the range 40 eV $\leq h\nu \leq$ 360 eV) and I-2 (8° line) (6 eV $\leq h\nu \leq$ 34 eV) at SSRL. The 4° line,[92] which employs a grazing-incidence "grasshopper" monochromator for photon energy tunability throughout the soft x-ray region, was utilized in experiments reported in Chapters VI-VIII, while the 8° line,[93] with its 1 m Seya-Namioka monochromator, was employed in experiments in Chapters II-IV. The details of both beam lines are described elsewhere.[78-80,84,92-94]

D. Summary of Chapters

Chapters II, III, and IV comprise Part I—by far the most extensive part of this thesis. Here, the problem of determination of valence band structure in single-crystalline metals is investigated. The detailed valence band structure of a solid is perhaps its most fundamental construct. Many properties, such as magnetic order, electrical and thermal conductivity, optical dielectric properties, chemisorption characteristics, and vibrational spectra can be calculated from known band eigenvalues and eigenvectors.[95] ARP has demonstrated its capability to determine detailed dispersion relations

in many Group VIII and IB metals, albeit non-trivially.[57] From a material science standpoint, it is interesting to conceive of models with which ARP data from any material can be interpreted in terms of detailed $E(\vec{k})$ curves--non-trivial, again. To get a grasp on the problem, it should not suffice just to show that ARP can be utilized to map valence band structure in model systems. Rather, the difficulties, uncertainties, and possible simplifications of current direct-transition models should be considered carefully (these are the most interesting problems, anyway). An example, perhaps, would clarify this important point: A key problem and presently the subject of considerable controversy is the nature of the ARP final state.[30-32,37,40-51] What is the relationship between the calculated, one-electron conduction band structure and photoelectron dispersion relations? This is not only an interesting and important problem from the standpoint of general lack of understanding and agreement about it, but also because our ability to apply ARP to complicated systems will depend quite heavily on the nature of the final state. If it is actually as complicated as the bulk band structure suggests for transition metals (or more so), band mapping will be a near-impossible task in complicated systems for which calculations probably do not exist or are not reliable. In this regard, it would be much more exciting to know that the final-state band structure in a prototype metal is plane-wavelike even in bulk band gap regions (Chapter II) than to know that EDCs can be used to map copper valence bands along high symmetry lines in k-space. Four of the major questions addressed by this work are:

1. What is the nature of photoelectron dispersion relations?

   a. relationship to bulk band structure
   b. relationship to empty lattice band structure
   c. importance of secondary Mahan cones

2. Where do the peak structures come from?

   a. direct transitions
   b. density-of-states features
   c. surface states
   d. surface umklapp peaks
   e. polarization selection rules for initial states

3. What is the nature of empirical valence-band $E(\vec{k})$ curves?

   a. bulk-like dispersion
   b. disagreement with bulk band structure
   c. antiferromagnetic bands
   d. complications at arbitrary points in the BZ

4. How does the surface influence normal-emission EDCs?

   a. surface reconstruction
   b. momentum broadening
   c. refraction of the photon beam
   d. surface umklapp processes

In Chapter II, Cu(211) ARNP studies are discussed. The focus is on ARP from a stepped crystal surface. In Chapter III, ARNP work with Pt(100)-(5x1) is discussed. This system gives indications of severe complications: (a) it is a 5d-valence-shell metal, (b) it is an open-shell metal, (c) it is a (100) face, (d) it has a reconstructed surface, and (e) it is a material that has historically been rather difficult to clean of bulk and surface impurities. The results are quite encouraging. In Chapter IV, ARNP studies of Cr(100) and Cr(110) are reported. Chromium is antiferromagnetic at room temperature. It will be shown that this strongly influences ARP spectra. Furthermore,

Cr(100) possesses a reconstructed surface; this introduces additional interesting problems. As the last on valence band structure, Chapter IV takes up a more detailed analysis of several of the above questions. In addition to this work, high resolution studies have recently been performed on Au(100)-(1x1) (Ref. 96), Au(100)-(5x20) (Ref. 96), and Ag(110) (Ref. 97). Although they are not represented in detail in this thesis, we shall have occasion to draw upon the important results therefrom in some of the discussion. Finally, a general theme conveyed earlier as applied to Part I is stressed: ARNP valence band structure studies of single crystals are characterized by conservation of crystal momentum. The corresponding $\vec{k}$-conservation delta function gives rise to such strong and sharply peaked angular distributions that atomic effects can be ignored.

Chapters V and VI comprise Part II. Atomic effects dominate in studies of (V) particle-size-induced valence electronic configuration changes in samarium clusters, and (VI) adsorbate sensitivity enhancement in photoemission from CO on Pd at the Cooper minimum in the Pd(4d) valence level. It is noteworthy that Chapter V represents the first definitive example of a change in electronic configuration with particle size. Chapter VI demonstrates that atomic effects in the PES cross section at a Cooper minimum can be utilized advantageously to enhance adsorbate valence level intensity relative to that of the substrate. In both experiments, the relaxation of linear momentum conservation (see Section B.4) suppresses band structure effects; therefore, atomiclike photoemission dominates the EDCs.

Chapters VII and VIII comprise Part III. Atomic (VII) and molecular (VIII) angular distribution effects dominate in (VII) studies of condensed phase photoelectron asymmetry in Ag, Pt, and Se on Pt, and (VIII) studies of adsorbate core-level shape resonances in $(\sqrt{3} \times \sqrt{3})R30^{\circ}$ CO-Ni(111) and c(2x2) CO-Ni(001). These chapters represent the first such identification of these two effects. The asymmetry results demonstrate that there is an atomiclike angular distribution, with an atomiclike $h\nu$ dependence, in the condensed phase. The shape resonance studies demonstrate that the condensed phase analogue of the gas-phase core-level resonance has a sharp angular distribution by virtue of molecular alignment, and otherwise has general characteristics very much like the predicted gas-phase resonance. Both of these experiments point out that localized (atomic and/or molecular) condensed phase effects are important not only in the total cross section but in the angular distribution as well, perhaps a somewhat surprising result. However, it is stressed in Part III that in each experiment, the influence of the condensed phase perturbs the shape of angular distributions relative to that in the gas phase.

CONDENSED PHASE PHOTOEMISSION REVIEWS

(a) D. E. Eastman and F. J. Himpsel, Inst. Phys. Conf. Ser. No. 55, Chapter 3, p. 115 (1981).

(b) C. R. Brundle and A. D. Baker, editors, Electron Spectroscopy: Theory, Techniques and Applications (4 vols.) (Academic, New York, 1977-81).

(c) F. J. Himpsel, Appl. Opt. 19, 3964 (1980).

(d) T. N. Rhodin and J. W. Gadzuk, in The Nature of the Surface Chemical Bond, edited by T. N. Rhodin and G. Ertl (North-Holland, New York, 1979).

(e) M. Cardona and L. Ley, editors, Photoemission in Solids (2 vols.) (Springer-Verlag, New York, 1978-79).

(f) B. Feuerbacher, B. Fitton, and R. F. Willis, editors, Photoemission and the Electronic Properties of Surfaces (Wiley, New York, 1978).

(g) L. Fiermans, J. Vennik, and W. Dekeyser, editors, Electron and Ion Spectroscopy of Solids (Plenum, New York, 1978).

(h) B. Feuerbacher and B. Fitton, in Electron Spectroscopy for Surface Analysis, edited by H. Ibach (Springer-Verlag, New York, 1977), and references therein.

(i) D. A. Shirley, J. Stöhr, P. S. Wehner, R. S. Williams, and G. Apai, Phys. Scripta 16, 398 (1977).

(j) E. G. Derouane and A. A. Lucas, editors, Electronic Structure and Reactivity of Metal Surfaces (Plenum, New York, 1976).

(k) B. Feuerbacher and B. Fitton, J. Phys. C 9, 169 (1976).

(l) E. W. Plummer, in Interactions on Metal Surfaces, edited by R. Gomer (Springer-Verlag, New York, 1975).

(m) P. J. Feibelman and D. E. Eastman, Phys. Rev. B 10, 4932 (1974).

(n) D. E. Eastman, in Vacuum Ultraviolet Radiation Physics, edited by E. E. Koch, R. Haensel, and C. Kunz (Pergamon, Vieweg, 1974), pp. 417-49; see, also, other articles in this volume as noted in reference section.

(o) L. F. Ley, J. Electron Spectrosc. Relat. Phenom. 15, 329 (1979).

(p) R. H. Williams, Contemp. Phys. 19, 389 (1978).

REFERENCES

1. See, for example, E. E. Koch, C. Kunz, and B. Sonntag, Phys. Rep. 29, 153 (1977); Reviews (j) and (n); Review (f), Chapter 1.
2. Condensed phase atomic effects have been discussed and reviewed by many authors. See, for example, K. Codling, J. Electron Spectrosc. Relat. Phenom. 17, 279 (1979); F. Combet Farnoux, J. de Physique 39, Coll. C4, 1 (1978); B. Sonntag, ibid. 39, Coll. C4, 9 (1978); F. C. Brown, in Synchrotron Radiation Research, edited by H. Winick and S. Doniach (Plenum, New York, 1980), Chapter 4, and references therein.
3. S. T. Manson, Adv. Electron. Electron Phys. 44, 1 (1977); S. T. Manson and D. Dill, in Review (b), Vol. 2.
4. J. L. Dehmer and D. Dill, Phys. Rev. Lett. 35, 213 (1975).
5. See, for example, R. F. Willis and B. Feuerbacher, in Review (f); N. V. Smith, in Review (e), Vol. I; Review (c).
6. F. R. McFeely, J. Stöhr, G. Apai, P. S. Wehner, and D. A. Shirley, Phys. Rev. B 14, 3273 (1976).
7. We assume, here, that the photon beam is linearly polarized, as is the case with synchrotron radiation.
8. E. E. Koch, C. Kunz, and B. Sonntag, Phys. Rep. 29, 153 (1977).
9. F. C. Brown, in Synchrotron Radiation Research, edited by H. Winick and S. Doniach (Plenum, New York, 1980).
10. G. Apai, P. S. Wehner, J. Stöhr, R. S. Williams, and D. A. Shirley, Solid State Commun. 20, 1141 (1976); Review (i).

11. P. S. Wehner, J. Stöhr, G. Apai, F. R. McFeely, R. S. Williams, and D. A. Shirley, Phys. Rev. B 14, 2411 (1976).

12. L. I. Johansson, I. Lindau, M. Hecht, S. M. Goldberg, and C. S. Fadley, Phys. Rev. B 20, 4126 (1979); M. H. Hecht and I. Lindau, Phys. Rev. Lett. 47, 821 (1981).

13. C. Guillot, Y. Ballu, J. Paigné, J. Lecante, K. P. Jain, P. Thiry, R. Pinchaux, Y. Pétroff, and L. M. Falicov, Phys. Rev. Lett. 39, 1632 (1977); D. Chandesris, G. Krill, G. Maire, J. Lecante, Y. Pétroff, Solid State Commun. 37, 187 (1981), and references therein.

14. M. Iwan, F. J. Himpsel, and D. E. Eastman, Phys. Rev. Lett. 43, 1829 (1979).

15. L. I. Johansson, J. W. Allen, T. Gustafsson, I. Lindau, and S. B. M. Hagström, Solid State Commun. 28, 53 (1978); J. W. Allen, L. I. Johansson, I. Lindau, and S. B. Hagström, Phys. Rev. B 21, 1335 (1980); L. I. Johansson, J. W. Allen, I. Lindau, M. H. Hecht, and S. B. M. Hagström, ibid. 21, 1408 (1980).

16. W. Gudat, S. F. Alvarado, and M. Campagna, Solid State Commun. 28, 943 (1978); W. Lenth, F. Lutz, J. Barth, G. Kalkoffen, and C. Kunz, Phys. Rev. Lett. 41, 1185 (1978); F. Gerken, J. Barth, and C. Kunz, ibid. 47, 993 (1981).

17. See, for example, D. Briggs, in Review (b), Vol. 3.

18. K. Siegbahn, et al., ESCA. Atomic, Molecular and Solid State Structure by Means of Electron Spectroscopy, Nova Acta Regiae Soc. Sci. Upsaliensis Ser. IV 20 (1967).

19. See, for example, N. V. Smith, in Review (e), Vol. I.

20. See, for example, G. D. Mahan, in Review (g), and references therein.

21. See Reviews (a) through (p), especially (f), (g), and (i).

22. A. Liebsch, Phys. Rev. Lett. 32, 1203 (1974); Phys. Rev. B 13, 544 (1976).

23. S. D. Kevan, Appl. Opt. 19, 3974 (1980), and references therein; S. D. Kevan, J. G. Tobin, D. H. Rosenblatt, R. F. Davis, and D. A. Shirley, Phys. Rev. B 23, 493 (1981); D. H. Rosenblatt, J. G. Tobin, M. G. Mason, R. F. Davis, S. D. Kevan, D. A. Shirley, C. H. Li, and S. Y. Tong, ibid. 23, 3828 (1981).

24. N. V. Smith, P. K. Larsen, and S. Chiang, Phys. Rev. B 16, 2699 (1977); D. P. Woodruff, D. Norman, B. W. Holland, N. V. Smith, H. H. Farrell, and M. M. Traum, Phys. Rev. Lett. 41, 1130 (1978); D. Norman, D. P. Woodruff, N. V. Smith, M. M. Traum, and H. H. Farrell, Phys. Rev. B 18, 6789 (1978); N. V. Smith, H. H. Farrell, M. M. Traum, D. P. Woodruff, D. Norman, M. S. Woolfson, and D. W. Holland, ibid. 21, 3119 (1980).

25. S. Kono, C. S. Fadley, N. F. T. Hall, and Z. Hussain, Phys. Rev. Lett. 41, 117 (1978); S. Kono, S. M. Goldberg, N. F. T. Hall, and C. S. Fadley, ibid. 41, 1831 (1978); Phys. Rev. B 22, 6085 (1980).

26. R. J. Baird, C. S. Fadley, and L. F. Wagner, Phys. Rev. B 15, 666 (1977); S. M. Goldberg, R. J. Baird, S. Kono, N. F. T. Hall, and C. S. Fadley, J. Electron Spectrosc. Relat. Phenom. 21, 1 (1980).

27. P. J. Feibelman, Surf. Sci. 46, 558 (1974).

28. A. Liebsch, in Review (g).

29. G. D. Mahan, Phys. Rev. B 2, 4334 (1970).

30. N. J. Shevchik and D. Liebowitz, Phys. Rev. B 18, 1618 (1978), and references therein.

31. J. W. Gadzuk, Phys. Rev. B 10, 5030 (1974).

32. J. W. Gadzuk, in Review (j).

33. J. B. Pendry, Surf. Sci. 57, 679 (1976).

34. C. Caroli, D. Lederer-Rozenblatt, B. Roulet, and D. Saint-James, Phys. Rev. B 8, 4552 (1973).

35. W. L. Schaich and N. W. Ashcroft, Phys. Rev. B 3, 2452 (1971); N. W. Ashcroft, in Review (n), pp. 533-44.

36. I. Adawi, Phys. Rev. 134, A788 (1964).

37. Review (m).

38. R. F. Willis and B. Feuerbacher, in Review (f).

39. (a) At photon energies of 20 and 200 eV, $|\vec{k}_{h\nu}|$ is 0.6 and 6.0 percent, respectively, of $k_{BZ}^{\langle 100\rangle}$ (copper), where $k_{BZ}^{\langle 100\rangle}$ is the Brillouin zone dimension between Γ and X.
(b) See, also, Z. Hussain, C. S. Fadley, S. Kono, and L. F. Wagner, Phys. Rev. B 22, 3750 (1980).

40. N. E. Christensen and B. Feuerbacher, Phys. Rev. B 10, 2349 (1974); B. Feuerbacher and N. E. Christensen, ibid. 10, 2373 (1974).

41. N. V. Smith, M. M. Traum, J. A. Knapp, J. Anderson, and G. J. Lapeyre, Phys. Rev. B 13, 4462 (1976).

42. N. J. Shevchik, Phys. Rev. B 16, 3428 (1977); D. Liebowitz, M. Sagurton, J. Colbert, and N. J. Shevchik, Phys. Rev. Lett. 39, 1625 (1977).

43. R. J. Baird, L. F. Wagner, and C. S. Fadley, Phys. Rev. Lett. 37, 111 (1976).

44. L. F. Wagner, Z. Hussain, and C. S. Fadley, Solid State Commun. 21, 257 (1977).

45. J. Stöhr, P. S. Wehner, R. S. Williams, G. Apai, and D. A. Shirley, Phys. Rev. B 17, 587 (1978).

46. R. S. Williams, P. S. Wehner, J. Stöhr, and D. A. Shirley, Surf. Sci. 75, 215 (1978).

47. F. J. Himpsel and D. E. Eastman, Phys. Rev. B 18, 5236 (1978).

48. E. Dietz and F. J. Himpsel, Solid State Commun. 30, 235 (1979).

49. Y. Pétroff and P. Thiry, Appl. Opt. 19, 3957 (1980).

50. L. Ilver and P. O. Nilsson, Solid State Commun. 18, 677 (1976).

51. P. O. Nilsson and N. Dahlbäck, Solid State Commun. 29, 303 (1979).

52. Of course, this would only be correct in the case that the electron and hole lifetimes were infinitely large. Equation (9) does not account for the everpresent finite lifetime effects that are discussed in Section B.4.

53. (a) See, for example, H. A. Bethe and E. E. Salpeter, Quantum Mechanics of One- and Two-Electron Atoms (Academic, New York, 1957), Chapter IV. (b) S. T. Manson and D. Dill, in Review (b), Vol. 2; J. T. J. Huang and J. W. Rabalais, ibid., Vol. 2; J. A. R. Samson, ibid., Vol. 4.

54. Review (i); Refs. 45, 49, and 51; Refs. 1 through 12 in Chapter IV.

55. H. Becker, E. Dietz, U. Gerhardt, and H. Angermüller, Phys. Rev. B 12, 2084 (1975).

56. J. T. J. Huang and F. O. Ellison, Chem. Phys. Lett. 29, 565 (1974); J. T. J. Huang and J. W. Rabalais, in Review (b), Vol. 2.

57. See, for example, Refs. 1 through 40 in Chapter IV.

58. Review (k).

59. Review (c), and references therein.

60. O. Madelung, Introduction to Solid-State Theory (Springer-Verlag, New York, 1978), Chapter 6.

61. N. J. Shevchik, Phys. Rev. B 16, 3428 (1977).

62. Z. Hussain, E. Umbach, J. J. Barton, J. G. Tobin, and D. A. Shirley, Phys. Rev. B, to be published, and references therein.

63. R. S. Williams, P. S. Wehner, J. Stöhr, and D. A. Shirley, Phys. Rev. Lett. 39, 302 (1977).

64. See, for example, J. B. Pendry, in Review (f).

65. D. J. Spanjaard, D. W. Jepsen, and P. M. Marcus, Phys. Rev. B 15, 1728 (1977).

66. The inelastic scattering length, $\lambda(E_f,\vec{k}_f)$, is usually replaced by the average over $\vec{k}_f$, i.e., $\lambda(E_f)$; see Review (k).

67. P. Heimann, H. Neddermeyer, and H. F. Roloff, Phys. Rev. Lett. 37, 775 (1976); T. Grandke, L. Ley, and M. Cardona, Phys. Rev. Lett. 38, 1033 (1977).

68. Review (o).

69. P. O. Nilsson, J. Kanski, and C. G. Larsson, Solid State Commun. 36, 111 (1980).

70. J. B. Pendry and D. J. Titterington, Commun. Phys. 2, 31 (1977).

71. P. Thiry, D. Chandesris, J. Lecante, C. Guillot, R. Pinchaux, and Y. Pétroff, Phys. Rev. Lett. 43, 82 (1979).

72. See, for example, S. Hüfner, in Review (e), Vol. II; A. Schulz, R. Courths, H. Schulz, and S. Hüfner, J. Phys. F 9, L41 (1979).

73. L. F. Mattheiss, Phys. Rev. 134, A970 (1964).

74. N. V. Smith, Phys. Rev. B 3, 1862 (1971).

75. Z. Hussain, S. Kono, L.-G. Petersson, C. S. Fadley, and L. F. Wagner, Phys. Rev. B 23, 724 (1981), and references therein.

76. C. N. Yang, Phys. Rev. 74, 764 (1948).

77. R. Gomer, editor, Interactions on Metal Surfaces (Springer-Verlag, New York, 1975); H. Ibach, editor, Electron Spectroscopy for Surface Analysis (Springer-Verlag, New York, 1977); C. S. Fadley, in Review (b), Vol. 2; G. A. Somorjai, Chemistry In Two Dimensions: Surfaces (Cornell University Press, Ithaca NY, 1981).

78. S. D. Kevan, Ph.D. thesis, University of California, Berkeley, 1980 (LBL-11017, unpublished).

79. P. S. Wehner, Ph.D. thesis, University of California, Berkeley, 1978 (LBL-7622, unpublished).

80. G. R. Apai, Ph.D. thesis, University of California, Berkeley, 1977 (LBL-6906, unpublished).

81. D. R. Denley, Ph.D. thesis, University of California, Berkeley, 1979 (LBL-9482, unpublished).

82. S. P. Kowalczyk, Ph.D. thesis, University of California, Berkeley, 1976 (LBL-4319, unpublished).

83. M. G. White, Ph.D. thesis, University of California, Berkeley, 1979 (LBL-9527, unpublished).

84. D. J. Trevor, Ph.D. thesis, University of California, Berkeley, 1980 (LBL-11434, unpublished).

85. P. W. Palmberg, J. Electron Spectrosc. Relat. Phenom. 5, 691 (1974).

86. See, also, S. D. Kevan and D. A. Shirley, Phys. Rev. B 22, 542 (1980).

87. R. A. Pollak, Ph.D. thesis, University of California, Berkeley, 1972 (LBL-1299, unpublished).

88. R. P. Godwin, in Springer Tracts in Modern Physics, Vol. 51, edited by G. Höhler (Springer-Verlag, New York, 1969).

89. C. Kunz, in Review (e), Vol. II; in Review (f).

90. C. Kunz, editor, Synchrotron Radiation (Springer-Verlag, New York, 1979).

91. H. Winick and S. Doniach, editors, Synchrotron Radiation Research (Plenum, New York, 1980).

92. F. C. Brown, R. Z. Bachrach, S. B. M. Hagström, N. Lien, and C. H. Pruett, in Review (n), pp. 785-87; F. C. Brown, R. Z. Bachrach, and N. Lien, Nucl. Instrum. Methods 152, 73 (1978).

93. V. Rehn, A. D. Baer, J. L. Stanford, D. S. Kyser, and V. O. Jones, in Review (n), pp. 780–82.

94. Review (i).

95. J. Callaway, Quantum Theory of the Solid State (Academic, New York, 1976), Chapter 4.

96. R. F. Davis, M. G. Mason, Z. Hussain, J. G. Tobin, L. E. Klebanoff, and D. A. Shirley, to be published.

97. K. A. Mills, M. G. Mason, R. F. Davis, R. Watson, G. Thornton, J. G. Tobin, Z. Hussain, E. Umbach, and D. A. Shirley, to be published.

FIGURE CAPTIONS

Fig. 1. General coordinate scheme utilized in condensed-phase photoemission studies, with the $\vec{z}$ axis parallel to the surface normal ($\vec{n}$). Thus, the polarization angle is $\theta_A = \angle(\vec{n},\vec{A})$ and the photoemission angle is $\theta_p = \angle(\vec{n},\vec{p})$, with $\vec{A}$ and $\vec{p}$ the radiation vector potential and photoelectron momentum vector, respectively. An additional angle, $\alpha = \angle(\vec{A},\vec{p})$, is important for angular distribution studies.

Fig. 2. The first Brillouin zone (first BZ) of the face-centered cubic (FCC) lattice (O_h^5 symmetry), with high-symmetry points and lines in an irreducible $(1/48)^{\underline{th}}$ wedge ($k_y \geq k_x \geq k_z \geq 0$) indicated by their respective point group labels. The entire zone contains 12 equivalent {110} mirror planes passing through $\Gamma\Lambda LUSX\Delta\Gamma$ in the various wedges. The $(01\bar{1})$ plane (corresponding to $k_y = k_z$) contains these symmetry elements in the wedge with $k_x \geq k_y \geq k_z \geq 0$. This plane is sufficient for a diagrammatic representation of the photoemission process in two dimensions because it contains the three high-symmetry lines (Δ, Λ, Σ).

Fig. 3. The $(01\bar{1})$ plane in extended-zone $\vec{k}$-space for the FCC lattice. Several reciprocal lattice points are labelled by their (h,k,l) coordinates. Also shown is the first BZ with various high-symmetry points labelled, and a surface of

constant energy (E_i) below the Fermi energy. The energy surface is circular because the nearly-free-electron approximation has been imposed for all bands.

Fig. 4. The same $\vec{k}$-space region as in Fig. 3, with constant energy (E_f) contours centered on the ($\bar{1}\bar{1}\bar{1}$) and ($\bar{2}00$) reciprocal lattice points, in addition to the energy surface (E_i) in the first BZ. The inset in the lower left corner shows details of the intersection of E_i with the E_f contour centered on ($\bar{1}\bar{1}\bar{1}$). At the two points of intersection, the energy- and $\vec{k}$-conservation requirements are both satisfied, and in three dimensions, the angular profile of the photoelectron wave vector ($\vec{k}_f$) is a cone centered about $\vec{G}_{\bar{1}\bar{1}\bar{1}}$ (or $\vec{G}_{\bar{2}00}$). See the text (Section B.2) for more details.

Fig. 5. The same $\vec{k}$-space region as in Figs. 3 and 4, with two sets of intersecting initial- and final-state constant energy contours [(E_{i1}, E_{f1}), and (E_{i2}, E_{f2}), respectively], corresponding to [111]-direction primary cones at two different photon energies ($h\nu_1$, $h\nu_2$). From this construction, it is clear that primary cones which propagate along [111] must involve (a) initial states with $\vec{k}_i$ along the [111] direction (the $\Gamma\Lambda$L line) in the first BZ, and (b) final states, $\vec{k}_f = \vec{k}_i - \vec{G}_{hkl}$, with $\vec{G}$ vectors of the form ($\bar{n}$, $\bar{n}$, $\bar{n}$) (where n is a nonnegative integer). At a particular photon energy, there is only one such $\vec{G}$ vector which satisfies both energy- and

momentum-conservation requirements. Furthermore, the entire ΓΛL-line valence band structure can be studied in the normal emission ($\vec{n} \parallel [111]$) geometry, provided that a sufficiently wide range of photon energies is employed.

Fig. 6. The $(01\bar{1})$ plane in extended-zone $\vec{k}$-space for the FCC lattice, with the first BZ shown as the shaded region, and various reciprocal lattice points labelled by appropriate (h,k,l) coordinates. The extended lines pass through reciprocal lattice points (i.e., $\vec{G}$ vectors) involved in primary-cone normal emission in various directions, as indicated. The main feature is that normal emission involves only those points which lie on one of the lines for that particular emission direction.

Fig. 7. The universal curve of electron scattering (or attenuation) length vs electron energy (E_f) for typical metals, drawn as a band that encompasses most of the existing experimental data (see Chapter VI and Ref. 82). Momentum broadening is most severe at energies corresponding to the minimum of this curve (approximately 50 to 250 eV). The energies of several laboratory photon sources are shown for reference.

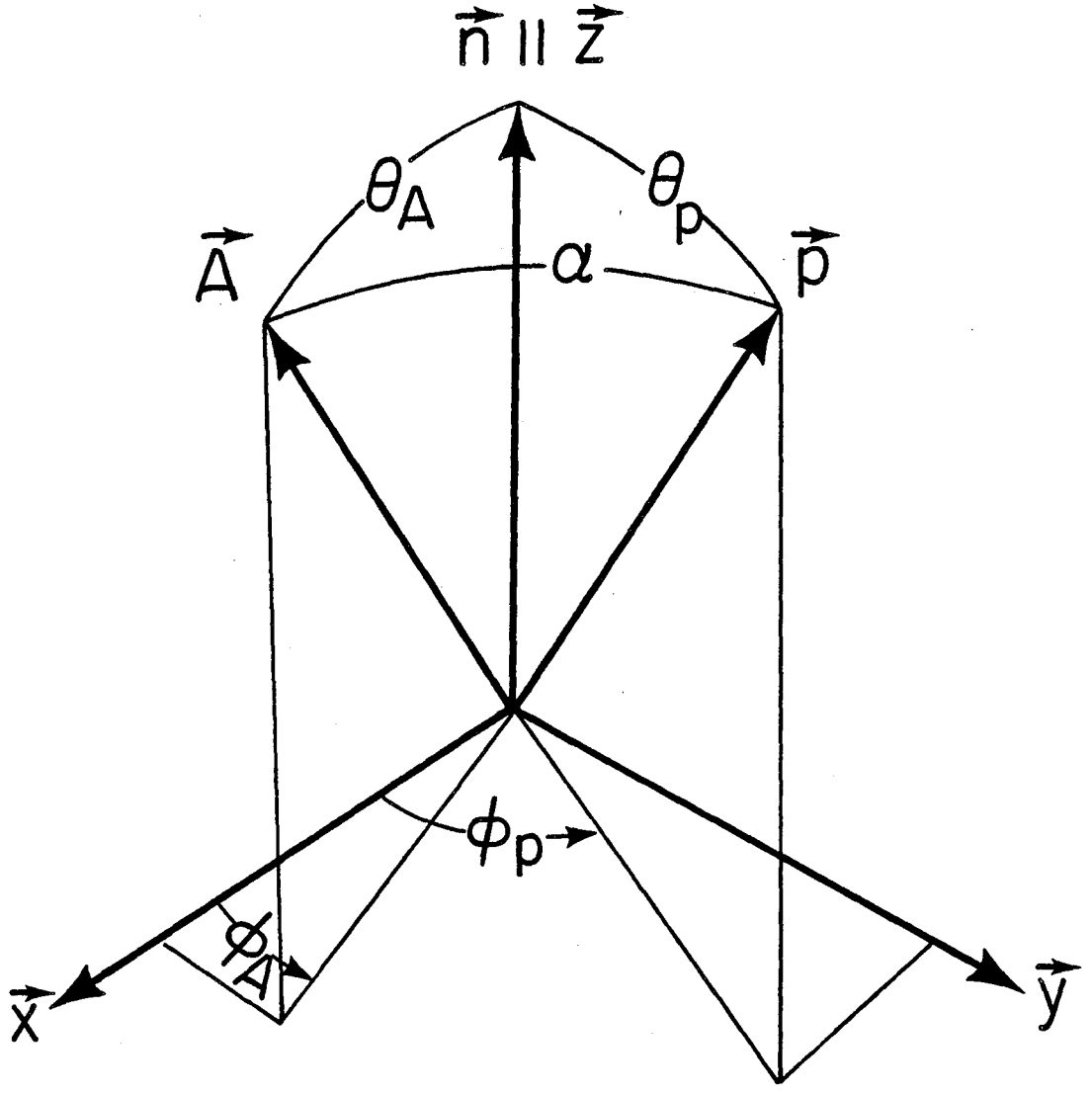

XBL8111-12052

Figure 1

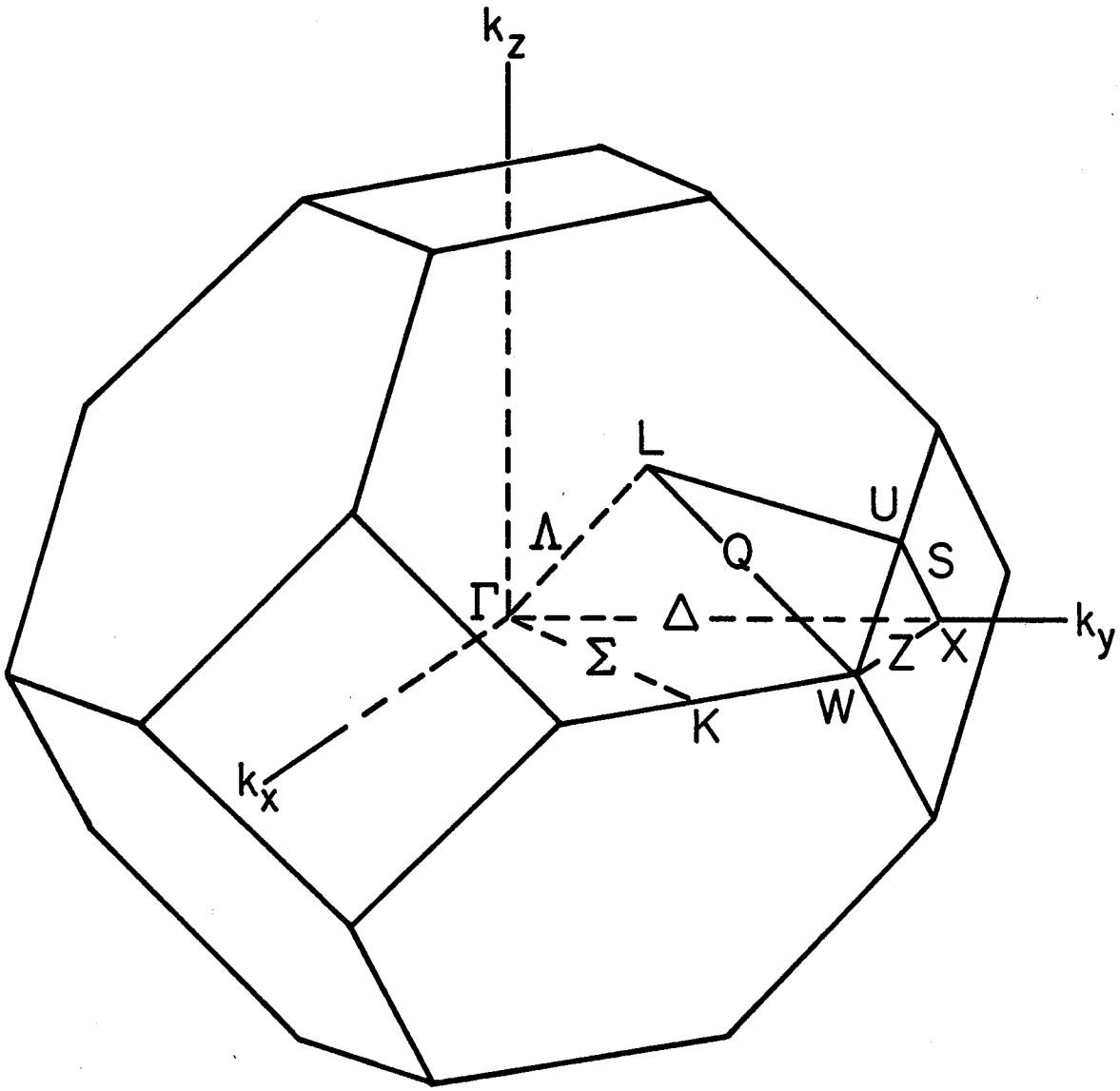

XBL 767-8928A

Figure 2

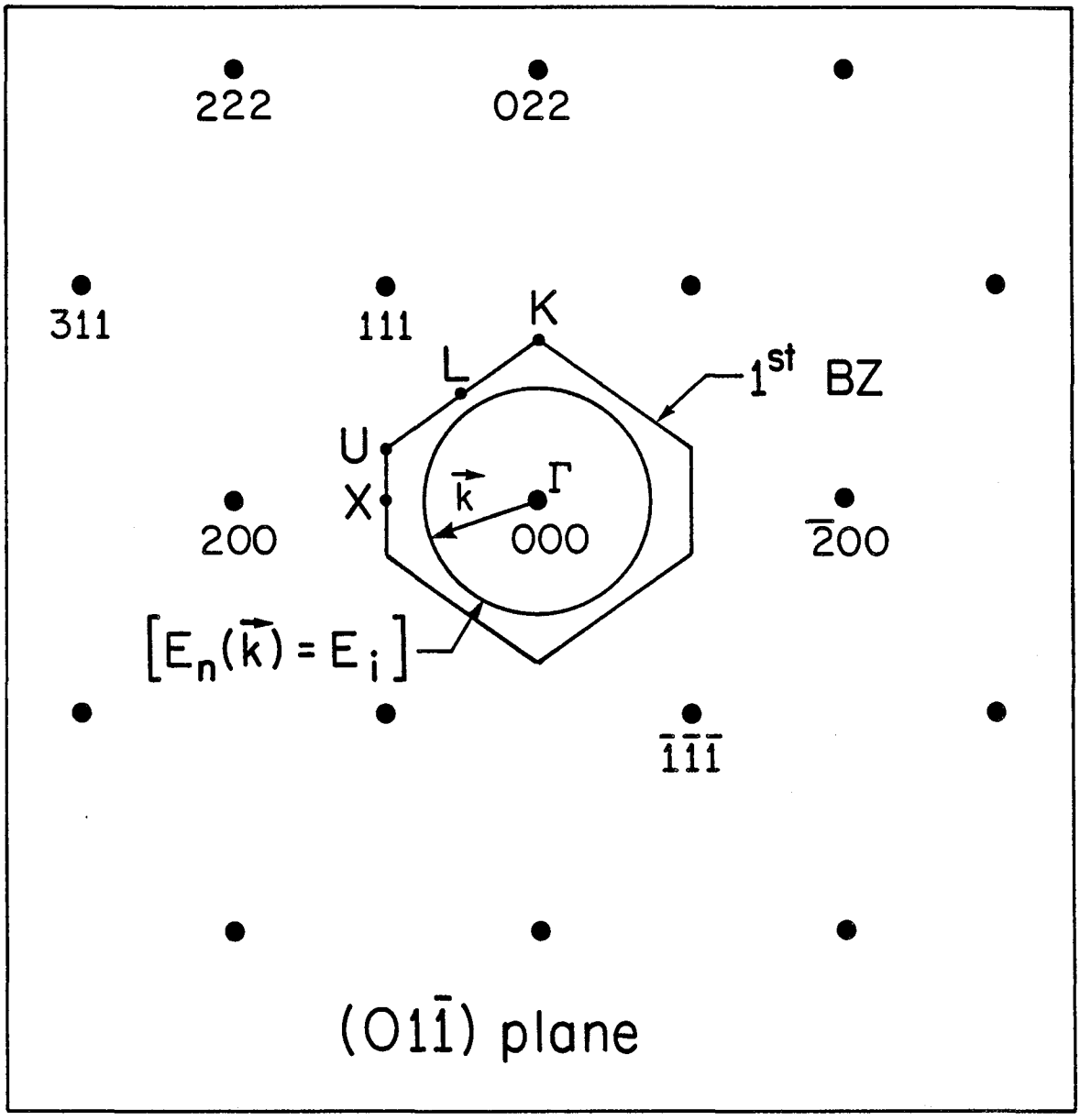

XBL8111 - 12036

Figure 3

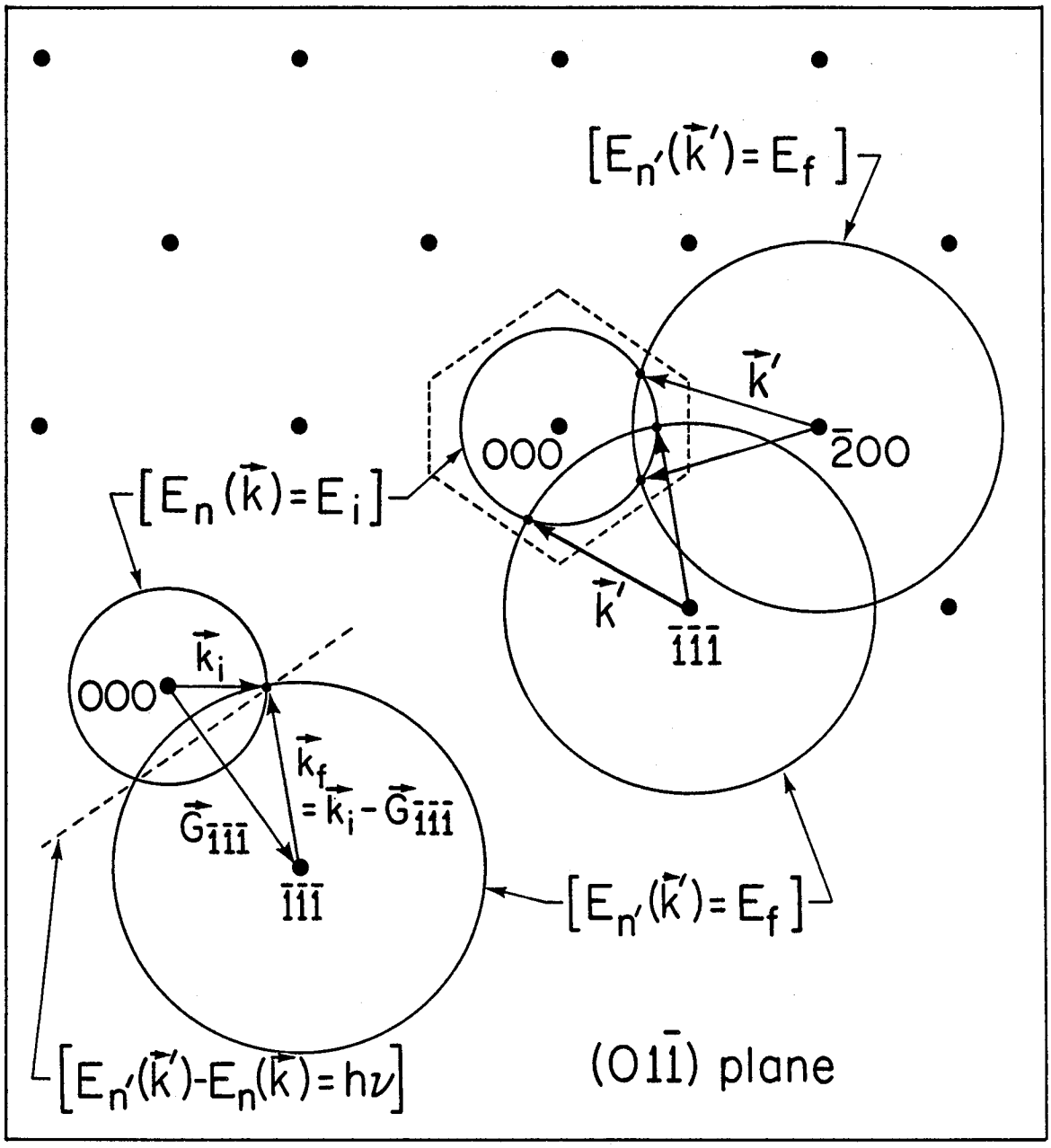

XBL 8111-12033

Figure 4

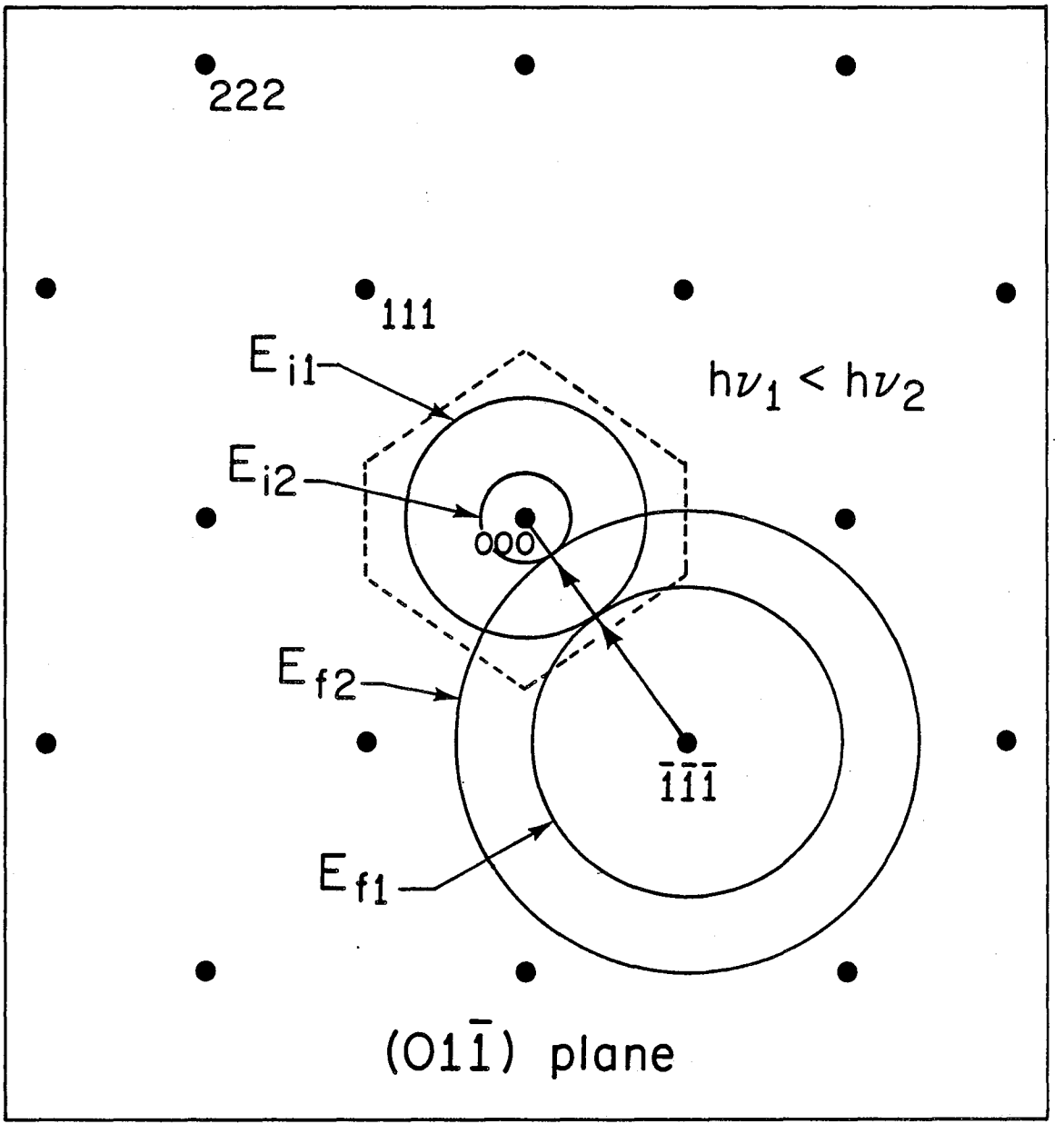

XBL 8111-12034

Figure 5

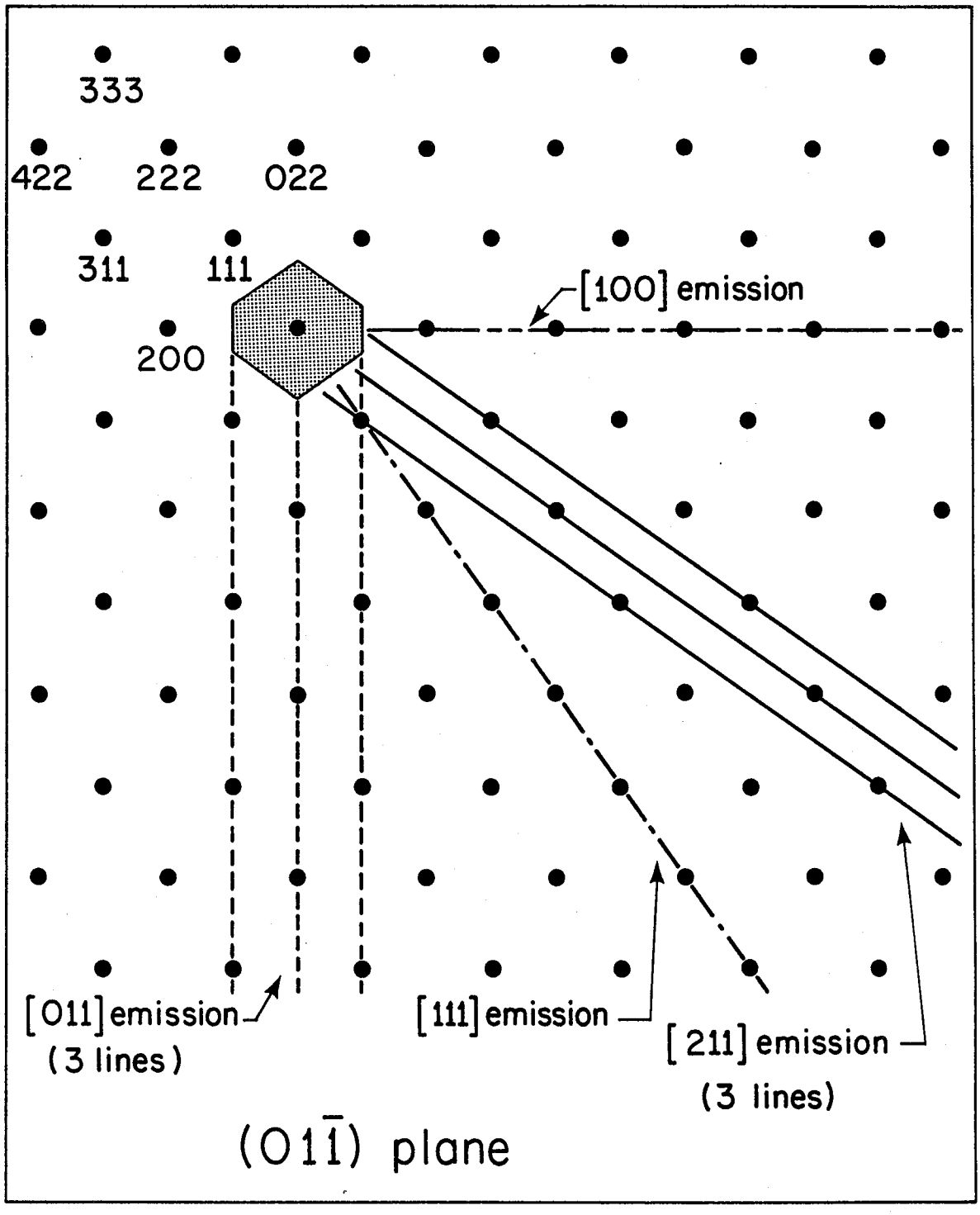

XBL8111-12032

Figure 6

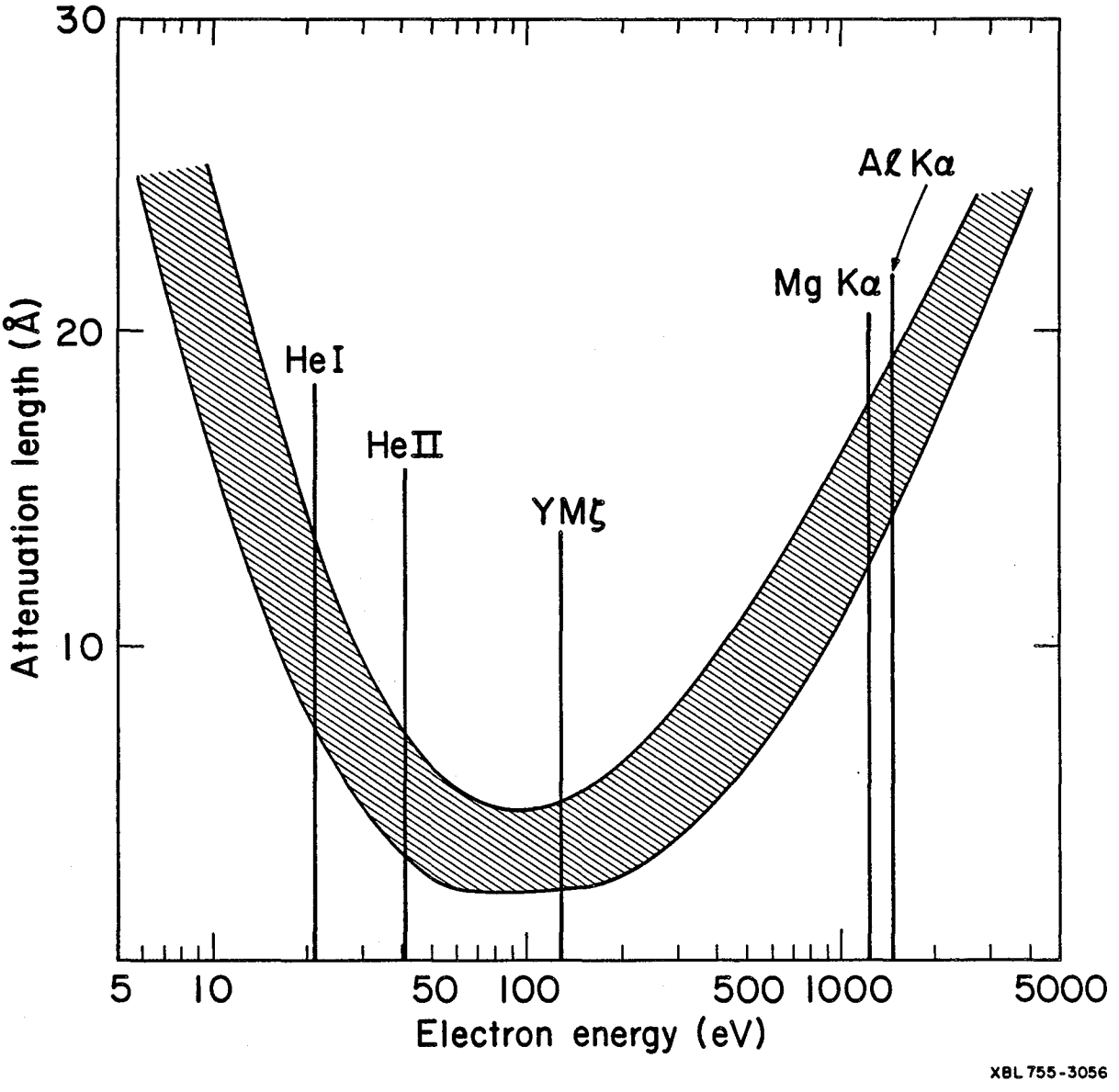
30
20
10
Attenuation length (Å)
HeI
HeII
YMζ
Mg Kα
Aℓ Kα
5
10
50
100
500
1000
5000
Electron energy (eV)
XBL 755-3056

Figure 7

PART I.

ITINERANT EFFECTS IN THE ANGULAR DISTRIBUTION: ANGLE-RESOLVED NORMAL PHOTOEMISSION STUDIES OF THE VALENCE BAND STRUCTURE OF SINGLE-CRYSTALLINE METALS

II. THE VALENCE BAND STRUCTURE OF STEPPED CRYSTAL SURFACES: Cu(S)-[3(111)x(100)] *

A. Introduction

Detailed angle-resolved photoemission (ARP) studies of the face-centered cubic (FCC) metals copper,[1-5] silver,[6,7] gold,[3,8-11] nickel,[12] palladium,[13] platinum,[8,14] and iridium[15] have shown that the peak structures in photoelectron energy distribution curves (EDCs) arise mainly from energy- and crystal momentum-conserving direct electronic transitions near or at the surface. Consequently, by combining the photon energy-variability of synchrotron radiation with a normal electron emission geometry, these studies[1,2,4,6,8,9,12-15] have resulted in the determination of empirical bulk valence-band dispersion relations along $\vec{k}_\perp$ (the surface perpendicular or normal component of the crystal momentum $\vec{k}$) with remarkable success. However, in each case, the surface studied was a low-Miller-index plane [i.e., (100), (110), or (111)]. These studies yielded experimental energy bands along high-symmetry lines in k-space, permitting ready comparisons to published theoretical band structure calculations.

In this chapter, we report angle-resolved normal photoemission (ARNP) valence-band studies of the Cu(211) face. These experiments directly address a number of important problems in photoemission from metals. The complexity of ARNP from (110) and (100) faces[16] relative to (111) suggests that a detailed understanding of ARNP from still lower symmetry faces--such as (211)--might be very difficult or

impossible. This hypothesis has several origins. First, low k-space symmetry induces a complete non-degeneracy of the energy levels at most reduced k points along the [211] line. Secondly, the relatively large surface unit cell of high-index faces gives rise to a set of small two-dimensional reciprocal lattice vectors which may induce surface umklapping of photoelectrons with higher cross section than on unreconstructed low-index faces.[17] Furthermore, like many high-index faces of the Group VIII and IB metals oriented in the [01$\bar{1}$] crystallographic zone,[18] the clean Cu(211) surface develops a stable stepped structure after annealing. The electronic structure of stepped and kinked surfaces is of considerable interest because the step and/or kink atoms on such surfaces are believed to influence surface reactivity.[19] Although there is some experimental[20] and theoretical[21] evidence that enhancement of surface reactivity may arise more from steric effects due to step-adsorbate geometry than from any particular electronic-structural property of the steps, some theoretical calculations predict, in certain cases, substantially different electronic environments for step or kink atoms relative to atoms on planar surfaces.[22,23]

An important result of this work concerns a conduction band gap along [211], which affects the band structure near, but not at, the Brillouin zone boundary. As demonstrated below, our data show essentially no evidence for the "band-gap photoemission" process discussed by previous workers.[17,24,25] Rather, we show that through a combination of different radiation polarization directions and

energies ($h\nu$), a detailed understanding of the photoemission process from Cu(211) is obtained within the framework of the direct-transition model using a quasi-free-electron final-state band structure. Furthermore, although the low symmetry of Cu(211) does indeed introduce a great deal of structure to the EDCs, it also allows us to investigate the symmetry and dispersion properties of each individual valence band.

In Section B, we discuss experimental procedures. Section C describes the results within a bulk direct-transition framework. Section D contains a general discussion, and Section E gives a summary.

B. Experimental

A high purity single crystal slab of Cu was cut and mechanically polished to within ± 0.5° of the (211) plane (19.5° from [111] in the [01$\bar{1}$] zone), with a mean surface roughness of 1 μm. After a chemical polish,[26] the crystal was installed in an ultrahigh-vacuum chamber (base pressure ~ 3 x 10^{-10} torr) for in situ preparation and characterization of the Cu(S)-[3(111)x(100)] stepped surface,[18,27] an ideal segment of which is depicted in Fig. 1. Preparation was accomplished by repeated cycles of Ar^+ sputtering, followed by annealing at ~ 875K. Immediately preceding the ARP experiments, the resulting surface was monitored by Auger electron spectroscopy (AES) for cleanliness and low energy electron diffraction (LEED) for crystallographic order, giving rise to AES impurity signals characteristic of $\lesssim$ 0.05 monolayer contamination and LEED patterns (with extremely sharp and intense

spots) characteristic of the stable step surface structure. As shown in Fig. 1, the (211) surface consists of (111) oriented terraces with three inequivalent atomic rows (labeled A, B, and C) that are parallel to the $[01\bar{1}]$ direction, and monatomic steps of (100) orientation. The only symmetry element that this surface contains is the $(01\bar{1})$ mirror plane which cuts through the surface perpendicular to the atomic rows.

The photoemission measurements were performed on the 8° branch of Beam Line I (BL I-2) at the Stanford Synchrotron Radiation Laboratory with the incident radiation highly polarized (> 97 percent) in the horizontal plane and in the energy range 9 eV $\leq h\nu \leq$ 34 eV. Our ARP instrument, described elsewhere,[28] employs a rotatable 5.40-cm mean radius hemispherical analyzer with an angular acceptance of ± 3°. In these measurements, the energy resolution (monochromator plus electron analyzer) varied from ca. 0.12 eV to ca. 0.25 eV (FWHM) at the lower and upper photon energies, respectively.

As shown in Fig. 2, experiments were done with two different normal emission geometries, conversion between which was achieved by azimuthal rotation of the crystal about its normal ($\vec{n}$) by 90°. For both orientations, the incident radiation vector potential ($\vec{A}$) was confined to the plane of incidence, and the photoemission direction ($\vec{p}$) was confined to the surface normal ([211]). In orientation I [Fig. 2(a)], $\vec{A}$ lies in a crystallographic plane perpendicular to the $(01\bar{1})$ mirror plane (M) with $\phi_A = 0°$, whereas in orientation II [Fig. 2(b)], $\vec{A}$ lies in M (M is the plane of incidence in this case) with $\phi_A = 270°$. The angle θ_A (between $\vec{n}$ and $\vec{A}$) could be varied between 10° and 45° in

either ϕ_A azimuth by coupling analyzer and crystal polar rotations, but the majority of measurements were performed with $\theta_A = 30^\circ$. At this angle, $\vec{A}$ is aligned with the [110] direction in orientation I, and is ~ 5° from alignment with [100] in orientation II. In situ polar crystallographic alignment (± 1°) was achieved using a He-Ne laser, and the azimuthal orientation (± 3°) was determined from LEED patterns. We shall henceforth refer to orientations I and II as simply (I) and (II), respectively.

Typical EDCs for the entire energy range are shown in Fig. 3 for both orientations and $\theta_A = 30^\circ$. Only 24 spectra are plotted here, for brevity. Our interpretation is based on a total of 82 spectra. In each spectrum, the Fermi level (E_F) was determined as $(dI/dE)_{max.}$, i.e., the point of maximum derivative of photoelectron intensity with respect to energy, in the region near the onset of the s-p plateau. Because of relatively low intensity (I), this procedure became progressively more difficult in the higher photon energy region ($h\nu \gtrsim 20$ eV), particularly for the spectra taken with the sample in (I). Nevertheless, the work functions derived from E_F placement and analyzer reference voltages showed an rms scatter of only ± 35 meV for the entire data set.

C. Direct-Transition Model Framework

The spectra shown in Fig. 3 clearly indicate that (a) the low symmetry of the (211) face introduces complexity to the valence band peak structure relative to the spectra of low-index Cu faces, and

(b) there is a strong dependence on radiation polarization, as the only difference between the two orientations is the direction of $\vec{A}$ relative to the crystallographic axes. The behavior of the various contributions to the spectra, which can be identified and shown to disperse as a function of photon energy, is highly indicative of bulk direct-transition processes, particularly because $\vec{k}_{\parallel}$ (surface component of momentum) is zero for normal emission. This behavior is demonstrated by the structure plots for both orientations, shown in Fig. 4. The circles represent strong peak (closed circles) or weak feature (open circles) energy positions relative to E_F for the range of photon energies used. The distinction between strong and weak features is somewhat artificial--indicative of greater peak position uncertainty but not necessarily of relative peak intensity--because the complexity of the spectra gives rise to substantial peak convolution. For example, the intensity of the most tightly bound peak in (II) appears to be weak for 14 eV $\leq h\nu \leq$ 16 eV and negligible for $h\nu <$ 14 eV, but this is probably because the peak is hidden behind the tail region of the second most tightly bound feature, which is an intense peak at these photon energies. The connecting lines on the plots in Fig. 4 have no significance other than to join and map the individual structures as a function of $h\nu$. The reproducibility between the two sets of plots [(I) and (II)] is excellent, as equivalent peaks which are found in spectra for both orientations (at a given $h\nu$) are typically separated by 0.04 eV or less.

In the normal emission geometry, peak energy dispersion with $h\nu$ as shown in Fig. 4 can only occur from direct transitions at reduced k-points which yield photocurrent in normal emission, i.e., those which either are part of the [211] direction crystal momentum space or which are in other directions but can excite transitions that result in normal emission via surface umklapp processes.[17,29] Normal emission from [211] line initial states could arise from primary Mahan cones[29] or from electrons excited away from [211] that reach the detector via surface umklapps (secondary cones). We proceed, below, to set up a bulk band structure framework[30] with which to interpret the data represented in Figs. 3 and 4, and we show that excellent agreement between experiment and theory is obtained if (a) only $\vec{k}_{\perp}$-conserving transitions from [211] initial states are assumed to occur, and (b) only one final state band is important in transmitting photocurrent to the analyzer (i.e., no secondary Mahan cones contribute <u>peak</u> structures).

1. <u>Characteristics of Cu[211] Bands</u>.

The irreducible portion of k-space lying along [211], all of which is contained in the $(01\bar{1})$ plane, is shown as the dashed line in Fig. 5. The point B = (3/4,3/8,3/8) (in units of $2\pi/a$, which will be used throughout this work) is equivalent to D = (-1/4,-5/8,-5/8), both being at the Brillouin zone boundary. Although these points have no other significance or special symmetry properties it is useful to designate them as B and D. The group of the $\vec{k}$-vector (the point group C_s)

corresponding to points along [211] ($\Gamma \rightarrow B$, $D \rightarrow X$) contains only the identity element (E) and the ($01\bar{1}$) mirror plane (σ_h). Thus, electronic states lying on the [211] crystal momentum axis may be symmetry classified as either even or odd (A' or A", respectively, in C_s) with respect to reflection through the mirror plane.

The energy bands for Cu were generated for the [211] crystal momentum line using Smith's parameterization[31] (with minor modification of several parameters) of the Hodges, Ehrenreich, and Lang interpolation scheme.[32] Although the fitting procedure considers only the occupied bands, this interpolation scheme reproduced the energy bands calculated by Janak, et al.[33] quite well up to E^F = +20 eV (E^F is energy relative to E_F). Thus, the resulting band structure shown in Fig. 6 should give a fairly good representation of both the valence bands and the conduction bands up to +20 eV. Energy bands were also calculated using interpolation parameters derived from the critical point eigenvalues of Janak, et al.,[33] and from experimental energy level positions based on Cu(111) and Cu(100) studies by Knapp, et al.[2] and Cu(110) studies by Thiry, et al.,[4] but neither of these two calculations agreed as well with our data as the one which utilized Smith's parameterization, which is based on Burdick's[34] augmented plane wave (APW) calculation. From careful inspection of the eigenvectors in our calculation, we determined the irreducible representations (A' or A") of the first nine bands at each k point, and have labeled the bands shown in Fig. 6 accordingly. We found it useful to label the bands of each type separately according to

increasing band index, but this has no group-theoretical significance. It does, however, remove ambiguities caused by band crossings. Of the six valence bands, four have A' symmetry, while two of the three lowest conduction bands also have A' symmetry. As shown, the band structure reveals a gap in the conduction bands between A_5' and A_6' from about 10.2 eV to 13.0 eV above E_F. In principle, a conduction band gap has implications for ARP if it involves the photoemission final states.[17,24,25] Although the precise location and width of the gap are not necessarily accurate in our calculation, the existance of a gap near E^F = 12 eV is guaranteed by symmetry considerations.

2. Photoemission Properties of Cu[211] Bands.

Hermanson[35] has discussed the polarization selection rules for photoemission normal to low-index faces of cubic crystals, and there have been several experimental studies of these polarization effects.[2,36] In this study, we have incorporated two different polarization geometries to investigate the importance of these effects for a stepped crystal face, for which the symmetry properties are simple. Polarization selection actually reduces considerably the problem of determining dispersion relations for each individual valence band in Cu(211), as will be discussed below. The selection rules governing ARNP from Cu(211) are summarized in Table I. The photoemission final state must belong to the A' (symmetric) irreducible representation because operations which leave the crystal invariant should not affect the electronic state sampled by the detector. Thus,

in order for a transition to be allowed, the irreducible representation of a particular initial state must be contained in the transition operator $\vec{A}\cdot\vec{P}$. Referring to Fig. 2 and Table I, the component of $\vec{A}$ along [01$\bar{1}$] (orthogonal to M) can excite A" initial states (A_1'' or A_2''), while components along [211] and [$\bar{1}$11] (lying in M) excite only A' (A_1' through A_4') initial states. Thus, for the geometries shown in Fig. 2, the spectra accumulated in (I) may arise from A' → A' and A" → A' transitions, with $|A_x/A_z| = 0.6$ at $\theta_A = 30°$. On the other hand, the spectra from (II), with $A_x = 0$, should arise from A' initial state bands only. Careful inspection of relative peak intensities in the spectra (Fig. 3) indicates a qualitative verification of these selection rules for Cu(211) direct transitions. Aided by direct comparison of theoretical and experimental band structures (vide infra), we have labeled the structure plots in Fig. 4 according to the initial states involved in the transitions. Symmetry effects in our spectra will be discussed at greater length in the next section.

In consonance with previous studies,[6,8,9,14] the photoemission final states were taken partly to be A' conduction band components which are derived from the empty lattice conduction band(s) that would be involved in [211] primary Mahan[29] cone emission (see, also, Chapters I, III, and IV). Between Γ and B, there are no unbound primary cone components in the energy range excitable with $h\nu \leq 34$ eV, as the smallest reciprocal lattice vector involved in a primary cone transition $\vec{k}_i \rightarrow \vec{k}_i - \vec{G}$ (in the empty lattice approximation) would be $\vec{G} = (4,2,2)$; this would require $h\nu > 170$ eV at $\vec{k}_i = B$. However,

there is primary emission in our energy range from final states between D and X, shown in Fig. 6 as the regions of A_5' and A_6' highlighted by filled circles. These states are derived from $\vec{G} = (\bar{1},\bar{1},\bar{1})$. In the band gap regions, 9.0 eV $\leq E^F \leq$ 14.0 eV and $E^F \geq$ 26.5 eV, the final states were derived from $E^F(\vec{k}) = (\hbar^2/2m^*)|\vec{k} - \vec{G}|^2 + V_0^F$, with $\vec{G} = (\bar{1},\bar{1},\bar{1})$. These states are shown in Fig. 6 as the two dashed curves connecting A_5' with A_6' and extending beyond A_6'. The parameters m* (effective mass) and V_0^F (inner potential) were calculated from a fit of this free-electron-like dispersion relation to the regions of A_5' and A_6' highlighted by filled circles in Fig. 6, yielding m* = 0.89 m_e and V_0^F = -8.0 eV. This value of m* is consistent with that determined experimentally by Knapp, et al.[2] for the Δ_1 conduction band in Cu(001) [(m^*/m_e) = 0.90 - 0.94]. Using the measured[37] value for the Cu(211) work function (Φ = 4.53 eV), we obtain V_0^V = -12.5 eV (V_0^V is the vacuum-referenced inner potential) for our final-state band, reasonably consistent with the value determined from LEED studies[38] of Cu(001) (V_0^V = -13.5 eV). In contrast to several previous studies (see, e.g., Ref. 14 and Chapters III and IV), this Cu(211) quasi-free-electron final-state dispersion relation was used without modification.

In Fig. 7, we show a comparison of our empirically derived valence band positions (symbols) with the interpolated dispersion relations (lines) for all six valence bands along [211]. The arrows at E_F indicate k values for which A_4' intersects the Fermi surface (from de Haas-van Alphen data[39]). The empirical bands in Fig. 7 represent the combined data of (I) and (II) (Figs. 3 and 4). If a peak appeared

in both orientations, the mean value was used to determine the band position. The points in Fig. 7 were positioned in the standard way[30] by determining $\vec{k}_i$ from the final-state band highlighted in Fig. 6. Then, for each valence band, the points were fitted to a smooth curve, yielding empirical dispersion relations. These are tabulated in Table II for selected values of $\vec{k}_i$ within the region of [211] k-space sampled by the 9 eV $\leq h\nu \leq$ 34 eV radiation [$\vec{k}_i$ between (-0.14,-0.57,-0.57) and (0.42,-0.29,-0.29)]. Considering both the complexity of the Cu(211) EDCs and the possible inaccuracies associated with our interpolation scheme calculation,[32] the theoretical and experimental bands generally agree quite well and both agree with the Fermi surface data.[39] The only feature in the EDCs which does not appear to arise from direct transitions is a weak shoulder at E^F = -2.30 ± 0.02 eV in the spectra for 9 eV $\leq h\nu \leq$ 16 eV. It is reasonable to attribute this nondispersive feature to the d-band edge in the density of states. A similar feature was noted in silver,[6] gold,[8] and platinum[8] ARNP spectra.

We can describe the "agreement" between experiment and interpolation theory quantitatively by calculating $\Delta E = E^F(\text{expt.}) - E^F(\text{int.})$ for each energy level listed in Table II, where E^F(int.) is the interpolated energy position. The results are listed in Table III, along with similar (theoretical) numbers reported by Hodges, et al.[32] for a general comparison of interpolated Cu bands with Burdick's[34] APW calculation. The theoretical ΔE values represent the general limitations of the interpolation method and thus are lower bounds on the size

of ΔE values that might reasonably be expected for these Cu(211) studies. Conversely, experimentally derived ΔE values that are smaller than those of Hodges, et al.[32] are not meaningful. By this criterion, the differences between the interpolated and experimental band structures are negligible for all bands except A_1' and A_4'. Inspection of the dispersion relations in Fig. 7 indicates that the greater deviations in A_1' and A_4' arise from the region of k-space near $\vec{k}_i$ = (0.38,-0.31,-0.31); i.e., halfway between D and X. The group velocity ($\vec{v}_g$) of the A_1' band approaches zero near E^F = -5.40 eV (expt.) and -5.68 (int.), yielding a value of ΔE (0.28 eV) that is consistent with deviations observed in the $v_g = 0$ region of the lowest s band on low-index faces of Cu.[2,4] Our measurements indicate that A_4' approaches $v_g = 0$ in this $\vec{k}_i$ region with E^F = -2.65 eV while the interpolation value is -2.34 eV, yielding ΔE = -0.31 eV. This is somewhat puzzling, because the experimental position of the uppermost s-p band on low-index faces[2,4] agrees well with the APW theory[33] along Σ, Λ, or Δ. Thus, the discrepancy observed in A_4' may well result from an associated larger error in its interpolated dispersion relation relative to the other bands. This is supported by the existence of large experiment - interpolation deviations in A_4' band energies throughout most of the region of the Brillouin zone sampled by our experiments. We cannot, however, completely rule out the possibility that transitions occur at or near Γ (i.e., transitions like $\Gamma_{12} \rightarrow \Gamma_{2'}, \Gamma_{15}, \Gamma_{25'}$), where the empty-lattice final states are highly degenerate and the valence-band density of states is large. This would yield peak

structure at or near $E^F = -2.85$ eV. The average of $E^F(\Gamma)$ and $E^F(0.38,-0.31,-0.31)$, -2.60 eV, is very close to the observed A_4' band position at $\vec{k}_i = (0.38,-0.31,-0.31)$. However, transitions at Γ are unlikely to yield the considerable intensity observed near $E^F = -2.60$ eV in the EDCs, because they produce photoelectrons with group velocities in directions other than [211]; i.e., they are secondary Mahan cones in normal emission, and secondary emission is expected to be negligible at the relatively high ($h\nu \gtrsim 30$ eV) photon energies required for Γ transitions (see Chapter I). This explanation of the deviation in A_4' near the minimum also does not address the deviations elsewhere along D - X.

Other than the shapes of the A_1'' and A_2'' experimental bands (especially near $\vec{k}_i = D$, where the $A_2'' - A_1''$ splitting is smaller than expected), the measured dispersion relations agree very well with the interpolated bands. Deviations are about as large as the errors expected in the interpolated bands alone (see Table III). This represents the most significant result of this work.

D. Discussion

A bulk direct-transition framework has been set up and shown to fit the Cu(211) data quite well. Now, the results will be discussed with particular emphasis on: (a) symmetry properties of the Cu(211) EDCs, and (b) final-state structure and the absence of band-gap photoemission.

1. General Symmetry Properties.

In Fig. 8, Cu(211) spectra ($\theta_A = 30^\circ$) at several photon energies are directly compared for the two orientations, (I) and (II). The EDCs in each set of curves are normalized to the most intense feature. Throughout the data range, the majority of peak intensity in (I) (where direct transitions from A" and A' states are allowed) arises from A_1', A_2', A_1'', and A_2'', whereas (II) (only A' states allowed) is dominated by photoexcitation from A_1', A_2', and A_4'. Relative intensity and dispersion characteristics of each valence band feature will be discussed separately, beginning with the uppermost band.

(1) A_4'. Below $h\nu = 19$ eV, A_4' clearly dominates the s-p-plateau region of the spectra in (II), while no peak is observed there in (I). The s-p plateau, which arises from indirect transitions, is larger in (II) than in (I) over most of the photon energy range. This is shown by the top curve in Fig. 9, where $R_{21} = \mathcal{I}(II)/\mathcal{I}(I)$ is plotted for the s-p region, and may be an indication that indirect transitions also follow a polarization selection rule in photoemission. If so, the s-p plateau arises largely from indirect transitions at k points which have point group symmetry no lower than that of the [211] line, i.e., those lying in the $(01\bar{1})$ plane. However, a selection rule for indirect transitions is only rigorously valid if there always exists a phonon of the correct symmetry[40] which can couple with the $\vec{k}$ vector of the electron in the photoexcitation transition. Indirect transitions undoubtedly arise from d bands also, but this is masked by the large direct-transition intensity in the d-band region. Between $h\nu = 9$ and

19 eV, A_4' disperses from E^F = -0.23 to -1.78 eV in (II). At $h\nu$ = 20 eV, the A_4' intensity in (II) has moved into coincidence with part of the A_2'' peak centered at E^F = -2.30 eV, making a definitive peak position assignment of A_4' impossible and giving the misleading appearance of a resonance in the A_2'' peak in this energy range (cf. $h\nu$ = 22 eV in Fig. 8). At $h\nu$ = 25 eV and E^F = -2.42 eV, A_4' again appears as a separate structure in (II), splitting away from A_2'' on the higher binding energy side. Additionally, A_4' appears in (I) for the first time at $h\nu$ = 26 eV with E^F = -2.51 eV. We note that the large intensity of the A_4' peak for $h\nu \geq 25$ eV is related to the large amount of d character that its wave function picks up near $\vec{k}_i$ = (0.38,-0.31,-0.31) because it mixes strongly with the uppermost A' d bands. Thus, A_4' is the dominant feature in the spectrum for (II) at $h\nu$ = 34 eV (see Fig. 8) with E^F = -2.55 eV, and is clearly discernable in (I) for $h\nu \geq 26$ eV. In (II) and (I), respectively, A_4' continues to disperse downward at $h\nu$ = 26 eV with E^F = -2.46 and -2.51 eV, to E^F = -2.68 and -2.70 eV at $h\nu$ = 30 eV, where it reaches a band minimum. It disperses upward toward E_F for $h\nu$ > 30 eV in both orientations.

(2) A_2''. A_2'' apparently contributes intensity to spectra in both orientations throughout the energy range studied. Possible causes for the large intensity in the A_2'' region of the EDCs in (II), where it is symmetry forbidden, can be discussed. First, A_2'' is convoluted with A_4' completely for 19 eV < $h\nu$ < 25 eV and partially for several electron volts on either side of this range, giving the misleading appearance of a large A_2'' intensity. In addition, the intensity of the A_2''

peak was found to be extremely sensitive to the azimuthal angle ϕ_A; thus, some of its intensity in (II) must arise from the relatively large ($\pm$ 3°) uncertainty in ϕ_A, as well as from the finite ($\pm$ 3°) geometric half-angular acceptance of the analyzer. In other words, if A_2'' intensity is very sensitive to ϕ_A, then it appears in our spectra for (II) because $\vec{A}$ has a small component along the x-axis ($\perp$ to M) because of the angular uncertainty in ϕ_A. Furthermore, while density-of-states (DOS) photoemission does not play a dominant role in our spectra, it yields a weak shoulder (E^F = -2.30 eV) in the spectra for $h\nu \leq 16$ eV. A photoelectron sampling depth argument suggests that DOS emission should be enhanced at higher photon energies.[41] Thus, although apparently absent from the spectra for $h\nu > 16$ eV, it is undoubtedly hidden beneath direct-transition intensity from A_2'' in (I) and may account for a large part of the intensity of A_2'' in (II). The empirical A_2'' band is extremely flat, with an average energy of E^F = -2.40 $\pm$ 0.08 eV. Thus, it could easily coincide with a DOS peak at -2.30 eV. But, if polarization selection is valid for DOS features, the DOS intensity in (II) cannot arise from a one-dimensional DOS because it would arise almost entirely from symmetry-forbidden A_2'' states, i.e., it must be from the three-dimensional DOS.

The energy-dispersive characteristics of A_2'' in both orientations are similar: E^F = -2.60 eV at $h\nu$ = 11 eV, dispersing up to E^F = -2.33 eV at $h\nu$ = 19 eV; it remains relatively flat until $h\nu$ = 23 eV where it begins to move away from E_F, moving to E^F = -2.41 eV at

$h\nu = 27$ eV. Above $h\nu = 27$ eV, A_2'' rises, reaching $E^F = -2.27$ eV at $h\nu = 34$ eV.

(3) A_1''. This is the most intense feature in (I), but it is essentially absent from (II), appearing only as a weak shoulder at most photon energies in the latter orientation. For this reason, definitive empirical dispersion relations for A_2' and A_3' near $\vec{k}_i$ = (0.38,-0.31,-0.31) could be determined. In (I), A_1'' masks the weaker A_2' feature for $h\nu > 23$ eV and the much weaker A_3' feature for $h\nu > 18$ eV. But, in (II) the A_1'' peak is small below $h\nu = 22$ eV and absent above, allowing the band positions of A_3' and A_2' to be determined. This is another important result of this work: symmetry considerations may be used to effectively "turn off" bands and determine individual band dispersion relations along what would otherwise be considered a complicated direction in k-space. The A_1'' peak can be clearly seen at low photon energies, starting with $h\nu = 12$ eV and E^F = -2.78 eV in (II) and $h\nu = 13$ eV, $E^F = -2.84$ eV in (I). At $h\nu = 12$ eV, A_2'' obscures the A_1'' peak in (I) (the empirical $A_1'' - A_2''$ splitting in this region is only about 0.25 eV). In (II), where it is symmetry forbidden, A_1'' becomes relatively weaker with increasing energy. In the range 20 eV $\leq h\nu \leq$ 22 eV, A_1'' is visible in (II) as a weak shoulder on the low-binding-energy side of the intense A_2' direct-transition peak, with $E^F = -3.42$ eV at $h\nu = 22$ eV (cf. Fig. 8). In (I), where it is symmetry allowed, A_1'' moves from $E^F = -2.84$ eV at $h\nu = 13$ eV (where it is still smaller than A_2''), to $E^F = -3.54$ eV at $h\nu = 27$ eV, becoming the dominant feature in the spectra for $h\nu \geq 15$ eV. Above $h\nu = 27$ eV,

A_1'' moves toward E_F again, reaching $E^F = -3.39$ eV at $h\nu = 34$ eV. It actually crosses the A_3' and A_2' dispersion relations; this can be seen in Fig. 8 in the spectra for $h\nu = 28$ eV, where $E^F(A_1'') = -3.53$, $E^F(A_2') = -3.46$, and $E^F(A_3') = -3.28$ eV.

(4) A_3'. This transition is apparently weak, appearing as a shoulder on the low binding energy side of A_2' in both orientations. In (I) it is seen at $h\nu = 13.0$, 13.5, 17.0, and 18.0 eV with energies in the range -3.74 eV $\leq E^F \leq -3.61$ eV. In (II), where A_1'' is not a strong feature, A_3' is observed in the range 17 eV $\leq h\nu \leq$ 29 eV with $E^F = -3.79$ and -3.28 eV at the low and high photon energy limits of this range, respectively.

(5) A_2'. This band contributes the largest intensity to the EDCs over most of the photon energy range in (II), and in (I) is a large peak although obscured for $h\nu \geq 24$ eV by the stronger symmetry allowed A_1'' transition. The A_2' onset is at $h\nu = 11$ and 13 eV with energies $E^F = -3.93$ and -3.81 eV in (II) and (I), respectively. By $h\nu = 13.5$ eV, A_2' is the dominant feature in (II), with $E^F = -3.89$ eV. It moves to $E^F = -4.01$ eV at $h\nu = 15.0$ eV, then disperses upward for $h\nu > 15$ eV, reaching $E^F = -3.40$ at $h\nu = 30$ eV. Finally, it is found at $E^F = -3.46$ at $h\nu = 34$ eV. In (I), A_2' disperses upward for $h\nu > 13$ eV, until it is obscured by the A_1'' peak at $h\nu = 24$ eV near the energy where these two bands cross.

(6) A_1'. A relatively large peak is observed from A_1' in both orientations and for $h\nu > 13.5$ eV. It appears to be somewhat weaker in (II) relative to (I) than would be expected by symmetry considerations,

but this is undoubtedly because it is obscured by the strong A_2' transition below $h\nu = 16$ eV. However, it is still clearly seen in each orientation starting at $h\nu = 13.5$ and 14.0 eV, with $E^F = -4.16$ and -4.21 eV, in (I) and (II), respectively. From there, A_1' disperses downward in both orientations, reaching a band minimum with $E^F = -5.42$ eV at $h\nu = 29$ eV. It would be somewhat difficult to determine the A_1' band position accurately for 14 eV $\leq h\nu \leq$ 18 eV without the aid of the spectra in (I). These spectra (cf. $h\nu = 14$ and 16 eV in Fig. 8) show that the A_2' transition in (I) does not obscure the A_1' transition.

2. Refraction of Incident Radiation and θ_i Dependence of Relative Peak Intensities.

As discussed in Section C, the components of $\vec{A}$ that are parallel to M (A_z, A_y) can excite A' transitions and A_x ($\perp$ M) excites A" transitions, if the polarization selection rules are obeyed in Cu(211) (see Table I). Finite angular acceptance of the analyzer ($\pm 3^\circ$), angular alignment ($\pm 1^\circ$ in θ, $\pm 3^\circ$ in ϕ), and incomplete polarization of the radiation (> 97 percent polarized) are among the effects which contribute to the apparent breaking of these rules; i.e., weak photoemission from A_1'' and somewhat stronger emission from A_2'' in (II), where they are both forbidden because $|A_x| = 0$ (see Fig. 2). In (I), where $|A_x|$ and $|A_z|$ are both greater than zero, the relative intensity ratio of A' to A" photoexcitation should be proportional to $|A_z/A_x|^2$ which is 3 for the incident radiation field. However, there

is no A_4' peak in (I) except at higher photon energies and A_1'' typically dominates over A_2' and A_3', suggesting that $|A_z/A_x|^2$ is effectively less than 1. This might arise from a classical Fresnel-type modification of the macroscopic electromagnetic field as it passes through the vacuum-solid interface.[42] Smith, et al.[43] have discussed these effects in the ARP polarization studies of Cu(111) by Knapp, et al.[2] They defined the parameter $\xi_t = \xi_t(h\nu,\theta_i) = |A_{zt}/A_{xt}|^2$ where $|A_{zt}|$ and $|A_{xt}|$ are the transmitted components of the $\vec{A}$ vector, and θ_i is the optical angle of incidence ($\theta_i = 60°$ in the present case). ξ_t can be determined from ε_1 and ε_2, the dielectric constants of the sample. Using known ε_1 and ε_2 values for Cu,[44] ξ_t has been calculated in the energy range 9 eV $\leq h\nu \leq$ 34 eV and is shown in Fig. 9 (bottom curve). It is generally $<<$ 3 ($\xi_i = |A_{zi}/A_{xi}|^2 = 3$) throughout, and is < 1 below $h\nu = 26$ eV. This effect accounts at least qualitatively for the large observed intensity for A" states in (I).

Radiation refraction effects in our data may be discussed further. Also shown in Fig. 9 are intensity ratio curves for the s-p-plateau region discussed above (energy window 0 eV $\leq -E^F \leq$ 1.8 eV) and the d bands (energy window 1.8 eV $\leq -E^F \leq$ 5.0 eV) as functions of photon energy. The ratio R_{21} is the ratio of intensity in (II) to the intensity in (I). As discussed before, the s-p region is more intense in (II) (where the A_4' transition is "most allowed") than in (I), with $R_{21}(sp) > 1$ for photon energies $h\nu > 13$ eV. The feature labeled "a" in Fig. 9 marks the energy at which the direct-transition peak from A_4' is centered in the 1.8 eV window in (II) ($E^F \sim -0.9$ eV). There is an

inflection point above this, presumably because part of the A_4' direct transition has moved out of the window. The point "b" locates the energy at which the center of the A_4' direct transition in (II) is at the edge of the window ($E^F \sim -1.8$ eV). At higher energies, the ratio drops, but it rises again from about 1.5 at $h\nu = 22$ eV to 1.8 at $h\nu =$ 25 eV. The d-band ratio $R_{21}(d)$ in Fig. 9 is more striking. It is less than 1 throughout the energy region, reaching its maximum value of 0.90 at $h\nu = 18$ eV. It remains essentially flat for about 4 electron volts thereafter, then dips suddenly to 0.67 at 26 eV, then rises to a second maximum of 0.90 at 32 eV. The large dip at 26 eV (feature "c") signals a sudden relative increase in d-band emission in (I), i.e., from A_1'' and/or A_2'' states near the center of the D - X line. The peak in $R_{21}(sp)$ indicates an increase in s-p emission in (II) relative to (I). The reason for the d-band ratio fluctuation could simply be the larger density of initial states in the center of the D - X portion of the zone, where $v_g \sim 0$ for these valence bands, but there is no reason to expect the observed differential increase in photoemission in (I) on this basis because A_2', A_3', and A_4' also have $v_g \sim 0$ at these $\vec{k}_i$ values. Also, this would not explain the s-p ratio fluctuation. The explanation is more likely in the sudden drop in ξ_t (lower curve) near $h\nu = 26$ eV. The ξ_t curve dips near $h\nu = 26$ eV because ε_2 rises[44] from 0.690 at $h\nu = 23$ eV to 0.761 at $h\nu = 25$ eV. In turn, ε_2 rises primarily because of $d \rightarrow f$ electron transitions[45] occurring at or near Γ. Although ξ_t cannot quantitatively account for R_{21} over the entire energy range, its rapid variation near $h\nu = 26$ eV suggests that R_{21} is

attenuated for d bands and enhanced for s-p electrons simply because of enhanced suppression of A_z, i.e., a relative attenuation of emission from bands of A' symmetry and/or an enhanced A" signal in (I) takes place. The intense A" d-band emission in (I) causes $R_{21}(d)$ to drop, while the absence of s-p electrons with A" symmetry causes $R_{21}(sp)$ to increase. We note that an analysis like this is possible only as the result of the simple symmetry selection rules for Cu(211). Smith, et al.[43] required a constant value of $\xi_t \sim 0.09$ (i.e., a factor of ~ 5 lower than the classical Fresnel value) to obtain good agreement between their theory and the experimental data of Knapp, et al.[2] While it is difficult to compare this with our experimental results without a theoretical calculation, a factor of ~ 5 reduction in ξ_t (e.g., $\xi_t \sim 0.18$ at $h\nu = 20$ eV) would not seem to be warranted by R_{21} near unity over a large part of the energy range above 16 eV. Furthermore, the striking similarity in the fluctuation of the R_{21} and ξ_t curves near 26 eV suggests that ξ_t is not an energy-independent constant in this photon energy range.

Finally, it is interesting to compare EDCs for different θ_i. In Fig. 10, spectra at $h\nu = 17$ eV are shown for both orientations and θ_i = 50°, 60°, and 80° corresponding to ξ_i = 1.4, 3.0, and 32; and ξ_t = 0.52, 0.64, and 0.78, respectively. For (II), the spectra are normalized to the intensity of $(A_2' + A_3')$ (this is essentially A_2' at this energy), and (I) EDCs are normalized to the A_1'' intensity. Generally, only changes in relative peak intensities are induced by varying θ_i at all photon energies studied. New peak structures are not

observed. For example, in (I) at 17 eV (Fig. 10), the s-p plateau, $(A_2' + A_3')$, and A_1' grow with increasing θ_i, in consonance with the trend in $\xi_t(\theta_i)$. In (II), $|A_x| = 0$; thus, the relative intensities of the four A' peaks in (II) [A_4', $(A_3' + A_2')$, and A_1'] do not significantly change with θ_i. However, it was noted above that residual experimental misalignment effectively leads to $|A_x| \gtrsim 0$. Therefore, increasing θ_i in (II) suppresses the residual $|A_x|$ component in a manner similar to (I), accounting for the observed attenuation of A_2'' intensity in (II) (Fig. 10).

3. Final-State Band Structure.

Previous experimental and theoretical work on low-index faces[17,24,25] showed evidence for unusual behavior in ARP when the excitation energy placed photoelectrons into bulk conduction band gaps. The main feature supporting this is a "lack of dispersion" of the initial-state bands,[25] arising because the $\vec{k}$ vector of the photoelectron is imaginary in the gap, thereby allowing only states at the surface to be excited.[17,24] Because $|\vec{k}_{\parallel}| = 0$ in normal emission, band-gap photoemission corresponds to photoexcitation from $\bar{\Gamma}$, independent of photon energy. Hence, sweeping the photon energy resulted in direct transitions with concomitant valence-band dispersion as $\vec{k}_{\perp}$ was varied across the zone, until the gap was reached.[25] However, bulk conduction band gaps along high symmetry directions invariably occur at Γ and/or zone boundaries, and it could be argued equally well that the lack of dispersion is simply a consequence of $v_g \sim 0$ for the

initial-state bands. Additionally, lack of dispersion in d bands is not necessarily indicative of band-gap photoemission, because they are already reasonably flat.

As a consequence of low symmetry, the conduction band gap between A_5' and A_6' in Cu[211] occurs away from the zone boundary, where initial-state s and s-p bands (A_1' and A_4', respectively) have large group velocities. Thus, an unambiguous test of band-gap photoemission should be possible in Cu(211). The experimental dispersion relations in Fig. 7 show that there is no evidence for the band-gap photoemission process discussed previously. The portion of the band structure expected to be affected by the bulk band gap is enclosed within the vertical dashed lines. Not only do the s and s-p bands disperse throughout the gap region, but the absolute s-p and d-band intensities used to derive the R_{21} curves in Fig. 9 show no unusual structure in the spectra for either orientation. Previous work in this laboratory on low-index faces of Ag,[6] Au,[8,9] and Pt[8,14] also showed initial-state dispersion at photon energies for which the final states should be in a conduction-band gap, but the present Cu(211) work is by far the most convincing evidence for this, because of the large slope in the A_1' and A_4' bands away from the zone boundary. Furthermore, Fig. 7 shows that d-band dispersion in the gap region is minimal in both theory (interpolated bands) and experiment, indicating that a dispersionless d band is not sufficient evidence for a band-gap photoemission process.

The apparent lack of band-gap photoemission leads directly to a discussion of the final-state band structure in ARP and the success of

the single-plane-wave approximation for its dispersion relation. It has been shown that the finite lifetime of the photoelectron (which is relatively short in Cu at these energies[2]) introduces an imaginary component to its $\vec{k}$ vector regardless of its position in the zone,[46] and that the effect of this is to remove gaps in the band structure, giving rise to more free-electron-like conduction bands.[46,47] It has also been pointed out that while k-broadening is still more important in the band-gap region than outside it, the increase in the spread in $\vec{k}$ (i.e., Im $\vec{k}$) is only by a factor of 2-3.[47] Physically, damping attenuates the interaction between the photoelectron and the periodic lattice potential.[47] Since band gaps arise from Bragg scattering, it is not surprising that damping closes these gaps. Strictly speaking, all of this points to the inadequacy of the one-electron band structure picture in describing photoelectron dispersion relations.[48] The photoelectron is short-lived, and the bulk band structure does not account for the symmetry-breaking influence of the hole, which is relatively long-lived. However, experimental[5,30] results suggest that the quasi-free-electron approximation works well over a wide range of final-state energies. The striking evidence for this in Cu(211) represents another important result of this work.

E. Summary and Conclusions

We have presented results of normal emission ARP studies using variable-energy synchrotron radiation for the stepped Cu(211) face. The photoemission process is similar to low-Miller-index faces of

copper.[1,2,4] All peak structures in the EDCs, except for a previously observed DOS feature at the leading edge of the 3d bands and the s-p plateau, are shown to derive from $\vec{k}_{\perp}$-conserving direct transitions along the [211] direction in k-space. The presence of the stepped surface does not introduce any other spectral features, although part of the photoemission intensity in various peaks (particularly A_2'' in orientation II) may arise from DOS photoemission. Excellent agreement between peak energy positions and bulk-initial state dispersion relations is obtained if the final-state wave function is assumed to contain only one plane-wave component; i.e., no secondary Mahan emission features were found. This excellent agreement with the interpolated bulk bands suggests that any photoelectron refraction effects associated with non-normal emission, i.e., from step and/or terrace directions, are negligible. In consonance with previous work,[5,30] a quasi-free-electron parabolic final-state dispersion relation was used successfully, even at energies corresponding to a symmetry band gap near the zone boundary. The top and bottom valence bands, A_4' and A_1', are shown to disperse even when the final state falls in this gap region, suggesting that the one-electron bulk-band-gap picture is not applicable to the description of photoelectron conduction-band structure. Finally, radiation polarization selection and refraction at the vacuum-solid interface are observed to play an important role in determining relative peak intensities. This is demonstrated in a particularly straightforward manner with Cu(211) because there are only two irreducible representations (A' and A") for

eigenstates along the [211] direction. In fact, polarization selection greatly reduces the problem of determining individual band empirical dispersion relations along the complicated [211] direction.

These studies suggest that the stepped structure of the Cu(211) surface does not significantly perturb its bulk-like electronic structure, a result which was anticipated in previous work.[20,49] In contrast to this, it would be interesting to investigate the valence-band structure properties of stepped crystal faces of the catalytically active Group VIII metals, particularly in light of recent Pt(100)-(5x1) results,[14] which showed large DOS contributions to the normal-emission EDCs for the reconstructed surface (see, also, Chapter III).

Based on these Cu(211) results, we conclude that bulk-valence band structure determination can be applied to low-symmetry directions in a manner analogous to the (111), (100), and (110) faces, thereby alleviating the necessity for crystal faces with a specific high-symmetry orientation. This has implications for band-structure studies of more complicated materials, where it may not be possible to obtain high-symmetry faces.

Finally, the four major results of this work are summarized: (1) it is possible to determine experimental valence-band dispersion relations for non-low-index directions; (2) valence-band dispersion relations for stepped Cu(211) show excellent agreement with bulk valence bands interpolated along the [211] direction; (3) the quasi-free-electron model describes photoelectron dispersion relations, but the one-electron bulk conduction bands do not; and (4) there is no evidence for band-gap photoemission.

REFERENCES

* This chapter is based on experiments performed in collaboration with R. S. Williams, S. D. Kevan, P. S. Wehner, and D. A. Shirley; submitted to Phys. Rev. B for publication (LBL-8511).

1. J. Stöhr, P. S. Wehner, R. S. Williams, G. Apai, and D. A. Shirley, Phys. Rev. B 17, 587 (1978); D. A. Shirley, J. Stöhr, P. S. Wehner, R. S. Williams, and G. Apai, Phys. Scripta 16, 398 (1977).
2. J. A. Knapp, F. J. Himpsel, and D. E. Eastman, Phys. Rev. B 19, 4952 (1979).
3. P. O. Nilsson and L. Ilver, Solid State Commun. 17, 667 (1975); L. Ilver and P. O. Nilsson, Solid State Commun. 18, 677 (1976).
4. P. Thiry, D. Chandesris, J. Lecante, C. Guillot, R. Pinchaux, and Y. Petroff, Phys. Rev. Lett. 43, 82 (1979).
5. Z. Hussain, S. Kono, L.-G. Petersson, C. S. Fadley, and L. F. Wagner, Phys. Rev. B 23, 724 (1981), and references therein.
6. P. S. Wehner, R. S. Williams, S. D. Kevan, D. Denley, and D. A. Shirley, Phys. Rev. B 19, 6164 (1979), and references therein; K. A. Mills, M. G. Mason, R. F. Davis, R. Watson, G. Thornton, J. G. Tobin, Z. Hussain, E. Umbach, and D. A. Shirley, to be published.
7. G. V. Hansson and S. A. Flodström, Phys. Rev. B 17, 473 (1978).
8. K. A. Mills, R. F. Davis, S. D. Kevan, G. Thornton, and D. A. Shirley, Phys. Rev. B 22, 581 (1980).

9. R. F. Davis, M. G. Mason, Z. Hussain, J. G. Tobin, L. E. Klebanoff, and D. A. Shirley, to be published.

10. P. Heimann, H. Miosga, and H. Neddermeyer, Solid State Commun. 29, 463 (1979).

11. G. V. Hansson and S. A. Flodström, Phys. Rev. B 18, 1572 (1978).

12. D. E. Eastman, F. J. Himpsel, and J. A. Knapp, Phys. Rev. Lett. 40, 1514 (1978); F. J. Himpsel, J. A. Knapp, and D. E. Eastman, Phys. Rev. B 19, 2919 (1979).

13. F. J. Himpsel and D. E. Eastman, Phys. Rev. B 18, 5236 (1978).

14. G. Thornton, R. F. Davis, K. A. Mills, and D. A. Shirley, Solid State Commun. 34, 87 (1980).

15. J. F. van der Veen, F. J. Himpsel, and D. E. Eastman, Phys. Rev. B 22, 4226 (1980).

16. R. F. Davis, K. A. Mills, G. Thornton, S. D. Kevan, and D. A. Shirley, VI International Conference on Vacuum Ultraviolet Radiation Physics (Charlottesville VA, 1980), Vol. I, pp. 1-3.

17. B. Feuerbacher and R. F. Willis, J. Phys. C 9, 169 (1976).

18. See e.g., G. A. Somorjai, Chemistry in Two Dimensions: Surfaces (Cornell University Press, Ithaca NY, 1981), Chapter 4.

19. G. A. Somorjai, Adv. Catal. 26, 1 (1977); D. W. Blakely and G. A. Somorjai, J. Catal. 42, 181 (1976).

20. R. S. Williams, P. S. Wehner, S. D. Kevan, R. F. Davis, and D. A. Shirley, Phys. Rev. Lett. 41, 323 (1978).

21. K. Ždánský and Z. Šroubek, J. Phys. F 6, L205 (1976).

22. M. C. Desjonquères and F. Cyrot-Lackmann, Solid State Commun. 18, 1127 (1976).

23. Y. W. Tsang and L. M. Falicov, J. Phys. C 9, 51 (1976).

24. P. J. Feibelman and D. E. Eastman, Phys. Rev. B 10, 4932 (1974); F. J. Himpsel, Appl. Opt. 19, 3964 (1980).

25. E. Dietz and F. J. Himpsel, Solid State Commun. 30, 235 (1979).

26. We used a solution of sodium 2-mercaptobenzimidazole-5-sulfonate and polyethylene glycol 400 in HCl; see J. S. Ahearn, J. P. Monaghan, and J. W. Mitchell, Rev. Sci. Instrum. 41, 1853 (1970).

27. B. Lang, R. Joyner, and G. A. Somorjai, Surf. Sci. 30, 440 (1972); 454 (1972).

28. S. D. Kevan and D. A. Shirley, Phys. Rev. B 22, 542 (1980).

29. G. D. Mahan, Phys. Rev. B 2, 4334 (1970).

30. See e.g., R. S. Williams, P. S. Wehner, J. Stöhr, and D. A. Shirley, Surf. Sci. 75, 215 (1978); Refs. 1, 6, 8, 9, 14, and 16.

31. N. V. Smith, Phys. Rev. B 3, 1862 (1971).

32. L. Hodges, H. Ehrenreich, and N. D. Lang, Phys. Rev. 152, 505 (1966). As a consequence of the plane-wave basis set utilized in the calculation, this interpolation scheme requires that $\vec{k}_i = (k_x, k_y, k_z)$ lies in the (1/48)th portion of the first Brillouin zone with $k_y \geq k_x \geq k_z \geq 0$. This procedure was followed precisely for Cu[211] in the present work. By symmetry, however, the resulting band structure is equivalent in all (1/48)th portions of the zone, including those actually diagrammed in figures and discussed in the text of this chapter.

33. J. F. Janak, A. R. Williams, and V. L. Moruzzi, Phys. Rev. B 11, 1522 (1975).

34. G. A. Burdick, Phys. Rev. 129, 138 (1963).

35. J. Hermanson, Solid State Commun. 22, 9 (1977).

36. F. J. Himpsel, Appl. Opt. 19, 3964 (1980), and references therein.

37. P. O. Gartland, S. Berge, and B. J. Slagsvold, Physica Norvegica 7, 39 (1973).

38. S. Andersson, Surf. Sci. 18, 325 (1969).

39. M. R. Halse, Phil. Trans. Roy. Soc. A 265, 507 (1969).

40. M. Lax and J. J. Hopfield, Phys. Rev. 124, 115 (1961).

41. See e.g., L. F. Ley, J. Electron Spectrosc. Relat. Phenom. 15, 329 (1979).

42. J. A. Stratton, Electromagnetic Theory (McGraw-Hill, New York, 1941), Chapter IX.

43. N. V. Smith, R. L. Benbow, and Z. Hurych, Phys. Rev. B 21, 4331 (1980).

44. H.-J. Hagemann, W. Gudat, and C. Kunz, J. Opt. Soc. Am. 65, 742 (1975), and Ref. 1 therein.

45. D. Beaglehole and B. Thieblemont, Nuovo Cimento B 39, 477 (1977), and references therein.

46. J. B. Pendry, Surf. Sci. 57, 679 (1976); Low Energy Electron Diffraction (Academic, New York, 1974).

47. P. O. Nilsson and N. Dahlbäck, Solid State Commun. 29, 303 (1979).

48. P. O. Nilsson, J. Kanski, and C. G. Larsson, Solid State Commun. 36, 111 (1980).

49. G. S. Painter, P. J. Jennings, and R. O. Jones, J. Phys. C 8, L199 (1975).

Table I. Polarization selection rules for normal photoemission from (211) faces of FCC crystals. (a)

Coordinate Axes			Irreducible Representations	Final-State Symmetry	Allowed Initial Symmetries		
x	y	z			A_x	A_y	A_z
$[01\bar{1}]$	$[\bar{1}11]$	[211]	A' A" (b)	A'	A"	A'	A'

(a) The photoelectron propagation direction defines the z-axis in each case.

(b) Since the [211] axis in momentum space has no special symmetry designation, the symbols A' and A" chosen to represent the even and odd states, respectively, are those for the usual C_s symmetry classification.

Table II. Values of empirical valence bands along [211] in copper.

$\vec{k}_i$(units of $2\pi/a$)		Energy, $-E^F$ (eV)					
k_x	$k_y=k_z$	A_1'	A_2'	A_3'	A_1''	A_2''	A_4'
-0.12	-0.56		3.89			2.41	
-0.08	-0.54		3.84			2.56	0.00
-0.04	-0.52	4.22	3.86	3.69	2.86	2.51	0.35
0	-0.50	4.38	3.97	3.77	2.94	2.49	0.67
0.04	-0.48	4.58	3.96	3.77	3.00	2.45	0.96
0.08	-0.46	4.79	3.86	3.69	3.14	2.39	1.33
0.12	-0.44	5.05	3.77	3.62	3.27	2.34	1.66
0.16	-0.42	5.18	3.68	3.58	3.41	2.33	1.91
0.20	-0.40	5.29	3.59	3.50	3.45	2.31	2.15
0.24	-0.38	5.36	3.52	3.39	3.49	2.30	2.36
0.28	-0.36	5.39	3.43	3.31	3.52	2.36	2.52
0.32	-0.34	5.40	3.40	3.27	3.51	2.39	2.63
0.36	-0.32	5.39	3.41		3.48	2.37	2.65
0.40	-0.30		3.45		3.42	2.32	2.59
0.44	-0.28		3.58		3.33	2.23	2.48

Table III. Deviations between experimental and theoretical valence bands along [211] in copper.

Deviation Parameter, ΔE (a)	Magnitude for Valence Bands Along [211] (eV)						Overall Theoretical ΔE (b)
	A_1'	A_2'	A_3'	A_1''	A_2''	A_4'	
$\overline{\Delta E}$	0.11	0.04	0.06	0.01	0.06	0.20	0.09
ΔE_{rms} (c)	0.10	0.05	0.06	0.11	0.10	0.14	0.11
$\lvert\Delta E\rvert_{max}$ (d)	0.29	0.10	0.11	0.24	0.21	0.32	0.37

(a) $\Delta E_i = E^F(\text{expt.}) - E^F(\text{int.})$; i refers to $\vec{k}_i$ from Table II.

(b) From comparison of interpolation scheme with Burdick's bands (Ref. 34) in copper, at 89 $\vec{k}_i$ points in the Brillouin zone; taken from Ref. 32.

(c) ΔE_{rms} = root-mean-square deviation.

(d) $\lvert\Delta E\rvert_{max}$ = maximum deviation.

FIGURE CAPTIONS

Fig. 1. A segment of an ideal Cu(S)-[3(111)x(100)] surface, showing three-atom terraces of (111) orientation separated by monatomic steps of (100) orientation. The $(01\bar{1})$ mirror plane cuts through the surface perpendicular to the atomic rows.

Fig. 2. Experimental geometries employed: (a) orientation I, with the plane of incidence perpendicular to the $(01\bar{1})$ mirror plane M; (b) orientation II, with the plane of incidence parallel to M. The majority of spectra were recorded with θ_A, the angle between the surface normal $\vec{n}$ and the incident radiation vector potential $\vec{A}$, equal to 30°.

Fig. 3. Selected normal photoemission spectra for Cu(211) with photon energies in the range 9 eV $\leq h\nu \leq$ 32 eV and $\theta_A = 30°$. The spectra in panel (a) were collected with the orientation I geometry, while those in (b) were recorded with orientation II.

Fig. 4. Plot of experimental peak position versus photon energy for each structure in the Cu(211) EDCs for $\theta_A = 30°$: (a) orientation I; (b) orientation II. Open and filled circles designate weak and strong features, respectively, and the connecting lines have no theoretical significance. The plots are labelled with the appropriate initial states involved in direct transitions (vide infra).

Fig. 5. The $(01\bar{1})$ mirror plane, showing the region of k-space in the first Brillouin zone along the [211] direction (dashed lines). The points B and D, both at the zone boundary, are separated

by an umklapp with $\vec{G} = (\bar{1},\bar{1},\bar{1})\ 2\pi/a$. The vector $\vec{k}_{DX}$, ending at a general point along the D - X line, is thus not actually in the [211] direction in the reduced zone scheme.

Fig. 6. The band structure of Cu interpolated along the [211] direction. The energy bands are symmetric about X, and the unoccupied bands are shown up to E^F = 30 eV. The bands are labeled by A' and A" irreducible representations. The A' symmetry final-state band that carries photocurrent in the [211] direction is highlighted by dashed lines in the bulk band-gap region and solid lines with filled circles elsewhere.

Fig. 7. Empirical [symbols: (•) A_1', A_2', A_4', DOS; (◇) A_3'; (○) A_1''; and (□) A_2''] and theoretical (solid lines, from interpolated bands in Fig. 6) valence-band dispersion relations for Cu(211). A partial photon energy scale is indicated at E_F, and the vertical arrows are from de Haas-van Alphen data (Ref. 39). The dashed vertical lines bracket the region for which the $\vec{k}$ vectors lie in the bulk conduction band gap.

Fig. 8. A direct comparison of photoemission spectra at selected photon energies for both orientations, with $\theta_A = 30°$, showing a strong dependence on radiation polarization orientation. The structures are labeled by the appropriate bands involved in direct transitions.

Fig. 9. Intensity ratio $R_{21} = I(II)/I(I)$ versus photon energy for s-p-electron intensity [$R_{21}(sp)$, upper curve] and d-band electrons [1.6 x $R_{21}(d)$ shown, middle curve]. The energy

windows for the ratio curves are indicated in the lower right corner, and the labels a, b, and c are discussed in the text. Also shown is a plot of the parameter $\xi_t = |A_{zt}/A_{xt}|^2$ versus photon energy for copper, where $|A_{zt}|$ and $|A_{xt}|$ are the transmitted components of the radiation vector potential.

Fig. 10. A direct comparison of photoemission spectra at $h\nu = 17$ eV and various values of the angle of incidence θ_i, for both orientations. The direct-transition peak positions are indicated on the horizontal axis.

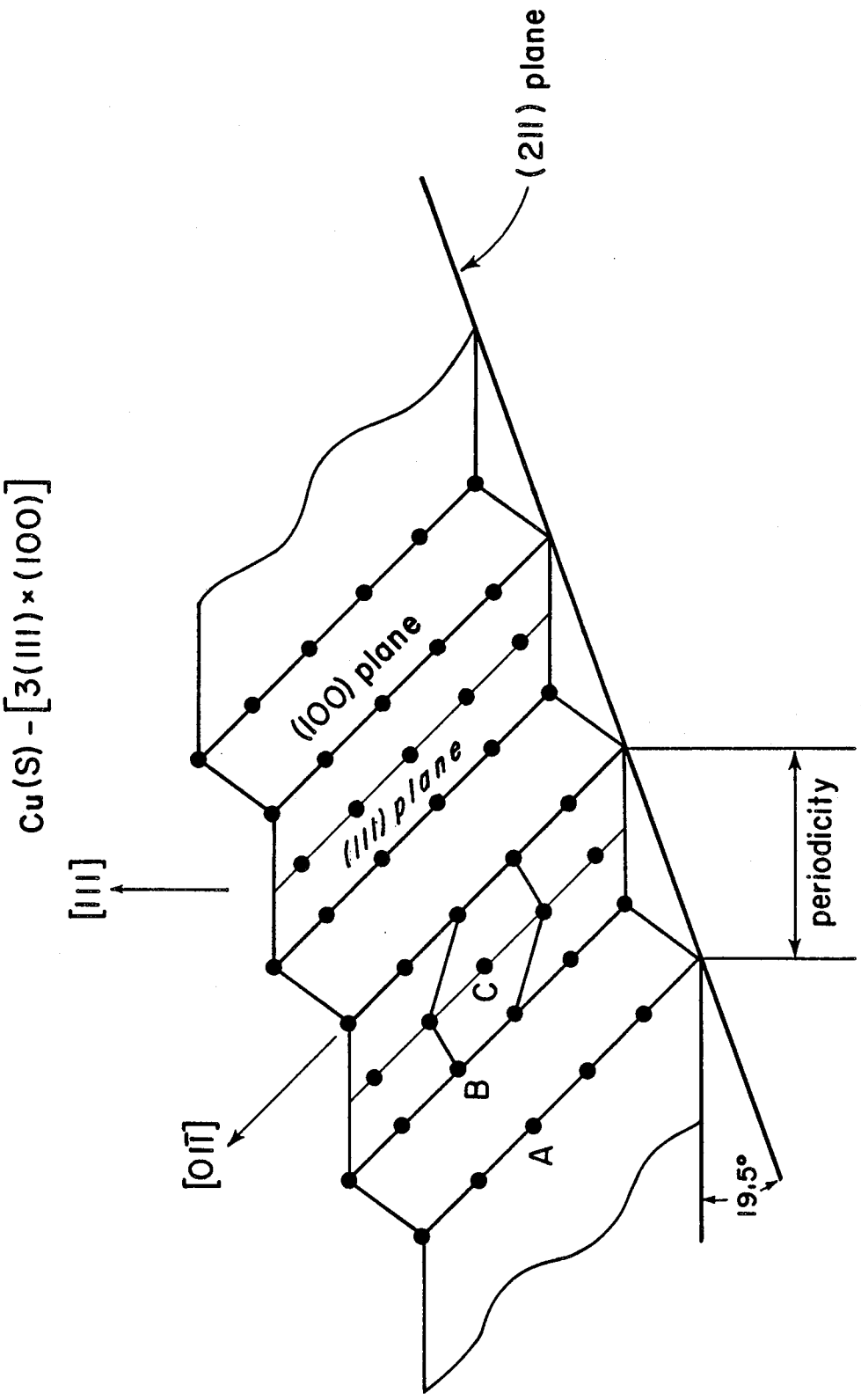

XBL 7610-4160

Figure 1

(a) Orientation I

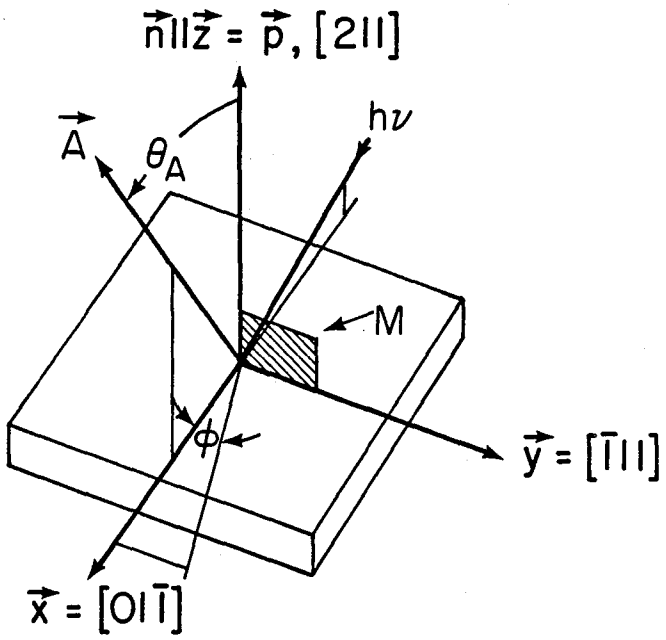

(b) Orientation II

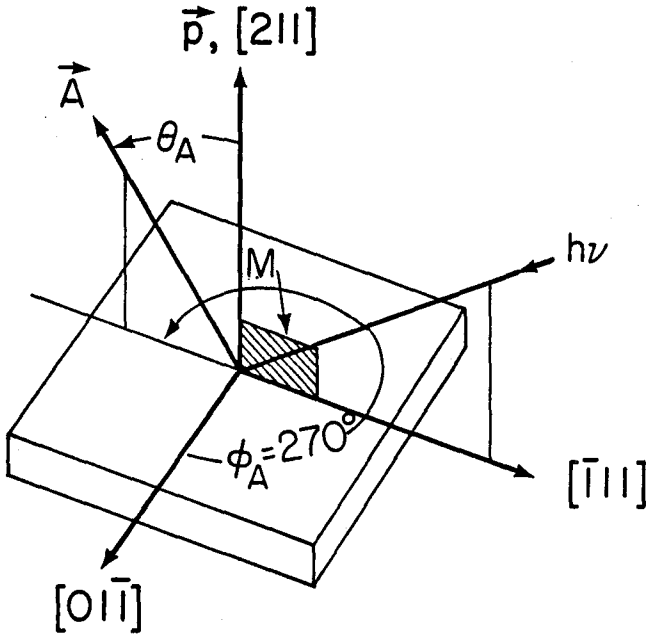

XBL 817-2379

Figure 2

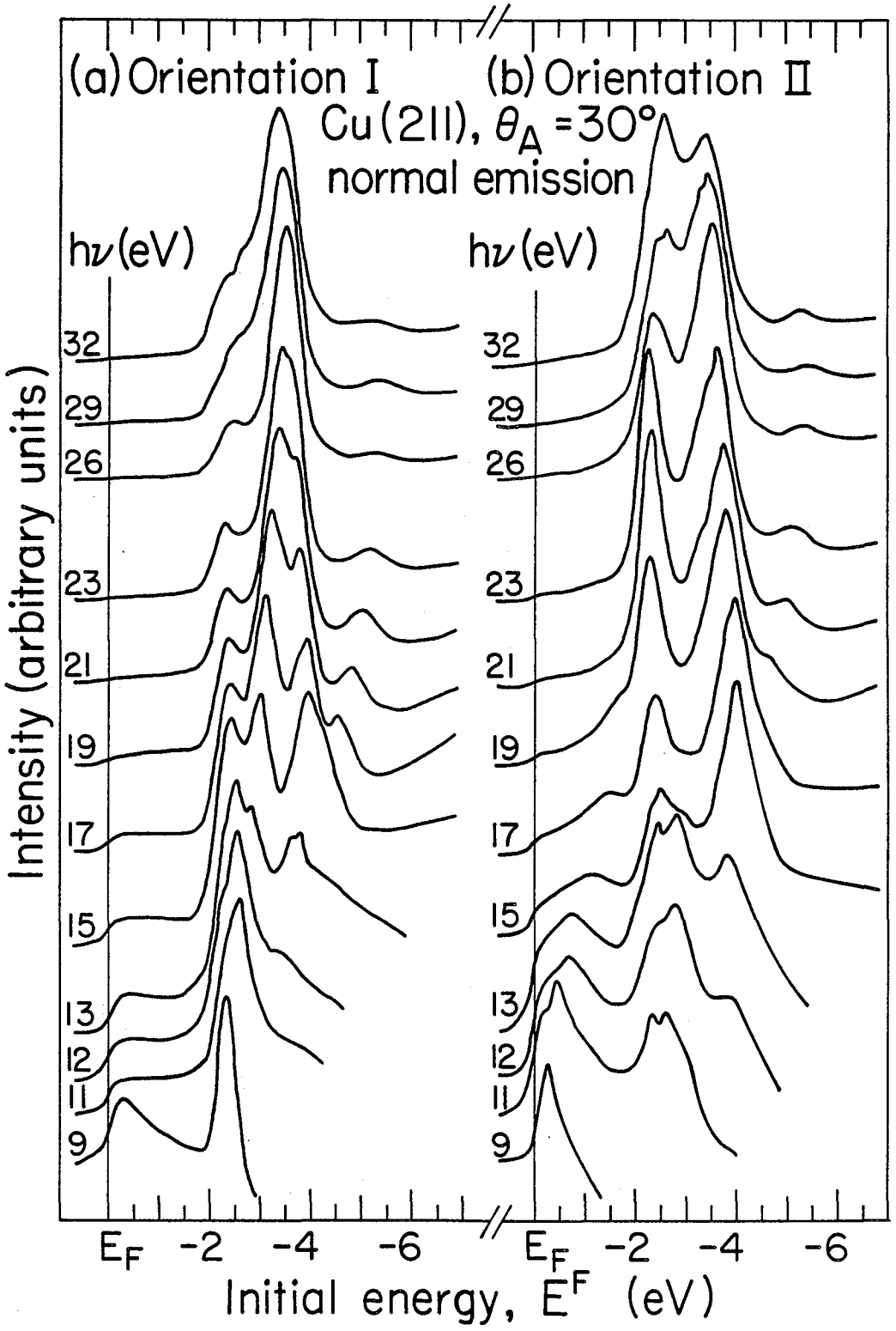

Figure 3

XBL 817-2377

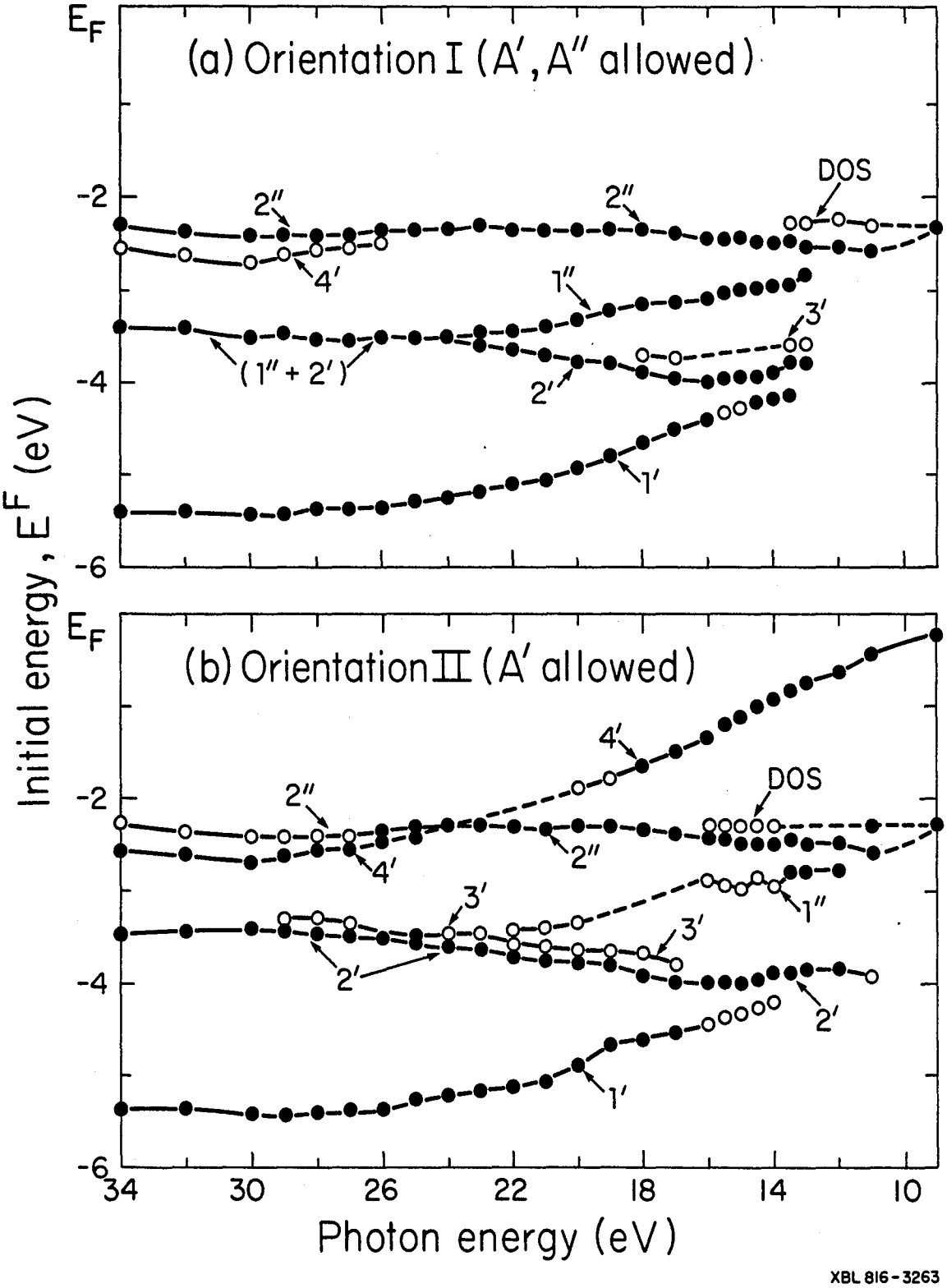
(a) Orientation I (A′, A″ allowed)
(b) Orientation II (A′ allowed)
E_F
DOS
2″
4′
1″
3′
2′
1′
(1″ + 2′)
Initial energy, E^F (eV)
-2
-4
-6
34
30
26
22
18
14
10
Photon energy (eV)
XBL 816-3263

Figure 4

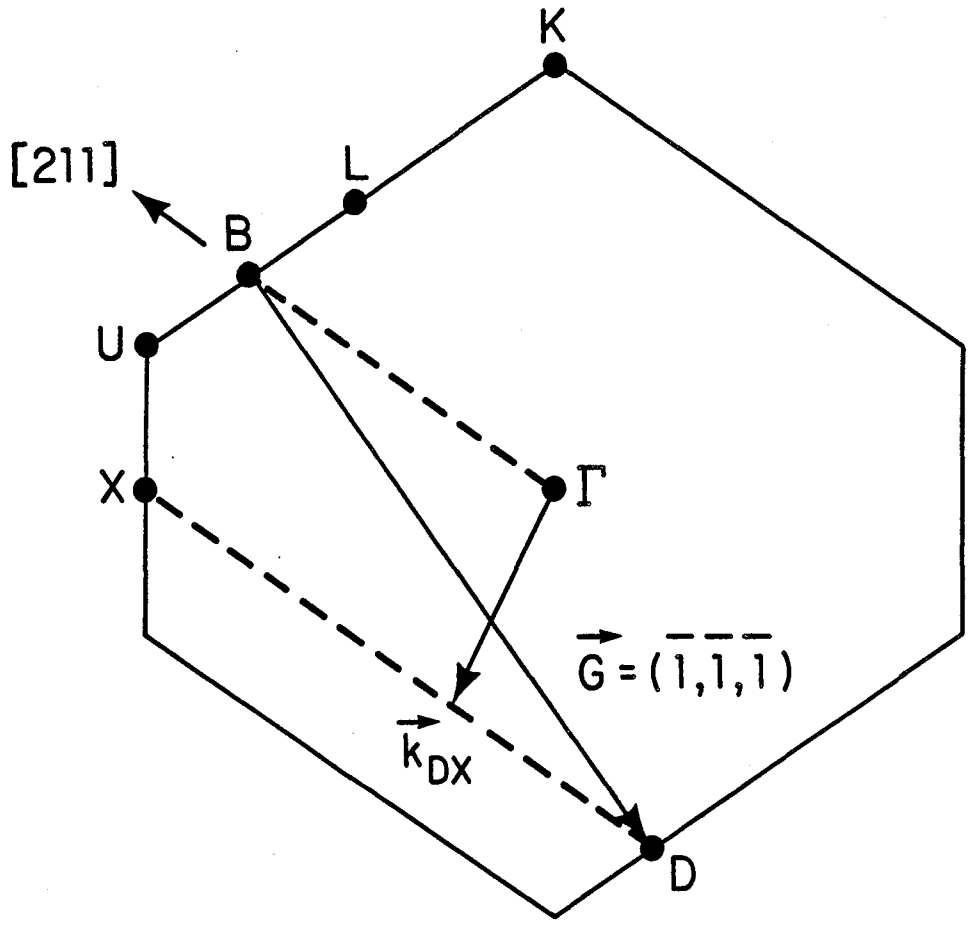

XBL816-3262

Figure 5

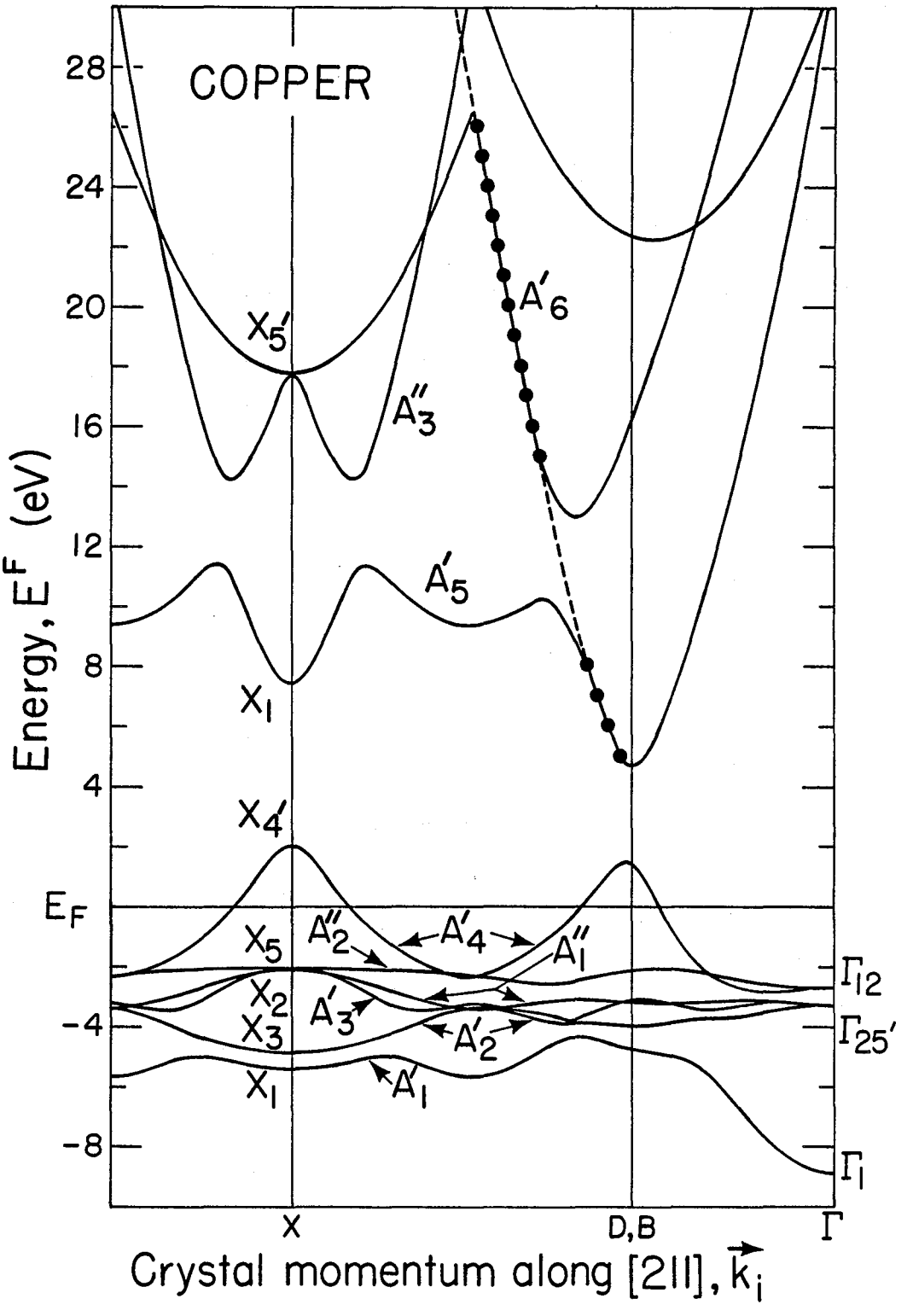
COPPER
28
24
20
16
12
8
4
-4
-8
Energy, E^F (eV)
E_F
X_5'
A_3''
A_6'
A_5'
X_1
X_4'
X_5
A_2''
A_4'
A_1''
X_2
A_3'
X_3
A_2'
X_1
A_1'
Γ_{12}
$\Gamma_{25'}$
Γ_1
X
D,B
Γ
Crystal momentum along [211], $\vec{k}_i$
XBL 817-2376

Figure 6

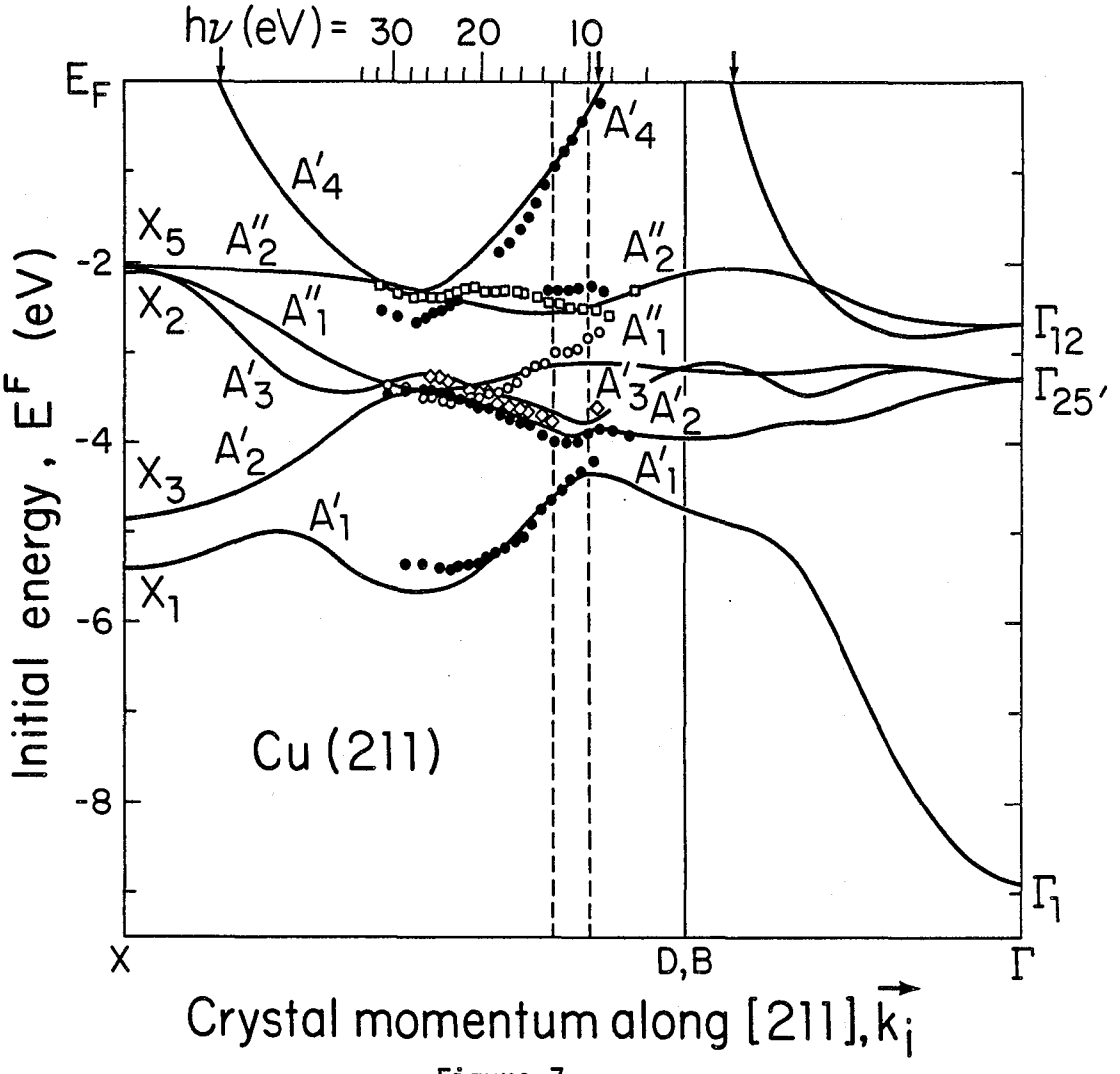

Figure 7

XBL 816-3265

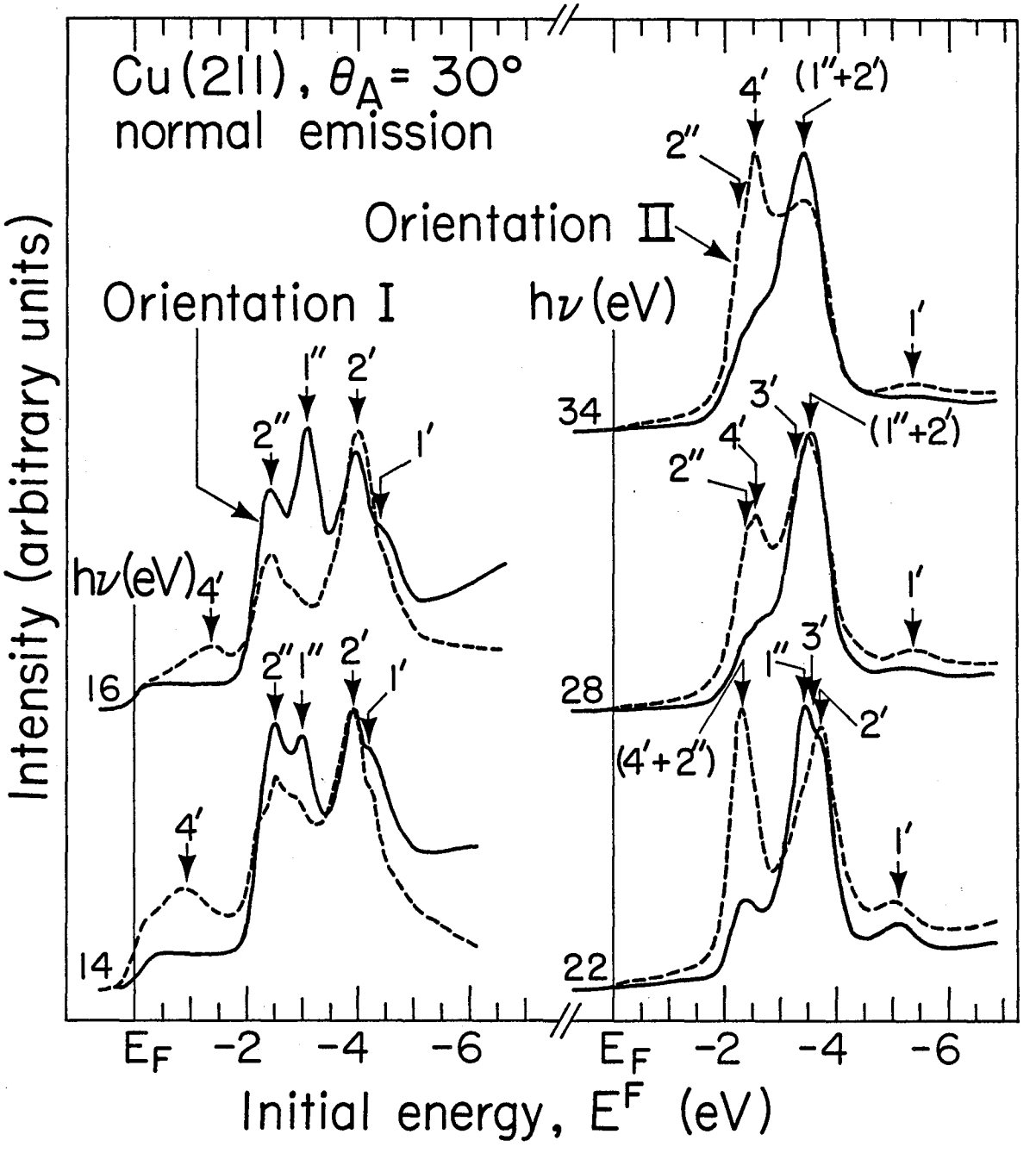

Figure 8

XBL 817-2378

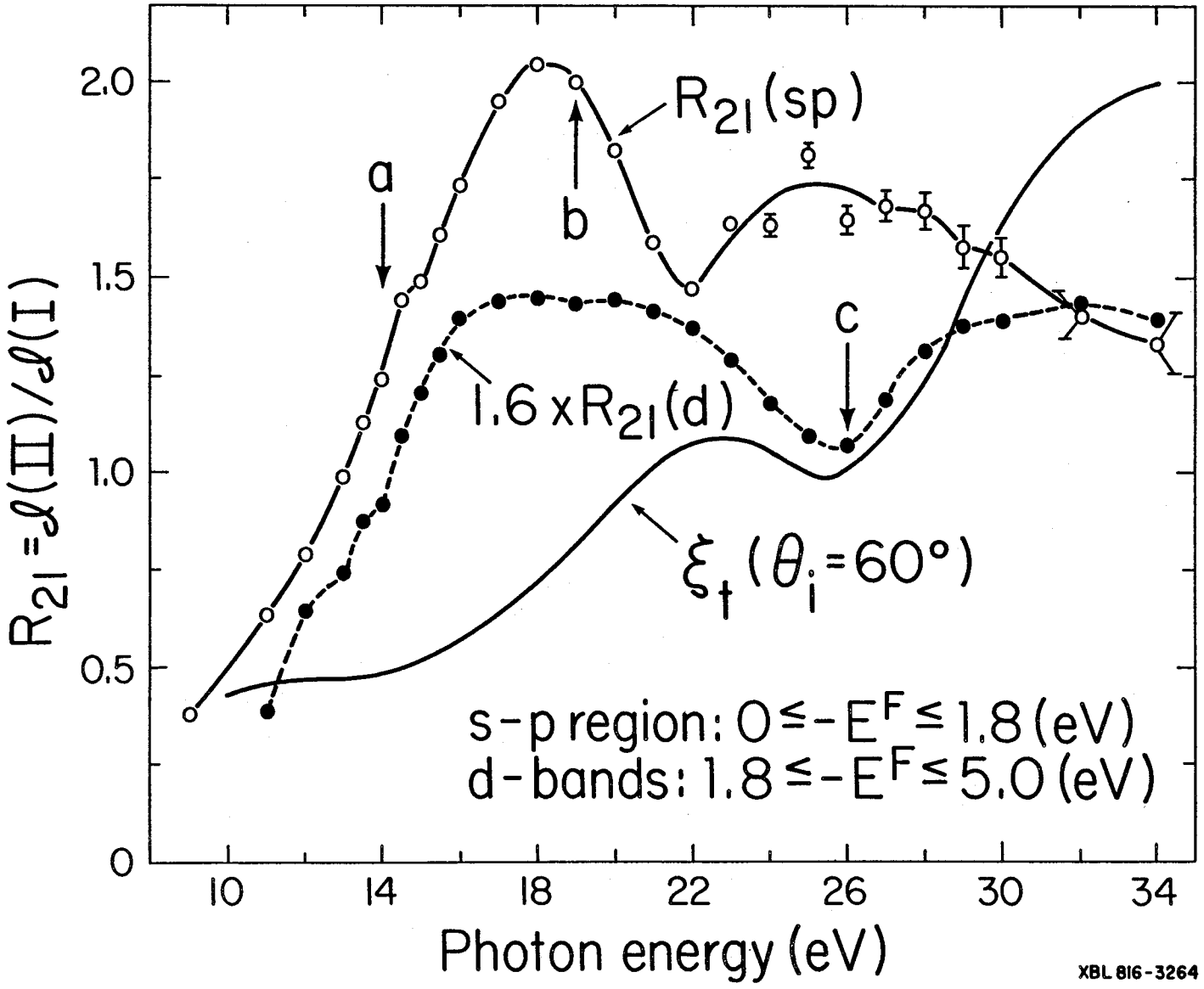
2.0
1.5
1.0
0.5
0
10
14
18
22
26
30
34
$R_{21} = \mathcal{I}(II)/\mathcal{I}(I)$
Photon energy (eV)
$R_{21}(sp)$
a
b
c
$1.6 \times R_{21}(d)$
$\xi_t(\theta_i = 60°)$
s-p region: $0 \leq -E^F \leq 1.8$ (eV)
d-bands: $1.8 \leq -E^F \leq 5.0$ (eV)
XBL 816-3264

Figure 9

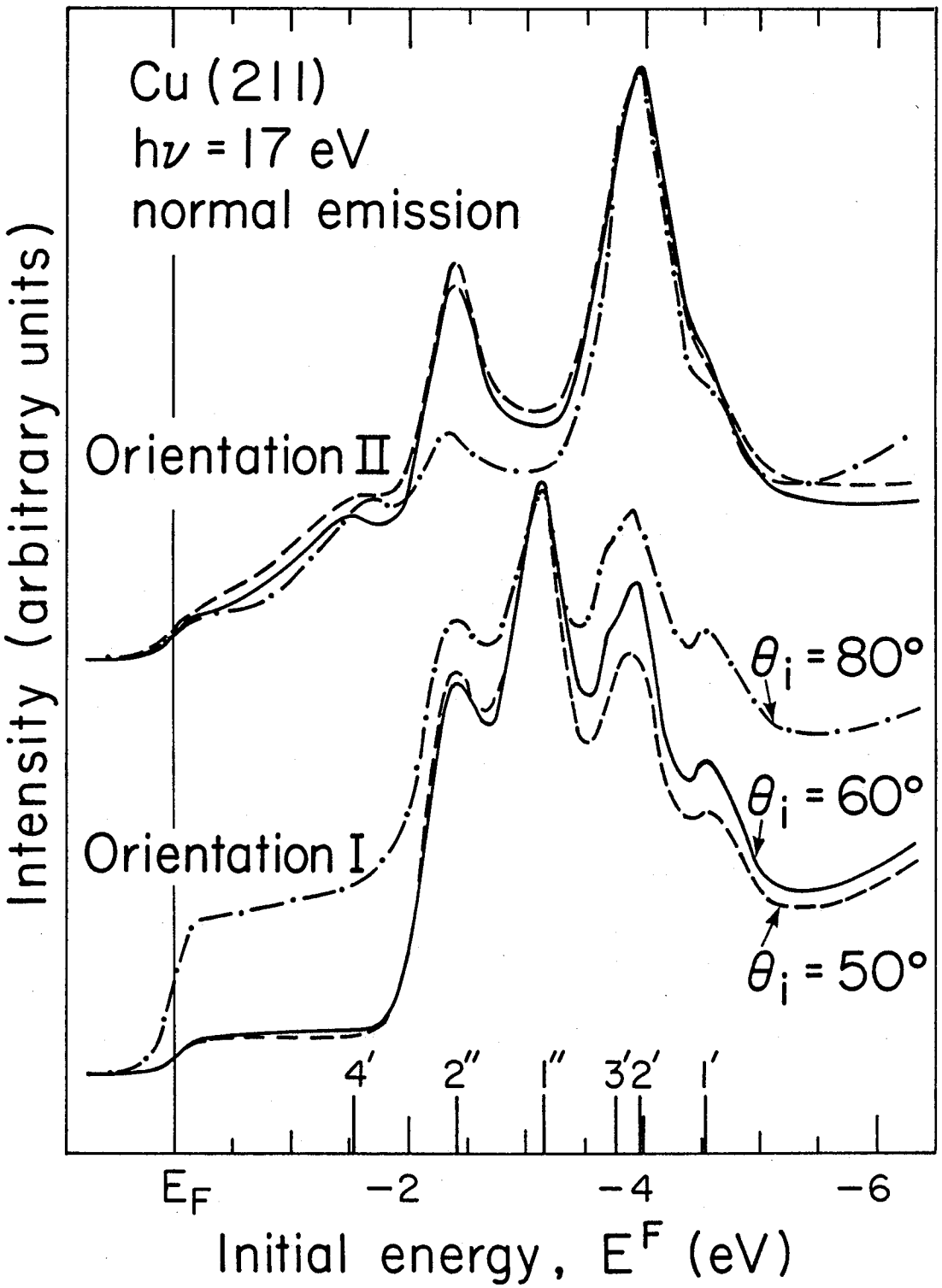

XBL 817-2381

Figure 10

III. THE VALENCE BAND STRUCTURE OF PLATINUM ALONG Δ *

A. Introduction

The study by angle-resolved photoemission (ARP), in conjunction with the use of synchrotron radiation, of crystal faces of the Group VIII and IB metals has been the subject of a number of recent investigations.[1] It is now fairly well established that the direct transition model, along with an appropriate final-state dispersion relation, can be used to determine valence-band dispersion relations, $E_n(\vec{k})$, from such data.[2] However, in several cases, the determination of the final-state band is somewhat ad hoc in nature and relies upon the knowledge of theoretical, one-electron conduction band structure.[3] Attention is now being focused on this problem, especially for photon energies where photoemission corresponds to a gap in the bulk conduction bands. Recent angle-resolved normal photoemission (ARNP) studies of various faces of Cu,[4,5] Ag,[6,7] Au,[8,9] Fe,[10] and Pt[8] suggests that a quasi-free-electron parabolic final-state dispersion relation can be used even when such a gap exists. In fact, the Cu(211) results[4] in Chapter II represent the most direct demonstration of this phenomenon.

The work presented in this chapter extends these studies because it represents an attempt to investigate, via ARNP, $E_n(\vec{k})$ along the Δ line of a 5d metal for which no bulk conduction bands have been calculated. More generally, it represents a further attempt to study the relative contribution of direct transitions and density-of-states

(DOS) features to ARP spectra, and to use the direct-transition features to derive $E_n(\vec{k})$ relations.

In Section B, experimental procedures are discussed. Section C contains results and Section D a general discussion. Finally, Section E gives a summary.

B. Experimental

The sample was a high-purity (99.999 percent) Pt crystal (Materials Research Corporation), which was cut and diamond-polished to within ± 1/4° of the (100) plane, with a mean surface roughness of 0.05 μm. The resulting (100) face was chemically etched briefly in warm (ca. 315K) aqua regia for about 1.5 minutes. This etching procedure works quite well for several different faces of Pt [i.e., (100), (111), (110), and (211)], typically yielding smooth surfaces with a high degree of visual reflectivity. The Pt(100) crystal was aligned azimuthally on a sample manipulator to better than ± 1° using the back-reflection Laue method, and installed in an ultra-high vacuum (UHV) chamber (base pressure $\leq 3 \times 10^{-10}$ torr). Bulk impurities (C, S, Ca) were removed from the sample by a combination of repeated Ar^+ sputtering (beam voltage = 1 kV)/annealing (970K) cycles and brief periods of heating (1070K) in 10^{-7} to 10^{-6} torr of oxygen. Residual oxygen adsorbed from this procedure was removed by several additional Ar^+ sputter/anneal (1170K) cycles. The resulting surface was monitored by Auger electron spectroscopy (AES) for cleanliness and low energy electron diffraction (LEED) for crystallographic order,

yielding AES impurity (C, O, S, Ca) signals characteristic of $\lesssim 0.05$ monolayer contamination and LEED patterns (with sharp and intense spots) characteristic of a reconstructed (5x1) surface, in agreement with previous studies.[11] Slight amounts of contamination above this level yielded a (1x1) surface structure. Immediately preceding the ARNP experiments, which were performed in a different UHV chamber, further Ar^+ sputter/anneal (1170K) cycles were performed in situ, and surface cleanliness was monitored by AES immediately before and after the experiments (again, the contamination level was $\lesssim 0.05$ monolayer). The surface structure could not be monitored by LEED during the ARNP experiments. But, as noted above, the achievement of a clean surface always yielded a (5x1) surface during the cleaning procedures, thus precluding the possibility that the experiments were performed on a disordered or unreconstructed surface. It is herein assumed that the ARNP spectra correspond to Pt(100)-(5x1).

The photoemission measurements were performed on the 8° branch of Beam Line I (BL I-2) at SSRL, with the incident radiation highly polarized (> 97 percent) in the horizontal plane and in the energy range $6 \text{ eV} \leq h\nu \leq 32 \text{ eV}$. The ARP apparatus, described elsewhere,[12] employs a double-pass cylindrical mirror analyzer as described in Chapter I (Section C), with the angular acceptance modified for these experiments to ± 2.5° (10 millisteradians). The combined energy resolution (monochromator plus electron analyzer) varied from ca. 0.1 eV (FWHM) at the lower limit of the photon energy range to ca. 0.2 eV at the upper limit.

The normal emission geometry utilized in these studies and representative ARNP energy distribution curves (EDCs) are shown in Fig. 1. A total of 32 spectra were recorded in the geometry depicted in the inset. The crystal was oriented so that the [011] azimuth ($\phi = 0^\circ$) was contained in the horizontal plane, along with the incident radiation vector potential ($\vec{A}$) and photon beam direction ($h\nu$); and the polarization angle (θ_A) was held fixed at 27.3° in the 0° azimuth ($\phi_A = 0^\circ$). In situ polar crystallographic alignment (± 1° or better) was effected by laser autocollimation.

C. Results

The spectra displayed in Fig. 1, as well as all others recorded, are rather complicated. The EDCs contain many features that are generally not as "sharp" and well-resolved from each other as is typically found in the case of the noble metals.[4-9,13] Part of this problem arises from the various photoemission mechanisms which contribute to these peak structures: although many peaks clearly arise from direct transitions, as evidenced by their initial-state energy dispersion with photon energy, others cannot be direct transitions, because they show no dispersion. These latter features are probably related to the initial-state DOS. Additionally, the problem of initial-state lifetime broadening is important in Group VIII metals[14,15] (see Chapter I). The severity of this effect, due in large part to the unfilled d bands, is discussed at greater length in Chapter IV for the case of chromium.

Even with these complications, individual peak structures can be identified and "mapped" as functions of photon energy, which in turn yields directly the dispersion relations, $E_n(\vec{k}_i)$, under the assumptions that[4-9,16] (1) only $\Gamma\Delta X$-line initial states contribute direct-transition peak structures to the spectra, and (2) only a single plane-wavelike final-state band is important in yielding $\vec{k}_\perp$ from energy positions corresponding to maxima in the peak structures (or the equivalent for shoulder-type features). The validity of and motivation for these conditions receives considerable attention in the first two chapters, and is further discussed in Chapter IV. Following the structure of Chapter II, the empirical dispersion relations will be derived first, clearly isolating the direct transitions from the DOS features which obviously do not fit the two conditions above. Then, a brief discussion of EDC features and the $E_n(\vec{k})$ curves will follow in the next section.

In order to analyze the direct-transition features found in Pt(100) EDCs in terms of the initial-state dispersion relations, it is first necessary to determine the photoelectron band structure. As discussed previously,[7] and in Chapters II and IV, the most straightforward procedure is to match the <u>form</u> of the final-state dispersion relation to the bulk, one-electron conduction-band components (i.e., the plane-wavelike, or s-p parts) that are derived from the empty-lattice band(s) which would yield primary Mahan cones[17] along $\vec{k}_\perp$. The final-state dispersion has the form

$$E_f^F(\vec{k}_f) = (\hbar^2/2m^*)\ |\vec{k}_f|^2 + V_0^F \quad , \tag{1}$$

with

$$\vec{k}_f = \vec{k}_i - \vec{G} \quad , \tag{2}$$

where m* and V_0^F are the effective electron mass and inner potential, respectively, to be determined from the bulk band structure, and all energies are referenced to the Fermi level, E_F. We further assume that one of the fitting parameters, specifically V_0^F, is adjustable subsequent to the initial fitting procedure, to account for the possibility that the true photoelectron dispersion relation does not scale absolutely with the bulk conduction bands. This aspect of the procedure receives further attention in Chapter IV, and should be considered as a direct consequence of the results of Chapter II: the one-electron conduction band structure does not account for the many-body nature of photoemission.[18] Obviously, Eq. (1) ignores the existence of conduction band gaps. The Cu(211) results (Chapter II) demonstrated the validity of this fact rather dramatically. Figure 6 in Chapter I demonstrates the fact that we need only consider conduction band components with $\vec{G} = (\bar{n}, 0, 0)$ character (n is a nonnegative integer) for normal emission along the [100] axis. Additionally, dipole selection rules[8,19] require that the final states have Δ_6 symmetry, where Δ_6 is the symmetric irreducible representation in the double group[20] of Δ.

The high energy conduction band structure of Pt was not given by Andersen,[21] who reported a relativistic augmented-plane-wave (RAPW) calculation for this metal. However, by analogy with band-structure calculations for palladium[22] and gold,[23] there are three appropriate Δ_6 conduction bands along Δ in the photon energy range employed here. Only the lowest of these, which is band 7 along most of the Δ line in gold, should give rise to primary emission, the other two producing emission into secondary Mahan cones[17] (i.e., involving surface umklapp processes). However, band hybridization near Γ renders the plane-wave character of band 7 somewhat ambiguous for $\vec{k}_i$ vectors smaller in magnitude than $(-0.4, 0, 0)2\pi/a$ in gold and palladium. Therefore, we should restrict our attention to the region of band 7 between $\vec{k}_i = (-0.4, 0, 0)$ and $(-1, 0, 0)$, for which the character contains $\vec{G} = (\bar{2}, 0, 0)$ (as usual, the units of $2\pi/a$ are assumed implicitly). The higher-lying Δ_6 conduction bands do not give rise to discernible features in the spectra and will not be considered further.

It should be noted that we are considering $\vec{k}_i$ vectors with k_{ix} negative to be consistent with Fig. 4 in Chapter I, where primary cones propagating with positive k_{fx} components are shown to originate at the $(\bar{2}00)$ reciprocal lattice point and intersect initial states with negative k_{ix}. Equivalently, we could consider k_{fx} to be negative (with cones propagating along $[\bar{1}00]$) and k_{ix} positive, with $\vec{G} = (2, 0, 0)$. There can be no distinction between these two constructions because the band structure must be symmetric about Γ.

The effective electron mass (m*) of the final-state band was found in studies of silver[7] and gold[8] by fitting Eq. (1) to the appropriate calculated bulk conduction bands. However, by necessity we followed the procedure used for Pt(111) (Ref. 8) where m* was taken to be the value found for the analogous state in gold. Along Δ, a fit of band 7 in gold[23] in the $\vec{k}_\perp$ region discussed above yields $m^* = 1.4\ m_e$ where m_e is the free-electron mass. The band minimum was adjusted to $V_0 = +3.3$ eV, which gave the best overall agreement between the empirical valence bands and the RAPW calculation of Andersen.[21] These parameters yield the photoelectron band structure displayed in Fig. 2 as the curve highlighted by filled circles. For comparison, Andersen's[21] Pt RAPW calculated bands are also shown, with the open circles at X representing his higher energy calculated conduction band values. It is clear that final-state energies below 10.4 eV involve $\vec{k}_i \rightarrow \vec{k}_i - (0, 0, 0)$ transitions, while those between 10.4 and 31.6 eV arise from $\vec{G} = (\bar{2}, 0, 0)$. Employing the final-state band shown in Fig. 2, the direct-transition features in the Pt(100) EDCs give rise to empirical dispersion relations along ΓΔX. A comparison between the empirical (circles) and theoretical[21] (lines) valence bands along Δ is shown in Fig. 3, and empirical band energies are given in Table I, along with the energy values at Γ derived from our Pt(111) studies[8] and from Andersen's[21] band calculation. The bands are labelled by their appropriate double group[20] irreducible representations, with the subscripts "ℓ", "m", and "u" differentiating between bands of the same symmetry. The $\vec{A}$ vector orientation shown in Fig. 1 yields

non-zero components of both $A_{\parallel}$ and $A_{\perp}$ (parallel and perpendicular to $\vec{n} \parallel [100]$). Within the framework of dipole-selection rules,[19] and in the Pt case of non-negligible spin-orbit coupling,[8] $A_{\parallel}$ can excite Δ_6 valence bands while $A_{\perp}$ excites both Δ_6 and Δ_7 bands. Therefore, all six valence bands represent allowed initial states. This is one of the reasons that the EDCs in Fig. 1 appear to contain many peak structures.

D. Discussion

1. Direct Transitions.

Except for $\Delta_{6\ell}$, Fig. 3 shows that detailed $E_n(\vec{k}_i)$ curves for all valence bands are obtained. Moreover, the agreement between experiment and theory is striking, not unlike our earlier Pt(111) work.[8] It is truly amazing that the (open d-shell) Group VIII 5d metals, platinum[8] and iridium,[24] both have empirical valence band structures that agree so well with RAPW band theory.[21,25] In fact, the Pt empirical bands along $L\Lambda\Gamma\Delta X$ show better agreement with band theory than do those of (the noble metal) gold.[8,9] Although all six valence bands are dipole-allowed initial states, the $\Delta_{6\ell}$ band was not observed in our spectra, presumably because of a low photoemission cross section due to its s-p character. However, the situation is complicated by the presence of secondary-electron structure in the inelastic tail, similar to that reported by Willis and co-workers[26] for tungsten, and band 1 (s-p like) was a very weak feature in Pt(111) ARNP spectra[8] in the same photon energy region.

Several points can be discussed concerning the general properties of the band structures shown in Fig. 3. A higher degree of self-consistency between the empirical valence band structure and the photoelectron dispersion relations would have been obtained had the photon energy range been extended to higher values, because initial Δ-line states on both sides of Γ would have been excited, yielding extended-zone $E_n(\vec{k})$ curves that would presumably have dispersion relations symmetrical about Γ. As discussed further in Chapter IV, it is always desirable to be able to cross high-symmetry points to obtain this self-consistency, expecially in the present case where there is no prior knowledge of the final-state band structure, thereby obtaining a valuable check of the validity of m* and V_0^F. The situation is nonetheless favorable for Pt(100) because the band positions extrapolated to Γ are consistent with initial-state energies for the DOS features derived from Γ (to be discussed below). Furthermore, inspection of values listed in Table I shows that all Pt(100)-derived Γ point energies agree well with the corresponding energy levels derived directly (except for band 4) from Pt(111) ARNP results.[8] The latter face is a more favorable case for measuring bands at Γ because the k_i points at the intersection of initial- and final-state energy contours along $\Gamma\Lambda L$ pass through Γ within the photon energy range available with the 8°-line monochromator, mainly because the BZ dimension is 13 percent smaller along [111] than the [100] direction. The general agreement between the Pt(100) and Pt(111) $E(\Gamma)$ values is particularly noteworthy because both sets of spectra suffer from more drastic peak-broadening

effects relative to gold (see Ref. 43, and associated text, in Chapter IV). Turning to the comparison between empirical and theoretical valence band structures, the major discrepancies are in the $\Delta_{7\ell}$, Δ_{7m}, and Δ_{6u} bands. A higher initial-state energy for Δ_{7m} is found at Γ (7^+), but this is consistent with the energy position of Γ_{7+} determined from DOS structure (see below), and also with the energy position estimated from Pt(111) data by extrapolation.[8] The Δ_{6u} band is seen to lie higher than calculated in part of the zone, although it should be noted that for $h\nu \geq 20$ eV the positions of peaks associated with this band were difficult to determine. The $\Delta_{7\ell}$ band was also found to be higher than calculated, and the remaining discrepancy is in band 3 between (-1/2, 0, 0) and (-3/4, 0, 0), where there is a deviation in the curvature.

We noted above that the empirical $\Delta_{7\ell}$ band (2) is higher than calculated, but it should also be pointed out that this band gives a very weak feature in the EDCs throughout the photon energy range employed for both Pt(100) and Au(100) (Ref. 9). Perhaps this low intensity can be understood by making use of simple symmetry arguments:[24]

In the neglect of spin-orbit coupling, which can be treated as a perturbation of the band structure, bands 2 and 6 ($\Delta_{7\ell}$ and Δ_{7u}, respectively, in Fig. 3) have Δ_2, and Δ_2 symmetry (in single-group notation), respectively, which are both dipole-forbidden in normal emission.[19] All other initial state bands would be dipole-allowed, in our experimental geometry, in the absence of spin-orbit coupling. However, the Δ_{7u} band (6) yields a relatively strong peak between

photon energies of 18 eV and 22 eV in Pt(100) spectra. The qualitative argument is that $\Delta_{7\ell}$ remains relatively isolated from the other d bands (except, of course, at Γ), whereas Δ_{7u} is close to and mixes strongly with the other d bands that are separated from Δ_{7u} by an amount roughly on the order of the spin-orbit coupling strength $\xi(5d)$ (ca. 0.7 eV in Pt metal[8]) or less. Therefore, $\Delta_{7\ell}$ can be assumed to adhere qualitatively to non-relativistic selection rules, but Δ_{7u} cannot, and since $\Delta_{7\ell}$ is forbidden in the absence of spin-orbit coupling, it should yield a weak feature in ARNP spectra, as observed. This argument is, by analogy, similar to the physics of atomic band-character mixing (or hybridization), with the crystal potential, $V(\vec{r})$, replaced by ξ. An example of band-character mixing was found in Cu(211) spectra (Chapter II): the upper s-p band (A_4') was observed to be a strong feature at photon energies corresponding to $\vec{k}_i$ for which A_4' experiences a strong admixture of d-electron character from the A' d bands via the crystal potential. At photon energies corresponding to primarily s-p character in its wave function, the A_4' band is weak [similar to the $\Delta_{6\ell}$ band in the case of Pt(100)].

A note of caution concerning the selection rules for the reconstructed faces of Pt(100) and Au(100) should be mentioned: Heimann, et al.[27] have shown that surface reconstruction of Au(100)-(1x1) to the (5x20) structure yields a drastic increase in the intensity of some ARNP-EDC features. These authors interpreted this effect as arising from the (100) surface symmetry change accompanying the reconstruction, which changes the "normal" Δ-line selection rules.[19]

However, if it is assumed that the only symmetry effect of the (1x1) → (5x20) or (5x1) transformation of the surface is to break the reflection symmetry of the ΓXWKΓ emission plane (i.e., a {100} plane), then Δ_2--but not $\Delta_{2'}$--becomes a dipole-allowed initial state.[28] Therefore, we do not expect band 2 to yield appreciable intensity through either spin-orbit coupling or surface reconstruction mechanisms, in accord with our findings for $\Delta_{7\ell}$ in Au(100)-(5x20) (Ref. 9) and Pt(100)-(5x1), and with the observation that surface reconstruction of Au(100) from (1x1) to (5x20) does not yield enhancement of the $\Delta_{7\ell}$ intensity. The latter is a result of our ARNP studies of Au(100) (Ref. 9).

2. Density-of-States Features.

In addition to the direct-transition peaks that yield the data points shown in Fig. 3, dispersionless peaks arising from the density of states (DOS) were also observed. ARP EDCs are typically dominated by either DOS intensity (e.g., chromium--see Chapter IV) or direct transitions (e.g., copper--see Chapter II), but not both. Pt(100) represents a somewhat unusual deviation from this pattern because both DOS and direct-transition intensity is observed in EDCs with equal propensity. Although the concomitant increased number of peak structures complicated the data reduction for Pt(100), it was relatively straightforward to separate DOS and direct-transition peaks partly because the empirical $E_n(\vec{k}_i)$ curves contain a great amount of detail [unlike Cr(100), see Chapter IV], but mainly because the DOS peaks

show no disperion: the DOS features do not fit the direct-transition model outlined above, so they are easily spotted when their energy positions are plotted in a band-structure diagram. This is clearly depicted in Fig. 4, where the same dispersion relations as in Fig. 3 are shown with the addition of the DOS features, the $\vec{k}_i$ positions of the latter being derived from the same simple final-state dispersion relation used for the direct-transition features. Fig. 4 shows that there are six "bands" of dispersionless features, which will be considered below starting with the uppermost feature. First, however, it should be noted that there are various mechanisms (e.g., those discussed in Chapter I) which can lead to an apparent breakdown of $\vec{k}$-conservation; in nearly every case, the resultant ARP EDC reflects either the three-dimensional DOS (TDOS) or one-dimensional DOS (ODDOS) along $\vec{k}_\perp$ (Ref. 29). Therefore, wherever there exist flat initial-state bands somewhere in the reduced BZ, we should expect the possibility that the DOS contributes to the EDCs. This does not imply that all DOS features are ODDOS-related for the normal emission geometry.

The DOS peak with most intensity occurs at an initial-state energy of about -0.5 eV. This peak can be seen in the spectra at 19.5 eV $\leq h\nu \leq$ 32 eV; it is masked at lower photon energies by direct-transition peaks in the same initial-state energy range. It is reasonable to assign this DOS feature to the ODDOS for the Δ_{7m} band, although there are other parts of the zone (e.g., the L point and the Q line) which also show flat bands in Andersen's[21] calculation in this initial-state energy region. The second DOS feature is a relatively weak

shoulder at -1.40 eV on the low initial-energy side of the main d-band direct-transition structure (Δ_{7m} and Δ_{6u}). It is observed in the range of 12 eV $\leq h\nu \leq$ 18 eV, except at energies where it crosses the Δ_{6m} direct-transition peak (ca. $h\nu$ = 16 eV). This DOS feature, like the first, is obscurred by direct-transition peak structures at higher photon energies. It has an energy position that is consistent with an assignment to DOS emission (TDOS or ODDOS) from initial states near the uppermost Γ_8^+ level [i.e., bands (5,6)]. The third DOS feature can be seen as an extremely weak peak at an initial-state energy of -2.1 eV in the range 13 eV $\leq h\nu \leq$ 20 eV, except where it is obscured by Δ_{6m} direct transitions (ca. $h\nu$ = 17 - 18 eV). This feature has no obvious relationship to any of the bands along $\Gamma\Delta X$, although it coincides with the theoretical band minimum for Δ_{6u}. It is probably derived from bands elsewhere in the zone [bands (4,5) along Σ or band 4 at W, for example]. The fourth feature is observed in the range 14 eV $\leq h\nu \leq$ 20 eV with an initial-state energy of -2.8 eV. This position coincides with $E_4(\Gamma_7^+)$; we therefore attribute its intensity to the DOS of band 4 near Γ. The fifth feature, at -4.1 eV, can be seen throughout most of the zone because there are no direct transitions to obscure its intensity. It undoubtedly arises from the DOS of bands (2,3) near Γ_8^+. Finally, the sixth DOS feature, with initial energies in the vicinity of -6.7 eV, is observed in the EDCs below $h\nu$ = 21 eV. Extraction of accurate initial-state energies for this feature is hindered by the secondary-electron structure alluded to above. We assign it to the ODDOS of $\Delta_{6\ell}$ and/or $\Delta_{7\ell}$ near X.

The relative intensities of both the 0.5 eV and the 4.1 eV DOS peaks increase with photon energy. To the extent that these peaks are related to the ODDOS, this trend can be interpreted as arising from a decrease in the electron mean-free path (λ), reducing the extent of $\vec{k}_{\perp}$ conservation and leading to an enhancement of ODDOS features[29] via the mechanism discussed in Chapter I. However, the intensities of these DOS peaks are unusually large for a Group VIII metal, where direct-transition features have generally been found to dominate.[30] This probably arises because both the ODDOS and TDOS contribute to the total intensity. In other words, we would not expect to observe such a large ODDOS intensity for a system like Pt(100) which has an abundance of strong direct-transition features; we look to additional DOS mechanisms. The finite hole lifetime[15] and its attenuation in open d-shell metals is one factor (see Chapters I and IV). A shorter lifetime induced by enhanced d-electron mobility localizes the hole,[14] leading to a DOS (TDOS in this case) effect (this is considered additionally in Chapter IV). However, this lifetime-broadening mechanism would probably be essentially independent of the initial-state axis in k-space, whereas the Pt(111) spectra do not suffer nearly as much from DOS photoemission.[8] A reasonable, alternative mechanism is enhanced surface umklapp scattering caused by the surface reconstruction.[24,31,32] Strong evidence for this comes from Au(100) results,[9] which showed a higher propensity for DOS photoemission with the reconstructed (5x20) surface. The details of this mechanism are presented in Section D.6 of Chapter IV, but the essential ideas are outlined briefly below.

Surface reconstruction gives rise to a completely new set of surface reciprocal lattice vectors, $\vec{G}_{\parallel}'$, which can result in a higher propensity for surface umklapp scattering [via Eq. (16b) in Chapter I] because the associated Fourier components of the crystal potential, $V_{\vec{G}_{\parallel}'}$, will be larger than those corresponding to the $\vec{G}_{\parallel}$ vectors for the unreconstructed surface. [The argument for the usual absence of umklapp scattering in most normal spectra is, in part, similar to the reasoning behind the apparent success of the single-plane-wave approximation for the final-state dispersion relation: the amplitudes of the higher-order components are small (see Chapters I and IV).] The result of enhanced surface umklapp scattering via the new set of reciprocal lattice vectors is a "smearing" of directional information within the energy and angular windows of the electron detector. This is most easily conceptualized by considering the photoemission process in three dimensions, rather than just along $\vec{k}_{\perp}$. There are many electrons propagating in many different directions inside the crystal. The redistribution of directions at the surface quite naturally leads to a buildup of intensity at energies corresponding to a large initial-state DOS. Although we anticipated that it might be, this effect was not important in the case of Cu(211) spectra (Chapter II), because the (211) surface reciprocal mesh is a simple projection of the bulk lattice. However, Pt(100)-(5x1) has a fine surface reciprocal lattice mesh with $\vec{G}_{\parallel}'$ as little as a fifth the size of $\vec{G}_{\parallel}$ vectors for the unreconstructed surface (corresponding to bulk projections). The $\vec{G}_{\parallel}'$ vectors, or course, give rise to the superstructure spots observed in LEED patterns[11] of Pt(100)-(5x1).

3. Final-State Structure.

An interesting aspect of these Pt(100) results is the occurrance of photon-energy-dependent intensity resonances in the DOS peaks at energies 17 eV $\leq h\nu \leq$ 22 eV. Resonances were also observed in ARP studies of Pt(111),[8] Au(111),[8] Ag(111),[6] Ag(100),[7] Ag(110),[7] Pd(111),[33] Ir(111),[24] and Ir(100).[24] They were found to arise at final-state energies corresponding to a large bulk conduction band DOS, especially near Γ (Γ_7-). The origin of these resonances has been discussed at great length elsewhere,[6-8] and will not be detailed here, except for several aspects. The resonant maxima in Pt(100) occur at nearly the same photon energies as those observed for Pt(111) (Ref. 8) [bands (2,3) at 20.5 eV, band 4 at 19.5 eV, and bands (5,6) at 17.5 eV], and occur at the same binding energies [bands (2,3) at 4.1 eV, band 4 at 2.8 eV, and bands (5,6) at 1.4 eV]. Thus, the resonant final-state energies (R) are essentially identical for the two faces, as depicted on the band structure diagram in Fig. 2. R($\Gamma\Lambda$L) and R($\Gamma\Delta$X) refer to the resonance energies for Pt(111) and Pt(100), respectively, with the average value given by the dashed line at 16.5 eV above E_F. In consonance with the resonances observed for other crystal faces,[6-8] this resonance level does not correspond to the photoelectron dispersion relation energy position at Γ. In fact, Fig. 2 shows that R intersects the final-state band closer to X than Γ. But, as discussed in Chapter I and elsewhere,[7] this is not inconsistent with the employment of a plane-wave final-state (PWFS) band, because we already know that the PWFS does not yield correct peak

intensities;[34] it cannot possibly give the correct atomiclike cross section in the core region, where the final state is not a plane wave.[35] Therefore, the validity of the utilization of a PWFS for determining initial-state dispersion relations cannot be criticized with intensity arguments! Additionally, the PWFS determines nothing about the photoelectrons which find their way to the detector via a mechanism other than a simple direct transition, i.e., the "DOS" features illustrated in the empirical band diagram in Fig. 4. These observations are equally supportive of two final-state resonance mechanisms: (1) an atomic cross section effect for which initial states are coupled directly to the resonant final-state energy (at the appropriate photon energy) in the photoexcitation step, and (2) an electron transport phenomenon by which photoelectrons originating from deeper within the bulk reach the detector by virtue of an increased lifetime in the resonant final states. Evidence for the first mechanism is the fact that the atomic character of the final states at the resonance energy is f-electron-like,[36] with an enhanced d → f photoemission cross section. Evidence for the second comes from two sources: (a) the observation of constant-kinetic-energy features corresponding to the "trapping" of electrons in conduction bands at the resonant final-state energy,[6,8] and (b) experimental evidence from thermomodulation spectroscopy suggesting that conduction electrons in the resonance bands have anomalously long lifetimes.[37] These two mechanisms are not necessarily mutually exclusive--the lifetime effect might be directly correlated with the f-electron character of the conduction bands.[37] Additionally, the second mechanism implies, in a time-reversed sense,

that the final-state wave function propagates deeper into the bulk. In principle, the wave function would then be more "bulklike", as the conduction electron would of necessity experience an influence from the periodic crystal potential. This is one case where photoelectrons from "bulklike" conduction bands might reach the detector. Both mechanisms above probably contribute to the resonances. Neither one suggests explicitly that the resonance is derived simply from the large conduction band DOS at the resonance energy, although this may be a factor. Furthermore, neither mechanism implies that resonances must occur only in direct-transition peaks, in agreement with the observation in Pt(100) that the DOS features undergo resonances.

It is apparent from our analysis of direct-transition features, shown in Fig. 3, that dispersion is observed when emission would otherwise correspond to a gap[38] in the bulk conduction bands, in accord with the Cu(211) results. Although the exact form of these bulk bands is not known, positions at both Γ and X are available. From the final-state resonances observed both in this work and in the spectra of Pt(111), Γ_7- lies 16.5 eV above E_F, as shown in Fig. 2. The positions of X_6+, X_6-, and X_7- were calculated by Andersen[21] and are shown in Fig. 2 as the open circles at X. By analogy with the bulk band structures of gold[23] and palladium,[22] bulk conduction-band gaps are expected at energies below $E(X_6+) = 8.9$ eV and in the vicinity of the resonance level near Γ_7- in Pt(100). While the Pt(100) results do not present evidence for the lack of band-gap photoemission as directly as Cu(211) (Ref. 4), it is nonetheless evident that the valence bands show dispersion throughout the zone except

near the high-symmetry points where they are expected to be flat regardless of the final-state band structure. As a final point concerning the details of the photoelectron band structure, we note that the detailed empirical valence-band dispersion relations are not expected to be particularly sensitive to errors in its estimation because group velocities of photoelectrons along $\vec{k}_\perp$ are much larger than those of the valence-band electrons; the main breakthrough in the simplification of the band-mapping problem is in knowing that the final-state band structure corresponds to a single, continuous, and smooth function of $\vec{k}_\perp$.

E. Summary and Conclusions

This chapter has described the experimental determination of the platinum valence band structure between Γ and X by analysis of direct-transition features in angle-resolved normal photoemission data for Pt(100)-(5x1). Before this could be achieved, features were identified in the spectra arising from the density of states and final-state resonances. The empirical band structure was derived using a single quasi-free-electron parabolic final-state dispersion relation and, as in earlier studies,[4-10] direct transitions into this band could be assigned even when a gap was present in the bulk conduction-band structure. Comparison of empirical $E_n(\vec{k})$ curves with RAPW theory[21] generally shows excellent qualitative and quantitative agreement, and symmetry selection rules are found to play a role in determining the

number and intensity of EDC direct-transition features. Finally, it is suggested that the propensity for DOS photoemission in Pt(100)-(5x1) is related in large part to enhanced surface umklapp scattering at the reconstructed surface. This is an effect which should be a general phenomenon. We anticipate further experiments with (a) Pt(100), to assess directly the influence of the surface atomic geometry on DOS photoemission, (b) Pt(110), which will complete the determination of empirical band structure diagrams along the high symmetry lines of platinum, and (c) 3d, 4d, and 5d metals, in general, to understand the detailed mechanism of resonance phenomena.

REFERENCES

* This chapter is based on experiments performed in collaboration with G. Thornton, K. A. Mills, and D. A. Shirley; published in Solid State Commun. 34, 87 (1980).

1. See Refs. 1-40 in Chapter IV.
2. See, for example, Reviews (a), (c), (i), and (o) in Chapter I.
3. See, for example, Refs. 6-11 in Chapter IV.
4. R. F. Davis, R. S. Williams, S. D. Kevan, P. S. Wehner, and D. A. Shirley, submitted to Phys. Rev. B (LBL-8511, see Chapter II of this work).
5. J. Stöhr, P. S. Wehner, R. S. Williams, G. Apai, and D. A. Shirley, Phys. Rev. B 17, 587 (1978).
6. P. S. Wehner, R. S. Williams, S. D. Kevan, D. Denley, and D. A. Shirley, Phys. Rev. B 19, 6164 (1979).
7. K. A. Mills, Ph.D. thesis, University of California, Berkeley, 1979 (LBL-9429, unpublished); K. A. Mills, M. G. Mason, R. F. Davis, R. Watson, G. Thornton, J. G. Tobin, Z. Hussain, E. Umbach, and D. A. Shirley, to be published.
8. K. A. Mills, R. F. Davis, S. D. Kevan, G. Thornton, and D. A. Shirley, Phys. Rev. B 22, 581 (1980).
9. R. F. Davis, M. G. Mason, Z. Hussain, J. G. Tobin, L. E. Klebanoff, and D. A. Shirley, to be published.
10. S. D. Kevan, P. S. Wehner, and D. A. Shirley, Solid State Commun. 28, 517 (1978).

11. S. Hagström, H. B. Lyon, and G. A. Somorjai, Phys. Rev. Lett. 15, 491 (1965); P. Heilman, K. Heinz, and K. Müller, Surf. Sci. 83, 487 (1979).

12. Ref. 59 in Chapter IV.

13. Refs. 22, and 26-29 in Chapter IV.

14. See, for example, S. Hüfner, in Photoemission in Solids II, edited by L. Ley and M. Cardona (Springer-Verlag, New York, 1979).

15. See, for example, J. B. Pendry, in Photoemission and the Electronic Properties of Surfaces, edited by B. Feuerbacher, B. Fitton, and R. F. Willis (Wiley, New York, 1978).

16. R. S. Williams, P. S. Wehner, J. Stöhr, and D. A. Shirley, Surf. Sci. 75, 215 (1978); Review (i) in Chapter I.

17. G. D. Mahan, Phys. Rev. B 2, 4334 (1970).

18. P. O. Nilsson and N. Dahlbäck, Solid State Commun. 29, 303 (1979).

19. J. Hermanson, Solid State Commun. 22, 9 (1977).

20. R. J. Elliott, Phys. Rev. 96, 280 (1954).

21. O. K. Andersen, Phys. Rev. B 2, 883 (1970).

22. N. E. Christensen, Phys. Rev. B 14, 3446 (1976).

23. N. E. Christensen and B. O. Seraphin, Phys. Rev. B 4, 3321 (1971); N. E. Christensen, ibid. 13, 2698 (1976).

24. J. F. van der Veen, F. J. Himpsel, and D. E. Eastman, Phys. Rev. B 22, 4226 (1980).

25. G. O. Arbman and S. Hörnfelt, J. Phys. F 2, 1033 (1972).

26. R. F. Willis, B. Feuerbacher, and N. E. Christensen, Phys. Rev. Lett. 38, 1087 (1977).

27. P. Heimann, J. Hermanson, H. Miosga, and H. Neddermeyer, Phys. Rev. Lett. 43, 1757 (1979).

28. The loss of the reflection symmetry of the ΓXWKΓ plane is analogous to a symmetry transformation like $\Delta \rightarrow \Sigma$, for which $\Delta_2 \rightarrow \Sigma_1$ and $\Delta_{2'} \rightarrow \Sigma_2$; in normal emission Σ_1 can be excited by $A_{\parallel}$, while Σ_2 cannot be excited by any linear polarization of the radiation via a dipole process.

29. L. F. Ley, J. Electron Spectrosc. Relat. Phenom. 15, 329 (1979).

30. See, for example, Review (a) in Chapter I; Ref. 31 in Chapter IV; F. J. Himpsel, P. Heimann, and D. E. Eastman, J. Appl. Phys. 52, 1658 (1981).

31. J. Anderson and G. J. Lapeyre, Phys. Rev. Lett. 36, 376 (1976).

32. J. F. van der Veen, F. J. Himpsel, and D. E. Eastman, Solid State Commun. 34, 33 (1980).

33. F. J. Himpsel and D. E. Eastman, Phys. Rev. B 18, 5236 (1978).

34. Ref. 44 in Chapter I.

35. Refs. 30 and 42 in Chapter I.

36. J. Hermanson, J. Anderson, and G. Lapeyre, Phys. Rev. B 12, 5410 (1975).

37. C. G. Olson, D. W. Lynch, and R. Rosei, Phys. Rev. B 22, 593 (1980).

38. B. Feuerbacher and N. E. Christensen, Phys. Rev. B 10, 2373 (1974); E. Dietz and F. J. Himpsel, Solid State Commun. 30, 235 (1979).

Table I. Values of valence bands along ΓΔX in platinum. (a)

$\lvert\vec{k}_i\rvert$ in units of $\left(\frac{2\pi}{a}\right)$	Source of data	Band energy, $-E^F$ (eV)				
		$\Delta_{7\ell}$	Δ_{6m}	Δ_{7m}	Δ_{6u}	Δ_{7u}
0.000(Γ)	(b)	4.05	4.05	2.97	1.40	1.40
0.000(Γ)	(c)	4.07	4.07	(2.80)	1.40	1.40
0.000(Γ)	(d)	4.07	4.07	2.77	1.41	1.41
0.125	(e)	4.13	4.02	2.62	1.56	1.43
0.250	(e)	4.34	3.77	2.49	1.71	1.36
0.375	(e)	4.53	3.69	2.28	1.59	1.14
0.500	(e)	4.88	3.45	1.91	1.41	0.85
0.625	(e)	5.18	3.08	1.32	1.01	0.43
0.750	(e)	5.54	1.47	0.73	0.36	
0.875	(e)	(5.83)	0.27	0.50		
1.000(X)	(e)	(5.95)		0.43		

(a) Error limits for empirical values are estimated as ± 0.05 eV. Values in parentheses are estimates based on extrapolation of empirical bands.

(b) RAPW band structure calculation by Andersen (Ref. 21).

(c) Empirical values, from Pt(111) ARNP data (Ref. 8).

(d) Empirical values, this work; based on average of empirical band extrapolation and density-of-states feature associated with the band energy at Γ.

(e) Empirical values, this work; based on detailed dispersion relations.

FIGURE CAPTIONS

Fig. 1. Selected electron energy distribution curves collected at normal emission from Pt(100) in the photon energy range 11 eV $\leq h\nu \leq$ 30 eV. The inset in the upper right corner gives the experimental geometry, as discussed in Section B of the text.

Fig. 2. Theoretical (lines and open circles at X) low-energy dispersion relations for Pt along $\Gamma\Delta X$, and the empirical final-state band (highlighted by closed circles) utilized to derive empirical valence-band dispersion relations from Pt(100) ARNP spectra. The theoretical bands are from Andersen's RAPW calculation (Ref. 21) with band symmetries indicated by the usual double-group designations. The photoelectron dispersion relation corresponds to $V_0^F = +3.3$ eV and $m^* = 1.4\ m_e$ in Eq. (1) of the text, and has two branches in the energy range below 31.6 eV with the $\vec{G}$ vectors as indicated [for substitution into Eq. (2)]. As shown, the final states are in the first Brillouin zone below $E^F = +10.4$ eV, and in the second zone above this energy. The two levels, $R(\Gamma\Lambda L)$ and $R(\Gamma\Delta X)$, refer to final-state resonance energies derived from Pt(111) (Ref. 8) and Pt(100) spectra, respectively, with the average value given by the dashed line at $E^F = +16.5$ eV (refer to discussion in Section D.3 of the text).

Fig. 3. Empirical (circles) and theoretical (lines, Ref. 21) valence-band dispersion relations for platinum along $\Gamma\Delta X$. The experimental points were derived from EDC direct-transition (DT) features by employing the final-state band illustrated in Fig. 2. The photon energy scale on the upper abscissa gives the initial-state wave vector ($\vec{k}_i$) at the Fermi level (E_F) corresponding to direct-transition photoexcitation at $h\nu$, and the Δ-line irreducible representation labels include "ℓ", "m", and "u", to distinguish between bands of the same symmetry.

Fig. 4. Empirical (closed circles) and theoretical (lines, Ref. 21) valence-band dispersion relations for platinum along $\Gamma\Delta X$, as in Fig. 3, with the inclusion of dispersionless density-of-states (DOS) features (open circles), the E vs $\vec{k}_i$ plots for the latter group of features being derived from the same final-state band (see Fig. 2) employed for direct-transition peaks.

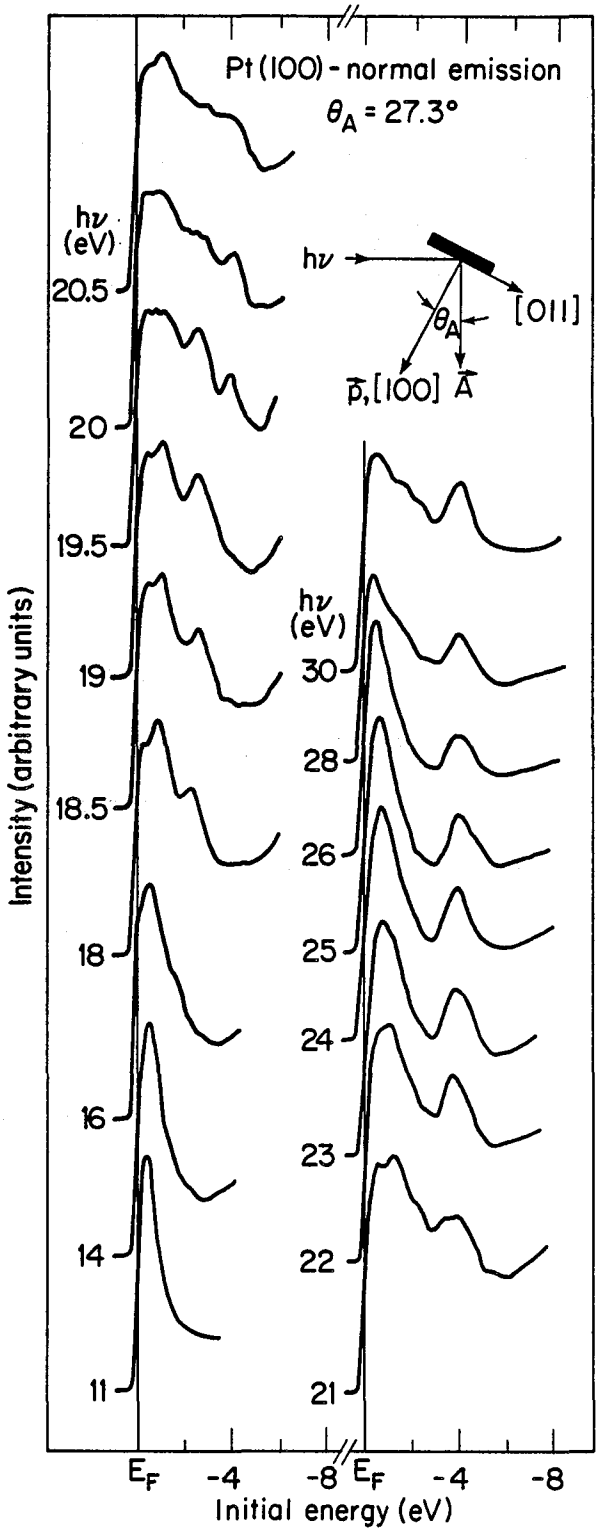

Figure 1

XBL 798-2700A

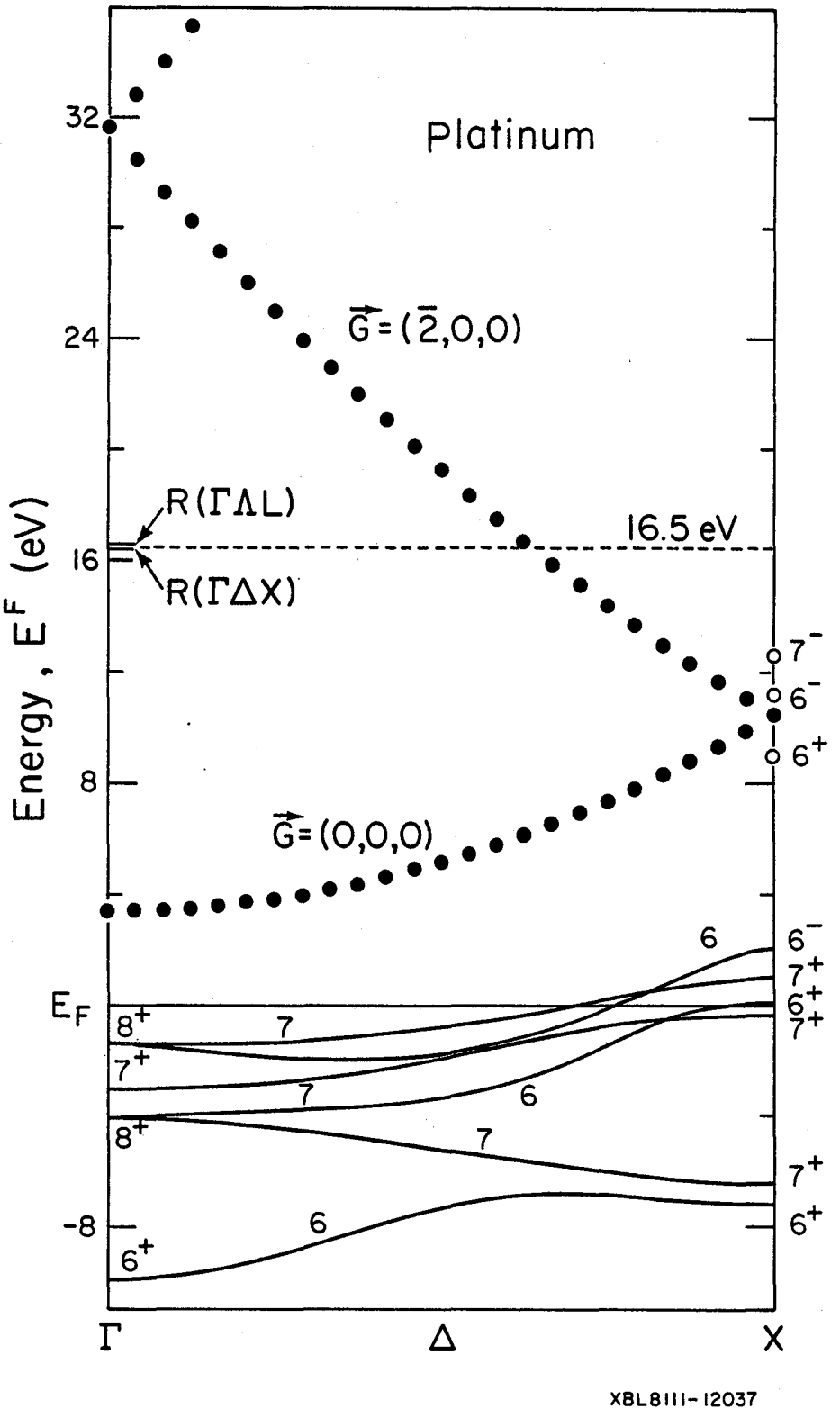
Platinum
Energy, E^F (eV)
32
24
16
8
-8
$\vec{G}=(\bar{2},0,0)$
$\vec{G}=(0,0,0)$
R(ΓΛL)
R(ΓΔX)
16.5 eV
E_F
7^-
6^-
6^+
8^+
7^+
7
6
Γ
Δ
X
XBL8111-12037

Figure 2

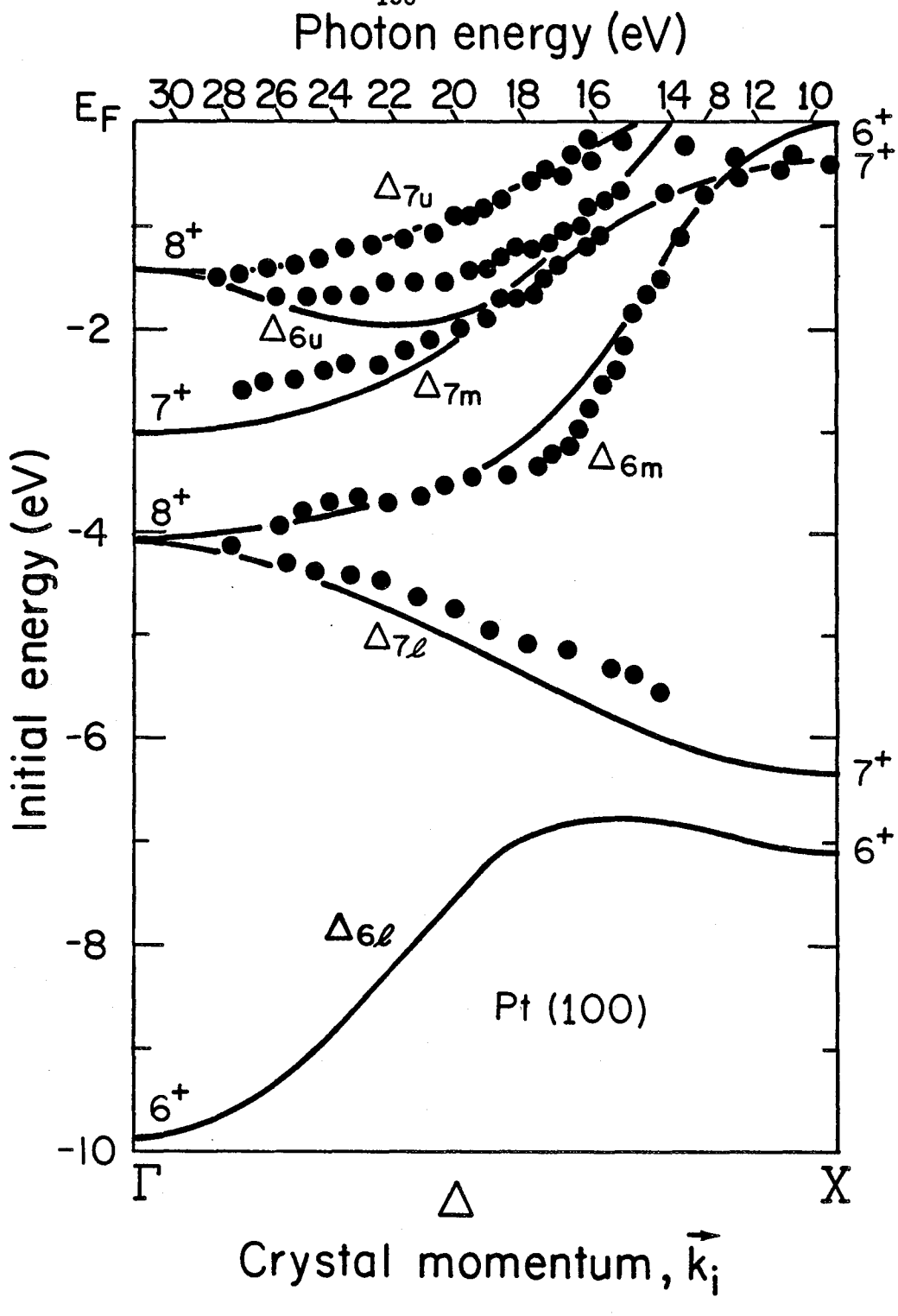

Figure 3

XBL 798 - 2699 A

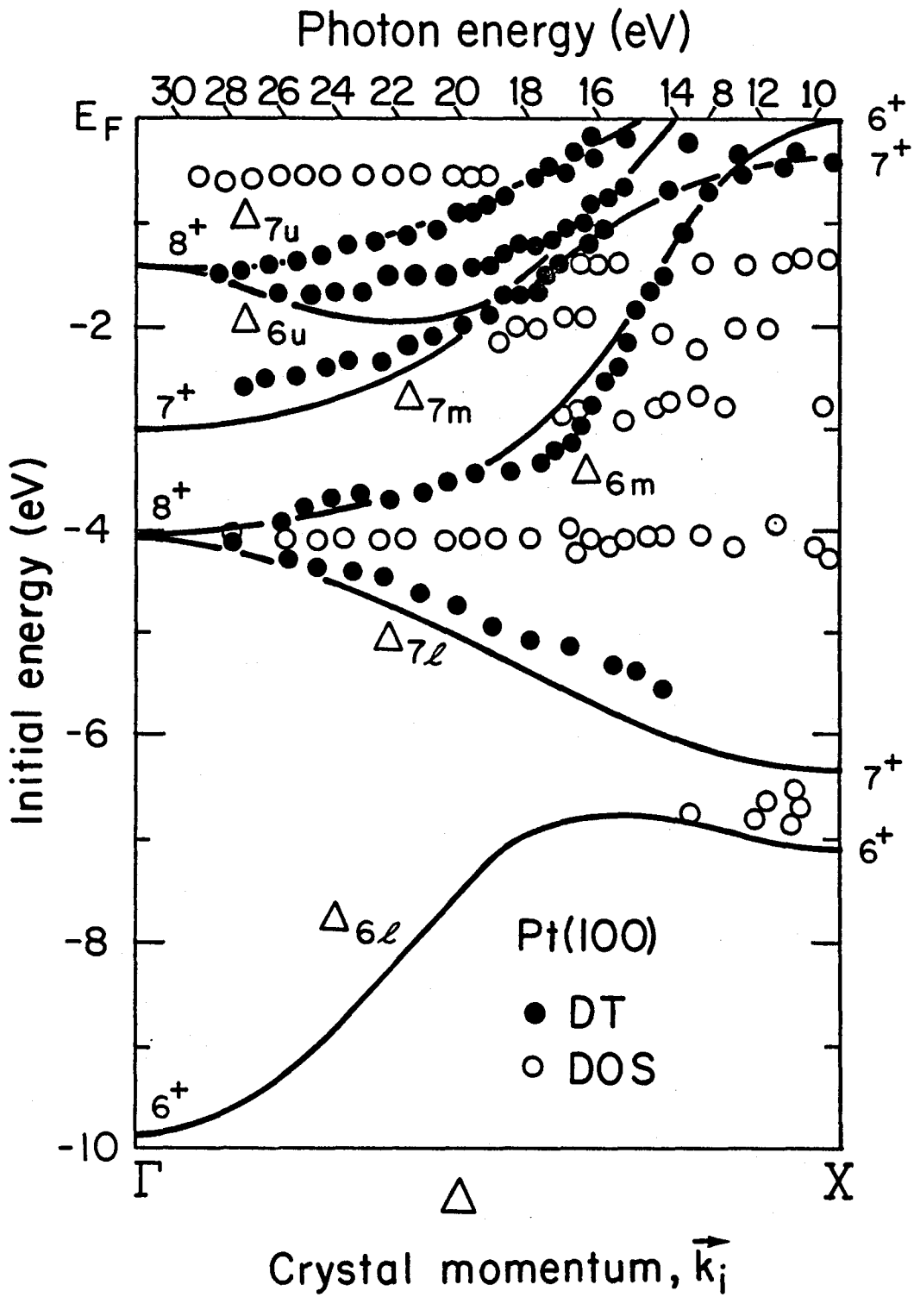

XBL 8111-12031

Figure 4

IV. THE VALENCE BAND STRUCTURE OF ANTIFERROMAGNETIC CHROMIUM ALONG Δ AND Σ*

A. Introduction

Valence band structure studies of metals with angle-resolved photoemission (ARP) have been limited, for the most part, to Group VIII and IB elements.[1-40] For these metals, the success of the direct-transition model in the interpretation of ARP spectra in the vacuum ultraviolet energy region has been remarkable. In nearly every case, it has been shown that most peak structures in valence band photoelectron energy distribution curves (EDCs) arise from energy- and momentum-conserving direct electronic transitions near or at the surface, and that the resulting empirical dispersion relations $E_i(\vec{k})$ closely resemble calculated bulk valence-band dispersion curves. Furthermore, the final-state or photoelectron band structure employed in $E_i(\vec{k})$ determination has a simple form relative to bulk one-electron conduction band structures,[1-12,26,32-36,40,41] thereby yielding a tremendous reduction of the complexity of the problem. In fact, we have shown, in studies utilizing synchrotron radiation in the $h\nu$ = 6 to 32 eV energy region, that a single quasi-free-electron parabolic final-state dispersion relation can be used in conjunction with the normal photoelectron emission geometry to determine empirical bulk valence-band dispersion relations along $\vec{k}_\perp$ (the surface perpendicular or normal component of the crystal momentum vector $\vec{k}$) in copper,[1] silver,[5-7] gold,[8,9] and platinum.[9,10]

It would appear, then, that we have a method of general applicability to the problem of bulk valence band structure determination. It is essential, however, that our conclusions concerning ARP be tested by extending measurements to materials in other regions of the periodic chart, i.e., outside Groups VIII and IB, where the conditions may not be ideally suited for bulk band structure determination. In this chapter, angle-resolved normal photoemission (ARNP) studies of the valence bands of the (100) and (110) faces of chromium (Group VIB) are reported. For at least three important reasons, chromium provides a useful test:

(1) In contrast to the filled or nearly filled d-electron shell of d-band metals studied previously, the isolated chromium atom d-shell is only half-filled [$(3d)^5$] and that of the metal is slightly less than half-filled. Thus, open-shell many-electron effects in photoemission[13,42] may be important in chromium. The valence-band structure picture discussed above is intrinsically a one-electron model; thus, many-electron effects would tend to compete with and induce band-structure-model breakdown. Actually, a comparison of valence band photoemission spectra for the nickel group metals (Z) with their corresponding (Z+1) noble metal neighbors shows that many-electron effects in the slightly-open-shell column (Z) may already be interfering, as evidenced by their generally broader peak structures[43] and poorer agreement with bulk band structures.[44]

(2) The (100) and (110) faces of the other Group VIB metals molybdenum and tungsten have valence-band ARP spectra that are complicated

by features associated with photoemission from intrinsic surface state bands and the one-dimensional density of states (ODDOS).[45-53] By analogy, surface states and the ODDOS may also be important in the spectra of corresponding faces of chromium. Surface-state bands, which disperse with $\vec{k}_{\parallel}$ (surface component of momentum) rather than $\vec{k}_{\perp}$, give rise to dispersionless features in ARNP EDCs (where $\vec{k}_{\parallel} = 0$). While they are important in the understanding of surface electronic properties, surface state peaks can interfere with attempts to measure bulk band structure properties, and it is crucial to differentiate between the surface and bulk features.

(3) Unique amongst metals, chromium displays itinerant antiferromagnetic behavior, with a Néel temperature of 312K.[54,55] As discussed below, antiferromagnetism and the associated spin-density wave (SDW) have profound influence on the bulk electronic structure of chromium. The extent to which this might be observable with ARP is an open question that represents an important part of this research.

It will be shown, below, that both surface- and bulk-derived photoemission features are observed in EDCs for the Cr(100) and Cr(110) faces, and that the presence of the SDW is directly evidenced in the spectra. However, for those peaks which are shown to arise from bulk-like direct transitions, the derived empirical dispersion relations disagree significantly with theoretical calculations for antiferromagnetic chromium along appropriate $\vec{k}_{\perp}$ directions. Furthermore, the experimental EDC curves for both faces are dominated <u>not</u> by the sharp direct-transition features which are characteristic of noble and Group

VIII metals, but by dispersionless peaks which are either surface-related or arise from the bulk density of states.

In Section B, experimental procedures are discussed. Section C discusses first antiferromagnetism and its relationship to the band structure of chromium and secondly, the essentials of the direct-transition model framework and empirical dispersion relations are developed. Section D discusses results and Section E gives a summary.

B. Experimental

Chromium, like molybdenum and tungsten, crystallizes in the body-centered cubic (BCC) lattice structure, with one atom per unit cell. Two high purity single crystals of Cr were cut and mechanically polished to within ± 1/4° of the (100) and (110) planes, respectively, with a mean surface roughness of 1 μm. The resulting (100) and (110) faces were electropolished in a solution containing acetic and perchloric acids,[56] yielding surfaces which were visually highly reflective, with mirror-like finishes. The crystals were then installed in an ultrahigh-vacuum chamber (base pressure ~ 3×10^{-10} torr) and cleaned by repeated cycles of Ar^+ sputtering (beam voltage = 1 kV) followed by annealing at ~ 900K, with surface cleanliness monitored by Auger electron spectroscopy (AES). Both surfaces were found to be relatively difficult to clean of the major impurities (C, N, and O), and as many as 100 sputter/anneal cycles were required before AES impurity (C, N, O, S) signals characteristic of $\lesssim 0.05$ monolayer contamination were observed. Furthermore, both clean surfaces were found to

be reactive with residual gases in vacuo. However, the contamination level could be kept below ~ 0.05 monolayer for at least 10 to 12 hours, which was sufficient time for a complete series of ARNP spectra to be recorded. Immediately preceding the ARNP experiments on each crystal face, further sputter/anneal cycles were performed, and surface cleanliness was monitored by AES immediately before and after each experiment. Because of experimental difficulties, the structure and crystallographic order of the surfaces could not be monitored by low energy electron diffraction (LEED) during the ARP experiments. However, the surface phases of these crystals were subsequently checked with LEED in a different vacuum chamber. Using the same clean-surface preparation procedure as above, LEED patterns (with extremely sharp and intense spots) of the Cr(100) and Cr(110) surfaces characteristic of $(\sqrt{2} \times \sqrt{2})R45^{\circ}$ and p(1x1) structures, respectively, were observed (with the sample temperature at 293K). Both patterns are consistent with other recent LEED studies,[57,58] particularly in that the recently reported Cr(100) clean-surface reconstruction[57] was confirmed here. The ease with which these excellent patterns were obtained after surface preparation treatments identical to the method used during the ARNP experiments serves as assurance that the identical surface phases were obtained there. It should be noted that LEED patterns for BCC crystal faces are somewhat different from those of the more familiar face-centered cubic (FCC) crystals. Because this difference sometimes leads to confusion, diagrammatic representations of Cr(110)-p(1x1), Cr(100)-p(1x1), and Cr(100)-c(2x2) LEED patterns are displayed in Fig. 1.

The photoemission measurements were performed on the 8° branch of Beam Line I (BL I-2) at the Stanford Synchrotron Radiation Laboratory with the incident radiation highly polarized (> 97 percent) in the horizontal plane and in the energy range 6 eV $\leq h\nu \leq$ 32 eV. The ARP apparatus, described elsewhere,[59] employs a double-pass cylindrical mirror analyzer (CMA), with the angular acceptance modified for these experiments to ± 2.5°. In these measurements, the energy resolution (monochromator plus electron analyzer) varied from ca. 0.1 eV to ca. 0.2 eV (FWHM) at the lower and upper limits of the photon energy range, respectively. All spectra were recorded with the sample temperature at 293K.

In Fig. 2, the experimental normal emission geometries utilized are shown for the Cr(100) and Cr(110) crystals. For both crystal faces, the incident radiation vector potential ($\vec{A}$) was confined to the (horizontal) plane of incidence with the angle θ_A (between $\vec{A}$ and the crystal surface normal $\vec{n}$) fixed at 27.3°. The crystal azimuthal orientations were also held fixed (ϕ_A constant), with the [011] and [001] azimuths contained in the plane of incidence (along $\phi_A = 0°$) for the Cr(100) and Cr(110) faces, respectively (see Fig. 2). Azimuthal crystallographic alignment (± 1° or better) was achieved (after mounting the samples for ARP experimentation) using the back-reflection Laue method external to the vacuum chamber. In situ polar crystallographic alignment (± 1° or better) was effected by laser autocollimation.

Typical EDCs for the entire energy range are shown in Figs. 3 and 4 for Cr(100) and Cr(110), respectively. In each spectrum, the Fermi

level (E_F) was determined as $(dI/dE)_{max.}$, i.e., the point of maximum derivative of photoelectron intensity (I) with respect to energy (E), in the region around the onset of photoemission. This method, although not necessarily rigorous, is probably more accurate than another popular technique which simply defines E_F as the energy at half-height of intensity in the onset region.[9] The distinction between these two methods, while typically minor, is particularly important for spectra that contain structure near E_F. For the present studies, it is expected that derived EDC peak position energies relative to E_F (E^F) are in error, <u>at worst</u>, by a minute constant because the work functions derived from E_F placement and analyzer reference voltages showed rms scatter of only ± 36 and ± 24 meV over the entire data ranges for Cr(100) and Cr(110), respectively.

C. Band Structure Characteristics

Before discussing chromium band-structure characteristics, it is informative to investigate the $h\nu$ dependence of the various features in the spectra displayed in Figs. 3 and 4. Peak structure plots for both crystals are shown in Fig. 5. The circles represent strong peak (closed circles) or weak feature (open circles) energy positions relative to E_F for the range of photon energies used. The distinction between strong and weak features is only a qualitative guide, because substantial peak convolution can give the appearance of drastically different peak intensities. The connecting lines on the plots in Fig. 5 have no significance other than to join and map the individual structures as functions of $h\nu$.

It is immediately apparent from Fig. 5 that while some features disperse with hν [B, C, and E for Cr(100); B, C, E, and G for Cr(110)], others, which are rather intense peaks, show little or no dispersion. This was not the case for Group VIII and IB metals,[1-40] where nearly all features showed dispersion. Thus, as speculated above, photoemission from chromium is fundamentally different from other metals studied. An attempt to understand this requires a detailed elucidation of the room-temperature chromium bulk band structure. In the spirit of the direct-transition model for the normal emission geometry, peak dispersion with hν is highly indicative of bulk direct-transition processes, particularly because $\vec{k}_{\parallel}$ is zero for normal emission. This dispersion occurs only from direct transitions at reduced k-points which yield photocurrent in normal emission, i.e., those which are either part of the appropriate $\vec{k}_{\perp}$ crystal momentum space or those which are in other directions but able to excite transitions that result in normal emission via surface umklapp processes.[52,60] Usually, the former mechanism dominates.[4] The appropriate regions of k-space are the Δ and Σ lines, for Cr(100) and Cr(110) direct transitions, respectively.

1. Antiferromagnetic Energy Bands of Cr.

As discussed above, metallic Cr is slightly antiferromagnetic (AF) at room temperature, with a magnetic moment of 0.59 μ_B per atom and a spin density wave (SDW) that is nearly commensurate with the x-ray lattice structure.[54] The "spin density wave" terminology,

which was introduced by Overhauser,[61] refers to an electron distribution that is uniform spatially but oscillatory in spin. Alternating spin density in the form of a standing wave (antiferromagnetism) occurs because it results in a net reduction of the total band energy.[62] In other words, the material in the AF state has taken advantage of its net magnetic moment by ordering its spins in some oscillatory (periodic) manner to lower its energy, producing an exchange potential perturbation periodic with the SDW. In a single AF domain, the Cr SDW runs along one of the cubic axes ($\vec{x}$, for example) with a periodicity that is 21 lattice spacings, corresponding to a wave vector $\vec{Q}$ = (0.95, 0, 0) (in units of $2\pi/a_{Cr}$, which will be used throughout this work; a_{Cr} = 2.88 Å). The most popular way of dealing with this perturbation theoretically in a band structure calculation is to treat the spin superlattice as a magnetic crystal, the symmetry of which differs from the real lattice. Unfortunately, the real situation is difficult to handle, because the unit cell corresponding to Q = 0.95 would contain a very large number of atoms in real space (and, thus, an enormous number of bands in k-space). However, the perfect AF state, Q = 1, is commensurate with the BCC lattice, and is treatable with present band-theoretical techniques.[63-65] It is generally considered to be an excellent model structure with which to describe the electronic properties of AF Cr.[54] Indeed, the commensurate state is not far from the real state and can be stabilized experimentally by alloying Cr with less than one percent of Mn.[66] From here on in this section, only commensurate antiferromagnetism will be discussed in relation to

band theory, but it is important to remember that this does not represent precisely the true incommensurate antiferromagnetic state in Cr.

The commensurate AF Cr unit cell, in which the spins at the corners and center are of equal magnitude but point in opposite directions, is illustrated in Fig. 6. This structure gives alternating planes of spin-up ($\uparrow$) and spin-down ($\downarrow$) atoms orthogonal to any of the cubic axes -- the SDW. The crystal atomic structure is still BCC, but as far as electrons are concerned, the AF unit cell has a magnetic structure that is equivalent to the CsCl crystal structure, i.e., simple cubic (SC) with a two-atom basis. The electron density has the periodicity of the BCC lattice while the magnetization periodicity is twice this. Thus, the primitive SC unit cell volume is twice the BCC volume, and the SC Brillouin zone (BZ) is half-size and contains twice as many occupied k states as the BCC zone.

To demonstrate how the AF reciprocal lattice structure and BZ are constructed, Fig. 7 illustrates the effect of the commensurate SDW on the (001) plane in k-space. Figure 7(a) shows a portion of repeated-zone k-space with the BCC structure (this is quite different from that of the FCC lattice encountered in earlier chapters). The open circles represent reciprocal lattice points with Γ symmetry, and the smaller, filled circles represent points having H symmetry. The first BZ is the region bound by the central square with Γ (0, 0, 0) at the center and H (1, 0, 0) points at the corners. Also shown is the direction and magnitude of the commensurate SDW wave vector $\vec{Q}$. The SDW adds $\vec{Q}$ to every point in k-space, essentially shifting the entire reciprocal

lattice past itself by one unit of $2\pi/a$ in the [100] direction. The result of this is shown in Fig. 7(b). Each reciprocal lattice point (Γ) has been moved to an H point of the BCC lattice, and every H point is now moved to Γ. Thus, Γ and H are equivalent and form a new lattice. The central square shown in Fig. 7(b) bounds the new first BZ (the SC zone) with Γ(H) at the center, and is half the size of the BCC zone. Now, let us consider, in detail, the effect of the SDW on the BCC → SC transition in the first BZ. Figure 7(c) shows the BZ (labelled "cell A") of the BCC lattice in the (001) plane with the irreducible portion highlighted by the triangle. The symmetry elements Γ, Δ, H, G, N, and Σ are the usual ones for BCC. In addition, the Δ line has been artificially broken into two regions separated by the central (X) point (the parenthetical notation indicates that X is equivalent to Δ, with no other special symmetry). Now, the $\vec{Q}$ vector is added, bringing a neighboring cell (B) into the picture with the partially-overlaid geometry shown in Fig. 7(d). An irreducible wedge from B coincides with the one from A, but each has a different orientation. For example, Δ_{1A} overlaps Δ_{2B}, and Σ_B and G_A are overlaid, etc. If the artificial "A" and "B" labels are removed, the Δ line becomes Γ,H → $\Delta_1\Delta_2$ → (X) → $\Delta_1\Delta_2$ → Γ,H. The irreducible portion is now between Γ,H and (X), because the two regions Δ_1 and Δ_2 are "umklapped" together. Using the symmetry compatibility relationships listed in Fig. 7(e) for the BCC → SC transformation,[54] the SC BZ is constructed from Fig. 7(d), resulting in the cell shown in Fig. 7(f). The SC irreducible wedge in the (001) plane is bound by Γ-Δ-X-Z-M-Σ-Γ.

The paramagnetic (P) to AF transition in the band structure along the [110] direction is demonstrated in Fig. 8, where the calculated results of Asano and Yamashita[63] are reproduced. In Fig. 8(a), the lowest bands are shown along the HGN and NΣΓ lines for the paramagnetic case, labelled by the appropriate irreducible representation symmetries. In Fig. 8(b), the NGH bands (dashed lines) from (a) have been overlaid on the NΣΓ bands (solid lines). An investigation of the Σ and G groups shows that G_1, G_2, G_3, and G_4 are identical to the Σ_1, Σ_2, Σ_3, and Σ_4 representations, respectively, for the simple cubic case.[54] Thus, the AF band structure should contain gaps wherever G and Σ bands of the same symmetry cross or join in Fig. 8(b). This situation occurs twice near N, once near the center of the Σ,G line where G_1 and Σ_1 bands meet, and more importantly once near E_F where G_3 and Σ_3 bands cross. In Fig. 8(c), the ΓΣM bands for AF-Cr are plotted, showing that these gaps are indeed realized in the presence of the periodic perturbation arising from the exchange potential. Because the band mixing and repulsion that occurs in the Σ_3 bands takes place near E_F, the sum of occupied one-electron energy parameters $\Sigma_{(n,\vec{k})} E_{n,\vec{k}}$ is decreased; i.e., the total band energy is reduced. This is the self-stabilizing effect discussed above which is the key to antiferromagnetism in Cr.[54,62] The three-dimensional situation is obviously more complicated, but one can resort to Fermi-surface terminology: the electron and hole octahedral surfaces that surround Γ and H, respectively, are nearly identical in shape and size. The P → AF transition causes the smaller (Γ) electron surface to "nest" within and annihilate

the larger (H) hole octahedron, introducing gaps containing E_F. The largest effect would occur if the two surfaces were identical, because gaps would be centered at E_F everywhere along the original surfaces and the largest energy reduction would be obtained. This would, for example, occur if G_3 and Σ_3 crossed exactly at E_F in Fig. 8(b). Lomer[62] was the first to point out that there is a relationship between the slight mismatch of electron and hole octahedra geometries and the observed incommensurate SDW. He suggested that the most favorable nesting would occur if the shift was $Q = 0.95(2\pi/a)$ instead of $1(2\pi/a)$. This would result in a maximum intersection of the paramagnetic Fermi surfaces. Detailed band structure calculations[67] (including the Asano and Yamashita work[63]) have since confirmed Lomer's conjecture.

Band separations induced by the magnetic exchange potential are generally small in Cr,[63-65] owing to the relatively small magnetic moment of constituent atoms. In fact, Skriver's[65] calculation, for example, places the lower Σ_3 band extremum slightly above E_F, because the gaps are generally even smaller than those of Asano and Yamashita.[63] Finite gaps are expected to exist near E_F along various k-space lines, and also at the SC zone boundary at energies which do not affect the total energy. Examples of the latter are the M_1-M_3 gaps shown in Fig. 8(c). In addition to Skriver's[65] calculation, which uses a local spin density (LSD) formalism, and the work of Asano and Yamashita,[63] which is a self-consistent Korringa-Kohn-Rostoker (KKR) calculation using an exchange potential with the Slater $X\alpha$ form, there is one other recent calculation of the electronic structure of commensurate

AF-Cr by Kübler,[64] using a method that is similiar to Skriver's. The band structure results of these three calculations are qualitatively similar, but there are quantitative differences in band gap widths and absolute band energy positions. These will be discussed in detail below.

There have been numerous experimental studies of AF-Cr.[67] The most relevant ones for the present work are optical studies,[68-70] which confirm the existence of spin-polarization band gaps in the incommensurate AF phase, de Haas-van Alphen effect experiments which (in the form of negative evidence) would appear to verify the self-annihilation of electron and hole octahedra in both the incommensurate[71] and commensurate[72] [Cr(Mn)] phases, and x-ray photoemission (XPS) measurements of Cr valence bands.[73] Additionally, there has been another recent ARP study of Cr(110) by Johansson, et al.[74] However, a meaningful comparison with the present work may not be feasible, because the Cr(110) surface studied by Johansson, et al.[74] was relatively contaminated with oxygen. Finally, it should be noted that in a very fundamental way, these spin-polarization gaps discussed in this section are similar to the s,p-d hybridization gaps normally encountered in band structures.[54,75] Thus, the existence of Shockley-type[76] surface states in spin-polarization gaps might be anticipated for the low-Miller-index faces of Cr.[75,77] The existence of these states is important partly because their identification would imply the presence of magnetic order on the surface.[78-81] Such states were not reported in the earlier ARP study of Cr(110).[74]

2. Empirical Valence-Band Dispersion Relations Along Δ and Σ.

In consonance with previous studies,[1-12] empirical $E_i(\vec{k})$ relations were derived from the hν-dependence curves of the initial-state energy (E_i) positions for each peak structure (Fig. 5) under the assumption that the peaks are derived from direct transitions along $\vec{k}_\perp$. In this way, non-direct-transition phenomena in the spectra become apparent in the resulting empirical band diagrams, and can be quantitatively analyzed. The initial-state crystal momentum, $\vec{k} = \vec{k}_i$, is along the Δ and Σ direction for Cr(100) and Cr(110), respectively. The final-state crystal momentum is $\vec{k}_f = \vec{k}_i - \vec{G}_{hkl}$, where $\vec{G}_{hkl}$ is a reciprocal lattice vector. If it is further assumed that the final-state Bloch-type wave function contains only one plane-wave component (i.e., only primary-Mahan-cone[60] photoemission is important), then $\vec{G}_{hkl}$ = (n, 0, 0) and (m, m, 0) (where n and m are integers) for Cr(100) and Cr(110), respectively. These assumptions are tantamount to a quasi-free-electron final-state dispersion relation as employed in other recent studies,[1,5-11] i.e.,

$$E_f^F(\vec{k}_f) = (\hbar^2/2m^*)|\vec{k}_i - \vec{G}_{hkl}|^2 + V_0^F \quad , \tag{1}$$

where $m^* = fm_e$ (m_e and m^* are free-electron and effective masses, respectively), and V_0^F is the inner potential. The most successful procedure is to fit Eq. (1) to the appropriate bulk, one-electron conduction band components that are derived from the empty lattice conduction band(s) that would be involved in primary-cone emission along

$\vec{k}_\perp$, with f and V_0^F as the fitting parameters (see, e.g., Refs. 1 and 7, and Chapters II and III). Generally, theoretical conduction band calculations in the E^F = 0 to 40 eV region are suitable for this. However, additional measures must usually be taken in order to yield a meaningful photoelectron dispersion relation in this manner, because, as previously discussed, one-electron ground-state conduction band structures do not account for the complicated many-body nature of the photoemission final state.[1,15,35,36,41] [This is in direct contrast to empirical valence-band $E_i(\vec{k})$ curves, which generally show a close resemblance to calculated bulk valence bands.[1-40]] Therefore, the conduction band structure does not even in principle describe photoelectron dispersion relations.[1] The method used here for Cr was shown to work quite well in studies of Pt(100)-(5x1) (Ref. 10 and Chapter III): the fit of Eq. (1) to theory yielded a value of f that was utilized without any change and a value of V_0^F that was adjusted to obtain the best agreement between experimental and theoretical valence-band structures. The adjustment of V_0^F might appear to be somewhat ad hoc in the case of Cr, except for one important point: symmetry arguments require that the valence bands be symmetrical about the zone boundary in the extended-zone scheme. Therefore, if the adjustment of V_0^F results in the fulfillment of this requirement, a kind of self-consistency between the photoelectron and empirical valence-band dispersion relations is achieved. In the present studies, the correct symmetry about X for Cr(100) data and M for Cr(110) data was obtained in addition to the best experimental-theoretical fit by

adjustment of V_0^F, thereby yielding this self-consistency. However, the totally correct physical picture regarding ARP final-state band structure is probably much more complicated, because other variations of the fitting procedure described here have also been utilized successfully. In Ag(110) ARNP studies,[7] adjustment of both f and V_0^F was necessary, whereas no adjustments were utilized in Au(111),[9] Pt(111),[9] Ag(111),[5] Cu(211),[1] and Ag(100) (Refs. 6 and 7) studies. In recent Au(100) studies,[8] no adjustments were utilized because the empirical $E_i(\vec{k})$ curves did not include any high symmetry points, but, the employment of de Haas-van Alphen data[82] in conjunction with the empirical structure plot for the uppermost Δ_6 valence band, and the theoretical Δ_6 conduction band structure,[83] yielded a reasonable final-state band. Other experimental methods of utilizing information about the empirical valence bands to determine ARP final-state band structures in Group VIII and IB metals self-consistently have been employed and/or discussed. These include the energy coincidence method[33-37,84,85] first proposed by Kane,[86] a symmetry method,[87] $h\nu$-dependent peak intensity methods,[15] a Fermi surface method,[88] an appearance angle technique[89] and the free-electron-final-state procedure.[3,40] It is not clear which method is best; the problem of final-state band structure in photoemission is still subject to considerable controversy.[1,25,90,91]

The published theoretical AF-Cr band structure calculations[63-65] do not contain bands for energies higher than several electron volts above E_F. Therefore, we resorted to P-Cr band structure for the determination of final-state bands. Consideration of the underlying

problems associated with one-electron conduction band structure[1] suggests that this is a reasonable alternative. A recent P-Cr calculation by Laurent, et al.[92] included the necessary conduction bands. Because the calculation was for paramagnetic Cr, the theoretical band structure was first adjusted [as in Fig. 8(b)] to account for the symmetry change of the BCC BZ to that of SC. The resulting band schemes are shown in Figs. 9 and 10 for the [100] and [110] directions, respectively. In Fig. 9, the dashed curves, which are Δ-line bands between H and (X), have been overlaid on the bands between Γ and (X) (solid curves) to simulate the AF structure. The conduction bands used in the final-state fit must have Δ_1 symmetry.[93] The appropriate curves in Fig. 9 are between (X) and H_{15} (dashed), H_1 and (X) (dashed), and between (X) and Γ_{15} (solid).[94] After V_0^F adjustment, this yielded a final-state band, highlighted by filled circles in Fig. 9, that corresponds to f = 2.53 and V_0^F = -3.95 eV. Note that in the energy region between ca. 6 eV and 30 eV, the entire $\Gamma\Delta(X)$ line in k-space is traversed twice. The band structure in Fig. 10 is similar to that shown in Fig. 8(b). The HGN-line bands (dashed curves) have been overlaid on the $\Gamma\Sigma N$ bands (solid curves). Both G_1 and Σ_1 final states are allowed[93] in this scheme, but there is only one such band--Σ_1 between Γ_{15} and N_1--related to the empty lattice primary-cone band.[95] After V_0^F adjustment, the Σ_1 fit to Eq. (1) yielded f = 1.03 and V_0^F = +1.32 eV, corresponding to the final-state band highlighted by filled circles in Fig. 10. Note that k-space along the [110] line is not covered as

extensively by this final-state band as the [100] line, but the entire irreducible portion, including the zone boundary (N), is covered within the energy range of these ARP experiments. In summary, $(f, V_0^F) = (2.53, -3.95\ eV)$ and $(1.03, +1.32\ eV)$ were obtained for utilization with Cr(100) and Cr(110) data, respectively. If the theoretical conduction band structure[92] had been used <u>directly</u> to determine $E_i(\vec{k})$, the results would have been erroneously complicated by band gaps. Actually, the AF exchange perturbation yields even more Δ_1 and Σ_1 conduction band gaps than are indicated by the P-Cr band structure[54,63-65] (Figs. 9 and 10). The absence of band gaps in true photoelectron dispersion relations is most likely a consequence of the many-body effects in the photoemission final state alluded to in Cu(211) ARNP studies[1] (Chapter II).

The derived parameters, f and V_0^F, along with Eq. (1) and the relationship $E_f^F = h\nu + E_i^F$, are now used to derive $\vec{k}_f$ and $\vec{k}_i$ from the experimental E_i^F values in the standard way.[1-12] The resulting extended-zone dispersion relations (symbols) are shown in Figs. 11 and 12, for Cr(100) (along $\Gamma\Delta X\Delta\Gamma\Delta X$) and Cr(110) (along $\Gamma\Sigma M\Sigma\Gamma$), respectively, along with Kübler's[64] commensurate AF calculated bands (lines). Of the three published calculations, Kübler's was chosen for comparison with these experiments because it generally shows the best agreement with the experimental results. The dashed lines refer to bands for which transitions are dipole-forbidden within the strict framework of polarization selection rules.[93] For normal emission from Cr(100), only Δ_1 and Δ_5 initial states are allowed to undergo transitions to

the Δ_1 final-state band, regardless of the orientation of $\vec{A}$, while for Cr(110) and the geometry depicted in Fig. 2(b), only $\Sigma_1 \rightarrow \Sigma_1$ and $\Sigma_3 \rightarrow \Sigma_1$ transitions should contribute to normal emission EDCs. Open symbols in the plots refer to curves which show dispersion, while closed circles indicate dispersionless features. The irreducible representation labels for the theoretical curves include "ℓ", "m", and "u" letters to differentiate between bands of the same symmetry.

The calculated bands which can be identified in the extended-zone plots as SDW-derived are Δ_{1u} and $\Delta_{2\ell}$ along Δ (Fig. 11), and Σ_{1m}, Σ_4, and Σ_3 between $\Sigma_3^{max.}$ (point of maximum Σ_3 band energy) and M_5 along Σ (Fig. 12). Spin-polarization gaps are opened inside Δ_1, Δ_2, Δ_5, and Δ_2, doublets at X (the Δ_5 and Δ_2, gaps are above E_F), and in Σ_1 (at M) and Σ_3 doublets (Σ_3 gap at E_F near the center of the $\Gamma\Sigma M$ line) along Σ. It is immediately apparent from Figs. 11 and 12 that mirror symmetry about X and M is obtained in the empirical bands, lending support to the additional shift of V_0^F as discussed above. This is evidenced particularly well by the curve for feature E (see Fig. 5) in Fig. 11 and the curves for features B and C (see Fig. 5) in Fig. 12. Finally, to aid in the correlation of both sets of experimental plots with the Cr band structure, the experimental and theoretical[64] results are plotted in the reduced-zone scheme along $X\Delta\Gamma\Sigma M$ in Fig. 13.

D. Discussion

The ARNP spectra will be discussed, below, with a view toward the mechanisms involved. This is aided by direct comparison of experimental and theoretical $E_i(\vec{k})$ relations. Then, an empirical band

structure assignment of spectral features will be developed. Finally, agreement and/or disagreement with bulk band structure predictions will be discussed, and possible causes of observed discrepancies with the direct-transition model will be elaborated.

Whenever there exist regions of k-space with a high density of initial states (DOS), the possibility must be considered that certain dispersionless features in ARP spectra will have arisen from interband transitions (severely k-broadened, thermally-assisted, impurity- or disorder-induced, or severely umklapp-scattered transitions, etc.) originating from this region.[52,53,96] The underlying background intensity which makes up a large part of valence band ARP spectra undoubtedly arises largely from the DOS, but peak structures corresponding to maxima in the DOS may also be found. In principle, we can distinguish between one-dimensional DOS (ODDOS) and three-dimensional or total DOS (TDOS) mechanisms, because the former is restricted to high initial-state density along $\vec{k}_\perp$. The distinction is ambiguous if either $\vec{k}$ states near Γ are involved (and Γ is contained in $\vec{k}_\perp$), or if the detailed $E_i(\vec{k})$ relation along $\vec{k}_\perp$ is not known. This ambiguity exists in several cases with Cr, mainly because some bands give rise only to dispersionless features. In the discussion which follows, the ODDOS or TDOS mechanism will be invoked wherever possible, but if this distinction is ambiguous or not important, the term "DOS" will be utilized.

1. Spectral Features and Mechanisms for Cr(100).

The Cr(100) spectra displayed in Fig. 3 contain six features, labelled A through F on their structure plots in Fig. 5. Features A, D, and F show essentially no dispersion within the limits of accuracy for the determination of initial-state energy values ($E_i = E_i^F$)--the rms scatter of the peak positions is typically similar to that quoted in Section B for the determination of E_F. Features B and C are nearly flat over most of the $\Gamma\Delta X$ line (Fig. 11), but show distinct dispersion near the X point. Feature E is the only peak which shows a large amount of dispersion.

Feature A is present over the entire range of $h\nu$ utilized, with a mean energy position $\langle E_i \rangle = -0.71$ eV. While it is difficult to see A in spectra for $h\nu \leq 20$ eV, it becomes increasingly more intense above 20 eV as the final-state band approaches Γ. The empirical $E_i(\vec{k})$ curve for A (Fig. 11) indicates that it lies close in energy to the calculated Δ_5 band, which itself shows very little dispersion. It is tempting to designate feature A as a Δ_5 ODDOS peak (arising from the breakdown of $\vec{k}_\perp$ conservation or some related mechanism), but this is ambiguous because the Δ_5 band is theoretically flat across most of the zone. The choice between Δ_5 ODDOS and $\Gamma_{25'}$ DOS is equally ambiguous.

Features B and C are observed in the spectra above $h\nu = 7$ and 9 eV, respectively, with C by far the largest of the two over the whole range of $h\nu$. The dispersive shapes of their $E_i(\vec{k})$ curves near X (see Fig. 11) suggest that B and C arise in part from Δ_{2u} and $\Delta_{2\ell}$, respectively, which theoretically show the same general trends. The Δ_2 bands are

dipole-forbidden initial states in the normal emission geometry;[93] thus, an explanation for their presence in the ARNP spectra is required (see Section D.5). Furthermore, B and C probably do not arise entirely from Δ_2 direct transitions because (a) the empirical band shapes away from X are far removed from those of theoretical Δ_2 dispersion relations; (b) the overall intensity of C is especially large, much too large for a dipole-forbidden transition;[1] and (c) feature D can be assigned to DOS emission near Γ_{12} (see below), which fixes energy positions for the $\Delta_{2\ell}$ curve near Γ_{12} that are far removed from the mean energy of feature C. The most reasonable explanation is that the intensities of B and C are derived mainly from the TDOS for Cr, but their peak positions are modified slightly by the presence of Δ_2 interband transitions at $h\nu$ values corresponding to initial states near the X point. This means that, at least near X, features B and C are each composed of two unresolved peaks--a Δ_2 feature and a TDOS peak. Evidence for this interpretation is presented below.

There is actually no problem in the assignment of B and C $E_i(\vec{k})$ curves near X to Δ_2 transitions. In the absence of selection rule requirements, this would be the obvious interpretation. The problem lies with the shapes of the curves and the intensities of the peaks away from X. This is why two separate mechanisms are invoked, one of which involves the TDOS. First, note the change in B and C peak energies as $\vec{k}_i$ goes from X to Γ. At X, where the peaks are closest, the energies are -1.92 and -3.18 eV for B and C, respectively, at least approximately indicative of $E(X_{3'})$ and $E(X_2)$. The flat portions of the $E_i(\vec{k})$ curves

have $\langle E_i \rangle$ = -1.63 and -3.38 eV for B and C, respectively, in qualitative one-to-one correspondence with the two uppermost maxima in the theoretical TDOS.[63-65,97] The change in B - C peak separation between these two extremes is 0.5 eV--this is a significant change. If Δ_{2u} and $\Delta_{2\ell}$ direct transitions away from X influence the EDCs, they undoubtedly are too weak to be observed as peaks because they would coalesce with the much stronger A and D features, but might contribute to their total intensities. Turning to the TDOS part of the interpretation, strong evidence for this is that feature D in Cr(110) EDCs ($\langle E_i \rangle$ = -3.44 eV) is a non-dispersive peak which, because of its close energy match to the flat portion of the Cr(100) feature C curve, can be identified with the same TDOS maximum. The main difference between the two faces is the relatively lower intensity of Cr(110) feature D and the absence of a peak corresponding to Cr(100) feature B. The identity of TDOS features corresponding to Cr(100) peaks B and C is complicated by the overall differences between experimental and theoretical bands along the $\Gamma\Delta X$ and $\Gamma\Sigma M$ lines; i.e., the energies of theoretical TDOS maxima in any of the three calculations[63-65] are not expected to match either B or C quantitatively. However, if the qualitative relationship between theoretical TDOS and detailed band structure for all three calculations is assumed to carry over to the empirical bands, the origin of B and C can be identified as follows:

There are three main maxima in the theoretical TDOS for AF-Cr ($TDOS_1$ through $TDOS_3$). The uppermost structure (nearest E_F) lies <u>below</u> $E(\Gamma_{25'})$ in each calculation (this is also true for the

theoretical P-Cr TDOS[98]). Rather, it appears to be derived from the energy region near $E(\Sigma_{1u}^{min.})$, i.e., the minimum energy of the Σ_{1u} band. It will be shown (Section D.3) that Cr(110) feature C is derived from Σ_{1u} direct transitions; its $E_i(\vec{k})$ curve in Fig. 13 (◇) represents the Σ_{1u} band. Thus, experimental values for $E(\Sigma_{1u}^{min.})$ and the flat part of the Cr(100) feature B curve (-1.70 and -1.63 eV, respectively) are consistent with an assignment of the latter to $TDOS_1$. In Kübler's[64] band structure, $TDOS_1$ lies just above $E(X_{3'})$, also consistent with this interpretation. $TDOS_2$ is the largest maximum, but cannot be matched to regions of k-space along high symmetry lines. However, it lies just below $E(X_2)$ in Kübler's[64] calculation, totally consistent with the energy of the flat portion of the Cr(100) feature C and the Cr(110) feature D curves (-3.41 eV). $TDOS_3$ is the smallest maximum, and is near $E(\Sigma_{1m}^{max.})$ and $E(\Delta_{1u}^{max.})$. Based on the total band structure assignment of Cr ARNP features, nothing in the spectra matches $TDOS_3$. Rather, a $TDOS_3$ peak would be expected to arise between C and D in Cr(100) spectra; thus, it might comprise part of the unresolved background intensity in the low-kinetic-energy tail of feature C (see Fig. 3). Furthermore, $TDOS_3$ does not coincide with $E(\Gamma_{12})$ in any of the calculations,[63-65,97] so it probably is not hidden beneath feature D in the Cr(100) spectra. As the final supporting evidence, the room-temperature x-ray photoemission (XPS) valence band spectrum of Cr,[73] the shape of which is expected to reflect the TDOS, contains two main features (at E_i = -1.8 and -3.5 eV) that are in good agreement with the interpretation [feature B as $TDOS_1$ and feature C as $TDOS_2$, respectively] presented here. Energy

positions for TDOS features are summarized in Table I. The agreement between photoemission experiments and theory is generally poor because the empirical critical point energy positions deviate from theory (see Section D.4), but Skriver's[65] TDOS matches experiment best.

Non-dispersive feature D ($\langle E_i \rangle$ = -5.03 eV) is the most intense peak in Cr(100) EDCs for 16 eV $\leq h\nu \leq$ 27 eV, above which it is partially obscured by feature E. Undoubtedly, this feature is derived from the DOS either at Γ (Γ_{12}) or X (X_1 and/or $X_{4'}$). With the aid of Cr(110) EDC peak positions, the assignment of other Cr(100) features, and the fact that photoemission from the symmetry-allowed Δ_{1u} band would otherwise be absent, feature D is readily assigned to DOS photoemission from $X_{4'}$, Δ_{1u}, or Γ_{12}. Although all three could contribute, the last (Γ_{12}) is the most acceptable origin of the DOS peak because the theoretical Γ_{12} region is quite flat. It cannot be ruled out, however, than Δ_{1u} is simply less dispersive than theory suggests, with a concomitant higher ODDOS. In either case, it is totally reasonable to expect a feature in the Cr(100) EDCs derived from the $X_{4'}\Delta_{1u}\Gamma_{12}$ band region, because photoemission is observed from all other symmetry-allowed bands for each face and even from symmetry-forbidden initial states (Δ_2) in Cr(100) spectra.

Features E and F are probably related to the $\Delta_{1\ell}$ band, E arising from $\Delta_{1\ell}$ direct transitions and F from the DOS near Γ_1. Feature E is first observed in the spectrum at $h\nu$ = 13 eV (E_i = -6.44 eV) as the lowest lying (highest binding energy) peak in the inelastic tail. At higher $h\nu$, it moves toward feature D until it is barely visible as a

shoulder on the low-kinetic-energy side of D at $h\nu = 17$ eV ($E_i = -5.21$ eV). At higher photon energies it disperses downward (higher binding energy), reaching $E_i = -6.86$ eV at $h\nu = 32$ eV. The most important points about feature E are (a) it has an empirical $E_i(\vec{k})$ curve that has the correct mirror symmetry about X (see Fig. 11) in the extended-zone scheme, (b) it is the strongest indication of direct-transition processes in Cr(100) spectra, (c) it is the most intense EDC feature for $h\nu \geq 28$ eV, (d) its assignment as a $\Delta_{1\ell}$ direct-transition peak is totally consistent with all other assignments, and (e) the detailed empirical $\Delta_{1\ell}$ dispersion relation is quite different from Kübler's[64] theoretical curve. Feature F ($\langle E_i \rangle = -7.00$ eV) is a weak shoulder in the spectra for 14 eV $\leq h\nu \leq$ 26 eV. Outside this range, it is obscured by the stronger E feature. The energy position, non-dispersive character, and similarity of F to the most tightly-bound feature in Cr(110) spectra are strong indications that F is derived from DOS photoemission near Γ_1.

It is important to note that the relative intensities of features B, C, and D are more sensitive to surface contamination than those of features A, E, and F. This was observed during the cleaning procedures discussed in Section B. Therefore, the possibility that the former set of peaks are either partially or totally derived from surface states or resonances at $\bar{\Gamma}$ cannot be totally ruled out. This consideration is further motivated by the possible band structure location of these features: if the assignments discussed above are ignored, the flat part of feature B could lie in the $X_{3'} - X_2$ spin-polarization gap, that

of feature C in an s,p-d hybridization gap analogously to similar states on W(100) (Refs. 46, 48, and 52) and Mo(100) (Refs. 47 and 48), and feature D might lie in the $X_{4'} - X_1$ spin-polarization gap. However, the possibility that features B, C, and D are surface states is rejected at the present time for the following reasons: (a) Mo(100) (Refs. 47, 48, 50, and 51) and W(100) (Refs. 46, 48, 52, and 53) ARNP spectra contain sharp structures near E_F ascribed to $\bar{\Gamma}$ surface states [possibly associated with the c(2x2) reconstruction of these surfaces[45]] while no such feature is observed in ARNP EDCs for Cr(100)-c(2x2), (b) the observation of peak intensity sensitivity to contamination is not conclusive because the extent and chemical identity of the contamination was not well characterized, (c) there is not yet enough experimental information about the valence band structure of chromium to determine unambiguously whether these "surface states" fall in gaps of the projected bulk band structure, (d) careful studies of the surface-band dispersion relations have not been done (angular distribution studies), and (e) assignment of features B, C, and D as surface states cannot be made consistent with the total experimental band structure because the flat part of the feature-B curve is either outside the $X_{3'} - X_2$ gap (if the idea discussed above of a multiple-peak structure is invoked) or not surface-state related by virtue of the total B curve dispersion in normal emission, and the somewhat puzzling absence of Δ_{1u} photoemission would be inferred by the assignment of features C and D to surface states.

2. Aside: Surface State or Bulk DOS?

Conclusive identification of any surface-state features on Cr(100) will require more work. There are generally four conditions which must be satisfied by surface-derived features:[52,81,99] (1) Surface sensitivity. Surface states are sensitive to the surface potential which in turn can be modified by introducing adsorbates (metal atoms, N_2, O_2, H_2, and CO are commonly utilized examples). The adsorbate test of a surface state must be done with a carefully controlled gas-exposure of the clean surface, usually with varying degrees of contamination and with different gases. Not every surface state is attenuated or removed by any adsorbate,[100] and photoemission is in general a surface-sensitive process, so the "impurity test" may not be conclusive alone. (2) Two-dimensionality. A surface state does not disperse with $\vec{k}_\perp$, thus there should be no $h\nu$ dependence to the initial-state energy if $\vec{k}_\parallel$ is held fixed (i.e., by using the normal emission geometry, for example). (3) Projection of the bulk band structure. A surface-sensitive, non-dispersive feature is not a surface state (or resonance) unless there exists a region of $\vec{k}_\parallel$ in the surface Brillouin zone (SBZ) where it lies in a gap of the bulk band structure components of the appropriate symmetry projected onto the SBZ.[77] If the $E_i(\vec{k}_\parallel)$ relation for the state lies in a gap throughout the SBZ, it is a true surface state; if not, it is a surface resonance.[52] (4) Polarization dependence. The surface photoexcitation matrix element M_s is modulated strongly by the angle θ_A (Refs. 101 and 102) (typically, $M_s \propto \cos \theta_A$). Thus, the intensity

of a surface-derived feature is highly sensitive to the degree of p-polarization of the incident radiation.

The four conditions above are necessary, but they are usually not sufficient for the identification of a surface state, because under certain conditions, bulk states can appear to behave like surface states. There are three additional tests which are not necessary, but may be useful in evaluating the possibility of surface states in the Cr(100) case, especially because it is not possible to evaluate features B, C, and D for condition 3 above since the true bulk band structure of Cr is not known. These are: (5) Surface band dispersion. Surface-state bands generally show dispersion with $\vec{k}_{\parallel}$ (Refs. 99 and 103). Thus, it could be argued that Cr(100) feature D, for example, is a surface state if it showed dispersion in non-normal emission. (6) Peak shape. Surface-state features generally are sharp relative to the bulk features[81] because they usually do not suffer from the same lifetime broadening mechanism as bulk states.[52,99] (7) Surface order. Surface-state intensity is sometimes quite sensitive to the degree of atomic order on the surface.

Cr(100) features B and C have not demonstrated that they meet any of the seven conditions, while only condition 2 is conclusively satisfied by feature D. The major problem with Cr(100) is classic: we must be able to distinguish between surface states and the bulk DOS for a case where there does not exist sufficient knowledge about the bulk bands to do so because most of the EDC features are either surface states or DOS features! This problem deserves immediate work, because

the identification of surface states on Cr(100), specifically in SDW-induced spin-polarization gaps along $\vec{k}_{\perp}$, would be a result of major significance. For example, recent theoretical[104,105] and experimental[106] evidence that magnetic order exists on the Cr(100) surface would be further supported by the identification of surface states lying in spin-polarization band gaps. Perhaps the most obvious and straightforward experiment would be to investigate valence band EDCs for P-Cr (i.e., above the Néel temperature of 312K), because the spin-polarization gaps and SDW-induced bands would no longer be present in the Δ-line band structure. Two notes of caution are: (1) evidence also suggests that magnetic ordering at the surface[105] and in the bulk[107] persists well above the bulk Néel temperature, and (2) changes in the bulk band structure induced by the AF → P transition would probably complicate the identification of surface states in ARP EDCs.

3. Spectral Features and Mechanisms for Cr(110).

The spectra for Cr(110), displayed in Fig. 4, are quite different from those of Cr(100). There are eight major features (labelled A through H in Fig. 5) for Cr(110), in contrast to six for Cr(100). Several of the Cr(110) features are generally sharper. Furthermore, Figs. 5 and 12 show that four of the features (B, C, E, and G) show dispersion and can be assigned to bulk direct transitions from bands along $\Gamma\Sigma M$. All four symmetry-allowed bands along the Σ line give rise to Cr(110) direct-transition features. The other features (A, D, F, and H) have flat $E_i(\vec{k})$ curves and, with the exception of feature H, have peak positions with rms scatter that is similar to that quoted in

Section B for the determination of E_F. Other than these eight features, the Cr(110) spectra contain a very weak feature ($h\nu$ = 9 to 11 eV) at E_i = -1.34 eV which is reproduced on the plots in Figs. 5, 12, and 13, and two other isolated weak features (E_i = -3.04 eV at $h\nu$ = 25 eV and -4.68 eV at $h\nu$ = 26 eV) that could not be assigned and will not be further discussed.

Feature A is striking in its intensity in the 6 eV $\leq h\nu \leq$ 8 eV region, its sharpness (FWHM on the order of 100 meV), and its lack of dispersion ($\langle E_i \rangle$ = -0.25 eV). It is ascribed to a surface state in the $\Sigma_{3u} - \Sigma_{3\ell}$ spin-polarization gap near E_F, and represents a major result of this work: an occupied $\bar{\Gamma}$ surface state is found to lie in a band gap induced by antiferromagnetism in chromium, implying that magnetic order exists on the Cr(110) surface.[75] In contrast to the situation for the dispersionless peaks in Cr(100) spectra, there is good evidence that feature A is a surface state. It satisfies at least four of the seven criteria discussed in Section D.2: (1) The intensity of feature A was found to be sensitive to surface contamination--exposure of the clean Cr(110) surface to 0.5 L (1 L = 10^{-6} torr sec) of O_2 induced an intensity attenuation relative to background of about 30 percent at $h\nu$ = 7 eV. (2) The lack of dispersion with $\vec{k}_\perp$ insures that feature A fulfills the two-dimensionality requirement. (3) The projection of the bulk band structure is a key condition. For Cr(100) dispersionless features, the lack of additional band structure information rendered this issue ambiguous. However, the strong dispersion characteristics of feature B in Cr(110) spectra,

which can be identified with the bound Σ_3 band, give a strong indication that feature A lies in a bulk, Σ_3 band gap. The shape of the empirical Σ_3 band confirms the presence of a spin-polarization gap near E_F (see Section C.1)--feature A obviously lies in this gap. An additional contrast is that ARNP spectra of the Mo(110) (Ref. 51) and W(110) (Ref. 53) faces both contain dispersionless peaks near E_F. However, these were attributed to the ODDOS because of their insensitivity to surface contamination. The lack of a dispersive feature [like peak B in Cr(110) spectra] near the ODDOS peaks on these faces is also striking. (6) Feature A is strikingly sharper than the other features in the Cr(110) spectra.

It was not possible to investigate the fourth criterion, polarization dependence (or θ_A dependence), because the orientation of the electron analyzer was fixed relative to the incident photon beam. However, the geometry shown in Fig. 2(b), with $\theta_A = 27.3^\circ$, would tend to enhance surface sensitivity because of the large component of $\vec{A}$ normal to the surface. This might be misleading, because refraction of the photon beam at the surface can have a large effect on the time-averaged orientation of $\vec{A}$ (Refs. 108 and 109). (In Chapter II, this was discussed in relation to bulk polarization selection rules.) One simple polarization test was performed at $h\nu = 7$ eV. The crystal was rotated by $\pm 6^\circ$ about the photoelectron emission direction $\vec{p}$; i.e., θ_p (angle between $\vec{n}$ and $\vec{p}$) was changed from 0° to 6° in either $\phi_p = 0^\circ$ or 180° azimuths, concomitant with changes in θ_A by $\mp 6^\circ$ to 21.3° and 33.3°, respectively. Rotation of the sample in the $\phi_p = 0^\circ$ azimuth

(component of p-polarization of $\vec{A}$ is higher) produced no major change in the intensity of feature A, but rotation in the $\phi_p = 180°$ azimuth (lower p-polarization component) produced a nearly complete attenuation of its intensity, consistent with expectations for a surface state based on criterion 4. This was not the ideal test, however, because θ_A and θ_p could not be varied independently. Therefore, it is not conclusive that condition 4 holds for Cr(110) feature A. Criterion 5, surface band dispersion, was not studied in a systematic way because of the fixed analyzer orientation, but the $\pm 6°$ variation of θ_p along with θ_A produced no change in the energy position of feature A.

Two final points about feature A can be made. The first deals with the $h\nu$ dependence of its intensity. A is observed in the $h\nu = 6$ to 8 eV region, absent from 9 to 12 eV, then it grows back into the spectrum with increasing intensity from 13 to 22 eV, above which it is dominated and obscured by the Σ_3 direct-transition peak. Thus, the relative intensity of feature A is minimal in the photon energy region corresponding to excitation of Σ_3 (feature B) at the M point, where the separation between A and B is largest, increasing as the A - B separation decreases until it is impossible to follow as A becomes obscured by feature B for $h\nu > 23$ eV. This intensity behavior is qualitatively similar to that observed for Cu(111) surface states and predicted for surface states in general by Louie, et al.[110]--the intensity ratio of the surface state to the bulk state from which it is derived, I_s/I_b, is periodic in $\vec{k}_\perp$ (thus, $h\nu$) and should be maximized at $\vec{k}_\perp$ ($h\nu$) corresponding to the smallest energy separation between the bulk and surface

features. Obviously, this lends further credence to the identification of feature A as a surface state. The second point concerns an additional important test of surface versus bulk photoemission for feature A. The existence of a surface state near E_F on Cr(110) is predicated on the presence of the spin-polarization gap. Feature A should be totally attenuated at a temperature high enough to induce the AF → P transition at the surface as well as in the bulk.

Features B and C in Cr(110) spectra are probably derived from direct transitions along ΓΣM. They are both seen at $h\nu = 7$ eV and $E_i = -1.39$ eV. Above this photon energy, C disperses upward toward E_F until it is apparently lost in the E_F-onset region for 9 eV $\leq h\nu \leq$ 11 eV, appearing again at $h\nu = 12$ eV ($E_i = -0.49$ eV) as a weak feature. Its relative intensity grows as it disperses downward until it crosses feature B just above $h\nu = 17$ eV ($E_i = -1.20$ eV). Feature B disperses downward (to higher binding energy) in the range 7 eV $\leq h\nu \leq$ 12 eV, growing in intensity, and reaching a band minimum at $E_i = -2.14$ eV. Above $h\nu = 12$ eV, feature B disperses upward toward E_F and continues to become more intense. Above $h\nu = 17$ eV, where B and C cross, B becomes a dominant feature and C becomes an intense shoulder on the high-binding-energy side of B. Feature B reaches a band maximum near $h\nu =$ 27 eV with $E_i = -0.53$ eV. Its initial energy at $h\nu = 31$ eV, -0.60 eV, indicates that a probable downward trend would occur at higher photon energies. Feature C reaches a band minimum at $h\nu = 19$ eV ($E_i =$ -1.73 eV), above which it disperses upward toward E_F again. Consideration of the general topology of Kübler's[64] band structure and

polarization selection rules[93] indicates that feature B can be assigned to the Σ_3 band, and C is most likely derived from Σ_{1u} direct transitions. Both empirical bands have the correct mirror symmetry about the M point (see Fig. 12) in the extended-zone scheme.

Feature D is a dispersionless, relatively weak peak and/or shoulder at $\langle E_i \rangle$ = -3.44 eV. As discussed in Section D.1, it can be assigned to the middle maximum in the TDOS ($TDOS_2$). However, the corresponding Cr(100) feature (at $\langle E_i \rangle$ = -3.38 eV) is much more intense relative to the other spectral features. Additionally, the first TDOS maximum ($TDOS_1$) [$\langle E_i \rangle$ = -1.63 eV in Cr(100) spectra] is not observed in Cr(110) spectra.

Apparently, the TDOS does not play a major role in Cr(110) photoemission. Thus, $TDOS_1$ is probably obscured by the Σ_{1u} direct-transition peak. However, the plot in Fig. 12 indicates that the empirical Σ_{1u} band does not appear to disperse upward as it approaches Γ. Although this could be an artifact of peak deconvolution problems for feature C, it could also be caused by interference from an otherwise unobserved $TDOS_1$ feature. Contrary to this, the isolated set of peaks (three filled circles at $\langle E_i \rangle$ = -1.34 eV in Fig. 12) lying very close in energy to the observed flat portion of Σ_{1u} (-1.32 eV), could be an indication (via a large Σ_{1u} ODDOS) that the empirical Σ_{1u} band is indeed flat somewhere between M and Γ. Whichever explanation is correct, it is unlikely that Σ_3 and Σ_{1u} are not degenerate at Γ ($\Gamma_{25'}$). This is based on symmetry considerations, and on the observation of a single feature (A) in the $E(\Gamma_{25'})$ region of

Cr(100) spectra. It would be useful, however, to study Cr(110) at energies $h\nu > 31$ eV so that the energy levels at Γ could be assessed. This would allow a comparison of $E(\Gamma)$ positions to be made between the two crystal faces and hopefully lend greater support to the assignment of the features.

The final four features in the Cr(110) spectra (E, F, G, and H), make up the complex, broad structure centered around the energy of the non-dispersive feature F ($\langle E_i \rangle = -5.25$ eV). Features E and G are dispersive shoulders on the low- and high-binding-energy sides of F, respectively, with onset photon energies of 11 eV (E) and 12 eV (G). Feature E remains a relatively weak shoulder over the entire photon energy range, while feature G increases in intensity with higher $h\nu$, becoming the dominant feature in this structure at $h\nu = 29$ and 31 eV. The shapes of the empirical E and G dispersion relations in Fig. 12 compare well with those of the Σ_{1m} and $\Sigma_{1\ell}$ bands, respectively, in Kübler's[64] calculation. Feature H, a dispersionless shoulder with $\langle E_i \rangle = -6.86$ eV in the range 14 eV $\leq h\nu \leq$ 31 eV, is undoubtedly related to the similar Cr(100) feature (F). Thus, its intensity comes from the $\Sigma_{1\ell}$ ODDOS or Γ_1 DOS near Γ. The identity of feature F can be deduced as follows: If E and G are assumed to be the Σ_{1m} and $\Sigma_{1\ell}$ direct-transition peaks, respectively, then feature F is derived from the DOS near Γ_{12}, M_1, and/or M_3. Association of F with the DOS near Γ_{12} is not consistent with an identical assignment for Cr(100) feature D; the two features differ in initial-state energy by ca. 0.25 eV. More likely, F is derived from the ODDOS of Σ_{1m} and/or $\Sigma_{1\ell}$. But, the

relationship between E (Σ_{1m}) and G ($\Sigma_{1\ell}$) empirical bands suggests that the experimental $E(M_1) - E(M_3)$ splitting may be too large for F to be from both Σ_{1m} and $\Sigma_{1\ell}$ ODDOS. Furthermore, the $E_i(\vec{k})$ curve for F is closer to $\Sigma_{1\ell}$ (G), and the theoretical $\Sigma_{1\ell}$ band is flatter than Σ_{1m} near M (higher ODDOS). Thus, feature F is probably derived from the ODDOS for $\Sigma_{1\ell}$ near M_3.

The problem of surface state versus bulk DOS must again be addressed in the case of photoemission from Cr(110), because the relative intensities of features D and F are moderately sensitive to contamination (0.5 L exposure of O_2). These features suffer from the same ambiguities as do dispersionless Cr(100) peaks. Namely, polarization dependence, existence of bulk band gaps at appropriate initial energies [-3.44 eV (D), -5.25 eV (F)], and surface band dispersion criteria for a surface state are not conclusively satisfied, whereas the assignment of these features to bulk DOS photoemission (either TDOS or ODDOS) fits together neatly with the total assignment of other Cr(110) and Cr(100) features. In the case of feature F, the ambiguity might be removed by inducing the AF → P transition, because, if surface derived, it lies in the $M_1 - M_3$ spin-polarization gap. The same cautions apply to this transition as discussed for Cr(100) (Section D.1): the transition temperature is uncertain, and it most likely modifies bulk-band features in addition to surface states.

4. Development of an Empirical Band Structure Along $X\Delta\Gamma\Sigma M$.

Based on the most reasonable mechanisms for the Cr(100) and Cr(110) spectral features, an empirical Δ and Σ line band structure

can be developed. The assignment of the main features to parts of the bulk band structure makes it possible to deduce energy levels of all important symmetry points from the ARNP data at least approximately (in some cases, accurately). In Tables II and III, the band assignments and symmetry point energy values which can be determined from our data are summarized for Cr(100) and Cr(110) data, respectively. Table IV lists the ARP-determined energy values, along with corresponding theoretical values from the three calculations[63-65] for comparison. Finally, with the knowledge of symmetry point energies and detailed $E_i(\vec{k})$ relations (for some bands), the band structure sketched in Fig. 14 is postulated.

Reference to Fig. 13 is helpful in this discussion. Starting with the Cr(100) data, feature A ($\langle E_i \rangle$ = -0.71 eV) fixes the position of the flat portion of the Δ_5 band and $E(\Gamma_{25'})$. Because the difference $E(X_5) - E(\Gamma_{25'})$ is theoretically small, this is also a reasonable approximation for $E(X_5)$. The $E_i(\vec{k})$ curve minimum for feature B (near X) determines an approximate position for $E(X_{3'})$ (-1.92 eV) because this feature contains either direct-transition or ODDOS intensity from the Δ_{2u} band near X; the flat part of the curve closer to Γ is derived from the uppermost peak in the TDOS (-1.63 eV, see Table I). Likewise, the X point maximum of the feature-C $E_i(\vec{k})$ curve approximately fixes $E(X_2)$ (-3.18 eV) because this region of the curve reflects direct transitions or the ODDOS from $\Delta_{2\ell}$ near X_2, and the non-dispersive portion of the curve ($\langle E_i \rangle$ = -3.38 eV), along with feature D in Cr(110) (-3.44 eV), determines the position of the middle peak in the TDOS

(-3.41 eV, see Table I). Cr(100) feature D has been assigned to $X_{4'}$, Δ_{1u}, and/or Γ_{12} DOS; the latter two are most likely, so the energy of D (-5.03 eV) fixes $E(\Gamma_{12})$ and (based on the theoretical shape of Δ_{1u}) determines an approximate position for $E(X_{4'})$. The direct-transition feature E determines the detailed dispersion relation for $\Delta_{1\ell}$, along with the critical-point energy $E(X_1)$ estimated to be -5.20 eV from the band maximum at X. The intersection of $E_i(\vec{k})$ for feature E with Γ (-6.86 eV), in combination with average energy positions of the lowest non-dispersive features [F for Cr(100) at -7.00 eV, H for Cr(110) at -6.86 eV], determines $E(\Gamma_1)$ (-6.91 eV).

Turning to the remaining bulklike features in Cr(110) spectra, B and C determine the detailed dispersion relations for Σ_3 and Σ_{1u}, respectively. Also, the intersection of the empirical Σ_3 band with M determines $E(M_5)$ (-2.05 eV), the Σ_3 band maximum ($\Sigma_3^{max.}$) is determined (-0.53 eV), and the $E(\Sigma_{1u}^{min.})$ value is found (-1.70 eV). The extrapolation of Σ_{1u} and Σ_3 to Γ is consistent with $E(\Gamma_{25'})$ determined from Cr(100) data. Features E and G determine detailed $E_i(\vec{k})$ curves for Σ_{1m} and $\Sigma_{1\ell}$, respectively. Additionally, the empirical Σ_{1m} curve can be extrapolated to M to locate the $E(M_1)$ critical point energy (-4.82 eV) and toward Γ to show that $E(\Gamma_{12})$ is consistent with the position deduced from Cr(100) data. Feature F ($\langle E_i \rangle$ = -5.25 eV), which is derived from the ODDOS of $\Sigma_{1\ell}$ near M, locates a value of $E(M_3)$ that is consistent with the extrapolation of $\Sigma_{1\ell}$ (feature G) to M.

The curves in Fig. 13 and the comparison of energy values listed in Table IV demonstrate that the agreement between experiment and theory is generally poor with respect to both the detailed shapes of the derived $E_i(\vec{k})$ relations and the critical point eigenvalues. None of the three calculations[63-65] compares particularly well with experiment, but Kübler's[64] agrees best, mainly because it does the best job with the energy splittings listed at the bottom of Table IV. The noteworthy exceptions are $E(\Gamma_{25'})$ [also, $E(X_5)$ and $E(\Delta_5)$], which agrees well with Kübler's[64] bands, and $E(\Gamma_1)$ which is close to its theoretical position in the calculation of Asano and Yamashita.[63] Apart from problems associated with bulk direct-transition model breakdown in the Cr photoemission process, and with possible differences between incommensurate and commensurate band structures (Section D.5), it is clear from these results that current band structure theories do not predict energy band positions of antiferromagnetic chromium quantitatively, but that they are qualitatively close enough to guide the interpretation of experimental data.

5. Assessment of (Dis)agreement Between Experiment and Theory.

The overall empirical band structure agrees quite well with the qualitative aspects of the commensurate AF-Cr band theory results, but as already noted above and displayed in Table IV, there is quantitative disagreement with theory. Specific aspects of disagreement are: (1) The empirical band shapes of Σ_3, Σ_{1u}, Σ_{1m}, $\Sigma_{1\ell}$, and $\Delta_{1\ell}$ deviate from theory. This is readily discernible if each individual empirical

band is shifted to overlap its theoretical counterpart. In this manner, the Σ_{1m} empirical band actually displays the best agreement with theory. (2) The empirical-band energy positions at high-symmetry points in the BZ generally show poor agreement with corresponding theoretical values. As a consequence, the experimental TDOS features do not match (in energy) the theoretical TDOS maxima from any of the calculations. Another result of this is that the observed d-band width, $|E^F(\Gamma_{12})|$, is actually larger than in theory (20 percent larger than the average value of the three calculations[63-65]), in contrast to the Group VIII metals which display (many-electron) band-narrowing effects[13] relative to corresponding one-electron theoretical band structures. (3) The observed SDW-induced band gaps [$E_F - \Sigma_3$ (actually $\Sigma_{3u} - \Sigma_{3\ell}$), $M_1 - M_3$, $X_{3'} - X_2$, and $X_{4'} - X_1$] are all larger than calculated. (4) The observed Δ_{2u} and $\Delta_{2\ell}$ dispersion curves are not properly symmetrical about the X point (whereas $\Delta_{1\ell}$ is quite symmetric), i.e., the experimental Δ_{2u} and $\Delta_{2\ell}$ band extrema do not coincide with the zone boundary [see Fig. 11, the deviation in either case is $(\Delta k^{\langle 100\rangle}/k_{BZ}^{\langle 100\rangle}) \sim 0.05$].

As discussed in Section D.4, the large deviations between experimental and calculated bands imply that modifications in the band theory are needed. Thus, an explanation of observed discrepancies in band shapes, energy positions, and band-gap and d-band widths in terms of real physical phenomena would constitute speculative guesswork. However, one point concerning the larger spin-polarization gaps can be made. The size of these gaps is very sensitive to the form of the effective exchange interaction energy,[54,63,64] because the gap

reflects the energy difference between states with the itinerant electron amplitude more localized on atoms with the net spin in the same direction (lower band) and those with the electron on atoms with opposite spin (upper band). Thus, the exchange interaction depends on the magnetization,[64] $\mu = \mu_0 \cos(\vec{Q}\cdot\vec{r})$. There is theoretical evidence[104] that on the Cr(100) surface, the magnetic moment (μ_0) is much larger than the measured bulk value (0.59 μ_B) which itself is actually rather small in Cr. A larger moment results in larger energy gaps. If both Cr(100) and Cr(110) surfaces have larger magnetic moments, there could be an intermediate region below the surface, probably the region sampled in these ARP experiments, in which the value of μ_0 would decrease to its bulk value.[104] In the commensurate AF band structure calculations, the correct bulk magnetization is either utilized as input or calculated from the results.[63-65] Thus, there are three likely possibilities: (1) the exchange interaction is not correctly incorporated in Cr band structure calculations, (2) both surfaces have larger magnetic moments than the bulk, and (3) the larger surface moment is concomitant with an intermediate layer in which μ_0 varies between surface and bulk values. Evidence for the first possibility is the overall poor agreement between experiment and theory. Evidence for the second one is that the Cr(110) surface state lies ca. 0.25 eV below E_F, whereas bulk band structure calculations give $|E^F(\Sigma_3^{max.})| \leq 0.10$ eV (see Table IV). We have no direct evidence for the third possibility.

The slight shift in extremal Δ_{2u} and $\Delta_{2\ell}$ empirical band positions away from the X point is small enough that it is probably indicative of greater peak position uncertainty for Cr(100) features B and C. In the photon energy region corresponding to this portion of $\vec{k}_\perp$-space (12 eV $\leq h\nu \leq$ 20 eV), these features are complicated by both TDOS and Δ_2 photoemission intensity. The $E_i(\vec{k})$ asymmetry about X gives rise to the scatter of data points (o) for B and C in Fig. 13. Obviously, the final-state band could be further adjusted to account for this, but there is only one other dispersion curve ($\Delta_{1\ell}$) that could be used to judge the effectiveness of such an ad hoc procedure. The effect of changes in either f or V_0^F on the empirical extended-zone-scheme plot (Fig. 11) would be to shift all of the curves in the same direction in k-space; i.e., a decrease in $|V_0^F|$ to bring the Δ_2 extrema into coincidence with the X point would have the effect of shifting the maximum of $\Delta_{1\ell}$ away from X (to lower $|\vec{k}_f|$). The final-state band utilized for Cr(100) (f = 2.53, V_0^F = -3.95 eV) corresponds to the following procedure: the set of ($h\nu$, E_i) values for the feature B, C, and E extrema in the structure plots (Fig. 5) are required to satisfy the condition

$$V_0^F = (h\nu + E_i) - (\hbar^2/2fm_e)\ |\vec{k}_f(ZB)|^2 \quad , \tag{2}$$

where f = 2.53 [from fit of Eq. (1) to theory[92]] and $|\vec{k}_f(ZB)|$ is at the zone boundary [1.50(2π/a)]. In principle, the term ($h\nu$ + E_i) in Eq. (2) is identical for each band at the zone boundary. Unfortunately,

this is not the case, here. Therefore, the adopted value of V_0^F corresponds to a weighted average of the three numbers calculated with Eq. (2), with a larger weighting factor for feature E than for B or C. Obviously, the weighting factors reflect much greater confidence in the detailed shape and extremal position of the $E_i(\vec{k})$ curve for feature E. If no weighting factors are used, $\langle V_0^F \rangle = -3.31$ eV, corresponding to a 16 percent change. The key point is that it is useful to have information about the empirical dispersion relations to derive self-consistently a reasonable final-state band structure. Unfortunately, with the Cr(100) data, only one $E_i(\vec{k})$ curve is effective in this regard.

Several observations should be made concerning the validity of the direct-transition model in Cr: (1) Direct transitions from all symmetry-allowed Σ-line bands and from one of the two dispersive, allowed Δ-line valence bands are observed. (2) No dispersive features are found which arise from secondary-cone or band-gap photoemission; i.e., the single plane-wavelike-final-state approximation is successful. (3) The bulk valence-band features are much broader than those of the noble metals.[1-9,22,26-29] (4) In Cr(100), observed normal emission intensity from Δ_2 initial states is symmetry forbidden.[93] (5) There is a large propensity for DOS photoemission from Cr, especially Cr(100) (this will be dealt with in Section D.6).

Concerning Δ_2 photoemission from Cr(100), most of the intensity in features B and C comes from the TDOS--Δ_2 is probably only a weak component that is observed at low $h\nu$, where the TDOS intensity is relatively weak. Actually, symmetry-forbidden bands are generally

observed as weak features even in noble metals.[1] Additionally, the only band for which symmetry-forbidden photoemission is not observed in Cr(100) is $\Delta_{2'}$; it is probably obscured by the strong Δ_5 photoemission peak. Typical causes of selection-rule breakdown include finite angular acceptance ($\pm$ 2.5°), incomplete polarization of the radiation ($\leq$ 3 percent non-polarized), and finite uncertainty in angular alignment of the crystal ($\pm$ 1° in θ and ϕ).[1] Two additional points are made: (1) the effect of an incommensurate SDW on symmetry selection rules (those discussed in this work are based on a commensurate structure) is not known, and (2) surface reconstruction can alter the symmetry selection of bulk initial states;[111] but, in the case of Cr(100)-c(2x2), the surface still has Δ symmetry, rendering Δ_2 dipole-forbidden unless the reconstruction is incommensurate with the bulk atomic structure. There is no additional experimental evidence that the reconstruction of Cr(100) is incommensurate, so this issue is not discussed further.

The peak broadening effect observed in Cr ARP spectra, especially for tightly bound features, is reminiscent of hole-lifetime broadening (Section B.4 in Chapter I) in the photoemission spectra of Group VIII metals.[9,10,12,13,16-21,23,24,30-32] In open d-shell metals, a concomitant larger d-electron mobility[112] enables these electrons to contribute more effectively to screening and Auger decay of photoholes.[42] Lifetime broadening is especially severe for states lying deep in the valence band (cf. structures near E_i = -5 eV in Figs. 3 and 4; see, also, Chapter I). As anticipated earlier (Section A), these effects

are important in chromium. The most important point, however, is that while lifetime-broadening effects compete with attempts to map $E_i(\vec{k})$ curves, they do not induce direct-transition model breakdown; it is still possible to measure an empirical band structure. Until more reliable band-structure calculations are performed, it remains to be seen whether open-shell effects contribute to discrepancies between experimental and theoretical bands in Cr as they do in Group VIII metals.[13]

The ARNP results <u>implicitly</u> imply that the commensurate antiferromagnetic band structure is a reasonably good model with which to describe the electronic properties of AF-Cr. However, there are three specific features in the empirical band structure which <u>directly</u> confirm that AF behavior (i.e., AF order) in the <u>bulk</u> is observed with ARP: (1) Nearly symmetrical dispersion relations about the X point for Δ_{2u}, $\Delta_{2\ell}$, and $\Delta_{1\ell}$ show that the irreducible portion of the [100] line in k-space is $\Gamma\Delta X$ (as in the SC structure), not $\Gamma\Delta(X)\Delta H$ (as in BCC). (2) The observation of direct transitions and detailed $E_i(\vec{k})$ curves obtained for several SDW-induced bands (Σ_{1m}, $\Delta_{2\ell}$ near X, and Σ_3 between $\Sigma_3^{max.}$ and M) are direct indications that the SDW state exists. (3) Critical point energy eigenvalues (Table IV) demonstrate that the spin-polarization band gaps [$X_{3'} - X_2$, $E_F - \Sigma_3$ (actually $\Sigma_{3u} - \Sigma_{3\ell}$), and $M_1 - M_3$] are indeed found in the empirical band structure.

Additionally, the Cr(110) surface state implies that the Cr(110) <u>surface</u> displays magnetic order.[75,78-81] But, because no such state

was observed in the Cr(100) spectra, magnetic order is not directly confirmed for the Cr(100) surface. With the absence of surface-state features in spin-polarized band gaps, surface magnetic order cannot even be inferred from the bulk band structure results, because a nonmagnetic surface would probably perturb only the final state (see Section D.6).

Finally, note the there are several empirical band structure features which do not confirm AF order in Cr: (1) Symmetrical dispersion relations [from Cr(110) data] about the M point do not indicate that the symmetry of the zone is simple cubic, because the P → AF transition does not introduce any additional high symmetry points along [110] (see Fig. 7). (2) Features derived from the TDOS ($TDOS_1$ and $TDOS_2$ in the spectra) do not imply AF behavior because the AF- and P-Cr structures have similar TDOS curves.[97] (3) Δ-line ODDOS structures do not suggest AF order (all AF and P states lie along [100]), and Σ-line ODDOS peaks are not indicative of AF order unless they are derived from SDW-induced bands (none observed).

6. Propensity for DOS Photoemission.

Possible causes for the abundance of DOS features in Cr will be discussed in this section. It is important to bring special attention to this issue, because the propensity for dispersionless photoemission is much larger in Cr ARP spectra than in Group VIII or IB metals. Possible DOS mechanisms can be divided into two main categories: (A) those which address the problem of much higher DOS intensity in

Cr(100) spectra relative to Cr(110), and (B) those which address the general problem of enhanced DOS photoemission in Cr. These are discussed separately below.

(A) Cr(100) versus Cr(110). In the spirit of the three-step model of photoemission[113]--photoexcitation, electron transport to the surface, and transmission across the solid-vacuum interface--the problem of higher DOS photoemission intensity in Cr(100) ARP spectra can be viewed mechanistically as arising from any of the three steps. Previous work on Group VIII and IB metals tends to suggest that the first two steps, which are bulk steps, are not important contributors to the differential DOS propensity mechanism that is sought after here. In other words, other than variations in the ODDOS, different crystallographic directions of electron excitation and transport probably do not yield different DOS intensities.[114] It will be shown that the difference in DOS propensity between Cr(100) and Cr(110) can be viewed as a final-state surface scattering effect which arises partly from the lower atomic density in the surface plane of Cr(100) relative to Cr(110). Additionally, greater effects may possibly result from the reconstruction of the Cr(100) surface, which not only can introduce a lowering of surface atomic density (depending on the reconstructed-surface geometry) but may also introduce a new set of (smaller) surface reciprocal lattice vectors that can enhance surface umklapp scattering. There is already other experimental evidence that surface umklapp scattering effects are important for reconstructed surfaces.[24,115,116]

It has previously been noted that in ARNP, the FCC metals Ag, Pt, and Au suffer from DOS photoemission from the open faces [(100) and (110)] but not from the closest-packed (111) face.[11] The Pt(100) face, which was a (5x1) reconstructed surface, was by far the most severe case (see Chapter III). In the BCC structure, the (110) face is the closest-packed; BCC(100) is quite open relative to FCC(100). Taking this one step further, Cr(100)-c(2x2) could have a surface atomic structure that is even less dense. Throughout this discussion, this will be assumed to be the case. In the previous report,[11] there was no explanation for the crystal-face dependence of DOS propensity for FCC metals, but there are more recent indications that this type of problem is a surface rather than a bulk effect (i.e., that surface atomic density is more important than density along a specific bulk crystallographic axis): reconstruction of Au(100)-(1x1) to -(5x20) enhances DOS photoemission intensity.[8] Three possible DOS enhancement mechanisms for Cr(100)-c(2x2) are invoked: (1) more surface umklapp processes occur because of the reconstruction and concomitant finer reciprocal-lattice mesh, (2) a lower surface Debye-Waller factor accompanies the reconstruction [or just the open (100) face], and (3) enhanced umklapp scattering occurs from a Cr surface without AF order. These mechanisms will be considered below.

In the following discussion, the effect of final-state lifetime broadening (see Chapter II) will be ignored. It should be recalled that the bulk photoexcitation process creates photoelectrons propagating in many different directions inside the crystal.

Therefore, the view taken here is to consider the general photoexcitation event, somewhere in the bulk BZ. Consider a direct-interband transition from an initial state with crystal momentum vector $\vec{k}_i$ to a final state with $\vec{k}_f = \vec{k}_i - \vec{G}_{hkl}$ in the bulk [perhaps deep (> 10 Å) in the bulk]. In general, $\vec{k}_f$ is in the second or third zone while $\vec{k}_i$ is always in the first BZ. There can be several different interband transition channels (each with a different $\vec{G}$) at a given E_i, depending on the photon energy and the orientation of $\vec{A}$ (θ_A); the intersection of initial- and final-state band structures (see Chapter I) is an important prerequisite. Now, in all the discussion of photoelectron band structure (see Section C.2) a single-plane-wavelike-final-state band has been assumed, described by a wave function of the form

$$\psi_{\vec{k}_f}(\vec{r}) \sim \exp(i\vec{k}_f \cdot \vec{r}) \quad . \tag{3}$$

However, the periodicity of the crystal potential

$$V(\vec{r}) = \sum_{\vec{G}} V_{\vec{G}} \exp(i\vec{G} \cdot \vec{r}) \tag{4}$$

requires that the final-state wave function be a Bloch function,[60] i.e.,

$$\psi_{\vec{k}_f}(\vec{r}) = \exp(i\vec{k}_f \cdot \vec{r}) \sum_{\vec{G}} u_{\vec{k}_f, \vec{G}} \exp(i\vec{G} \cdot \vec{r}) \quad . \tag{5}$$

For a particular emission direction, all of the extra terms in Eq. (5) (other than $|\vec{G}| = 0$) can usually be ignored for direct-transition peak structures, because $u_{\vec{k}_f,\vec{G}}$ is proportional to $V_{\vec{G}}$ (Ref. 60) and Eq. (4) is generally a quickly converging series for a d-band metal.[4,117] However, the angle-integrated total intensity from a particular initial state can be much larger than the single-peak-direct-transition intensity if all of the $u_{\vec{k}_f,\vec{G}}$ terms are accounted for. Therefore, the real situation does correspond to the wave function in Eq. (5). The surface acts as a filter, selecting plane-wave components from Eq. (5) for transmission across the metal-vacuum interface (the total wave function does not correspond to an allowed eigenstate of the vacuum) via the matching condition[52,60]

$$\vec{p}_{\parallel} = \hbar(\vec{k}_{f_{\parallel}} + \vec{G}_{\parallel}) \tag{6}$$

where $\vec{p}_{\parallel}$ is the surface component of the photoelectron momentum vector in the vacuum, and Eq. (6) is subject to total energy conservation.[4] Thus, each term in Eq. (5) can result in a photoemitted electron. However, the $\vec{k}$ vector of a Bloch wave $\psi_{\vec{k}}(\vec{r})$ is only determined modulo a $\vec{G}$ vector; any $\vec{G}_{\parallel}$ can add in Eq. (6). Surface umklapp scattering corresponds to a $\vec{G}_{\parallel}$ in Eq. (6) that changes the photoelectron propagation direction (before refraction[4]). Considering the photoemission process on a gross scale, there are many electrons propagating in many directions beside the normal ($\vec{k}_{\perp}$). At the surface, the wave-matching condition, Eq. (6), gives rise to a redistribution of propagation

directions. There is a constraint on $\vec{G}_{\parallel}$ similar to the bulk process [Eq. (5)]; i.e., the propensity for a surface umklapp scattering event with $\vec{G}_{\parallel}$ depends (amongst other things) on the magnitude of $V_{\vec{G}_{\parallel}}$. Therefore, umklapp scattering can generally be ignored for the same reason that most terms in Eq. (5) are small. However, if the surface is reconstructed, there is a new mesh of small $\vec{G}_{\parallel}$ vectors ($\vec{G}'_{\parallel}$, with concomitant larger values of $V_{\vec{G}_{\parallel}}$), having no bulk $\vec{G}$ analogue, that can induce umklapp scattering with high cross section.[52,115] The redistribution of electron emission directions via $\vec{G}'_{\parallel}$ can be severe for a reconstructed surface. Now, it is clear how a higher propensity for DOS photoemission can occur via the first mechanism. Within the angle and energy windows of the detector, the redistribution process can imitate quite naturally the apparent $\vec{k}$-conservation-breakdown process that normally gives rise to DOS photoemission[96] by "smearing" the angular information ($\vec{k}_f$) that accompanies a direct transition. It is then quite likely that ARP-EDC peaks would arise at energies (E_i) corresponding to regions of high DOS in k-space. These energies are where angle-averaged intensity would naturally build up.

The second mechanism, similar to the LEED[118] and x-ray diffraction[119] temperature-dependent-intensity problem, is related to DOS photoemission much the same way that indirect (phonon-assisted) transitions occur in the initial (bulk) photoexcitation process.[120,121] In any of these measurements, the elastically scattered intensity (in ARP, "elastic" refers to $\vec{k}$-conserving direct transitions) is governed by the Debye-Waller factor[118,119]

$$W(T) = \exp\left[-\langle(\Delta\vec{k}\cdot\Delta\vec{r})^2\rangle_T\right] \quad , \tag{7}$$

where $\Delta\vec{r}$ is the displacement of atoms from their equilibrium positions, $\Delta\vec{k}$ is the crystal momentum wave-vector change, and $\langle\cdots\rangle_T$ refers to a thermal average at temperature T. For a bulk direct transition, $\Delta\vec{k} = \vec{k}_f - \vec{k}_i = \vec{G}_{hkl}$. Surface umklapp scattering, as it has been described here [Eq. (6)], is an elastic process which should be subject to the same thermal diffuse scattering mechanism as bulk photoexcitation. This is evidenced by the thermal behavior of LEED beams.[118] In a time-reversed sense, LEED beams are similar to surface umklapp scattering of photoelectrons.[52] In the photoexcitation event, thermal disorder gives rise to DOS emission because phonon assistance implies that a larger sampling of the first BZ occurs (see Chapter I), concomitant with a buildup of intensity at energies corresponding to high initial DOS.[120,121] It has been shown experimentally[121,122] and theoretically[120] that both T (in the form of increased Δr) and $h\nu$ (via larger Δk) give rise to enhanced thermal disorder in photoemission. The conjecture here is that reconstruction, by leading to an effectively larger Δr, can introduce thermal diffusivity to the surface umklapp scattering process, resulting in decreased elastic (direct-transition) intensity and increased DOS intensity. The surface analogue of momentum transfer in the bulk ($\vec{G}_{hkl}$) is the surface $\vec{G}_{\parallel}$ or $\vec{G}'_{\parallel}$ vector which also gives rise to thermal diffuse scattering in LEED.[118] It is quite reasonable to assume that a surface reconstruction, which "opens up" the surface

lattice, increases Δr. In the Debye model, this would come from the Debye temperature, θ_D. Assuming that the lattice vibrations are isotropic, the Debye model gives for $\langle \Delta r^2 \rangle$ and θ_D in the high-temperature limit:[118]

$$\langle \Delta r^2 \rangle = 3T\hbar^2/m_a k_B \theta_D^2 \quad ; \quad \theta_D = \hbar\omega_D/k_B \quad . \tag{8}$$

In Eqs. (8), m_a is the atomic mass, k_B is Boltzmann's constant, and ω_D is the characteristic Debye frequency. Depending on the geometry of the surface atoms in the reconstructed phase, ω_D could be expected to decrease with increasing interatomic distance. A surface-phase-dependent and temperature-dependent LEED intensity analysis of diffracted beams might be a useful probe of the magnitude of this effect;[123] unfortunately, it would appear that none have been performed to date. Another implication of this mechanism is that DOS intensity can also be enhanced for BCC(100) relative to BCC(110) simply by virtue of the more open (100) face. This can be demonstrated with LEED intensity data by extracting effective surface Debye temperatures.[124] Tabor, et al.[125] reported a ratio $\theta_{Ds}^{(100)}/\theta_{Db}^{(100)} = 0.40$ for a slightly contaminated and unreconstructed Cr(100) surface, where $\theta_{Ds}^{(100)}$ and $\theta_{Db}^{(100)}$ are effective surface and bulk Debye temperatures, respectively. Also, Kaplan and Somorjai[126] reported $\theta_{Ds}^{(110)}/\theta_{Db}^{(110)} = 0.56$ for Cr(110). Under the assumption that the two sets of data can be correlated, they give $\theta_{Ds}^{(110)}/\theta_{Ds}^{(100)} = 1.40$, reflecting a larger $\langle \Delta r^2 \rangle$ for Cr(100)

surface atoms. This thermal mechanism (2), combined with the effects of Cr(100) reconstruction (mechanism 1), could account for a large portion of the higher propensity for DOS photoemission from Cr(100).

Several additional points concerning higher Cr(100) DOS propensity can be made. The third mechanism, magnetic disorder at the surface, implies the existence of a paramagnetic SBZ. There are two reasons for considering this possibility. First, these studies have not shown that the Cr(100)-c(2x2) surface is magnetic. Secondly, the DOS mechanism would be similar to the surface umklapp process discussed above, because angular smearing would result from a surface reciprocal lattice mesh different from the bulk. However, the possibility that this mechanism contributes to DOS photoemission can be rejected because of the experimental evidence that the Cr(100)-c(2x2) surface is magnetic,[106] and because the paramagnetic reciprocal unit cell is larger than that of the AF structure. Finally, one additional mechanism that has not been discussed here will be mentioned anyway: the existence of an "open" surface on Cr(100), especially the reconstructed surface, might somehow influence DOS photoemission via decreased overlap of valence-shell atomic wave functions near the surface, concomitant with a smearing of $\vec{k}$ (angular) information.

(B) Chromium in general. The general problem of higher DOS propensity in Cr is empirically similar to that found in Mo (Ref. 51) and W (Ref. 53) ARP spectra, and can probably be directed toward the first two steps in the three step model--photoexcitation and electron transport. Several conceivable mechanisms can be isolated. Among

them are: (1) problems caused by the nature of the open shell, (2) a thermal (i.e., enhanced phonon assistance) effect, (3) severe final-state momentum broadening, and (4) an incommensurate antiferromagnetism effect. Each will be briefly considered below.

The first two mechanisms are probably not important in Cr. Considering that the observed Cr d-band width is larger than in theory, and that Cr should have the largest width amongst the 3d-band metals,[127] it is difficult to conceive that Cr is subject to any DOS mechanism that would be prevalent in narrow-band metals. It cannot be ruled out, however, that a much shorter hole lifetime in Cr gives rise to effective momentum broadening (as discussed in Chapter I), producing a breakdown of the $\vec{k}_\perp$ selection rule.[128] It has already been demonstrated (Section D.5) that hole-lifetime effects are important in Cr because of the open d-electron shell. The possibility that phonon-assisted transitions are important in Cr can be rejected after comparison of $\langle \Delta r^2 \rangle_{300K}$ for Cr to the other 3d metals:[129] Cr has, by far, the lowest value on account of its large Debye temperature (630K). In fact, a comparison with Cu gives $[\langle \Delta r^2 \rangle_{Cu} / \langle \Delta r^2 \rangle_{Cr}]_{300K} = 2.6$, and DOS photoemission from Cu in the UPS region is negligible.[22,26]

Final-state momentum broadening effects are induced by the finite photoelectron lifetime (τ_e) (Ref. 130). It has already been discussed (Chapter II) that photoelectron lifetime broadening contributes to the validity of the quasi-free-electron-final-state approximation utilized in ARNP band structure studies. One of the most direct experimental probes of final-state lifetime broadening is the energy-dependent

photoelectron escape depth, $\lambda_e(E)$ ($\lambda_e \propto \tau_e$) (Ref. 130). The empirical effect of momentum broadening is to relax the $\vec{k}_\perp$-conservation requirement by spatially confining the electron to a region [governed by $\lambda_e(E)$] inside the crystal adjacent to the surface.[52,96,130] In the worst case, ARP spectra would reflect the ODDOS along $\vec{k}_\perp$. However, Pendry[130] has pointed out that τ_e varies remarkably little from one material to another (in contrast to hole lifetimes, τ_h, which vary widely), and measured $\lambda_e(E)$ curves are also quite similar for those materials studied (hence, the term "universal curve" is used to describe their general shape). Therefore, in the absence of detailed data on $\lambda_e(E)$ in Cr, it is conjectured that this effect is intrinsically no more important in Cr than in other metals. Two contradictory facts concerning this are: (1) the AF BZ is half the size of the P BZ, thus any momentum broadening effect in Cr would be more important for the AF structure; and (2) the propensity for DOS photoemission in Cr is consistent with that observed for Mo (Ref. 51) and W (Ref. 53).

The fourth mechanism, incommensurate antiferromagnetism, might be an important initial-state broadening effect leading to DOS photoemission. The commensurate AF model (Q = 1) has been shown to work quite well in explaining the direct-transition process in Cr, but the true electronic structure is incommensurate (Q = 0.95) with the crystal lattice. If this is viewed as a small perturbation of the commensurate structure, with $\Delta k^{\langle 100\rangle}/k_{BZ}^{\langle 100\rangle} = 0.05$, then the effect is small. If the correct unit cell (21 lattice spacings on a side) and BZ are constructed for the incommensurate case, then the effect is

large, because within the energy and angular window of the electron detector, the details of the many dispersion relations would certainly be completely smeared together. The fact that dispersion is observed for some bands suggests that both views are partially correct. Consideration of the possibility that μ_0 is not a constant within the photoemission sampling region near the surface (see Section D.5) is suggestive of an additional, related initial-state broadening effect. Overall, the effects of the incommensurate structure on photoemission are not well enough understood to clarify the fourth mechanism quantitatively. Based on this discussion, however, the conclusion would be that incommensurate antiferromagnetism contributes in some way to the general trend toward DOS photoemission in Cr. It is again stressed that temperature dependence studies of Cr valence-band spectra would be extremely valuable in assessing these and other antiferromagnetic effects.

E. Summary and Conclusions

Angle-resolved normal photoemission studies of antiferromagnetic Cr(100)-c(2x2) and Cr(110)-p(1x1) have been presented. In these studies, variable-energy synchrotron radiation in the range $6\ \text{eV} \leq h\nu \leq 32\ \text{eV}$ was utilized to probe the detailed valence-band structure of these faces at 293K. The resulting peak structure plots of observed features indicated that some features were derived from $\vec{k}$-conserving direct transitions while others were dispersionless, the latter being derived either from the bulk density of states or from

surface states. Comparison of the empirical $E_i(\vec{k})$ curves with the results of commensurate antiferromagnetic band theoretical calculations[63-65] shows qualitative agreement but quantitative disagreement between experiment and theory. In consonance with previous work,[1-12] a single-quasi-free-electron-final-state dispersion relation for the final-state band structure was used successfully, even at energies corresponding to band gaps in the one-electron conduction band structure. The comparison between experiment and theory along the Δ and Σ lines indicates that the dispersive features are all derived from direct transitions along $\vec{k}_\perp$ while the dispersionless features can all be assigned to the bulk ODDOS or TDOS (although, in several cases, the distinction between bulk DOS and surface state is somewhat ambiguous), except for the peak near E_F in Cr(110) spectra. The latter peak is a $\bar{\Gamma}$ surface state lying in the spin-density-wave-induced Σ_3 band gap near E_F along [110]. From the assignment of spectral features to parts of the antiferromagnetic band structure, a complete empirical band structure along X$\Delta\Gamma\Sigma$M was derived. It was suggested that the resulting larger spin-polarization band gaps are either indicative of a larger magnetic moment near the surface or of problems associated with the incorporation of the exchange interaction in the antiferromagnetic band theory. Furthermore, the broadening of peak structures in the spectra, reminiscent of broadening in photoemission spectra of Group VIII metals, is probably induced by many-body effects.[42] Finally, the rather large propensity for dispersionless DOS photoemission in chromium was discussed mainly in terms of final-state

scattering at the surface, which induces the observed larger propensity in Cr(100) spectra relative to Cr(110). Although the general trend toward enhanced dispersionless photoemission in chromium relative to Group VIII and IB metals may have origins similar to the molybdenum[51] and tungsten[53] cases, especially with regard to finite-lifetime-induced momentum broadening, it was indicated that the problem might be derived in part from the incommensurate spin-density wave but is not well understood.

The main results of this work are summarized: (1) It was mentioned at the outset of this chapter that a major reason for studying chromium was to test the direct-transition model (with its characteristics concerning the photoelectron band structure) in a metal that is far removed from Group IB in the periodic chart. The main result is that this model works quite well in chromium, considering the complications that are present (antiferromagnetism, DOS photoemission, and peak broadening). (2) Sufficient information is contained in the spectra and $E_i(\vec{k})$ curves for Cr(100) and Cr(110) to derive a detailed empirical band structure along $X\Delta\Gamma\Sigma M$. This is the first determination of a detailed electronic structure diagram for chromium. (3) The antiferromagnetic state and its spin-density wave are <u>directly</u> evidenced in the spectra and $E_i(\vec{k})$ curves for both Cr(100) and Cr(110). (4) An antiferromagnetic-band-gap surface state is observed on Cr(110), indicating that the (110) surface is magnetically ordered. (5) The surface-atomic-density dependence of the magnitude of DOS photoemission can be understood in terms of final-state

scattering effects at the surface. (6) Although the general qualitative agreement between theory and experiment suggests that the commensurate antiferromagnetic model is a good approximation to the real structure, the quantitative disagreement--especially at high symmetry points--indicates that the band calculations for chromium are not accurate.

The results of this work are suggestive of a variety of further experiments. Most importantly, the effect of the AF → P transition on the Cr band structure should be investigated. Furthermore, additional experimental and theoretical studies of the Cr(110) surface would hopefully provide further evidence that the surface is magnetic. LEED has shown the capability of probing antiferromagnetic surface structure, for example.[124] The problem of surface state versus bulk DOS for Cr(100) should be examined in more detail, presumably with off-normal angular distribution ARP studies. The capability of ARP to probe antiferromagnetism has implications for electronic structure studies of all antiferromagnetic materials. Finally, the general correlation between DOS photoemission and surface structure opens up the possibility of many interesting structural- and temperature-dependence studies with ARP and LEED.

REFERENCES

* This chapter is based on experiments performed in collaboration with G. Thornton, C. C. Parks, K. A. Mills, and D. A. Shirley; to be submitted to Phys. Rev. B for publication (LBL-13695). Note that in this chapter we have replaced $E_n(\vec{k}_i)$, the expression utilized in Chapter I for valence-band dispersion relations, with $E_i(\vec{k}_i)$. The two expressions have the same meaning.

1. R. F. Davis, R. S. Williams, S. D. Kevan, P. S. Wehner, and D. A. Shirley, submitted to Phys. Rev. B (LBL-8511, see Chapter II of this work).
2. J. Stöhr, P. S. Wehner, R. S. Williams, G. Apai, and D. A. Shirley, Phys. Rev. B 17, 587 (1978).
3. D. A. Shirley, J. Stöhr, P. S. Wehner, R. S. Williams, and G. Apai, Phys. Scripta 16, 398 (1977), and references therein.
4. R. S. Williams, P. S. Wehner, J. Stöhr, and D. A. Shirley, Surf. Sci. 75, 215 (1978).
5. P. S. Wehner, R. S. Williams, S. D. Kevan, D. Denley, and D. A. Shirley, Phys. Rev. B 19, 6164 (1979), and references therein.
6. K. A. Mills, M. G. Mason, R. F. Davis, R. Watson, G. Thornton, J. G. Tobin, Z. Hussain, E. Umbach, and D. A. Shirley, to be published.
7. K. A. Mills, Ph.D. thesis, University of California, Berkeley, 1979 (LBL-9429, unpublished).
8. R. F. Davis, M. G. Mason, Z. Hussain, J. G. Tobin, L. E. Klebanoff, and D. A. Shirley, to be published.

9. K. A. Mills, R. F. Davis, S. D. Kevan, G. Thornton, and D. A. Shirley, Phys. Rev. B 22, 581 (1980).

10. G. Thornton, R. F. Davis, K. A. Mills, and D. A. Shirley, Solid State Commun. 34, 87 (1980) (see Chapter III of this work).

11. R. F. Davis, K. A. Mills, G. Thornton, S. D. Kevan, and D. A. Shirley, VI International Conference on Vacuum Ultraviolet Radiation Physics (Charlottesville VA, 1980), Vol. I, pp. 1-3.

12. S. D. Kevan, P. S. Wehner, and D. A. Shirley, Solid State Commun. 28, 517 (1978).

13. F. J. Himpsel, P. Heimann, and D. E. Eastman, J. Appl. Phys. 52, 1658 (1981), and references therein.

14. D. E. Eastman and F. J. Himpsel, Inst. Phys. Conf. Ser. No. 55 (Chapter 3), 115 (1981), and references therein.

15. F. J. Himpsel, Appl. Opt. 19, 3964 (1980), and references therein.

16. P. Heimann, F. J. Himpsel, and D. E. Eastman, Solid State Commun. 39, 219 (1981).

17. F. J. Himpsel, K. Christmann, P. Heimann, and D. E. Eastman, Phys. Rev. B 23, 2548 (1981).

18. F. J. Himpsel and D. E. Eastman, Phys. Rev. B 21, 3207 (1980).

19. D. E. Eastman, F. J. Himpsel, and J. A. Knapp, Phys. Rev. Lett. 44, 95 (1980).

20. F. J. Himpsel, J. A. Knapp, and D. E. Eastman, Phys. Rev. B 19, 2919 (1979).

21. D. E. Eastman, F. J. Himpsel, and J. A. Knapp, Phys. Rev. Lett. 40, 1514 (1978).

22. J. A. Knapp, F. J. Himpsel, and D. E. Eastman, Phys. Rev. B 19, 4952 (1979).

23. F. J. Himpsel and D. E. Eastman, Phys. Rev. B 18, 5236 (1978).

24. J. F. van der Veen, F. J. Himpsel, and D. E. Eastman, Phys. Rev. B 22, 4226 (1980).

25. Y. Pétroff and P. Thiry, Appl. Opt. 19, 3957 (1980), and references therein.

26. P. Thiry, D. Chandesris, J. Lecante, C. Guillot, R. Pinchaux, and Y. Pétroff, Phys. Rev. Lett. 43, 82 (1979).

27. E. Dietz and U. Gerhardt, J. Phys. F 8, 2213 (1978); H. Becker, E. Dietz, U. Gerhardt, and H. Angermüller, Phys. Rev. B 12, 2084 (1975).

28. G. V. Hansson and S. A. Flodström, Phys. Rev. B 18, 1572 (1978).

29. G. V. Hansson and S. A. Flodström, Phys. Rev. B 17, 473 (1978).

30. W. Eberhardt and E. W. Plummer, Phys. Rev. B 21, 3245 (1980).

31. G. Borstel, M. Neumann, and W. Braun, Phys. Rev. B 23, 3113 (1981); G. Borstel, W. Braun, M. Neumann, and G. Seitz, Phys. Status Solidi B: 95, 453 (1979).

32. N. Dahlbäck, P. O. Nilsson, and M. Pessa, Phys. Rev. B 19, 5961 (1979).

33. M. Lindroos, H. Asonen, and M. Pessa, Proc. Fourth Int. Conf. Solid Surfaces (Cannes, France, 1980), Vol. II, pp. 1174-77.

34. M. Lindroos, H. Asonen, M. Pessa, and N. V. Smith, Solid State Commun. 39, 285 (1981).

35. R. Courths, V. Bachelier, and S. Hüfner, Solid State Commun. 38, 887 (1981).

36. P. O. Nilsson and N. Dahlbäck, Solid State Commun. 29, 303 (1979).

37. P. Heimann, H. Miosga, and H. Neddermeyer, Solid State Commun. 29, 463 (1979).

38. L. Ilver and P. O. Nilsson, Solid State Commun. 18, 677 (1976).

39. P. O. Nilsson and L. Ilver, Solid State Commun. 17, 667 (1975).

40. Z. Hussain, S. Kono, L.-G. Petersson, C. S. Fadley, and L. F. Wagner, Phys. Rev. B. 23, 724 (1981), and references therein.

41. P. O. Nilsson, J. Kanski, and C. G. Larsson, Solid State Commun. 36, 111 (1980).

42. See, for example, S. Hüfner, in Photoemission in Solids II, edited by L. Ley and M. Cardona (Springer-Verlag, New York, 1979).

43. This comparison can be made most readily in the case of ARNP spectra for nonmagnetic d-band metals. For the 4d shell, compare Pd(111) (Ref. 23; 120 meV overall energy resolution) with Ag(111) (Ref. 5; 260 meV total energy resolution, FWHM). Recent experiments with Ag(110) and Ag(100) (Ref. 6) demonstrate that even higher spectral contrast in Ag is obtained with higher energy resolution. For the 5d shell, compare Pt(111) with Au(111) (Ref. 9), both with similar total energy resolution (100-200 meV FWHM).

44. Compare Ni(111) and Ni(100) ARNP results (Ref. 20) with Cu(111) and Cu(100) ARNP results (Ref. 22).

45. I. Terakura, K. Terakura, and N. Hamada, Surf. Sci. 103, 103 (1981), and references therein.

46. J. C. Campuzano, D. A. King, C. Somerton, and J. E. Inglesfield, Phys. Rev. Lett. 45, 1649 (1980).

47. S.-L. Weng, T. Gustafsson, and E. W. Plummer, Phys. Rev. Lett. 44, 344 (1980).

48. S.-L. Weng, E. W. Plummer, and T. Gustafsson, Phys. Rev. B 18, 1718 (1978), and references therein; S.-L. Weng, T. Gustafsson, and E. W. Plummer, Phys. Rev. Lett. 39, 822 (1977).

49. M. W. Holmes, D. A. King, and J. E. Inglesfield, Phys. Rev. Lett. 42, 394 (1979).

50. C. Noguera, D. Spanjaard, D. Jepsen, Y. Ballu, C. Guillot, J. Lecante, J. Paigne, Y. Pétroff, R. Pinchaux, P. Thiry, and R. Cinti, Phys. Rev. Lett. 38, 1171 (1977).

51. R. C. Cinti, E. Al Khoury, B. K. Chakraverty, and N. E. Christensen, Phys. Rev. B 14, 3296 (1976).

52. B. Feuerbacher and R. F. Willis, J. Phys. C 9, 169 (1976).

53. B. Feuerbacher and N. E. Christensen, Phys. Rev. B 10, 2373 (1974).

54. See, for example, J. C. Slater, The Self-Consistent Field for Molecules and Solids (McGraw-Hill, New York, 1974), Chapter 12.

55. See, for example, C. Herring, in Magnetism, edited by G. T. Rado and H. Suhl (Academic, New York, 1966), Vol. 4, Chapter XIII.

56. S. Ekelund and C. Leygraf, Surf. Sci. 40, 179 (1973).

57. G. Gewinner, J. C. Peruchetti, A. Jaegle, and R. Riedinger, Phys. Rev. Lett. 43, 935 (1979).

58. H. Kato, Y. Sakisaka, M. Nishijima, and M. Onchi, Surf. Sci. 107, 20 (1981).

59. J. Stöhr, G. Apai, P. S. Wehner, F. R. McFeely, R. S. Williams, and D. A. Shirley, Phys. Rev. B 14, 5144 (1976); P. S. Wehner, Ph.D. thesis, University of California, Berkeley, 1978 (LBL-7622, unpublished).

60. G. D. Mahan, Phys. Rev. B 2, 4334 (1970).

61. A. W. Overhauser, Phys. Rev. Lett. 4, 462 (1960); Phys. Rev. 128, 1437 (1962).

62. W. M. Lomer, Proc. Phys. Soc. 80, 489 (1962).

63. S. Asano and J. Yamashita, J. Phys. Soc. Japan 23, 714 (1967).

64. J. Kübler, J. Magn. Magn. Mat. 20, 277 (1980).

65. H. L. Skriver, J. Phys. F 11, 97 (1981).

66. W. C. Koehler, R. M. Moon, A. L. Trego, and A. R. Mackintosh, Phys. Rev. 151, 405 (1966).

67. See, for example, D. G. Laurent, J. Callaway, J. L. Fry, and N. E. Brener, Phys. Rev. B 23, 4977 (1981), and references therein.

68. A. S. Barker Jr., B. I. Halperin, and T. M. Rice, Phys. Rev. Lett. 20, 384 (1968).

69. A. S. Barker Jr. and J. A. Ditzenberger, Phys. Rev. B 1, 4378 (1970).

70. L. W. Bos and D. W. Lynch, Phys. Rev. B 2, 4567 (1970).

71. J. E. Graebner and J. A. Marcus, Phys. Rev. 175, 659 (1968).

72. J. E. Graebner, Proc. 12th Int. Conf. Low Temp. Phys. (Kyoto, Japan, 1970), pp. 601-03.

73. L. Ley, O. B. Dabbousi, S. P. Kowalczyk, F. R. McFeely, and D. A. Shirley, Phys. Rev. B 16, 5372 (1977).

74. L. I. Johansson, L.-G. Petersson, K.-F. Berggren, and J. W. Allen, Phys. Rev. B 22, 3294 (1980).

75. J. B. Pendry and S. J. Gurman, Surf. Sci. 49, 87 (1975).

76. W. Shockley, Phys. Rev. 56, 317 (1939).

77. See, for example, F. Forstmann, in Photoemission and the Electronic Properties of Surfaces, edited by B. Feuerbacher, B. Fitton, and R. F. Willis (Wiley, New York, 1978).

78. J. L. Erskine, Phys. Rev. Lett. 45, 1446 (1980).

79. C. S. Wang and A. J. Freeman, Phys. Rev. B 21, 4585 (1980).

80. W. Eberhardt, E. W. Plummer, K. Horn, and J. Erskine, Phys. Rev. Lett. 45, 273 (1980).

81. E. W. Plummer and W. Eberhardt, Phys. Rev. B 20, 1444 (1979).

82. M. R. Halse, Phil. Trans. Roy. Soc. A 265, 507 (1969).

83. N. E. Christensen, Phys. Rev. B 13, 2698 (1976).

84. H. Asonen, M. Lindroos, M. Pessa, and N. Dahlbäck, Solid State Commun. 35, 69 (1980).

85. R. R. Turtle and T. A. Callcott, Phys. Rev. Lett. 34, 86 (1975).

86. E. O. Kane, Phys. Rev. Lett. 12, 97 (1964).

87. E. Dietz and D. E. Eastman, Phys. Rev. Lett. 41, 1674 (1978).

88. R. Rosei, R. Lässer, N. V. Smith, and R. L. Benbow, Solid State Commun. 35, 979 (1980).

89. N. E. Christensen, Solid State Commun. 38, 309 (1981).

90. N. E. Christensen, Solid State Commun. 37, 57 (1981).

91. E. Dietz and F. J. Himpsel, Solid State Commun. 30, 235 (1979).

92. D. G. Laurent, J. Callaway, J. L. Fry, and N. E. Brener, Phys. Rev. B 23, 4977 (1981). Pre-publication energy eigenvalues were graciously provided to us by Prof. J. Callaway.

93. J. Hermanson, Solid State Commun. 22, 9 (1977).

94. For the Δ_1 band between (X) and H_{15}, only the portion that is $0.2(2\pi/a)$ closest to H was used in the fitting procedure. Between H_1 and (X), all but the region $0.2(2\pi/a)$ nearest H was used, and the entire curve between (X) and Γ_{15} was utilized.

95. The portion of the Σ_1 band with $0.1 \leq k_x \leq 0.4$ was utilized in the fitting procedure.

96. See, for example, L. F. Ley, J. Electron Spectrosc. Relat. Phenom. 15, 329 (1979); N. E. Christensen and B. Feuerbacher, Phys. Rev. B 10, 2349 (1974); P. J. Feibelman and D. E. Eastman, Phys. Rev. B 10, 4932 (1974).

97. J. W. D. Connolly, Electronic Density of States, Spec. Publ. Natl. Bur. Stand. (U. S. GPO, Washington, D.C., 1971), Vol. 323, p. 27.

98. See, for example, R. P. Gupta and S. K. Sinha, Phys. Rev. B 3, 2401 (1971).

99. R. F. Willis and B. Feuerbacher, in Photoemission and the Electronic Properties of Surfaces, edited by B. Feuerbacher, B. Fitton, and R. F. Willis (Wiley, New York, 1978).

100. See, for example, R. L. Billington and T. N. Rhodin, Phys. Rev. Lett. 41, 1602 (1978); Ref. 47.

101. W. F. Egelhoff Jr., J. W. Linnett, and D. L. Perry, Phys. Rev. Lett. 36, 98 (1976).

102. K. L. Kliewer, Phys. Rev. B 15, 3759 (1977).

103. See, for example, S. D. Kevan and D. A. Shirley, Phys. Rev. B 22, 542 (1980), and references therein; Z. Hussain and N. V. Smith, Phys. Lett. A 66, 492 (1978).

104. G. Allan, Surf. Sci. 74, 79 (1978).

105. D. R. Grempel, Phys. Rev. B 24, 3928 (1981).

106. C. Rau and S. Eichner, Phys. Rev. Lett. 47, 939 (1981).

107. Ref. 74, and references therein.

108. S. P. Weeks and E. W. Plummer, Solid State Commun. 21, 695 (1977).

109. P. J. Feibelman, Surf. Sci. 46, 558 (1974).

110. S. G. Louie, P. Thiry, R. Pinchaux, Y. Pétroff, D. Chandesris, J. Lecante, Phys. Rev. Lett. 44, 549 (1980).

111. P. Heimann, J. Hermanson, H. Miosga, and H. Neddermeyer, Phys. Rev. Lett. 43, 1757 (1979).

112. See, for example, N. W. Ashcroft and N. D. Mermin, Solid State Physics (Holt, Rinehart and Winston, New York, 1976).

113. See, for example, G. D. Mahan, in Electron and Ion Spectroscopy of Solids, edited by L. Fiermans, J. Vennik, and W. Dekeyser (Plenum, New York, 1978), and references therein.

114. See, e.g., Ref. 12. This is also based on general experience with ARP, especially in noble metals.

115. J. Anderson and G. J. Lapeyre, Phys. Rev. Lett. 36, 376 (1976).

116. J. F. van der Veen, F. J. Himpsel, and D. E. Eastman, Solid State Commun. 34, 33 (1980).

117. N. J. Shevchik and D. Liebowitz, Phys. Rev. B 18, 1618 (1978).

118. J. B. Pendry, Low Energy Electron Diffraction (Academic, New York, 1974).

119. B. E. Warren, X-Ray Diffraction (Addison-Wesley, Reading MA, 1969).

120. N. J. Shevchik, Phys. Rev. B 16, 3428 (1977).

121. Z. Hussain, E. Umbach, J. J. Barton, J. G. Tobin, and D. A. Shirley, Phys. Rev. B, to be published, and references therein.

122. R. S. Williams, P. S. Wehner, J. Stöhr, and D. A. Shirley, Phys. Rev. Lett. 39, 302 (1977).

123. In LEED, multiple scattering effects preclude accurate applications of the simple Debye model because θ_D is a function of $\Delta\vec{k}$ in Eq. (7) (see Ref. 118).

124. See, for example, G. A. Somorjai, Chemistry in Two Dimensions: Surfaces (Cornell University Press, Ithaca NY, 1981), Chapter 4 and references therein.

125. D. Tabor, J. M. Wilson, and T. J. Bastow, Surf. Sci. 26, 471 (1971).

126. R. Kaplan and G. A. Somorjai, Solid State Commun. 9, 505 (1971).

127. L. Hodges, R. E. Watson, H. Ehrenreich, Phys. Rev. B 5, 3953 (1972).

128. A. Schulz, R. Courths, H. Schulz, and S. Hüfner, J. Phys. F 9, L41 (1979).

129. Z. Hussain, C. S. Fadley, S. Kono, and L. F. Wagner, Phys. Rev. B 22, 3750 (1980).

130. See, for example, J. B. Pendry, in Photoemission and the Electronic Properties of Surfaces, edited by B. Feuerbacher, B. Fitton, and R. F. Willis (Wiley, New York, 1978).

Table I. Energies of primary maxima in the chromium total density of states (TDOS). (a)

TDOS maximum (b)	Experiment, this work	Experiment, XPS (c)	Commensurate AF-Cr band theory (d)		
			Kübler (e)	Skriver (f)	Asano and Yamashita (g)
1	-1.63 (h)	-1.8	-1.19	-1.32	-1.10
2	-3.41 (i)	-3.5	-2.25	-2.43	-2.31
3			-3.36	-3.41	-3.27
ave. (1,2)	-2.52	-2.7	-1.72	-1.88	-1.71
1-2	1.78	1.7	1.06	1.11	1.21

(a) Energy values are in electron volts relative to E_F.

(b) $TDOS_1$ lies nearest E_F.

(c) X-ray photoemission valence band spectrum peak positions, Ref. 73.

(d) Peak positions estimated from TDOS plots.

(e) Ref. 64.

(f) Ref. 65.

(g) TDOS calculation in Ref. 97, based on band structure calculation in Ref. 63.

(h) From non-dispersive portion of $E_i(\vec{k})$ curve for Cr(100) feature B.

(i) From Cr(110) feature D and non-dispersive portion of $E_i(\vec{k})$ curve for Cr(100) feature C.

Table II. Summary of band structure assignments for Cr(100) EDC peak structures.

Peak structure (a)	$\langle E_i \rangle$ (b)	Band structure assignment (c)	Symmetry point energies determined (d)
A	-0.71	Δ_5 DT and/or DOS from Δ_5 and $\Gamma_{25'}$	$\Gamma_{25'}$, (X_5), $\langle \Delta_5 \rangle$ (e)
B		Δ_{2u} DT and/or ODDOS near X, and TDOS elsewhere	($X_{3'}$)
C		$\Delta_{2\ell}$ DT and/or ODDOS near X, and TDOS elsewhere	(X_2)
D	-5.03	DOS from Γ_{12}, Δ_{1u}, and/or $X_{4'}$	Γ_{12}, ($X_{4'}$)
E		$\Delta_{1\ell}$ DT	X_1, Γ_1
F	-7.00	ODDOS from $\Delta_{1\ell}$ near Γ_1 or TDOS from Γ_1	Γ_1

(a) Peak structure labels are as indicated in Fig. 5.

(b) Average initial-state energies listed for non-dispersive features, in electron volts.

(c) DT: direct transition, DOS: density of states, TDOS: total DOS, ODDOS: one-dimensional DOS.

(d) Parenthetical notation indicates that approximate position is determined by EDC peak positions.

(e) $\langle \Delta_5 \rangle$ = mean value of nearly-dispersionless portion of Δ_5 band.

Table III. Summary of band structure assignments for Cr(110) EDC peak structures.

Peak structure (a)	$\langle E_i \rangle$ (b)	Band structure assignment (c)	Symmetry point energies determined
A	-0.25	surface state in $\Sigma_{3u} - \Sigma_{3\ell}$ spin-polarization gap	
B		Σ_3 DT	M_5, $\Sigma_3^{max.}$
C		Σ_{1u} DT	$\Sigma_{1u}^{min.}$, (k_F) (d)
D	-3.44	TDOS	
E		Σ_{1m} DT	M_1, $\Sigma_{1m}^{max.}$
F	-5.25	ODDOS from $\Sigma_{1\ell}$ near M_3	M_3
G		$\Sigma_{1\ell}$ DT	M_3
H	-6.86	ODDOS from $\Sigma_{1\ell}$ near Γ_1, or TDOS from Γ_1	Γ_1

(a) Peak structure labels are as indicated in Fig. 5.

(b) Average initial-state energies listed for non-dispersive features, in electron volts.

(c) DT: direct transition, DOS: density of states, TDOS: total DOS, ODDOS: one-dimensional DOS.

(d) Approximate value of $k_F = k[E_i(\Sigma_{1u})=0] = 0.70$ (in units of $2\pi/a$).

Table IV. Comparison of experimental energy values and energy differences with theoretical calculations for valence bands of antiferromagnetic chromium. (a)

Energy level	Experiment, this work (b)	Commensurate AF-Cr band theory			
		Kübler (c)	Skriver (d)	Asano and Yamashita (e)	Best agreement (f)
X_5	(-0.71) (g)	-0.67	-0.56	-0.57	K
$X_{3'}$	(-1.92)	-1.33	-1.23	-1.68	AY
X_2	(-3.18)	-2.00	-1.45	-2.05	AY
$X_{4'}$	(-5.03)	-3.86	-4.14	-3.36	S
X_1	-5.20	-4.06	-4.19	-3.50	S
$\Gamma_{25'}$	-0.71	-0.85	-1.16	-0.96	K
Γ_{12}	-5.03	-4.06	-4.19	-4.36	AY
Γ_1	-6.91	-7.78	-8.05	-7.00	AY
M_5	-2.05	-2.30	-2.70	-2.43	K
M_1	-4.82	-4.20	-4.56	-4.21	S
M_3	-5.25	-4.24	-4.59	-4.24	S
$\Sigma_3^{max.}$	-0.53	-0.10	+0.05	-0.06	K
$\Sigma_{1u}^{min.}$	-1.70	-1.16	-1.27	-1.13	S
$\Sigma_{1m}^{max.}$	-4.35	-3.36	-3.37	-3.46	AY
$X_{3'}-X_2$	(1.26)	0.67	0.22	0.37	K
$X_{4'}-X_1$	(0.17)	0.20	0.05	0.14	K,AY
M_1-M_3	0.43	0.04	0.03	0.03	K
$M_5-M_{1,3}$	2.99	1.92	1.88	1.80	K
$\Sigma_{3u}^{min.} - \Sigma_{3\ell}^{max.}$	> 0.53	0.73	0.37	0.45	

(a) Energy values in electron volts relative to E_F.
(b) Based on empirical band structure assignment of peak structures (see Fig. 13 and Tables II and III).
(c) Ref. 64.
(d) Ref. 65.
(e) Ref. 63.
(f) Best agreement between ARP experiment and band theory; K: Kübler's calculation, S: Skriver, AY: Asano and Yamashita.
(g) Parenthetical notation indicates that approximate value is determined by EDC peak positions.

FIGURE CAPTIONS

Fig. 1. Diagrammatic representation of chromium LEED patterns at 60 eV for various surface structures: (110)-p(1x1), (100)-p(1x1), and (100)-c(2x2).

Fig. 2. Experimental normal emission geometries employed for (a) Cr(100) and (b) Cr(110). The crystal surface normal ($\vec{n}$), radiation vector potential ($\vec{A}$), and photoemission direction ($\vec{p}$) were all confined to the plane of incidence, with θ_A [$\angle(\vec{n},\vec{A})$] fixed at 27.3° in the $\phi_A = 0°$ azimuth {this azimuth contains the [011] and [001] directions in (a) and (b), respectively}. The relative orientation of $\vec{A}$ and $\vec{p}$ was not variable, but θ_A and θ_p [$\angle(\vec{n},\vec{p})$] could be adjusted concurrently by virtue of polar rotation of the crystal ($\vec{n}$) in the plane of incidence.

Fig. 3. Electron energy distribution curves collected at normal emission and 293K for Cr(100) in the range $6 \text{ eV} \leq h\nu \leq 32 \text{ eV}$. For each spectrum, the Fermi level (E_F) was positioned as discussed in the text.

Fig. 4. Electron energy distribution curves collected at normal emission and 293K for Cr(110) in the range $6 \text{ eV} \leq h\nu \leq 31 \text{ eV}$. For each spectrum, the Fermi level (E_F) was positioned as discussed in the text. Note, especially, the sharp feature near E_F in the spectra for $h\nu \leq 8$ eV and $h\nu \geq 13$ eV.

Fig. 5. Plot of experimental peak energy position versus photon energy for each structure in (a) Cr(100), and (b) Cr(110) normal-emission EDCs. Open and filled circles denoted weak and strong features, respectively, and the connecting lines have no theoretical significance. The structures are labelled A through F for Cr(100) and A through H for Cr(110) spectra. Peak dispersion with $h\nu$ in the plots is indicative of direct-transition processes.

Fig. 6. Spin structure of the chromium unit cell in the (perfect) commensurate antiferromagnetic state. The magnetic space lattice is simple cubic with a two-atom basis, corresponding to the cesium chloride crystal structure.

Fig. 7. Demonstration in reciprocal space of the transformation from paramagnetic (P) to commensurate antiferromagnetic (AF) structures, as discussed in the text: (a) and (b) show P and AF lattices, respectively; (c) and (d) contain body-centered cubic (BCC) Brillouin zones (BZs) before and after the incorporation of the spin-density wave ($\vec{Q}$), respectively; (e) lists P $\rightarrow$ AF transformations of symmetry points; and (f) shows the simple cubic (SC) BZ resulting from the P $\rightarrow$ AF transition.

Fig. 8. Valence band $E(\vec{k})$ curves for chromium calculated by Asano and Yamashita (Ref. 63): (a) energy bands along HGN and $N\Sigma\Gamma$ for the paramagnetic state; (b) paramagnetic energy bands from (a) arranged in antiferromagnetic k-space (i.e., the

SC zone), with the NGH line (dashed curves) overlaid on the NΣΓ line (solid curves); (c) antiferromagnetic energy bands along MΣΓ, corresponding to incorporation of the periodic exchange perturbation. Viewed in a stepwise manner, the sinusoidally modulating perturbation causes a separation of the energy bands in (b) at N and along Σ(G), resulting in the band scheme shown in (c).

Fig. 9. Theoretical paramagnetic band structure of chromium by Laurent, et al. (Ref. 92) along the Δ line, arranged in the simple-cubic zone so that the bands between (X) and H (dashed curves) are overlaid on bands between Γ and (X) (solid curves). Also shown (solid circles) is the photoelectron dispersion relation ($m^* = 2.53\ m_e$, $V_0^F = -3.95$ eV) employed in $E_i(\vec{k})$ determination with Cr(100) ARNP data, obtained in part from a fit of the appropriate Δ_1 conduction bands to a quasi-free-electron dispersion relation, Eq. (1) (see text).

Fig. 10. Theoretical paramagnetic band structure of chromium by Laurent, et al. (Ref. 92) along the Σ and G lines, arranged in the simple-cubic zone so that the HGN bands (dashed curves) are overlaid on ΓΣN bands (solid curves). Also shown (solid circles) is the photoelectron dispersion relation ($m^* = 1.03\ m_e$, $V_0^F = +1.32$ eV) employed in $E_i(\vec{k})$ determination with Cr(110) ARNP data, obtained in

part from a fit of the $\Gamma_{15} - \Sigma_1 - N_1$ conduction band to a quasi-free-electron dispersion relation, Eq. (1) (see text).

Fig. 11. Dispersion relations for chromium along [100] in the extended-zone scheme. Empirical curves derived from Cr(100) ARNP data are represented by symbols: (•) for the non-dispersive features (A, D, and F); (○) for features B and E; and (□) for feature C. Kübler's theoretical bands (Ref. 64) for commensurate antiferromagnetic chromium along $\Gamma\Delta X$ are represented by solid (symmetry-allowed initial states) and dashed (symmetry forbidden) curves. To distinguish between bands of the same symmetry, the irreducible representation labels include "ℓ" and "u" wherever necessary. The photon energy scale at the top gives $|\vec{k}_f|$ corresponding to photoexcitation of initial states at E_F, where primary transitions $\vec{k}_i \rightarrow \vec{k}_f = \vec{k}_i - \vec{G}_{hkl}$ [$\vec{k}_i$ is between (0, 0, 0) and (1/2, 0, 0)] occurs with $\vec{G}$ = ($\bar{1}$, 0, 0) between 6 eV and 12 eV, $\vec{G}$ = (2, 0, 0) between 13 eV and 24 eV, and ($\bar{2}$, 0, 0) above 24 eV. The empirical bands are reasonably symmetric about the zone boundary at X ($|\vec{k}_f| = 1.50$).

Fig. 12. Dispersion relations for chromium along [110] in the extended-zone scheme. Empirical curves derived from Cr(110) ARNP data are represented by symbols: (•) for dispersionless features (A, D, F, and H); (○) for features B and G;

and (◇) for features C and E. Kübler's theoretical bands (Ref. 64) for commensurate antiferromagnetic chromium along ΓΣM are represented by solid (symmetry-allowed initial states) and dashed (symmetry forbidden) curves. To distinguish between bands of the same symmetry, the irreducible representation labels include "ℓ", "m", and "u" wherever necessary. The photon energy scale at the top gives $|\vec{k}_f|$ corresponding to photoexcitation of initial states at E_F, where primary transitions $\vec{k}_i \rightarrow \vec{k}_f = \vec{k}_i - \vec{G}_{hkl}$ [$\vec{k}_i$ is between (0, 0, 0) and (1/2, 1/2, 0)] occur with $\vec{G}$ = (0, 0, 0) below 10 eV and $\vec{G}$ = (1, 1, 0) above 10 eV. The empirical bands are reasonably symmetric about the zone boundary at M ($|\vec{k}_f| = 0.71$).

Fig. 13. Dispersion relations for chromium along [100] and [110] in the reduced-zone scheme, derived from experimental and theoretical (Ref. 64) curves shown in Figs. 11 and 12 (refer to the corresponding figure captions for details). Empirical bands along XΔΓ and ΓΣM are derived from Cr(100) and Cr(110) ARNP data, respectively, and are represented by open symbols (○, □, ◇) for dispersive curves and closed circles for non-dispersive curves. Non-dispersive empirical curves can be assigned to features of the band structure by invoking a density-of-states-photoemission mechanism, except for the uppermost ΓΣM curve which corresponds to a $\bar{\Gamma}$ surface state on the Cr(110) surface as discussed in the text.

Fig. 14. Empirical band structure of antiferromagnetic chromium along $X\Delta\Gamma\Sigma M$, at 293K. Solid lines correspond to bands deduced directly from detailed empirical curves in Fig. 13 and critical point energy eigenvalues listed in Table IV (solid circles), while dashed lines refer to dispersion relations estimated from Table IV and the general topology of the theoretical (Ref. 64) band structure.

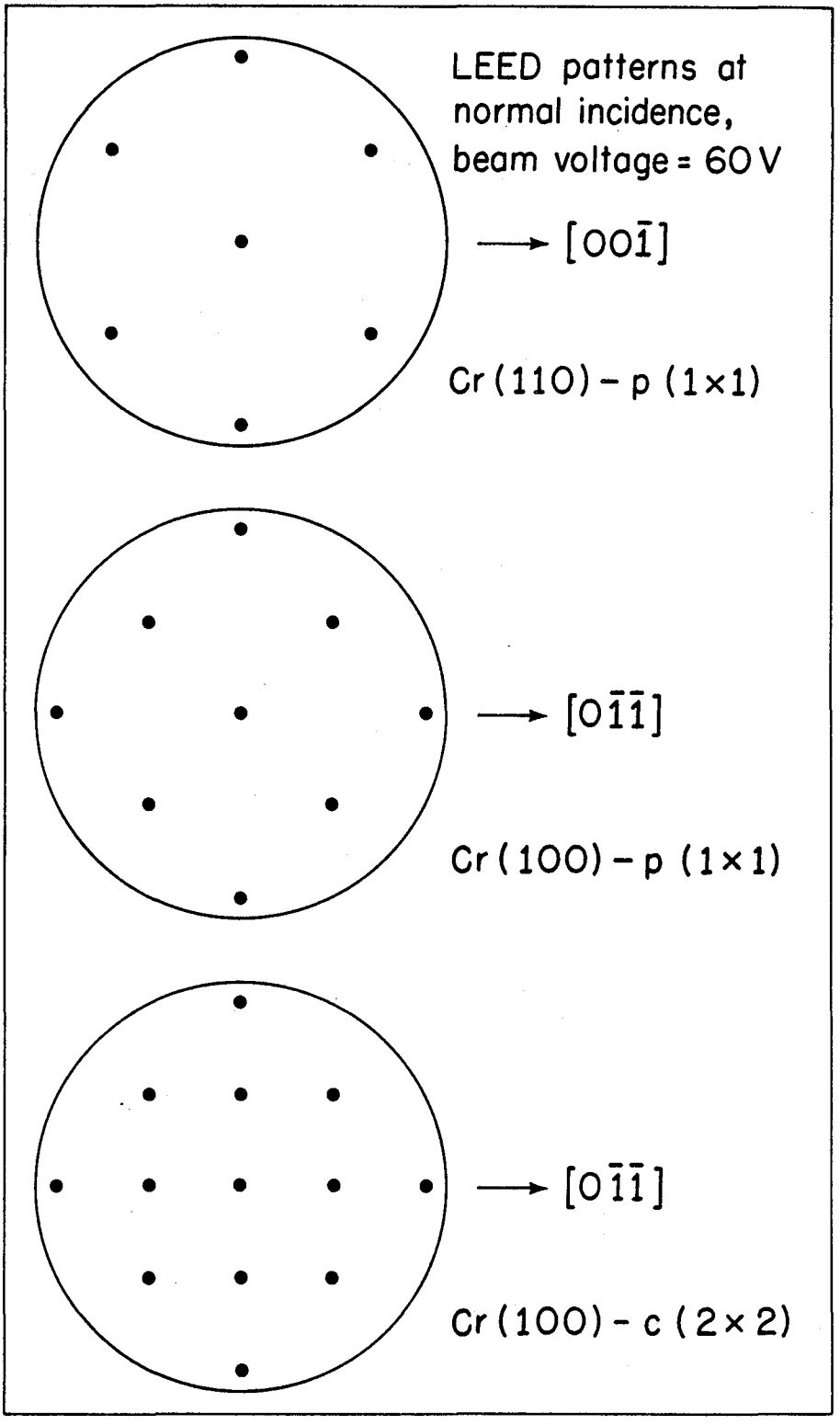

XBL8110-7376

Figure 1

(a) Cr(100) – normal emission

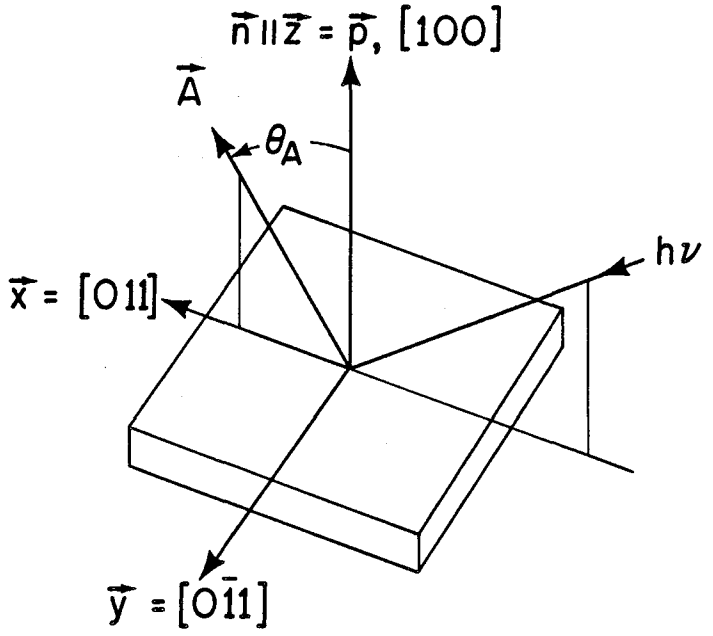

(b) Cr(110) – normal emission

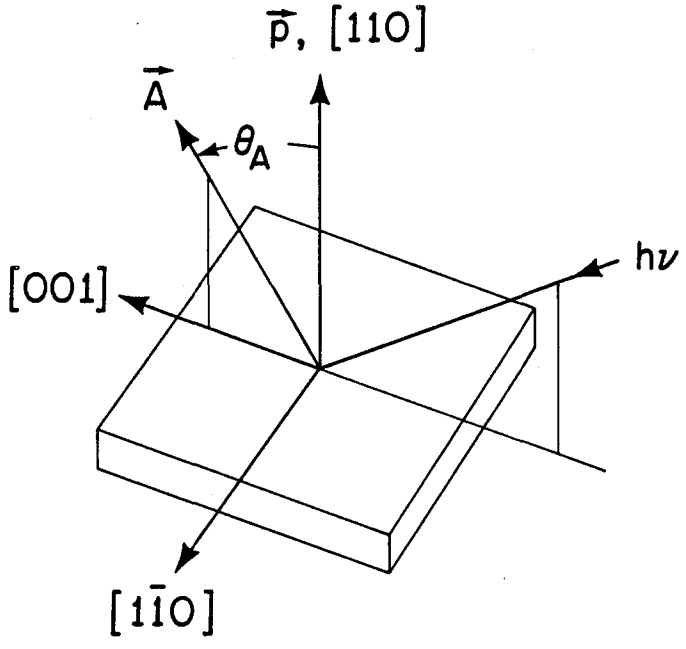

XBL 8110-7377

Figure 2

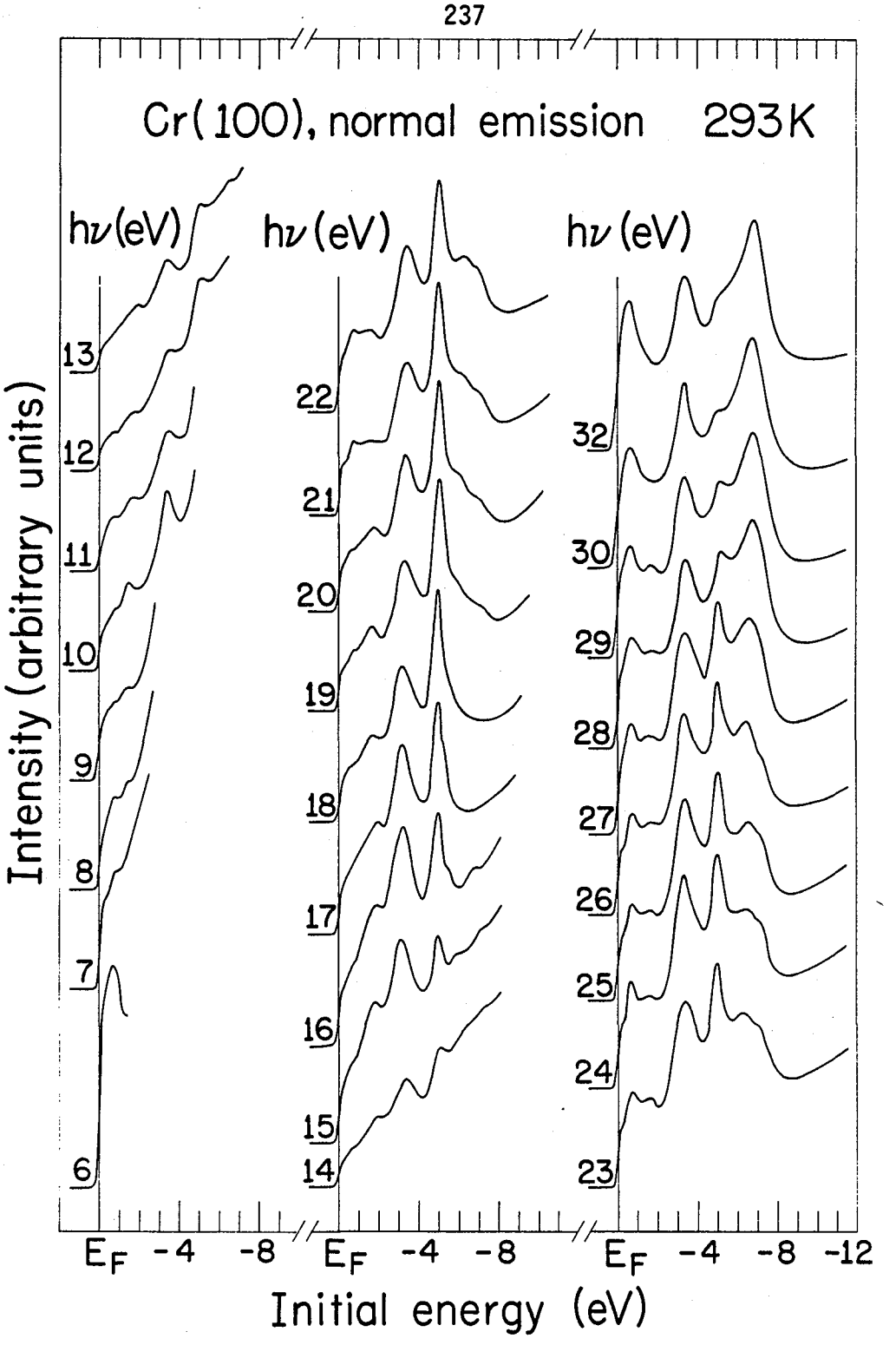

XBL8110-7385

Figure 3

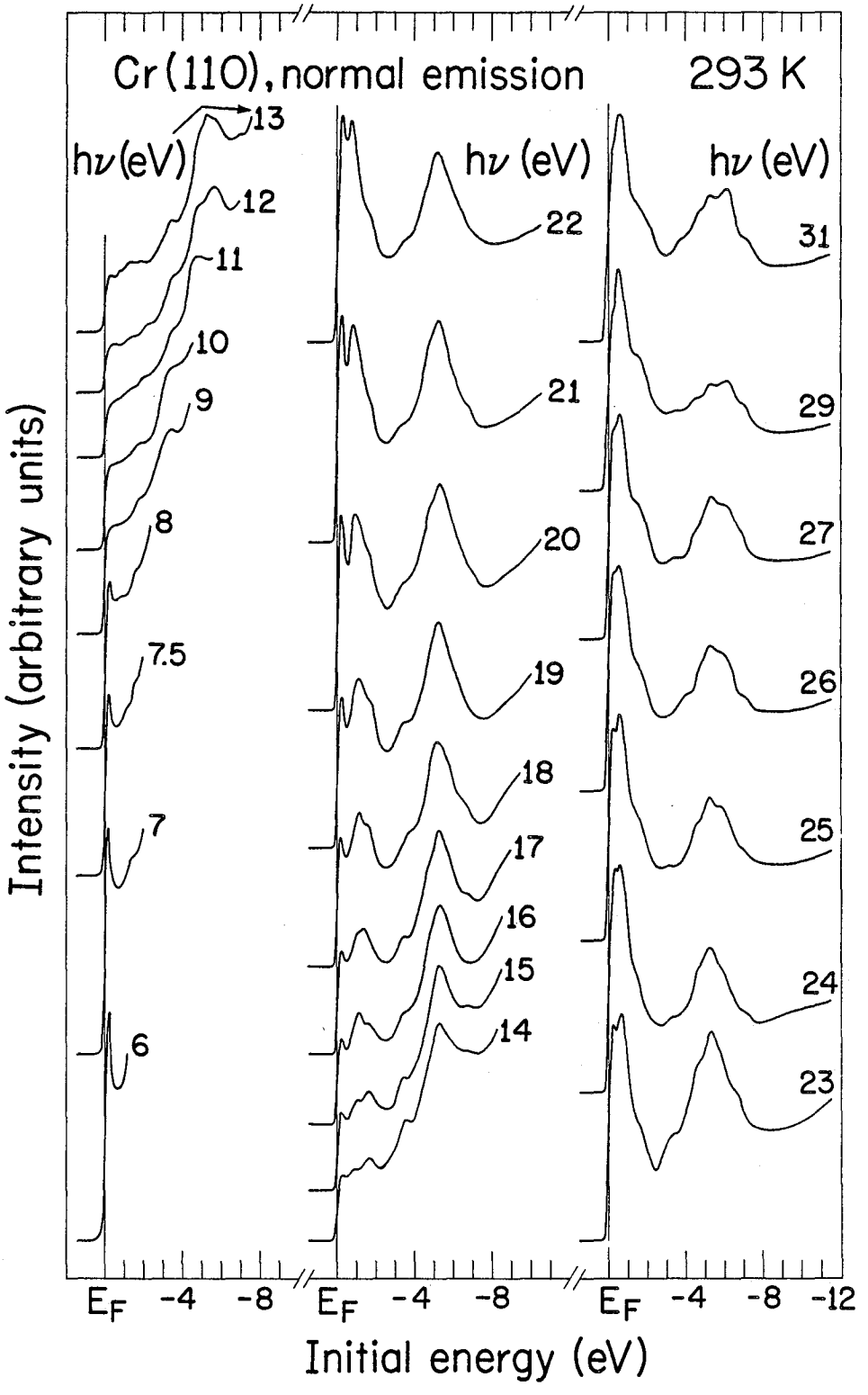

XBL8110-7386

Figure 4

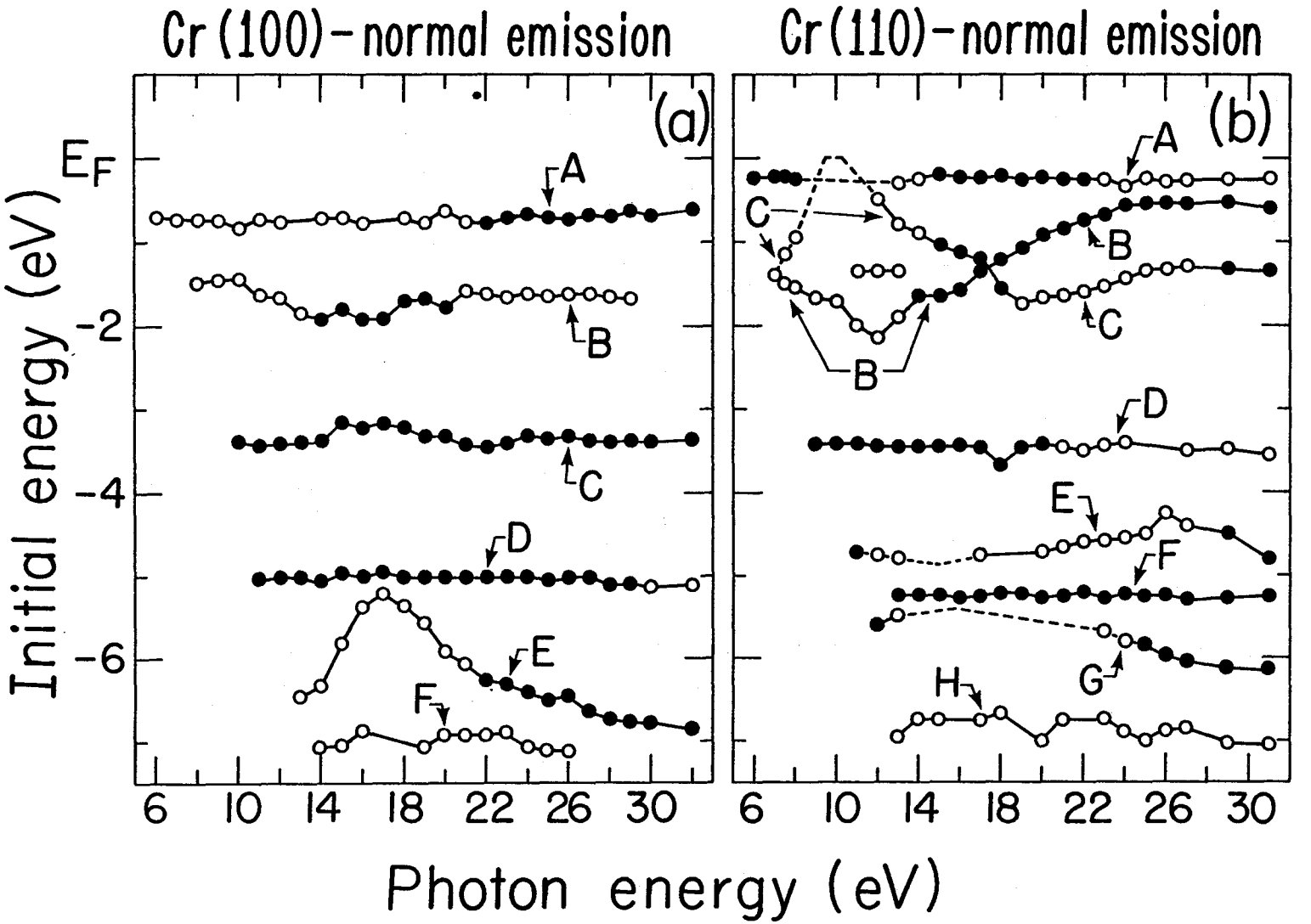

Figure 5

XBL 8110-7382

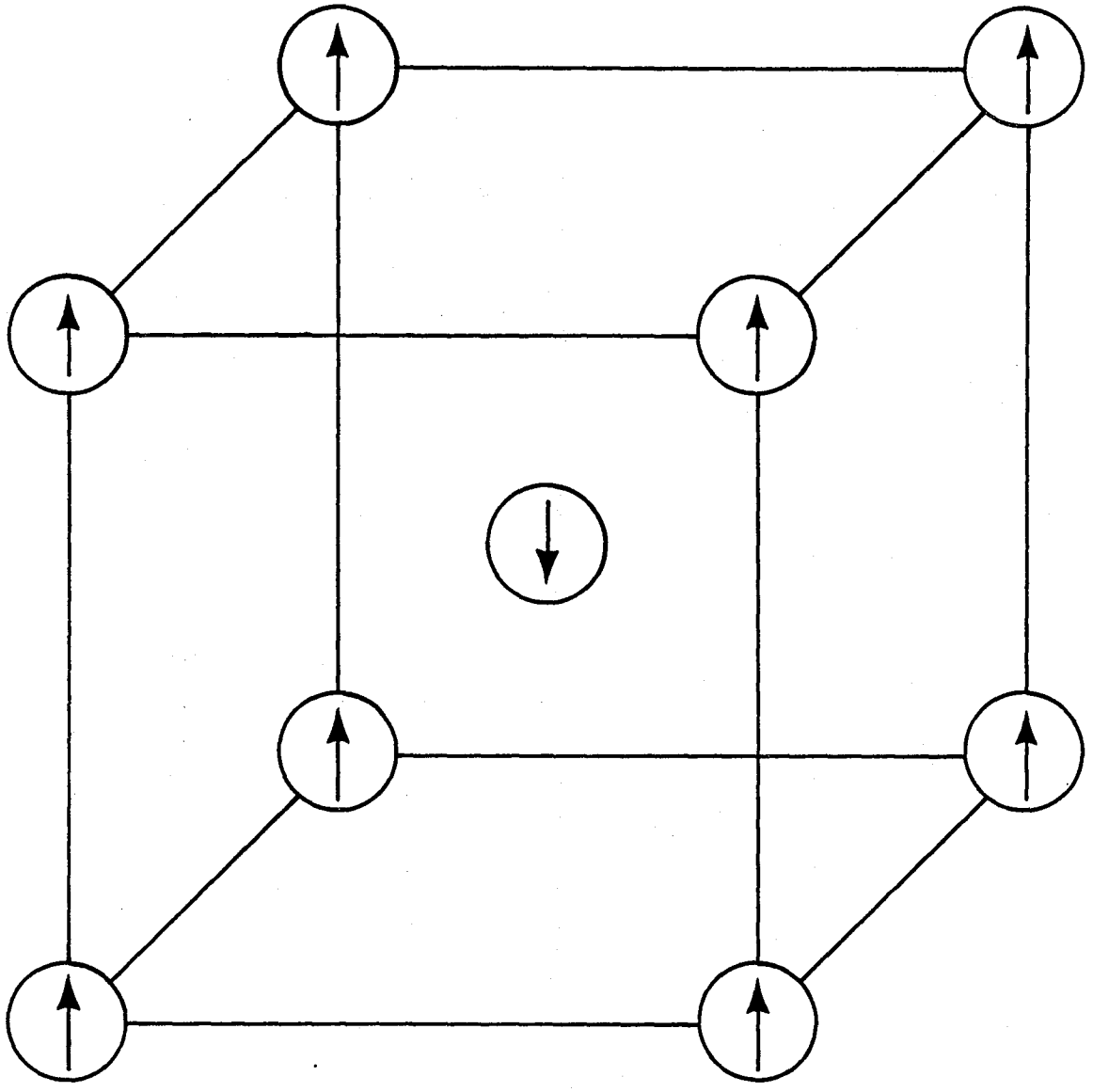

XBL 8110-7378

Figure 6

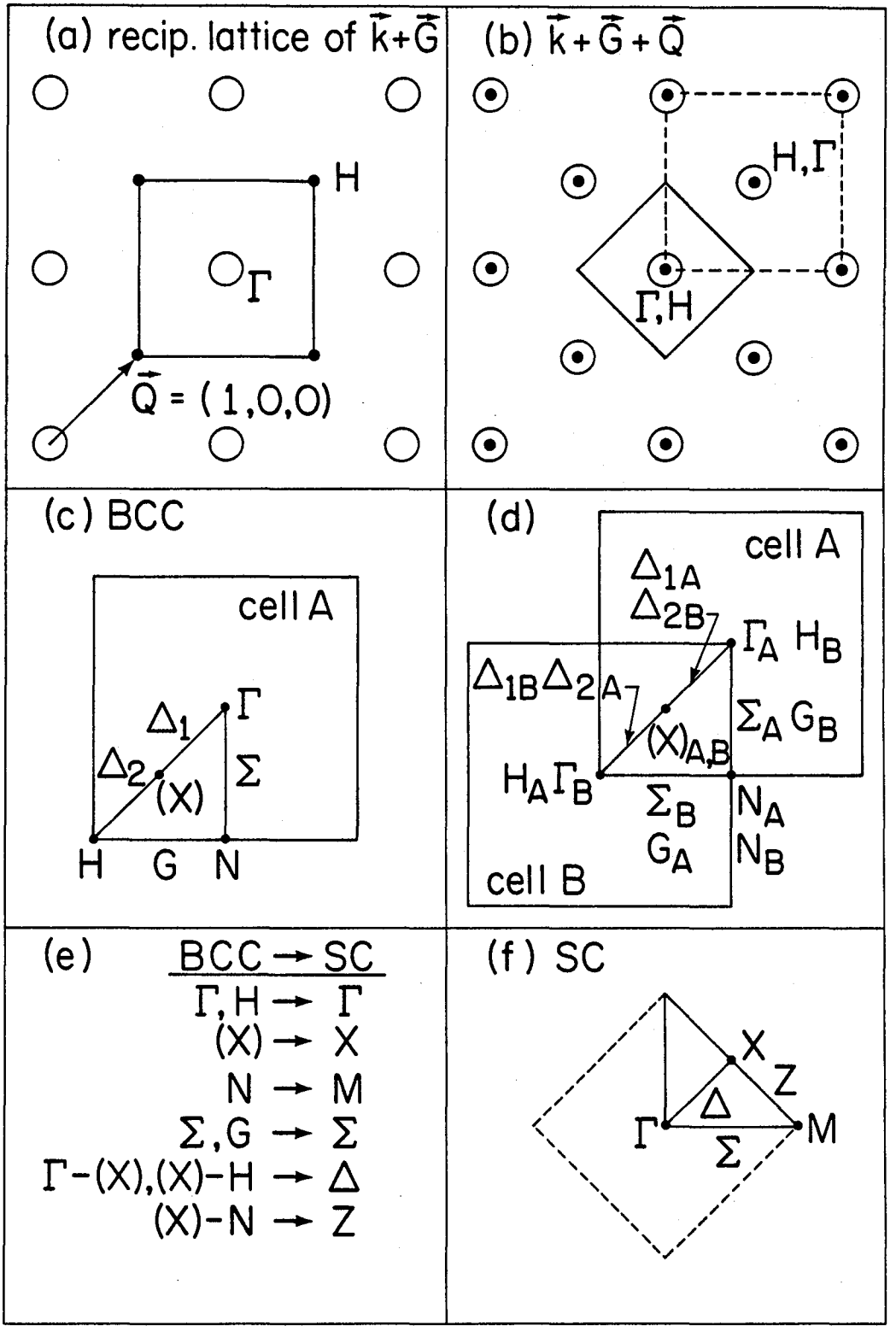

XBL 8110-7379

Figure 7

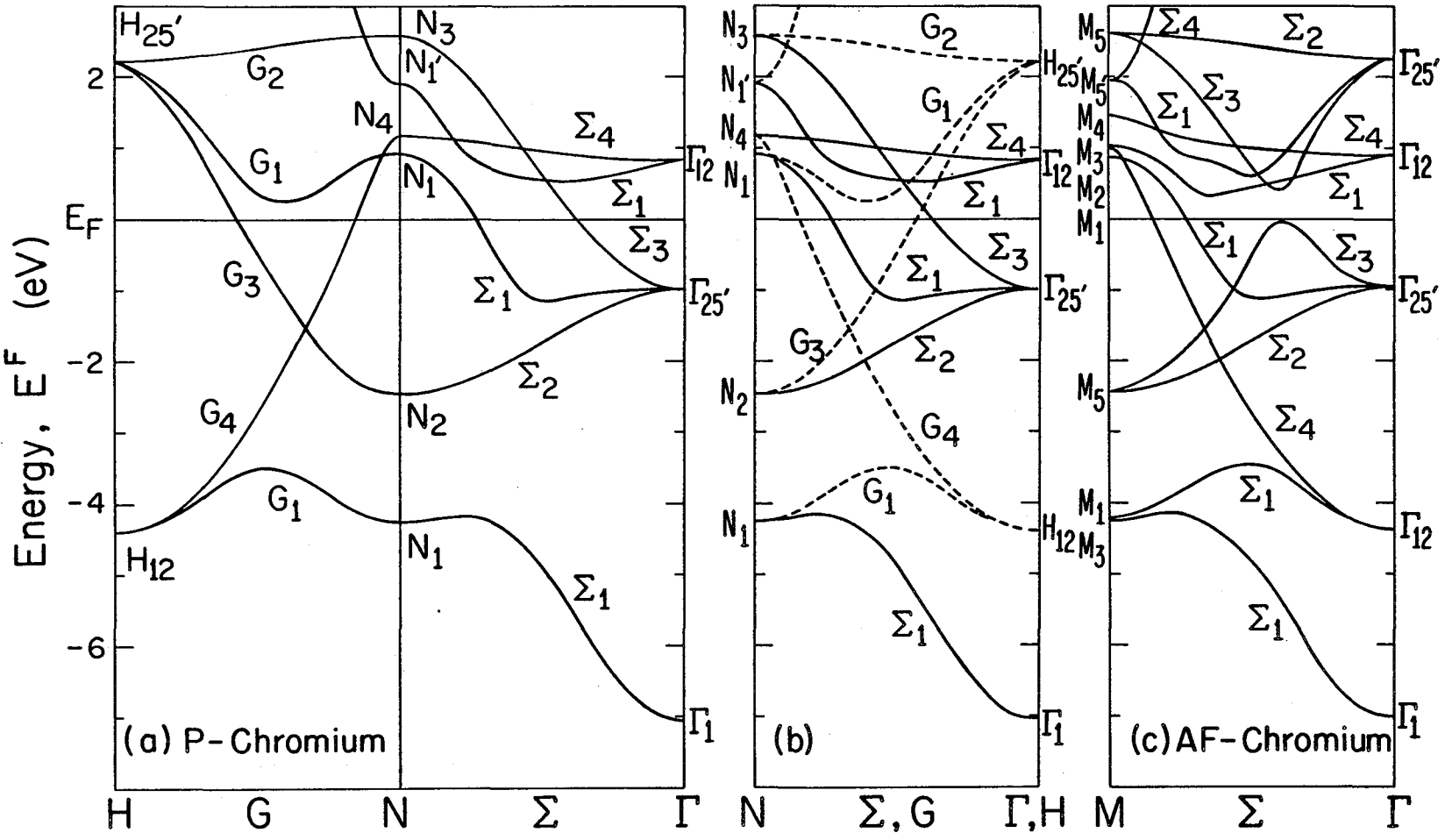
Energy, E^F (eV)
2
-2
-4
-6
E_F
H_25'
G_2
G_1
G_3
G_4
H_12
N_3
N_1'
N_4
N_1
N_2
Σ_4
Σ_1
Σ_3
Σ_2
Γ_12
Γ_25'
Γ_1
(a) P-Chromium
H
G
N
Σ
Γ
(b)
N
Σ, G
Γ, H
(c) AF-Chromium
M_5
M_4
M_3
M_2
M_1
M
XBL 8110-7384

Figure 8

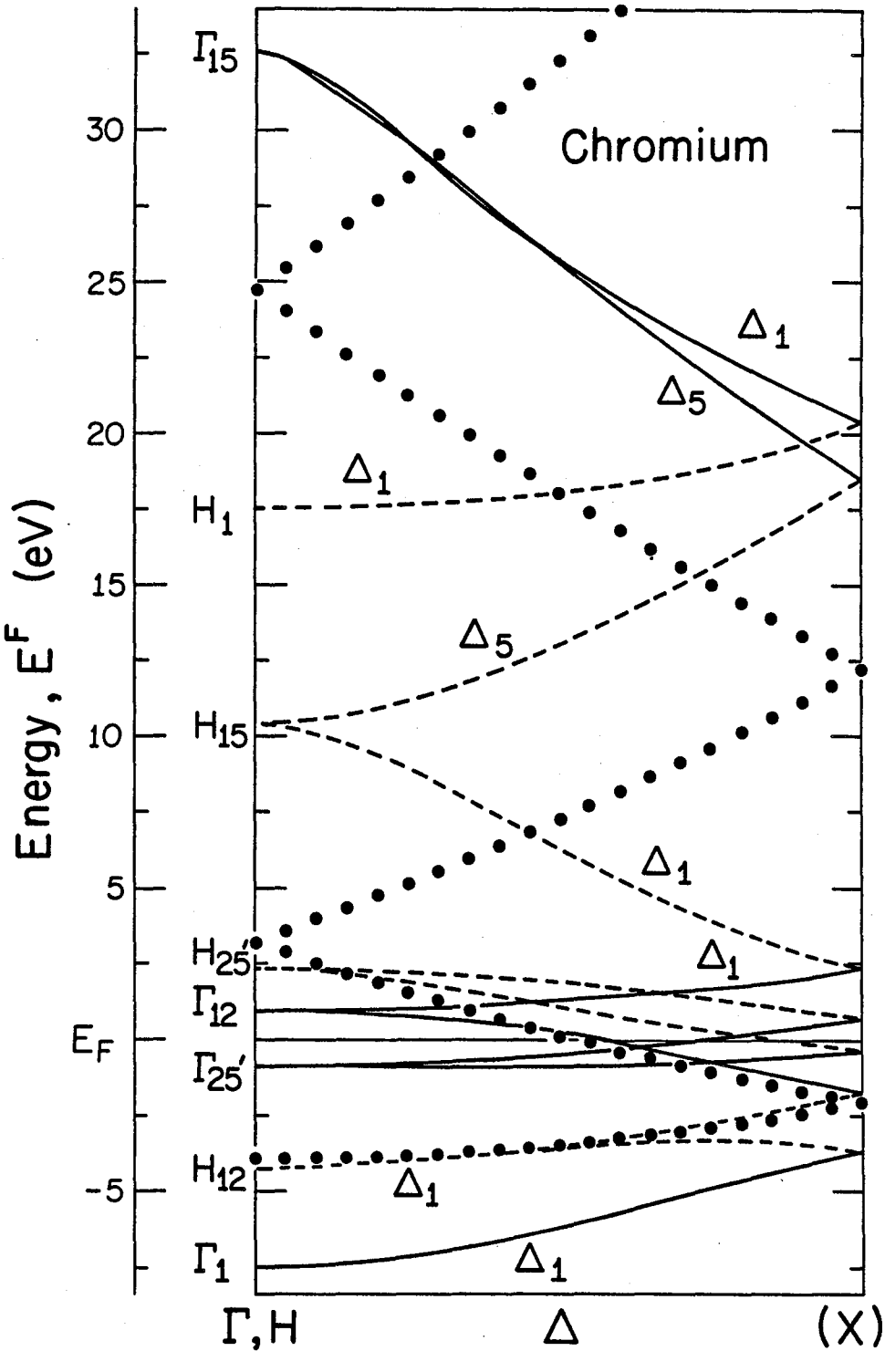

XBL 8110-7397

Figure 9

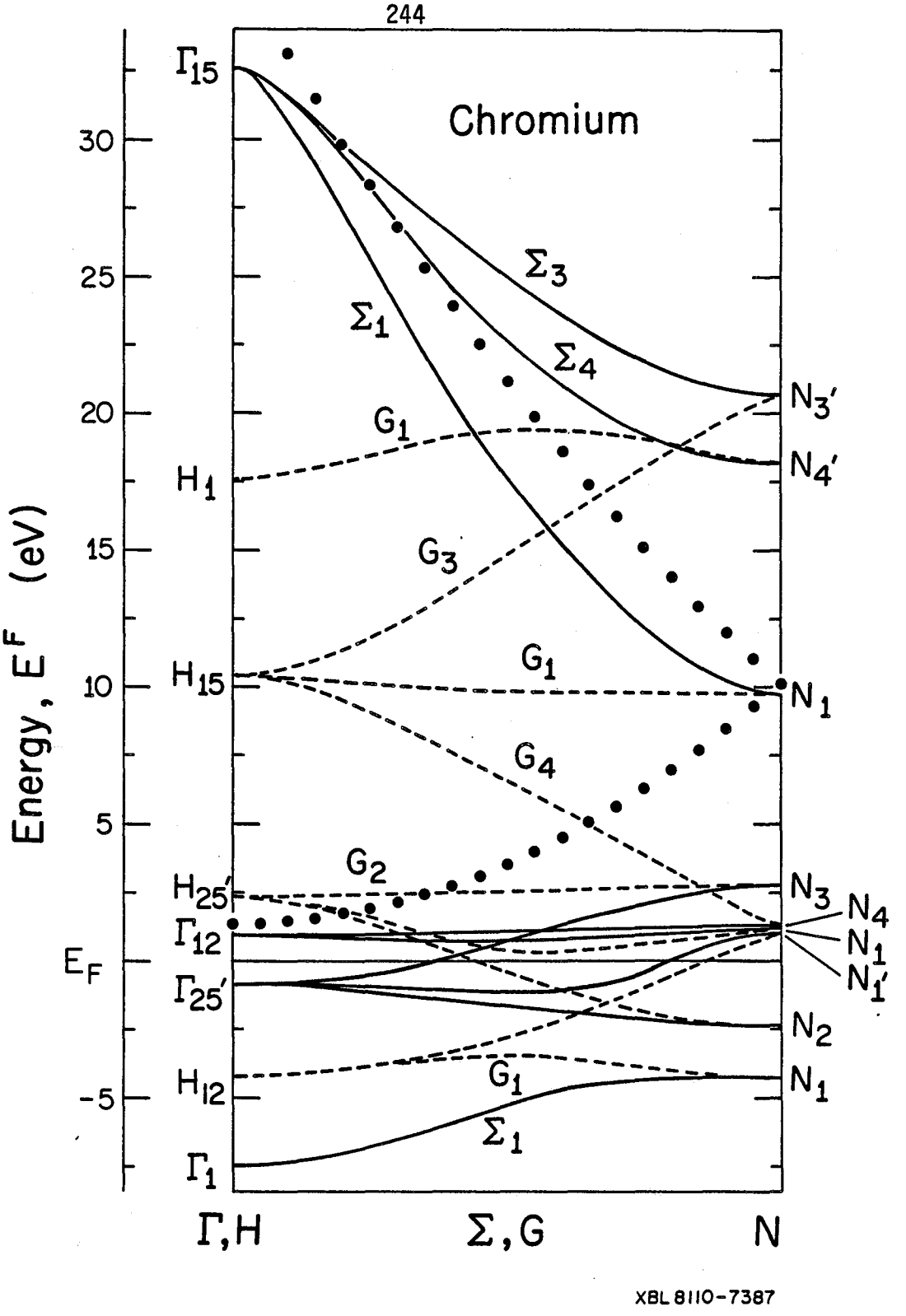

XBL 8110-7387

Figure 10

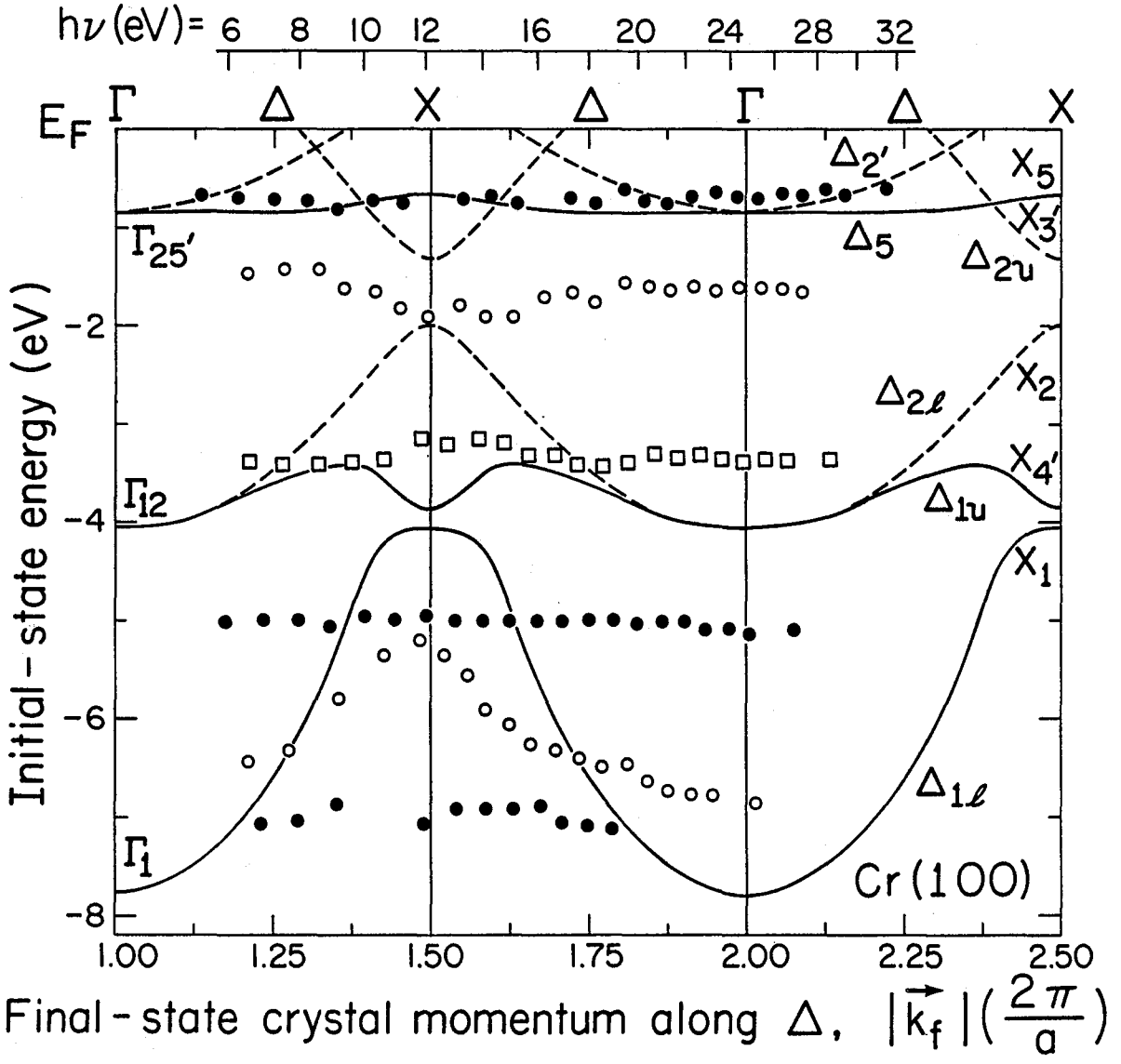

Figure 11

XBL 8110-7381

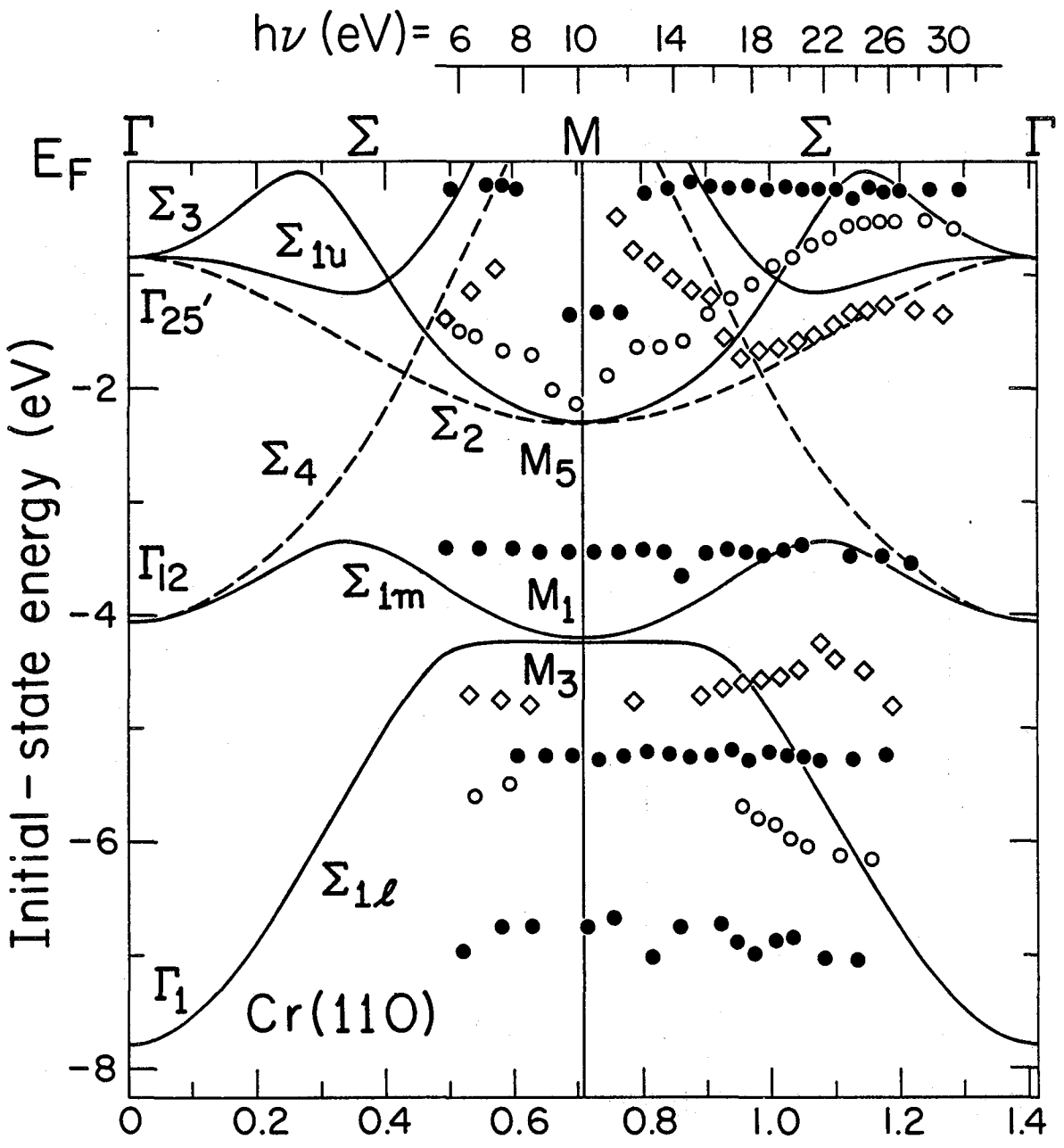

XBL8110-7380

Figure 12

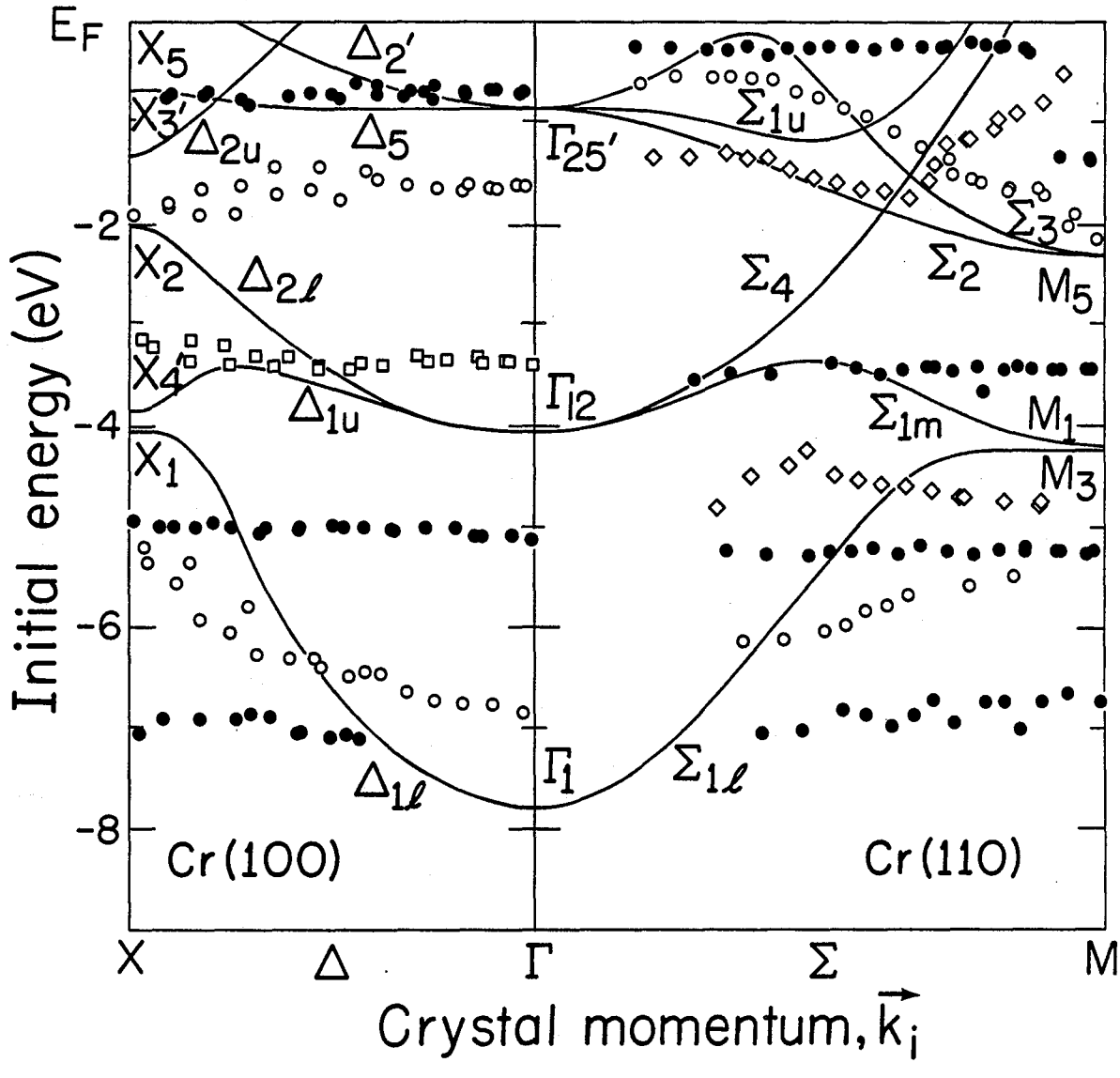

Figure 13

XBL8110-7383

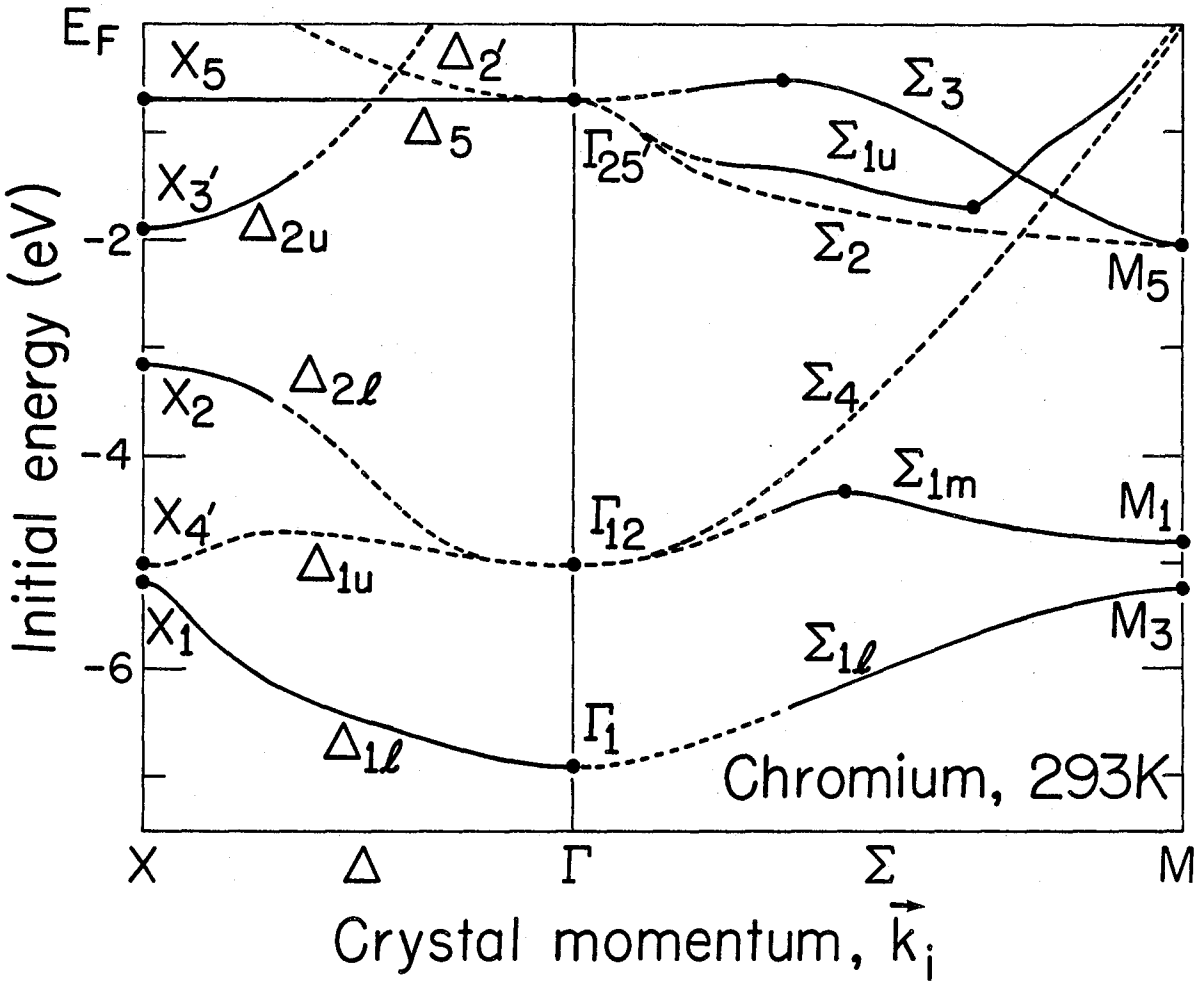

XBL 8111-12035

Figure 14

PART II.

ATOMIC CROSS SECTION EFFECTS IN VALENCE- AND CORE-LEVEL PHOTOEMISSION

V. PARTICLE-SIZE-INDUCED VALENCE CHANGES IN SAMARIUM CLUSTERS *

In this, and the next chapter, the concept of angular distributions in photoemission is explicitly ignored. The experiments therefore fit into the category of "traditional" atomic effects (mechanisms 2, and 5-7 in Section B.4 of Chapter I). However, it is important to keep in mind that the changes in atomic properties elucidated in this chapter are a direct consequence of the existence of the condensed phase.

A. Introduction

Changes in electronic configuration or orbital occupation numbers with particle size have been predicted theoretically[1] and have been used as a basis for interpreting the photoemission spectra from clusters of platinum-group metals.[2] That electronic configurations will normally change in going from an atom to a bulk metal is clear at the extremes of size. Free atoms have integral configurations, whereas bulk metals, in general, do not. The concept of a size-dependence for the electronic configuration of an isolated particle is therefore so fundamental that it can be considered to be axiomatic. Surprisingly, however, there has been no clear demonstration of this general phenomenon. Gas-phase studies have been limited to clusters of several atoms,[3] below the size-threshold for the effects discussed in this chapter, and surfaces of condensed phase systems yield electronic state energy distributions that differ from the bulk[4-8] but can not be

construed as being directly indicative of the size-dependence axiom. Therefore, a viable approach would involve the study of small metallic clusters in the condensed phase, i.e., supported on inert and amorphous substrates. The nucleation characteristics of many supported metallic-cluster systems produced by vapor deposition are now well-enough understood that these represent ideal systems for electronic-structure studies.[2,9-13] However, size-dependent changes in core-level binding energies or valence-level intensities, such as observed in photoemission studies of clusters reported to date, are subject to various interpretations[13] and cannot be considered as proof of electronic configuration changes. In this chapter, we report the first definitive example of change in electronic configuration with particle size. This has been accomplished by measuring both core- and valence-level photoemission from samarium clusters on carbon substrates.

Sm has several characteristics which make it uniquely suited for a study of this type. The free Sm atom has a divalent $[(Xe)4f^6 6s^2]$ configuration compared with the trivalent $[(Xe)4f^5(6s5d)^3]$ ground state of the bulk metal. These states are separated by 2.2 eV in the isolated atom,[14] but the divalent state (2^+) is known to be nearly degenerate with the trivalent (3^+) state in metallic Sm (Refs. 15 and 16). At the surface of the metal, the change in local symmetry and reduced coordination number generates a perturbation of the Fermi level (E_F) and the valence bands large enough that the nearly degenerate 2^+ and 3^+ states are both observed in condensed-phase photoelectron spectra of Sm (Refs. 17-21).

Additionally, these two states coexist in intermediate-valence materials such as SmB_6 (Refs. 19 and 22). On these grounds alone, one might anticipate a significant particle-size-dependent effect in the valence configuration. Furthermore, like all rare-earth metals, Sm is unique in that the 4f electrons lie near E_F but are highly localized (atomic radial maximum of 0.32 Å, Ref. 23). In fact, the 4f levels are so localized that they behave like highly-correlated core electrons.[24] This has two consequences of major importance to the facility of electronic configuration elucidation in the present work: (1) the core-level spectra of the divalent and trivalent configurations show a large (2+) - (3+) separation of 7.6 eV,[17] and (2) the 4f photoemission final-state multiplet structures, $4f^5$ and $4f^4$, permit a clear distinction between the two possible initial-state configurations.[18-20] Thus, the physics that facilitates the observation of valence changes in Sm clusters is that of the 4f levels: they do not participate directly in chemical bonding, but their final-hole-state structure and strong chemical-shift or screening effects represent direct "fingerprints" of valence electronic configuration.

The remainder of this chapter is divided as follows: Section B contains a discussion of experimental procedures. In Section C, results are presented, and a general discussion is found in Section D. Finally, Section E gives a summary.

B. Experimental

The main experimental procedure in these studies was to measure core- and valence-level photoemission spectra of samarium clusters of various sizes on amorphous carbon substrates, utilizing both x-ray photoemission (XPS) and ultraviolet photoelectron spectroscopy (UPS). The XPS spectra were recorded with a Hewlett-Packard 5950A ESCA spectrometer,[25] which utilizes a monochromatized Al Kα ($h\nu$ = 1486.6 eV) radiation source and had been modified previously to enable operation under ultra-high vacuum conditions (see Chapter I, Section C). The UPS spectra were recorded with a cylindrical mirror analyzer at a photon energy of 60 eV. The monochromatization at 60 eV was achieved by utilizing a toroidal grating monochromator in conjunction with synchrotron radiation from the Tantalus I storage ring at the University of Wisconsin, Synchrotron Radiation Center. This photon energy was chosen to maximize resolution and count rate. It is well known, for example, that the 4f levels in rare-earth metals have very small photoemission cross sections near threshold.[24] The base pressures in both instruments were in the mid-10^{-11} to low-10^{-10}-torr region. Prior to cluster preparation, the substrates were cleaned *in situ* by Ar^+ etching, followed by electron bombardment annealing (ca. 1000-1050K) to remove Ar implanted by the etching procedure. The resulting surfaces showed no indication of oxygen or any other contaminants, as monitored by impurity core-level XPS and Auger electron spectroscopy in the XPS and UPS instruments, respectively. The clusters were prepared *in situ* by slow (ca. 10-30 min per cluster system) vapor

deposition of Sm metal from a tungsten filament, which caused the pressure to rise into the low-10^{-9}-torr region during deposition. Under similar conditions, it is known that vapor deposition of Group VIII and IB metals gives rise to cluster formation, with a mean cluster size proportional to the total overlayer coverage.[9,12] The coverages in these Sm experiments were monitored by a quartz-crystal oscillator and subsequently checked by neutron activation analysis. Additionally, the coverages were monitored in the XPS instrument by measuring relative intensities of the C(1s) and various Sm core-level lines. Throughout the XPS experiments, all accessible Sm photoemission lines were measured, but only the Sm($3d_{3/2}$) and Sm($3d_{5/2}$) lines, which are simplest to analyze because they are relatively free of complicated structures induced by the multiplet interaction with the open 4f shell,[17] will be discussed below. The UPS studies probed only the valence region [(6s5d) and 4f].

Incidentally, Sm metal, like most rare earths, is extremely reactive with residual gases (especially oxygen) in vacuo,[26] and simple arguments suggest that the clusters are even more reactive. Therefore, great care was taken to insure that the clusters remained oxygen-free throughout the measurements. During the XPS measurements, possible oxygen contamination was monitored continuously via the O(1s) photoemission line. Finally, a note about the structure of samarium clusters is in order: Fig. 1 shows a transmission electron micrograph of Sm clusters (measured under different vacuum conditions in an instrument at Kodak Research Laboratories[27]) corresponding to a

coverage of 2.0×10^{15} atoms cm^{-2}, and a mean particle size of 30 ± 10 Å as estimated from the micrograph. The nucleation and growth processes appear to be very similar to those observed in Group VIII and IB metals.[12] During the photoemission experiments, identical results obtained from different areas of the surface served as assurance that the cluster distribution (like the one shown in Fig. 1) was uniform throughout the surface area probed.

C. Results

Because of their large photoemission cross section, the $Sm(3d_{3/2,5/2})$ lines were relatively easy to measure with good statistics at low Sm surface concentrations. A strong coverage dependence of the electronic configuration is clearly seen in Fig. 2, which shows these spectra for various coverages including the bulk metal. The predominance of the 2^+ species at low coverages is clearly observed and remains almost constant for coverages below $(2\text{-}3) \times 10^{15}$ atoms $\cdot$ cm^{-2}. Above this coverage region the 3^+ intensity increases rapidly until a bulklike spectrum is achieved at about 1.2×10^{16} atoms cm^{-2}. The $3^+/2^+$ intensity ratio is plotted graphically (filled circles) in Fig. 3 as a function of coverage.

For these clusters, valence region photoemission intensity was too weak to be measured accurately with Al $K\alpha$ radiation. However, the UPS spectra shown in Fig. 4 for $h\nu = 60$ eV (after subtraction of the carbon background) clearly identify the 4f levels. In these spectra, peaks C, D, and E are due to the $4f^4$ final-state multiplets produced

by ionization of trivalent Sm.[19] Peaks A and B are primarily due to the $4f^5$ multiplets from divalent Sm with some contribution to A from 5d and 6s photoemission. The qualitative trends in valence-region spectra with coverage are very similar to those of the Sm(3d) levels discussed above. As shown graphically in Fig. 3 (crosses), the variation of valence state with coverage, as determined from intensities in the UPS spectra in Fig. 4, is nearly identical to the XPS results. The UPS results are meant to be qualitative in regard to the absolute 3+/2+ ratio and the UPS data in Fig. 3 show the peak-C/peak-A intensity ratio which has been normalized to the XPS value at a coverage of 2.6×10^{15} atoms cm^{-2}.

D. Discussion

The data plotted in Fig. 3 would appear to show a striking demonstration of a Sm cluster size dependence of the electronic configuration (3+ vs 2+) that is clearly observed in both the XPS and UPS spectra. We will see below that this is indeed the most reasonable conclusion. However, several possible competing mechanisms for the observed photoemission peak structures must nonetheless be considered. The close agreement between the two sets of data rules out the possibility that the 2+ peaks in XPS are low-binding-energy satellites due to final-state screening effects[28] ("shakedown") of the type observed weakly in some rare-earth metals.[29] This possibility seemed unlikely, even in the absence of the UPS results, because of the high intensity of the 2+ peak. On the contrary, one might postulate that the small

3+ contribution in the low-coverage XPS spectra is due to a 4f-to-valence "shakeup" satellite associated with the 2+ initial state. Some evidence for such a shakeup satellite appears in the 4d spectrum of metallic Eu.[30] An alternative explanation for the residual Sm(3d) 3+ intensity at low coverages is oxide formation resulting from oxygen contamination below our detection limits.

It is important to note that either of the two satellite-producing mechanisms discussed above would yield peak structures that would be difficult or impossible to separate from the main 3+ or 2+ lines in the Sm(3d) spectra. This is illustrated diagrammatically for $Sm(3d_{5/2})$ in Fig. 5. In the case of a bulk final-state screening effect [Fig. 5(a)], we would expect a shakedown satellite (S_a) to appear on the low-binding-energy side of the 3+ peak and separated from it by an amount approximately equal to: $\Delta(E_B) - \Delta_+(3^+ \rightarrow 2^+)$, where $\Delta(E_B) = E_B(3^+) - E_B(2^+)$ is the difference in $Sm(3d_{5/2})$ binding energies for trivalent and divalent initial states and $\Delta_+(3^+ \rightarrow 2^+)$ is the energy required to excite the lowest $3^+ \rightarrow 2^+$ electronic transition in the bulk metal;[31] i.e., $\Delta_+(3^+ \rightarrow 2^+) = E[3d^{10}4f^6(6s5d)^2] - E[3d^{10}4f^5(6s5d)^3]$. A satellite, S_a, would be virtually indistinguishable[20] from the $Sm(3d_{5/2})$ 2+ peak because Δ_+ as measured by bremsstrahlung isochromat spectroscopy (BIS)[15,20] is about 0.5 eV. Analogously, a shakeup satellite (S_b) involving the 2+ initial state [Fig. 5(b)] would appear on the high-binding-energy side of the $Sm(3d_{5/2})$ 2+ line, separated by an amount given by: $\Delta(E_B) + \Delta_-(2^+ \rightarrow 3^+)$, where $\Delta_-(2^+ \rightarrow 3^+) = E[3d^{10}4f^5(6s5d)^3] - E[3d^{10}4f^6(6s5d)^2]$ is the energy required to

excite the lowest $2^+ \rightarrow 3^+$ electronic transition from a divalent ground state.[31] This excitation energy is probably less than 1 eV for the divalent ground state on the surface of Sm metal.[20] Thus, a shakeup satellite might very likely be convoluted with the true 3^+ line for a Sm cluster.

The possibility of the 2^+ state resulting from the formation of a divalent carbide was also considered. Divalent samarium carbide can be made from the elements at high temperature (1675-1875K),[32] and its formation under the conditions used here cannot be ruled out a priori. We find no evidence for carbide formation such as changes in the C(1s) spectrum. For comparison, in studies of reactive Al and Fe films the formation of a carbide is immediately obvious from the change in C(1s) line shape.[33] No such anomalies were observed in Sm clusters until the samples were heated to ~ 775K, at which time a weak shoulder appeared on the low-binding-energy side in the region characteristic of carbide carbon. Furthermore, it can be shown that changes in the $3^+/2^+$ ratio shown in Fig. 3 are much too abrupt to result from carbide formation at the cluster-support interface. The observed slope must result from a collective effect such as a size-dependent electronic configuration.

It is clear from both the XPS and UPS spectra that Sm exists primarily in the divalent state at coverages below (3-4) x 10^{15} atoms cm^{-2}. From the electron microscopy studies,[27] we estimate that a coverage of ~ 2 x 10^{15} atoms cm^{-2} corresponds to a mean particle size of 30 ± 10 Å. This also corresponds to the coverage range where the

photoemission spectra of the noble and platinum-group metals begin to show bulklike characteristics.[2,10,11]

At higher coverages of ~ 10^{16} atoms cm^{-2}, the clusters are no longer discrete but have coalesced to form a semicontinuous film with a very high surface-to-volume ratio. The approximate surface-to-bulk atom ratio is shown along the top of Fig. 3. The known stabilizing effect of a surface for the divalent species causes the 3+/2+ ratio to remain below that of the bulk even at these high coverages where the transition and noble metals have achieved most of their bulklike properties. As illustrated schematically in Fig. 6, the stability of the divalent state in small clusters and on surfaces can be accounted for by a narrowing of the valence band as a result of reduced coordination. This raises the Fermi energy relative to the 4f levels and thus shifts a valence electron to populate the $4f^6(2+)$ state.[17] There is still some question, however, concerning the possible coexistence of divalent and trivalent species on the surface in either homogeneous or inhomogenous phases.[17-21]

The only previously reported studies of size-dependent configurations in rare earths were based on x-ray emission and bond-distance changes as determined by electron diffraction.[34] In the divalent metals Eu and Yb, a discontinuous lattice contraction at small sizes was taken to indicate a change from the 2+ to 3+ configuration. Surface tension was proposed as the mechanism for the lattice contraction, which raised the 4f levels relative to the Fermi level and caused a 4f electron to transfer to the conduction band. However, the vacuum

conditions for these experiments were so poor that the results are highly questionable.[35] Understandably, increased surface tension in small clusters favors the trivalent state. The competing factors of band broadening induced by surface tension and band narrowing as a result of reduced coordination will determine the actual electronic configuration for any specific small cluster. For samarium we have shown that band narrowing is the dominant effect, and thus the divalent state is dominant in these small clusters.

Changes in configuration with particle size should be a general feature of the rare-earth metals. All of the rare earths except cerium, gadolinium, and lutetium are divalent in the free atoms and except for europium and ytterbium are trivalent in the bulk metals. The remaining nine rare-earth elements must undergo a configuration change from 2^+ to 3^+ with increasing particle size. The size at which the changeover occurs is likely to depend upon the energy required to excite a conduction electron to the lowest empty 4f level.[16] In the notation of Herbst, et al.,[16] this energy is given by $\Delta_+(f^n \rightarrow f^{n+1}) = E[4f^{n+1}(6s5d)^{m-1}] - E[4f^n(6s5d)^m]$, where n and m are the 4f and valence-band occupancies, respectively, in the ground state of the metal. In Fig. 7, we illustrate graphically Δ_+ values obtained spectroscopically (BIS) by Lang, et al.,[15] throughout the rare-earth series. Simplistically, the value of Δ_+ reflects a tendency for the 4f shell to approach a more nearly half- or completely-filled configuration by increasing the 4f electron population by one electron, with concomitant smallest values for Sm and Tm. The transition from 2^+ to 3^+ is

expected to occur at a larger particle size for those elements with a smaller Δ_+. The value of this parameter for Sm is small enough that it is not surprising that the divalent state is stabilized by the Sm surface, or in relatively large clusters. It would be interesting to draw a correlation between data like the points plotted in Fig. 3 and the values of Δ_+, for the entire rare-earth series.

For the sake of completeness, values of $\Delta_-(f^n \rightarrow f^{n-1}) = E[4f^{n-1}(6s5d)^{m+1}] - E[4f^n(6s5d)^m]$ from the BIS studies of Lang, et al.[15] are also plotted in Fig. 7. This parameter is the minimum energy required to excite a 4f electron into the conduction band. To the extent that the photoemission process yields adiabatic final states, Δ_- is obtained directly from the energy position of the 4f levels relative to E_F in photoemission energy distribution curves. In fact, theoretical values of Δ_- calculated by Herbst, et al.[16] are in excellent agreement with the experimental 4f positions plotted in Fig. 7. However, it is important to discern Δ_- from one-electron orbital (band) energies (ϵ_{4f}). As alluded to above, correlation, screening, and relaxation effects in the 4f photoemission final state result in a nearly complete breakdown of the one-electron approximation for the localized 4f shell: values of ϵ_{4f} disagree severely with Δ_- measurements.[24] Nonetheless, this has a pleasing consequence on Sm core-level photoemission spectra, as observed and also discussed above: the 4f levels play such a strong role in determining the observed binding energies of the core electrons that the 2+ ($4f^6$) and 3+ ($4f^5$) states yield core-level spectra that are easily isolated from each other. We note the

contrast in facility of XPS data reduction between these spectra and those arising from surface core-level binding energy shifts.[4]

E. Summary and Conclusions

In summary, we have shown, for the first time, an unambiguous example of size-dependent electronic configurations. Both XPS [Sm($3d_{3/2,5/2}$)] and UPS [Sm(4f)] spectra show a predominance of the atomiclike divalent state at small particle size. With increasing size, the bulklike 3+ state is formed, but a large divalent contribution from surface atoms remains. The transition from 2+ to 3+ valence state occurs over a relatively small range of cluster sizes, indicating that the effect is indeed collective as would be expected for a change in electronic configuration, and not simply related to macroscopic quantities such as the surface-to-volume ratio or the cluster-substrate contact area. We anticipate similar experiments with other elements in the rare-earth series, especially Tm. Finally, these results may have significant implications for understanding the particle-size-dependence of demanding reactions in heterogeneous catalysis. In such systems involving transition-metal clusters we may reasonably expect that electronic configurations will change in the same size region as observed here for Sm.

REFERENCES

* This chapter is based on experiments performed in collaboration with M. G. Mason, S.-T. Lee, G. Apai, D. A. Shirley, A. Franciosi, and J. H. Weaver; published in Phys. Rev. Lett. 47, 730 (1981). XPS results were obtained at U. C. Berkeley (Mason, Davis, and Shirley), while UPS work was performed at the Univ. of Wisconsin, Synchrotron Radiation Center (Lee, Apai, Franciosi, and Weaver). To preserve the continuity of this topic, both XPS and UPS results are included, here.

1. R. C. Baetzold, in Catalysis in Chemistry and Biochemistry. Theory and Experiment, edited by B. Pullman (D. Reidel, Boston, MA, 1979), p. 191-206, and references therein.
2. M. G. Mason, L. J. Gerenser, and S. T. Lee, Phys. Rev. Lett. 39, 288 (1977).
3. T. G. Dietz, M. A. Duncan, D. E. Powers, and R. E. Smalley, J. Chem. Phys. 74, 6511 (1981).
4. P. H. Citrin, G. K. Wertheim, and Y. Baer, Phys. Rev. Lett. 41, 1425 (1978).
5. T. M. Duc, C. Guillot, Y. Lassailly, J. Lecante, Y. Jugnet, and J. C. Vedrine, Phys. Rev. Lett. 43, 789 (1979).
6. F. J. Himpsel, P. Heimann, T.-C. Chiang, and D. E. Eastman, Phys. Rev. Lett. 45, 1112 (1980), and references therein.
7. S. Brennan, J. Stöhr, R. Jaeger, and J. E. Rowe, Phys. Rev. Lett. 45, 1414 (1980).

8. See, for example, R. F. Willis and B. Feuerbacher, in Photoemission and the Electronic Properties of Surfaces, edited by B. Feuerbacher, B. Fitton, and R. F. Willis (Wiley, New York, 1978).

9. M. G. Mason and R. C. Baetzold, J. Chem. Phys. 64, 271 (1976); R. C. Baetzold, M. G. Mason, and J. F. Hamilton, ibid. 72, 366 (1980).

10. S.-T. Lee, G. Apai, M. G. Mason, R. Benbow, and Z. Hurych, Phys. Rev. B 23, 505 (1981).

11. G. Apai, S.-T. Lee, and M. G. Mason, Solid State Commun. 37, 213 (1981).

12. J. F. Hamilton and P. C. Logel, Thin Solid Films 23, 89 (1974).

13. W. F. Egelhoff and G. G. Tibbetts, Solid State Commun. 29, 53 (1979); Phys. Rev. B 19, 5028 (1979).

14. J. Blaise, C. Morillon, M. G. Schweighofer, and J. Verges, Spectrochim. Acta, Part B: 24, 405 (1969).

15. J. K. Lang, Y. Baer, and P. A. Cox, Phys. Rev. Lett. 42, 74 (1979); J. Phys. F 11, 121 (1981).

16. J. F. Herbst, R. E. Watson, and J. W. Wilkins, Phys. Rev. B 17, 3089 (1978), and references therein.

17. G. K. Wertheim and G. Crecelius, Phys. Rev. Lett. 40, 813 (1978).

18. G. K. Wertheim and M. Campagna, Chem. Phys. Lett. 47, 182 (1977).

19. J. W. Allen, L. I. Johansson, R. S. Bauer, I. Lindau, and S. B. M. Hagström, Phys. Rev. Lett. 41, 1499 (1978); J. W. Allen, L. I. Johansson, I. Lindau, and S. B. Hagstrom, Phys. Rev. B 21, 1335 (1980).

20. J. K. Lang and Y. Baer, Solid State Commun. 31, 945 (1979).

21. R. Rosei, J. H. Weaver, M. Campagna, W. Gudat, F. Hulliger, and H. Bach, Bull. Am. Phys. Soc. 25, 237 (1980).

22. J.-N. Chazalviel, M. Campagna, G. K. Wertheim, and P. H. Schmidt, Phys. Rev. B 14, 4586 (1976).

23. J. B. Mann, Los Alamos Scientific Laboratory Report LA-3691 (1968).

24. See, for example, M. Campagna, G. K. Wertheim, and Y. Baer, in Photoemission in Solids II, edited by L. Ley and M. Cardona (Springer-Verlag, New York, 1979).

25. See Refs. 82 and 87 in Chapter I.

26. See, for example, P. O. Hĕden, H. Löfgren, and S. B. M. Hagström, Phys. Rev. Lett. 26, 432 (1971).

27. Because of the reactivity of samarium and its tendency to aggregate, evaporated overlayers were made to inhibit such effects.

28. J. C. Fuggle, M. Campagna, Z. Zolnierek, R. Lässer, and A. Platau, Phys. Rev. Lett. 45, 1597 (1980).

29. G. K. Wertheim and M. Campagna, Solid State Commun. 26, 553 (1978); G. Crecelius, G. K. Wertheim, and D. N. E. Buchanan, Phys. Rev. B 18, 6519 (1978); J. F. Herbst, J. M. Burkstrand, and J. W. Wilkins, Phys. Rev. B 22, 531 (1980).

30. S. P. Kowalczyk, N. Edelstein, F. R. McFeely, L. Ley, and D. A. Shirley, Chem. Phys. Lett. 29, 491 (1974).

31. It should be pointed out that Δ neglects multiplet coupling, i.e., we restrict our attention to the minimum energy difference between the initial- and final-state configurations. See Refs. 15, 20, and 29.

32. J. M. Haschke and T. A. Deline, Inorg. Chem. 19, 527 (1980).

33. R. C. Baetzold, private communication.

34. C. Bonnelle and F. Vergand, J. Phys. Chem. Solids 36, 575 (1975), and references therein.

35. The Eu and Yb were evaporated on Al and Ti substrates at pressures in the 10^{-6}-to-10^{-5}-torr range.

FIGURE CAPTIONS

Fig. 1. Transmission electron micrograph of samarium clusters on carbon at a coverage of 2.0×10^{15} atoms cm^{-2} and with an estimated mean particle size of 30 ± 10 Å. The scale is given at the lower left.

Fig. 2. Al Kα x-ray photoemission energy distribution curves for the 3d region of carbon-supported samarium clusters at various coverages (atoms cm^{-2}). The abscissa is scaled in binding energy (E_B^F) relative to the Fermi level, where the latter energy position was determined from the measured C(1s) kinetic energy position and its known E_B^F value.

Fig. 3. Sm trivalent (3+) - divalent (2+) intensity ratio as a function of coverage and estimated surface-to-bulk atom ratio. XPS values (closed circles) were determined from $Sm(3d_{5/2})$ peak intensities, and UPS values (crosses) were determined from the peak C and A intensities (see Fig. 4). UPS data have been normalized to the XPS data at a coverage of 2.6×10^{15} atoms cm^{-2}.

Fig. 4. Photoemission difference spectra of the 4f and valence-band region of carbon-supported samarium clusters at a photon energy of 60 eV and various coverages (atoms cm^{-2}); the carbon background intensity has been subtracted.

Fig. 5. Diagrammatic representation of hypothetical (a) shakedown (S_a) and (b) shakeup (S_b) satellite energy positions with respect to the divalent (2+) and trivalent (3+) $Sm(3d_{5/2})$

peaks in the x-ray photoemission energy distribution curve. The satellites, S_a and S_b, would be difficult to distinguish experimentally from the 2+ and 3+ lines, respectively, because the values of both $\Delta_+(3^+ \rightarrow 2^+)$ and $\Delta_-(2^+ \rightarrow 3^+)$ are probably smaller than the experimental energy (FWHM) resolution.

Fig. 6. Schematic representation of the effect of Sm valence-band narrowing in clusters and on surfaces relative to the bulk metal: the Fermi energy (E_F) is raised relative to the 4f levels, thereby shifting a valence electron to populate the $4f^6$ (divalent) state.

Fig. 7. Plots of Δ_+ and Δ_- as functions of rare-earth metal, from BIS measurements (Ref. 15). These parameters are defined as the minimum energy to increase (Δ_+) and to decrease (Δ_-) by one electron the population of the 4f shell. The values are plotted relative to E_F with Δ_- defined as a negative quantity (see, also, Ref. 31).

XBB 818-7823

Figure 1

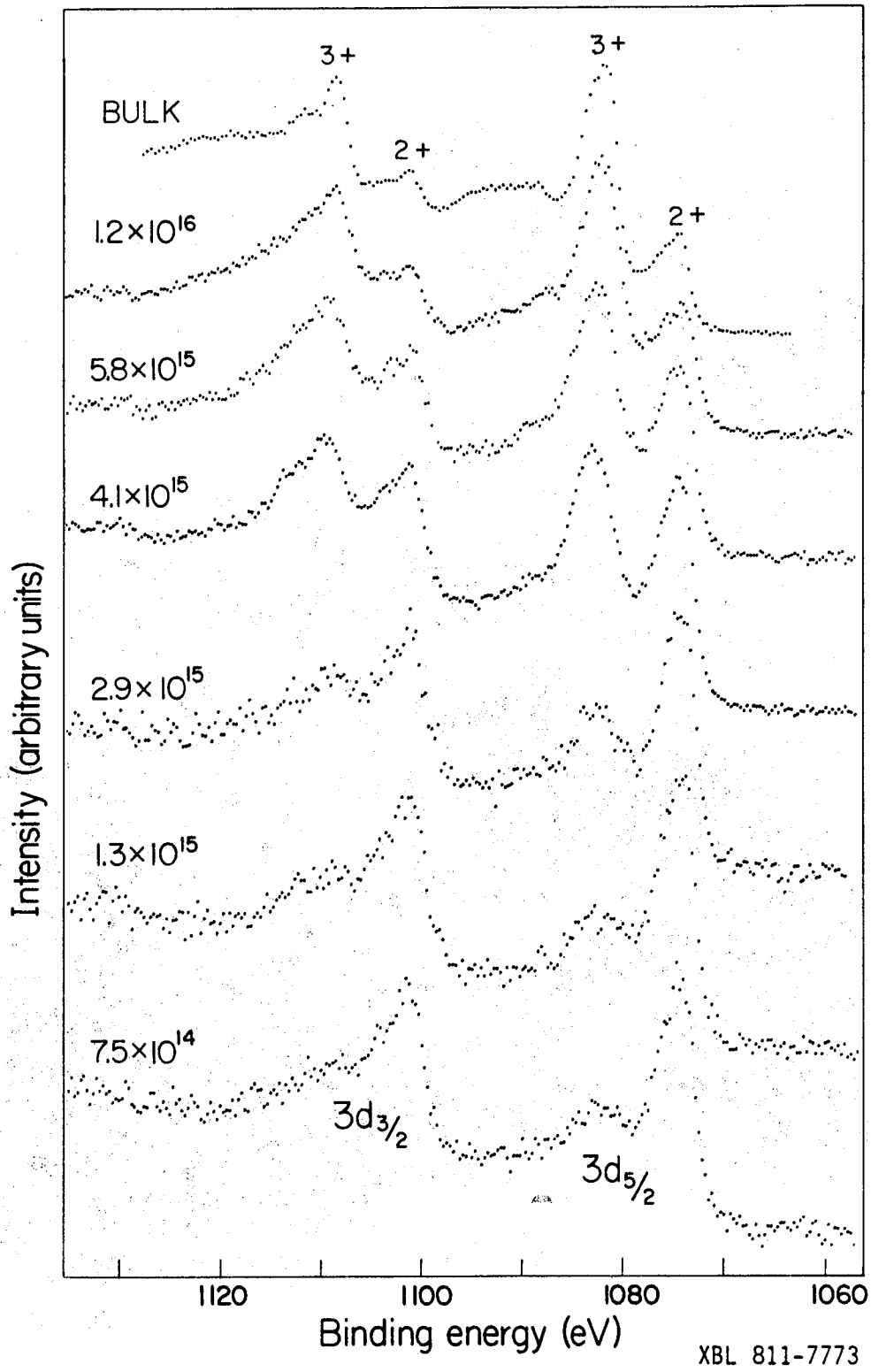
3+
3+
BULK
2+
2+
1.2×10^16
5.8×10^15
4.1×10^15
2.9×10^15
1.3×10^15
7.5×10^14
3d3/2
3d5/2
Intensity (arbitrary units)
1120
1100
1080
1060
Binding energy (eV)
XBL 811-7773

Figure 2

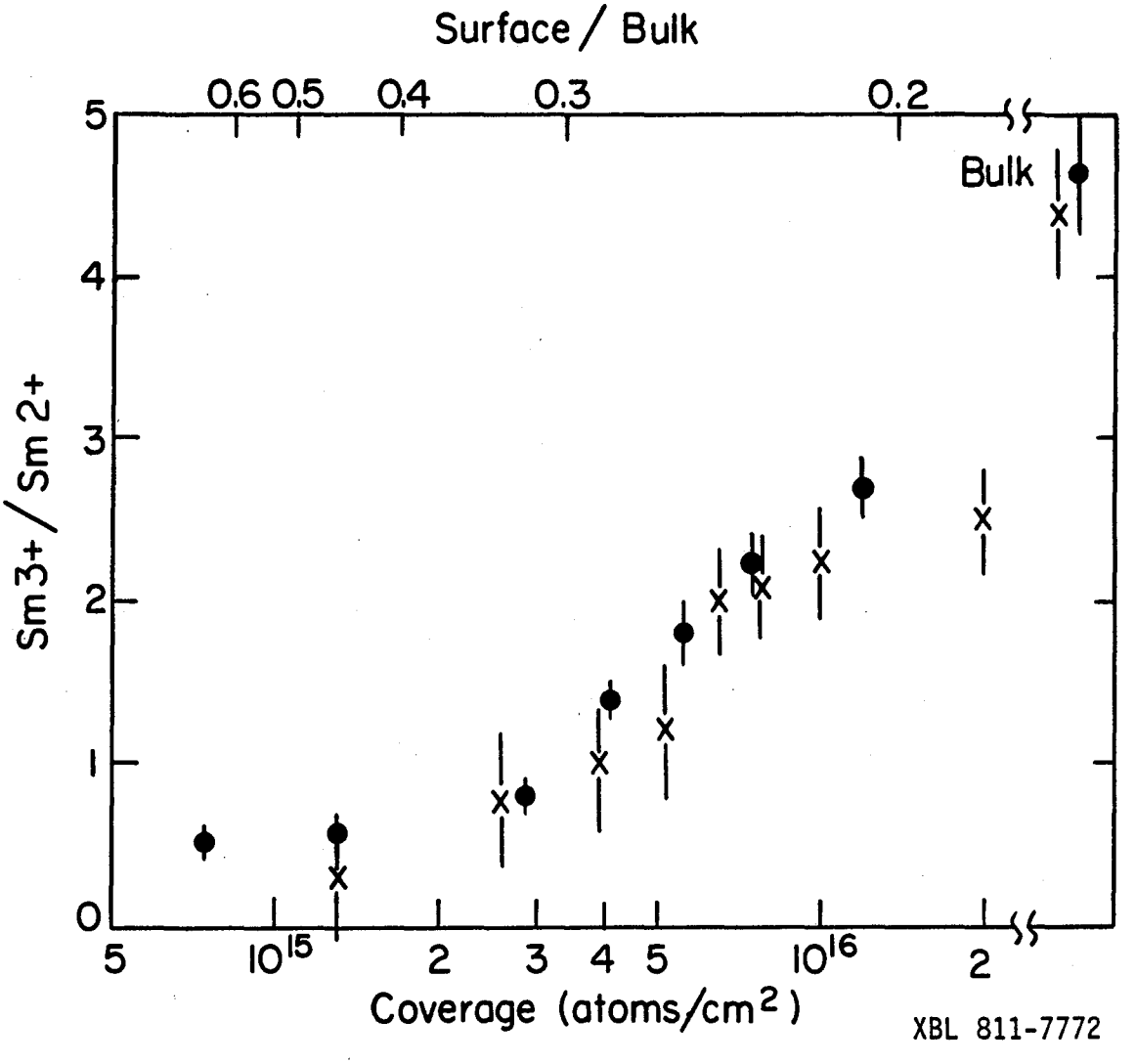
Surface / Bulk
0.6 0.5 0.4 0.3 0.2
Bulk
Sm3+ / Sm 2+
0
1
2
3
4
5
5 10^15 2 3 4 5 10^16 2
Coverage (atoms/cm^2)
XBL 811-7772

Figure 3

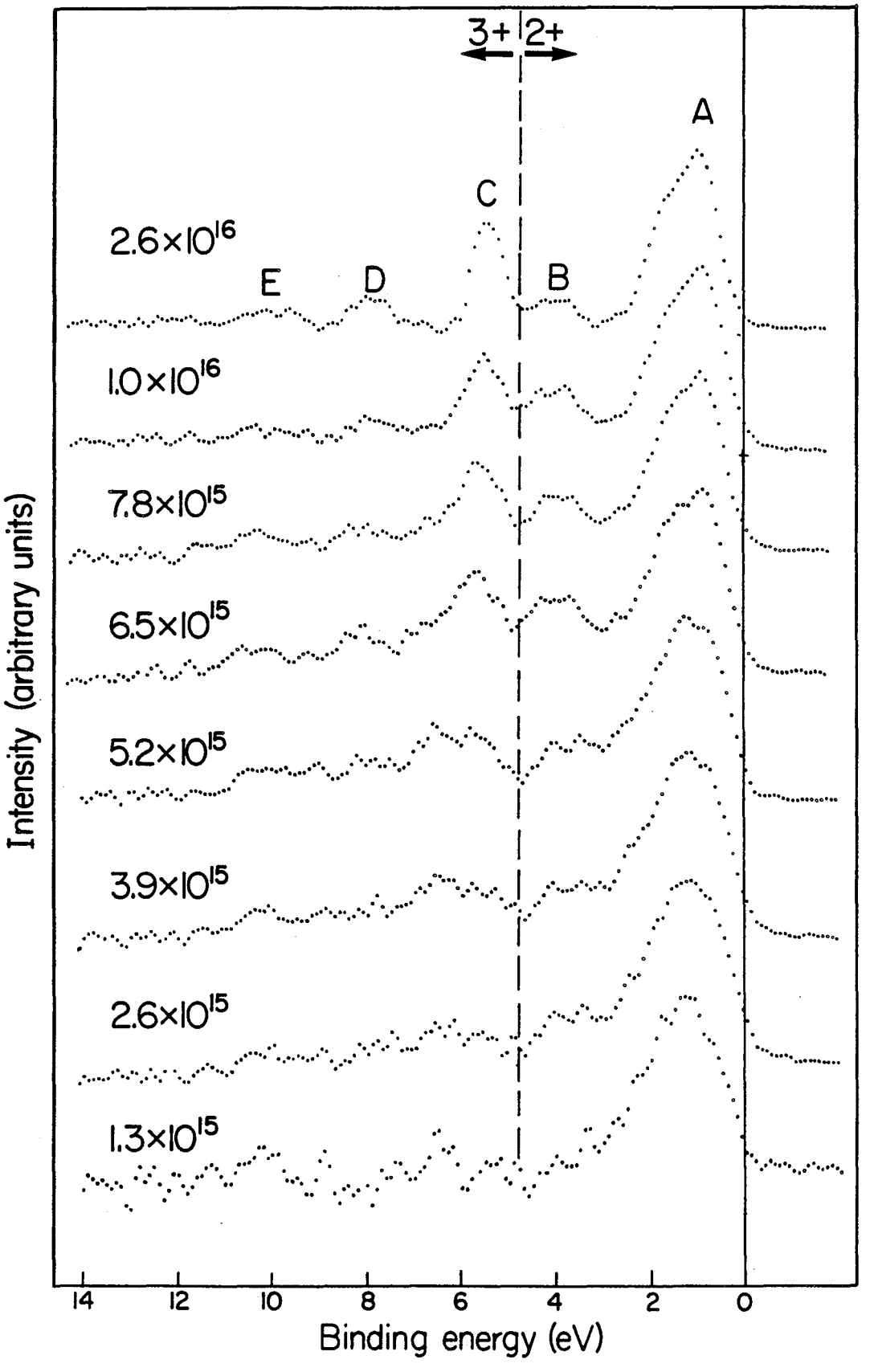

XBL 815-9592

Figure 4

Sm($3d_{5/2}$) region, low coverages

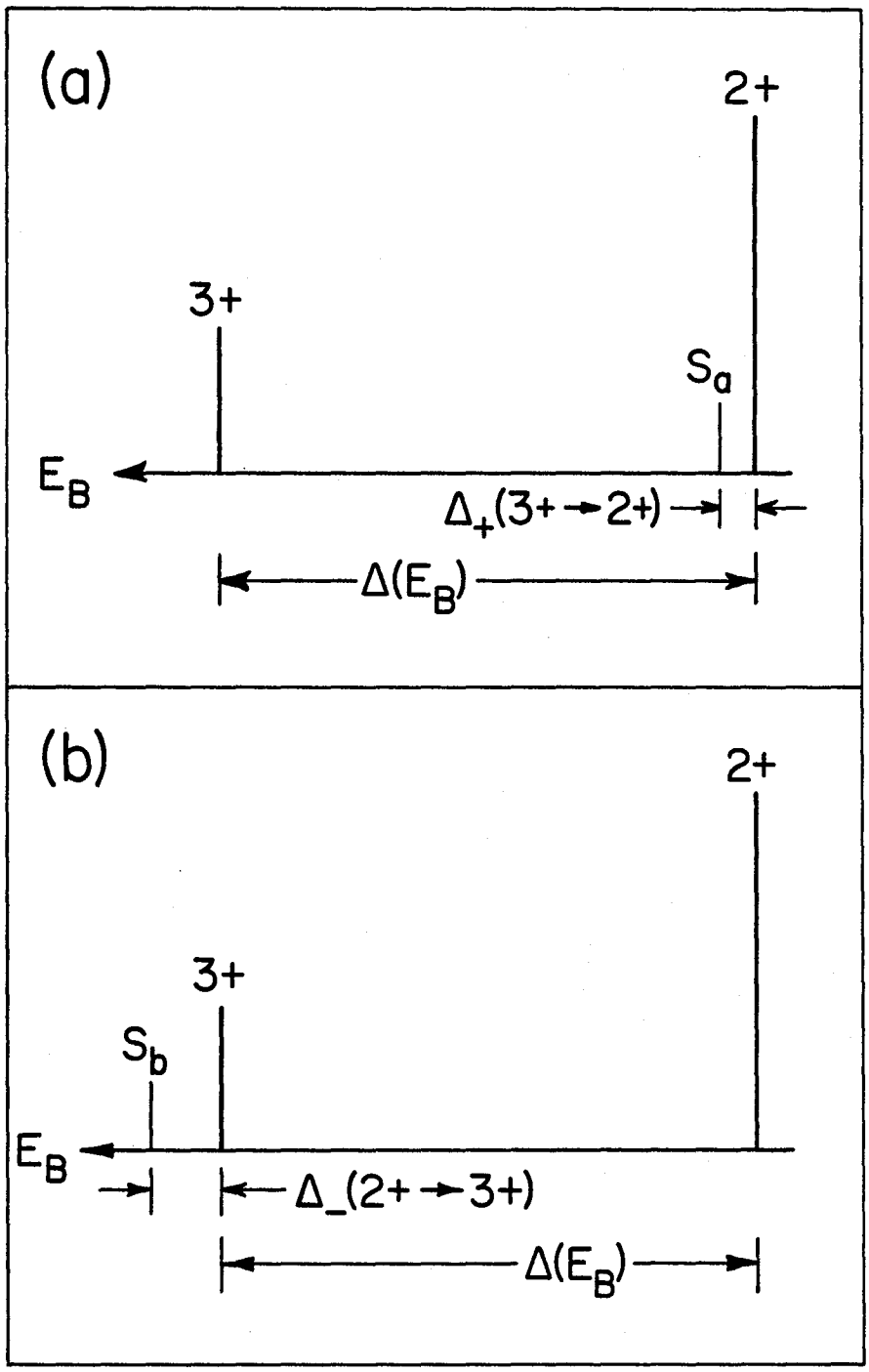

XBL 821-7560

Figure 5

EFFECTS of BAND NARROWING

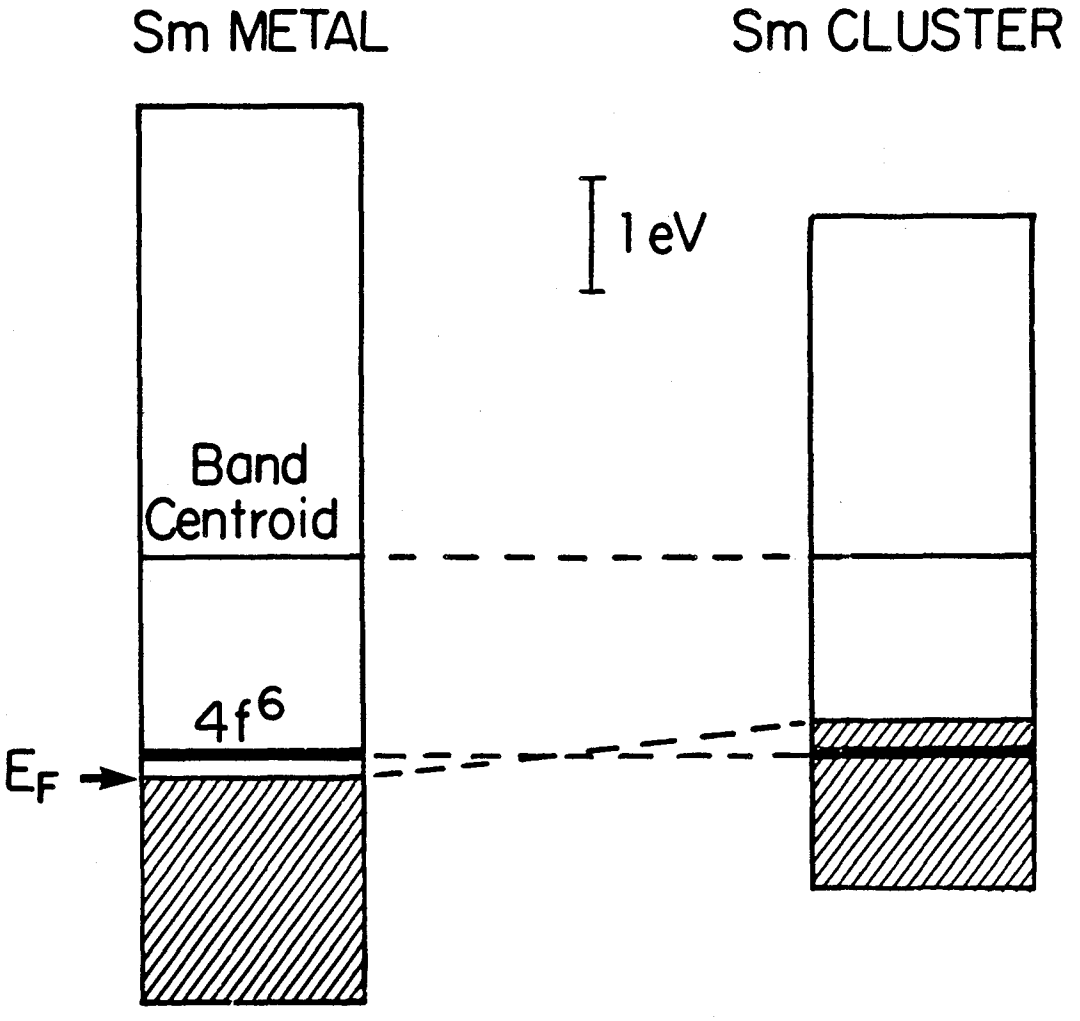

XBL 818-11421

Figure 6

MINIMUM ENERGY REQUIRED TO INCREASE (Δ_+) AND TO DECREASE (Δ_-) BY ONE ELECTRON THE POPULATION OF THE 4f SHELL IN THE RARE EARTH METALS.

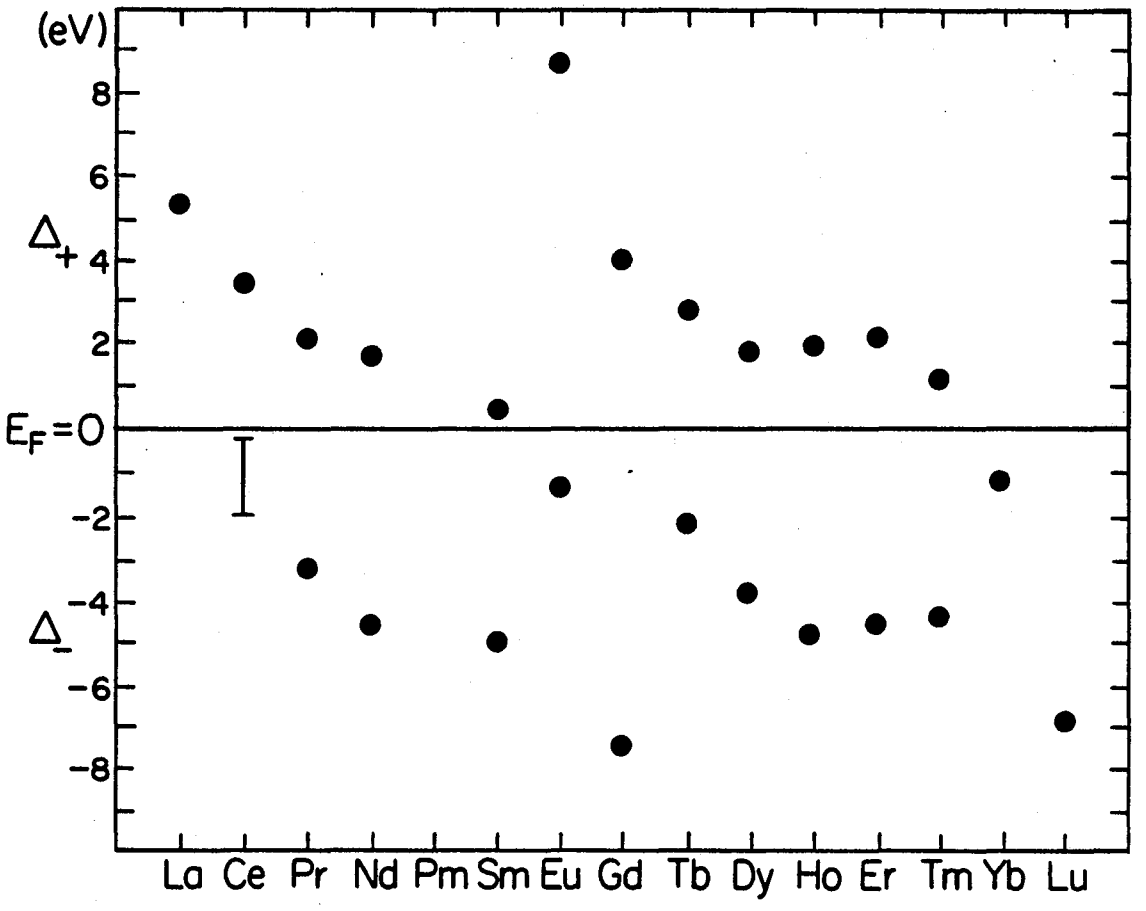

XBL 818-11420

Figure 7

VI. COOPER MINIMUM FOR Pd(4d) AND ADSORBATE SENSITIVITY ENHANCEMENT IN PHOTOEMISSION FROM CO-Pd *

A. Introduction

In this chapter, atomiclike effects in the energy dependence of the photoemission cross section $\sigma_{fi}(E_f)$, are investigated by means of angle-integrated photoemission from the valence band (VB) region of palladium. It will subsequently be demonstrated that the atomic effects in $\sigma_{fi}(E_f)$ for Pd as a substrate can be utilized to enhance the sensitivity of valence region photoemission to the adsorbate molecular-orbital-derived levels for the system CO-Pd. The experiments with this adsorbate-substrate system represent the most dramatic demonstration of this phenomenon to date, and will be compared with previous studies of other systems.

The experiments discussed in Part I of this thesis illustrated via angle-resolved photoemission the itinerant nature of valence bands in metals. The single most important mechanism governing the angle-resolved photoemission intensity [Eq. (9) in Chapter I] was $\vec{k}$-conservation. However, it was also shown (Chapter I) that various mechanisms, both intrinsic and extrinsic, can lead to an effective breakdown of $\vec{k}$-conservation. The resulting angle-resolved intensity in nearly every case was found to become more dominated by the atomic-like part of the photoemission cross section, which for a plane-wave final state is governed by the expression (Chapter I): $\cos^2\alpha_f|\Phi_n(\vec{k}_f)|^2$. It has already been pointed out (Chapter I) that atomic and itinerant

effects in photoemission can be rationalized as simultaneous mechanisms in most systems. Therefore, we would expect that angle-integrated measurement of the total valence band intensity of a disordered metal yields a photoemission cross section the energy dependence of which is similar to the corresponding atomic cross section. In earlier work, the photon energy variation of d-band photoemission intensity $I(h\nu)$ for Cu,[1] Ag,[1,2] Au,[1,3] Pt,[4] In,[5] and Sb (Ref. 5) indicated that the above expectations were at least qualitatively fulfilled in these systems. More recent studies provide further demonstrations of the importance of atomic effects in the total photoemission cross section of various subshells in condensed phase systems.[6]

The underlying theme of this chapter is the existence and properties of so-called "Cooper minima"[7] in the VB photoemission cross section of 4d and 5d valence-shell metals. Owing to non-hydrogenic behavior of the photoelectric effect, the cross section for certain subshells--those with at least one radial node--can undergo dramatic attenuation well above threshold, i.e., at a Cooper minimum.[7] This is a general phenomenon familiar from absorption studies[8] and more recently from photoemission work,[1-5] and will be illustrated below for Pd(4d). Furthermore, the attenuation of VB photoemission intensity at the substrate Cooper minimum will be shown to yield a dramatic relative enhancement of adsorbate-level intensity in adsorbate-substrate systems, particularly in prototype systems with CO as the adsorbate.

In Section B experimental procedures are discussed. Section C contains results and general discussion. Finally, Section D gives a summary.

B. Experimental

A single crystal of palladium, cut along the (110) plane, was polished to a mean surface roughness of 0.05 μm, etched in hot aqua regia, and mounted in a photoemission chamber with a base pressure of $\leq 2 \times 10^{-10}$ torr. It was cleaned of bulk and surface impurities by cycles of Ar^+ ion bombardment (beam voltage = 1 kV) and annealing (ca. 950K). Immediately preceding the photoemission measurements of the clean surface, extensive Ar^+ etching without annealing was performed to reduce possible angular effects. A similar procedure was also followed prior to the preparation of the CO overlayer, which was achieved by exposing the clean, unannealed Pd surface at ambient (room) temperature to 4 L (1 L = 1×10^{-6} torr sec) of CO. Under these conditions of exposure, the sample should have a monolayer coverage of chemisorbed CO.

The photon source was the 4° port of Beam Line I (BL I-1) at SSRL,[9] with incident radiation in the energy range $40 \text{ eV} \leq h\nu \leq 220 \text{ eV}$. Angle-integrated photoemission (AIP) spectra were collected using a double-pass cylindrical mirror analyzer (CMA) (as discussed in Chapter I and described elsewhere[3,10]) at pass energies of 50 eV and 100 eV for CO-Pd and clean Pd, respectively. For these AIP measurements, of course, a mask over the front of the analyzer was <u>not</u> employed. The crystal orientation was adjusted for maximum photoemission intensity into the 360° acceptance cone of the CMA, yielding $\theta_A = \angle(\vec{n},\vec{A}) = 24.3°$, with the orientation of the CMA symmetry axis fixed at 77.7° relative to the photon beam direction.

This experimental geometry is shown schematically in Fig. 1. Spectra were collected for clean Pd and for Pd + 4 L of CO, with an analyzer energy resolution of 1.6 eV and 0.8 eV FWHM, respectively, and with an approximate 0.3 eV resolution of the synchrotron radiation selected by the "grasshopper" grazing-incidence monochromator.

AIP spectra for CO-Pd at selected photon energies are shown in Fig. 2. These spectra are all characterized by a Pd(4d) valence-band feature peaked near E_B = 2 eV, and adsorbate-induced peaks at $E_B \approx$ 8 eV and 11 eV, attributable to the ($5\sigma + 1\pi$) and 4σ CO molecular orbitals, respectively.[11] At the relatively low resolution used and with AIP from a randomly-oriented surface, it is impossible to distinguish individual Pd valence-band peak structures as was done in Part I, but this is the desired situation here because we only wish to measure <u>total</u> intensities in the main peaks in each spectrum. These intensities (for the clean metal VB as well as the three peaks for the adsorbate-substrate system) were determined as areas under the peaks after normalization to the incident photon flux and the electron analyzer efficiency, and after correcting for the inelastic electron background.

C. Results and Discussion

1. Clean Pd and the Cooper Minimum in $\sigma(h\nu)$.

The relative photoemission intensity of Pd(4d) is illustrated as a function of photon energy in Fig. 3, along with previously measured

curves for Pt(5d),[4] Cu(3d),[1] Ag(4d),[1,2] and Au(5d).[1,3] The variations of $\sigma(h\nu)$ for 3d, 4d, and 5d subshells are fully illustrated in this figure. The scales in Fig. 3 are not absolute, however, nor is $I(h\nu)$ strictly proportional to $\sigma(h\nu)$ because of variations in the escape depth with photon energy. Nonetheless, the behavior of $I(h\nu)$ in Fig. 3 can be understood within the framework of the atomic photoionization process.[7]

Electric dipole selection rules ($\Delta\ell = \pm 1$) allow only p- or f-symmetry partial-wave final states to be reached from d-shell initial states. For the high photon energies of interest here the d $\rightarrow$ f channel dominates over the d $\rightarrow$ p channel, and it will suffice for our purpose to discuss the d $\rightarrow$ f channel. Above threshold the d-band intensities first exhibit maxima in $\sigma(h\nu)$, which for the noble metals occur in the order Au(5d) (< 40 eV), Ag(4d) (≈ 60 eV), and Cu(3d) (≈ 130 eV), and similarly for other members of the 5d, 4d, and 3d series: Pt(5d) $\lesssim 40$ eV and Pd(4d) at ~ 80 eV. These maxima have been observed in absorption studies[8] as well as in photoemission.[1,5] The shift in energy of the maximum arises because, close to threshold, the f radial final-state wave function is held away from the nucleus by a centrifugal barrier proportional to $\ell(\ell + 1)/r^2$, permitting little overlap with the initial-state d function. With increasing energy the continuum f wave penetrates further, giving more overlap with the d function and a larger cross section. Because the d wave functions vary in radial extent in the order 5d > 4d > 3d, the energy of maximum overlap will vary in the reverse order, as observed.

Beyond the maximum the photoelectric cross section simply decreases monotonically with energy for 3d initial states, which have no radial node: this has been observed, for example, in copper.[1] For $n > 3$, however, there are $n - 3$ radial nodes in the nd wave function which cause $\sigma(h\nu)$ to fall more steeply at higher energies. Because the total photoelectric cross section is proportional to the sum of the squares of the $d \rightarrow p$ and $d \rightarrow f$ channel matrix elements, a local minimum occurs at the energy for which one matrix element (generally, that of the $d \rightarrow f$ channel) vanishes. This minimum is referred to as a "Cooper minimum,"[7,12] and may be sharp, as in the 4d case with a single radial node, or it may be smeared out as in the 5d case, which has two radial nodes.

Because the initial-state wave functions for Ag(4d) and Pd(4d) contain a single radial node, the corresponding Cooper minima seen in Fig. 3 at $h\nu \approx 140$ eV and ≈ 130 eV, respectively, are very sharp. With the convention that all wave functions have a positive slope at the origin, the radial dipole matrix element, $R_{\ell+1,\ell} = \langle \varepsilon, \ell+1 | \vec{\nabla} | n\ell \rangle$, is negative at threshold for the $|4d\rangle$ initial state; i.e., $R_{f,d} = \langle \varepsilon, f | \vec{\nabla} | 4d \rangle$ is less than zero. The reason for this is that the final state ($|\varepsilon, f\rangle$), having a wave function corresponding primarily to the unbound level that is occupied in the rare-earth metals (i.e., $|\varepsilon, f\rangle \sim |4f\rangle$), is positive and in a region of large overlap with the negative-going part of the 4d function.[7] Fano and Cooper[7] have shown that all radial matrix elements are positive at the high-energy limit. Therefore, $R_{f,d}$ must go through a change in sign at some intermediate

photon energy; $R_{f,d} = 0$ corresponds to the Cooper minimum. The total 4d photoemission cross section is not zero at the Cooper minimum because the d → p channel still has a finite (albeit small), positive matrix element at this energy. Above the Cooper minimum, $R_{f,d}$ is expected to go through a second maximum before approaching zero asymptotically at higher energies. In the next chapter, it will be shown that the Cooper minimum effect gives rise to interesting properties in the Ag(4d) photoemission angular distribution.

2. CO-Pd and Adsorbate Sensitivity Enhancement.

Photoelectron spectroscopy is a very sensitive technique for studying submonolayer coverages of adsorbate atoms or molecules on catalytic substrates. Using photons in the UV range, adsorbate molecular orbitals with binding energies (E_B's) up to about 20 eV give rise to peaks alongside the substrate valence-band features, with favorable signal/noise ratios.[13-17] This was first demonstrated by Bordass and Linnett,[18] who observed molecular orbital peaks of methanol adsorbed on tungsten in one-to-one correspondence with the gas-phase photoemission peak structures. Since this early work, many similar ultraviolet photoemission experiments have been performed, leading to a large increase in our understanding of adsorbate systems.[13-17] An important factor in this work has always been surface sensitivity, i.e., the spectral intensity of adsorbate-derived levels relative to that of the substrate valence band and associated inelastic-electron background. Surface sensitivity is, however,

usually not optimal with UV sources, and core levels of adsorbates, as well as tightly-bound valence levels, are either energetically inaccessible or unobservable because of their low cross sections. Conventional laboratory photon sources in the x-ray range (e.g., Mg Kα x-rays at 1254 eV) yield photoemission spectra in which the molecular-orbital to valence-band intensity ratio is much smaller,[14,19] although core levels can be readily observed.[13,14,19] It follows, therefore, that the use of any one particular laboratory photon source places severe constraints on the study of adsorbates by photoelectron spectroscopy.

With the availability of an intense source of variable-energy synchrotron radiation in the vacuum-ultraviolet-to-soft-x-ray range at SSRL, it has now become feasible to adjust photon energies to optimize overall sensitivity to surface effects in photoemission spectra.[1] For several reasons it is particularly desirable to extend the photoemission spectroscopy of adsorbate systems to photon energies somewhat above those commonly available with laboratory UV sources; i.e., into the $h\nu$ = 100–150 eV region. A major advantage from the standpoint of surface studies is the maximal surface sensitivity of electron spectroscopy using photoelectron kinetic energies

$$E_f = h\nu - E_B \tag{1}$$

given by photons in this energy range and E_B values of valence-band electrons from the substrate. Figure 4 shows the electron attenuation lengths in relevant metals,[13,20] plotted against energy. Because the

minimum attenuation length in the $E_f \sim 100$ eV region is roughly 3 Å, the substrate valence-band peaks should be sensitive to the first substrate layer and show the effects of adding adsorbate molecules.

Early studies of the molecular-orbital to valence-band area intensity ratios, hereafter termed MO/VB, for the CO-Ni and CO-Pd adsorbate-substrate systems were carried out by Gustafsson, et al.,[11] up to energies of 90-100 eV using synchrotron radiation. These early results were discouraging: the ratio MO/VB dropped by over a factor of 10 for CO-Ni as the photon energy was changed from 40 eV to 90 eV. For CO-Pd, MO/VB dropped from 0.16 at $h\nu = 40$ eV to 0.08 at $h\nu = 80$ eV, then increased very slightly to 0.10 at $h\nu = 100$ eV. What was needed was a method of removing part of the photoemission intensity from the substrate VB, which as we have already seen increases in the 40 to 80 eV range for Pd, and by analogy with Cu increases in the 40 to 90 eV range for Ni.

Subsequent work by Apai, et al.,[4] on CO-Pt up to $h\nu = 150$ eV showed that MO/VB passed through a minimum at $h\nu \sim 100$ eV, and increased at higher photon energies, to a value

$$(MO/VB)_{150\ eV} = 2.9\ (MO/VB)_{40\ eV} \quad . \tag{2}$$

Later, Miller, et al.,[21] found the same result for a stepped Pt crystal. The reason for this relative increase in molecular-orbital sensitivity is the Cooper minimum in the Pt(5d) VB photoemission cross section,[4] as illustrated in Fig. 3. The relative cross sections of

the MO derived features decrease with increasing energy above $h\nu$ = 40 eV, but the Cooper minimum leads to such a drastic attenuation of the Pt(5d) intensity (by more than an order of magnitude between 100 and 150 eV) that the minimum gives rise to the large enhancement in adsorbate sensitivity: by tuning the photon energy to the Cooper minimum, substrate VB photoemission can be effectively suppressed, and the MO-VB ratio correspondingly enhanced.

By the use of the $I(h\nu)$ curves for Cu and Ag (used in place of Ni and Pd, respectively) shown in Fig. 3, plus approximate theoretical molecular orbital photoemission cross sections for CO, based on a plane-wave final state,[22] Apai[23] estimated the variation of MO/VB with photon energy for the two systems CO-Ni and CO-Pd studied by Gustafsson, et al.,[11] and found very good agreement. This result, together with the success of a similar approach in explaining the MO/VB enhancement at $h\nu$ = 150 eV for CO-Pt, lead Apai to predict[23] a rather sharp resonance in MO/VB for CO-Pd, with significant enhancement in this ratio near $h\nu$ = 140 eV. The experimental observation of this resonance for CO-Pd is one of the main results of this work.

It is obvious from visual inspection of the spectra in Fig. 2 that MO/VB increases dramatically just beyond the photon energy range covered in the work of Gustafsson, et al.,[11] peaking well above 100 eV. The CO-Pd case is even more dramatic than CO-Pt (Ref. 4) because the substrate intensity decreases more sharply at energies just below the Cooper minimum (Fig. 3), and the minimum itself is quite narrow. The improvement in adsorbate sensitivity is truly dramatic from $h\nu$ = 80 eV to $h\nu$ = 130 eV, where the CO molecular orbitals actually

dominate the spectrum (see Fig. 2)! Fig. 5 is a plot of the area ratio MO/VB for CO-Pd against photon energy, with MO taken in this case to include just the least-bound ($1\pi + 5\sigma$) peak and VB taken as the main 4d-band peak. The expected resonance is observed with the peak at $h\nu \cong 130$ eV, in excellent agreement with prediction.[1,23] From the curve in Fig. 5, we have

$$(MO/VB)_{130\ eV} = 7.5\ (MO/VB)_{40\ eV} \tag{3}$$

for the CO-Pd system. This is, of course, a large improvement over CO-Ni, where there is no substrate Cooper minimum, but it is also a substantial increase in adsorbate sensitivity enhancement relative to CO-Pt [Eq. (2)] by almost a factor of 3. In fact, it should be noted that the increase in MO/VB is a factor of 10 between $h\nu \approx 80$ eV and 130 eV for CO-Pd.

D. Summary and Conclusions

Under certain conditions, an atomic view of photoemission is indeed appropriate in the understanding of the behavior of the total angle-integrated cross section. This is readily apparent from measurements of the photon energy dependence of the cross section, $\sigma_{fi}(h\nu)$. Based on the resulting $I(h\nu)$ curves, we can say that Cooper minima are general phenomena in the valence bands of 4d and 5d valence-shell metals. Therefore, the employment of these metals--particularly the catalytically important members of Group VIII--as substrates

should facilitate adsorbate studies with photoemission in the appropriate photon energy region. The 4d metals give rise to a larger adsorbate intensity enhancement at the Cooper minimum than the 5d metals, but the latter, with two radial nodes in the 5d wave function, offer a somewhat larger range of photon energies for adsorbate enhancement. Actually, examples of the application of this approach already exist: previously unobserved higher-lying MO features can be seen in photoemission spectra at the substrate Cooper minimum.[21,24]

Two main conclusions concerning adsorbate molecular orbital sensitivity can be drawn from this work. First, for 4d as well as 5d transition series metals the suppression of valence-band intensities near Cooper minima facilities the study of molecular orbitals of chemisorbed molecules for photon energies somewhat above 100 eV, where proximity to the minimum in the electron attenuation length also emphasizes contributions to the photoemission spectrum of the valence band of the substrate surface layer.

Second, certain laboratory photon sources fall at very useful energies for studying photoemission spectra from chemisorbates on 4d and 5d metals. For example, the Zr Mζ line at 151 eV is well-suited for experiments with Pt, while the Y Mζ line[25] at 132 eV is exactly at the maximum in MO/VB for the CO-Pd system. It should be mentioned, however, that in order for these sources to be useful in solid state photoemission studies, methods for suppressing bremsstrahlung radiation, which produces a large background of secondary electrons under the spectrum from the characteristic line, must be devised.

REFERENCES

* This chapter is based on experiments performed in collaboration with P. S. Wehner, S. D. Kevan, R. S. Williams, and D. A. Shirley; published in Chem. Phys. Lett. 57, 334 (1978).

1. D. A. Shirley, J. Stöhr, P. S. Wehner, R. S. Williams, and G. Apai, Phys. Scripta 16, 398 (1977).
2. P. S. Wehner, J. Stöhr, G. Apai, F. R. McFeely, R. S. Williams, and D. A. Shirley, Phys. Rev. B 14, 2411 (1976).
3. J. Stöhr, G. Apai, P. S. Wehner, F. R. McFeely, R. S. Williams, and D. A. Shirley, Phys. Rev. B 14, 5144 (1976).
4. G. Apai, P. S. Wehner, J. Stöhr, R. S. Williams, and D. A. Shirley, Solid State Commun. 20, 1141 (1976).
5. I. Lindau, P. Pianetta, and W. E. Spicer, Phys. Lett. A 57, 225 (1976).
6. See, for example, Ref. 12 in Chapter I.
7. J. W. Cooper, Phys. Rev. Lett. 13, 762 (1964), and references therein; U. Fano and J. W. Cooper, Rev. Mod. Phys. 40, 441 (1968).
8. R. Haensel, C. Kunz, T. Sasaki, and B. Sonntag, Appl. Opt. 7, 301 (1968); F. C. Brown, Solid State Phys. 29, 1 (1974).
9. F. C. Brown, R. Z. Bachrach, S. B. M. Hagström, N. Lien, and C. H. Pruett, in Vacuum Ultraviolet Radiation Physics, edited by E. E. Koch, R. Haensel, and C. Kunz (Pergamon, Vieweg, 1974), p. 785; F. C. Brown, R. Z. Bachrach, and N. Lien, Nucl. Instrum. Methods 152, 73 (1978).
10. P. S. Wehner, Ph.D. thesis, University of California, Berkeley, 1978 (LBL-7622, unpublished).

11. T. Gustafsson, E. W. Plummer, D. E. Eastman, and J. L. Freeouf, Solid State Commun. 17, 391 (1975).

12. The general properties of Cooper minima have been discussed by several authors; see, for example, S. T. Manson, Adv. Electron. Electron Phys. 44, 1 (1977), and references therein.

13. C. R. Brundle, J. Vac. Sci. Technol. 11, 212 (1974); ibid. 13, 301 (1976); Surf. Sci. 48, 99 (1975).

14. D. Menzel, CRC Crit. Rev. Solid State Mater. Sci. 7, 357 (1977).

15. J. E. Demuth, IBM J. Res. Develop. 22, 265 (1978); Surf. Sci. 84, 315 (1979); J. E. Demuth and D. E. Eastman, Phys. Rev. B 13, 1523 (1976).

16. T. E. Fischer, S. R. Kelemen, and H. P. Bonzel, Surf. Sci. 64, 157 (1977).

17. T. Gustafsson and W. E. Plummer, in Photoemission and the Electronic Properties of Surfaces, edited by B. Feuerbacher, B. Fitton, and R. F. Willis (Wiley, New York, 1978).

18. W. T. Bordass and J. W. Linnett, Nature 222, 660 (1969).

19. D. Menzel, J. Vac. Sci. Technol. 12, 313 (1975); J. C. Fuggle, T. E. Madey, M. Steinkilberg, and D. Menzel, Phys. Lett. A 51, 163 (1975).

20. I. Lindau and W. E. Spicer, J. Electron Spectrosc. Relat. Phenom. 3, 409 (1974).

21. J. N. Miller, D. T. Ling, I. Lindau, P. M. Stefan, and W. E. Spicer, Phys. Rev. Lett. 38, 1419 (1977).

22. J. W. Rabalais, T. P. Debies, J. L. Berkosky, J. J. Huang, and F. O. Ellison, J. Chem. Phys. 61, 516 (1974).

23. G. R. Apai, Ph.D. thesis, University of California, Berkeley, 1977 (LBL-6906, unpublished).

24. R. F. Davis, P. S. Wehner, S. D. Kevan, R. S. Williams, and D. A. Shirley, unpublished work [C_2N_2-Pt(111)].

25. M. S. Banna and D. A. Shirley, J. Electron Spectrosc. Relat. Phenom. 8, 255 (1976).

FIGURE CAPTIONS

Fig. 1. Experimental arrangement for photoemission studies, as viewed schematically from above the apparatus. Electrons are analyzed by a cylindrical mirror analyzer (CMA).

Fig. 2. Selected angle-integrated photoemission energy distribution curves for Pd + 4 L of CO in the photon energy range 40 to 180 eV. Experimental resolution was 0.8 eV. Note the increase in intensity of the CO-derived peaks (at ~ 8 eV and ~ 11 eV E_B) as $h\nu$ is increased to 130 eV.

Fig. 3. Relative d-band intensity of Cu (Ref. 1), Ag (Ref. 1), Au (Ref. 1), Pt (Ref. 4), and Pd as a function of the incident photon energy. The curves have been corrected for the collecting efficiency of the electron energy analyzer, the transmission of the monochromator, and inelastic background.

Fig. 4. Experimental values of the inelastic mean-free-path (λ_e) of electrons in Ni, Cu, Ag, and Au as a function of electron kinetic energy (Refs. 13 and 20).

Fig. 5. Photoemission intensity ratio (MO/VB) of the ($5\sigma + 1\pi$) CO-derived peak at ~ 8 eV E_B to the Pd valence band as a function of photon energy, with a large peak seen at $h\nu \approx$ 130 eV.

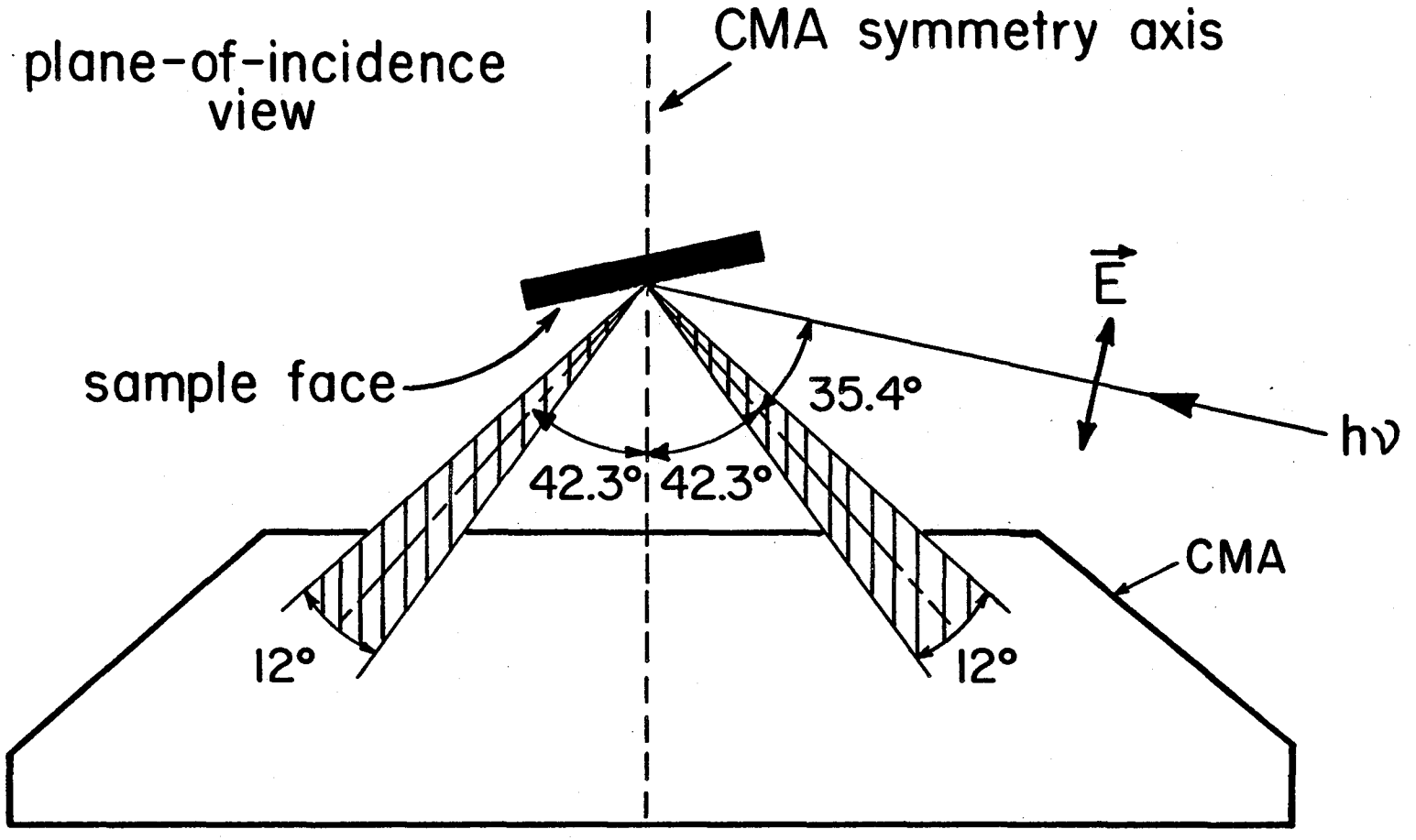

XBL 821-7559

Figure 1

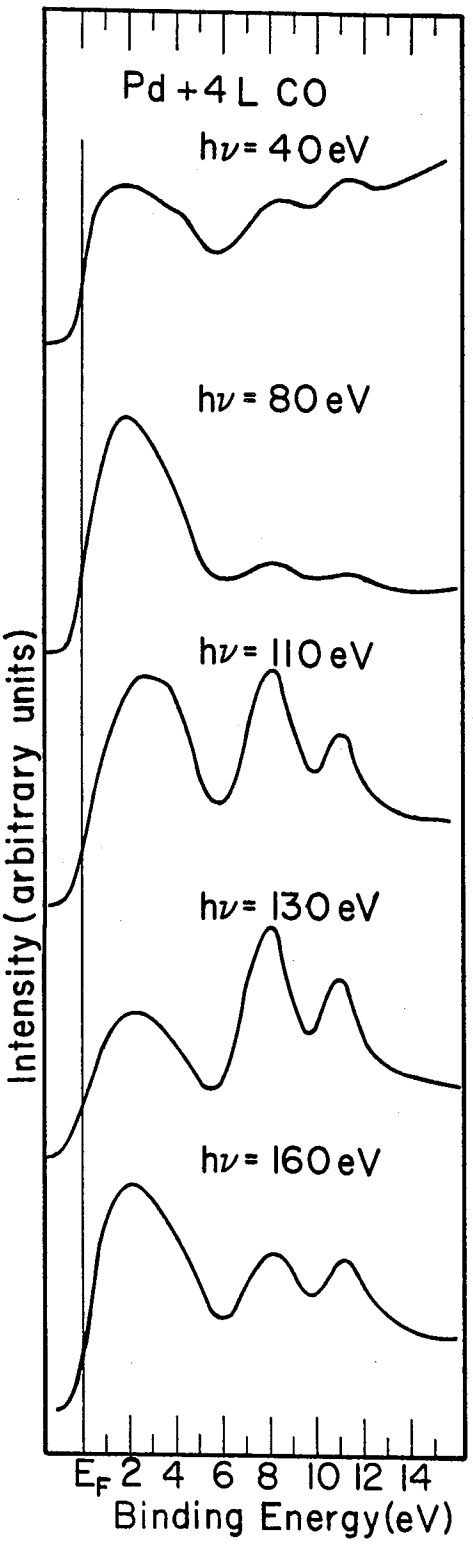
Pd + 4 L CO
hν = 40 eV
hν = 80 eV
hν = 110 eV
hν = 130 eV
hν = 160 eV
Intensity (arbitrary units)
E_F 2 4 6 8 10 12 14
Binding Energy (eV)
XBL782-304

Figure 2

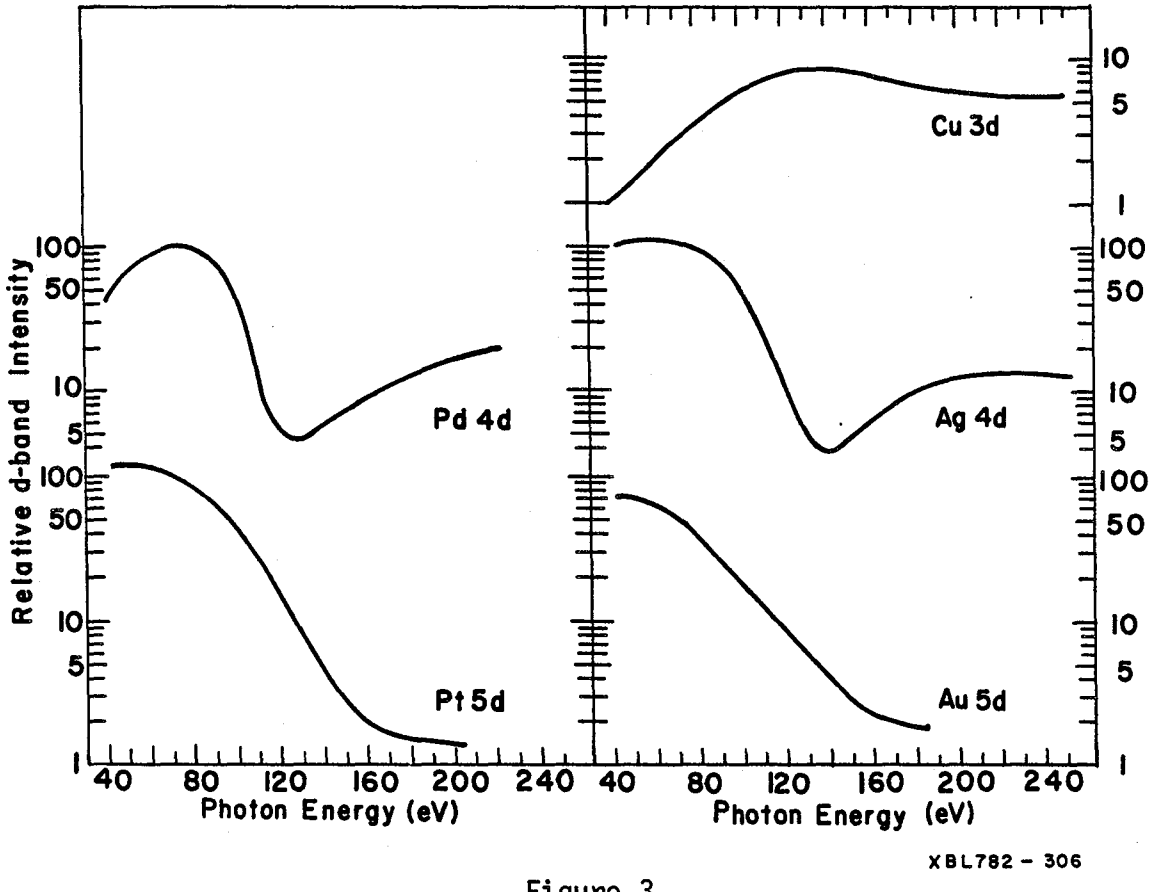
Relative d-band Intensity
Pd 4d
Pt 5d
Cu 3d
Ag 4d
Au 5d
Photon Energy (eV)
Photon Energy (eV)
XBL782 - 306

Figure 3

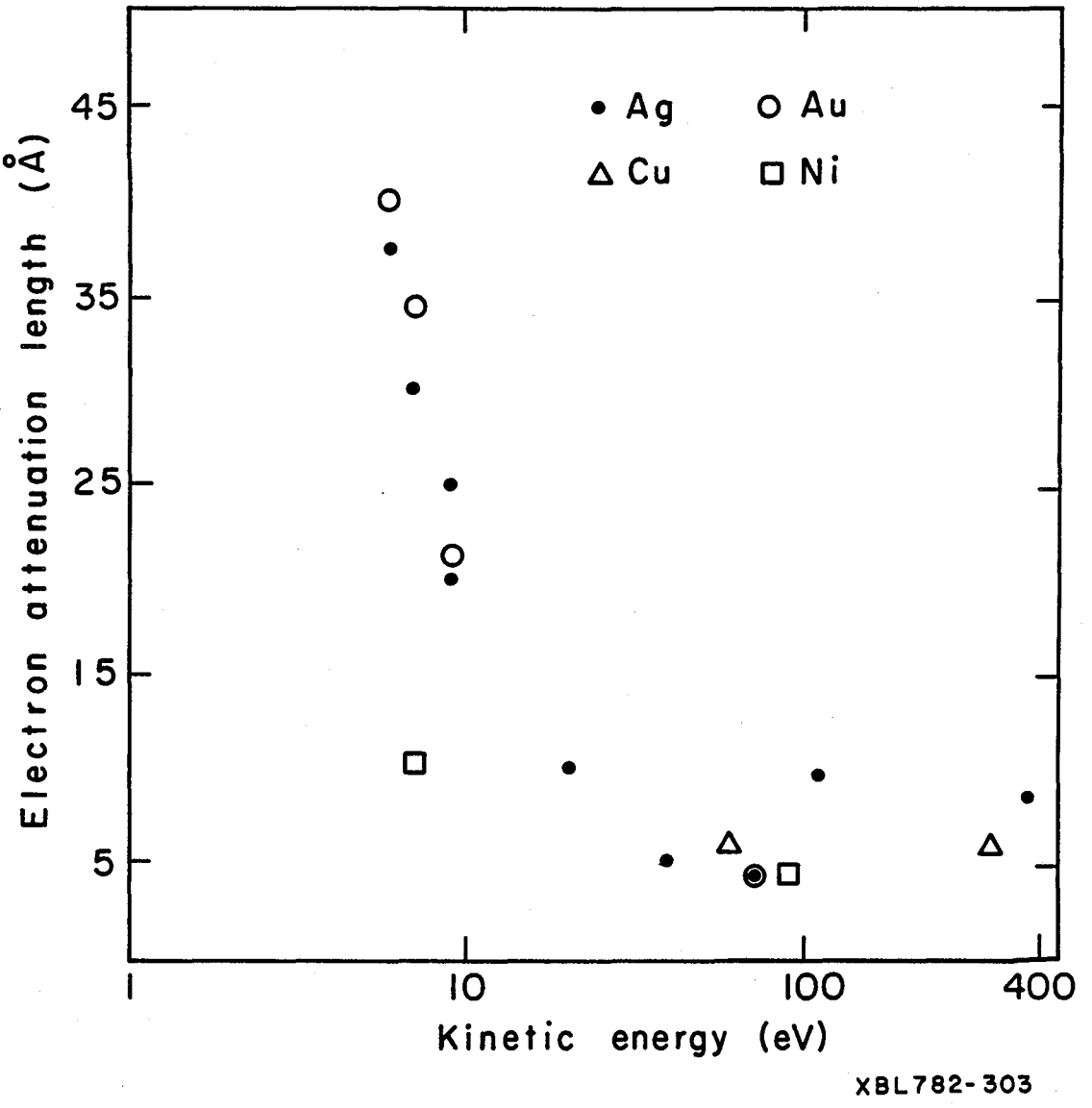
Ag
Au
Cu
Ni
45
35
25
15
5
Electron attenuation length (Å)
1
10
100
400
Kinetic energy (eV)
XBL782-303

Figure 4

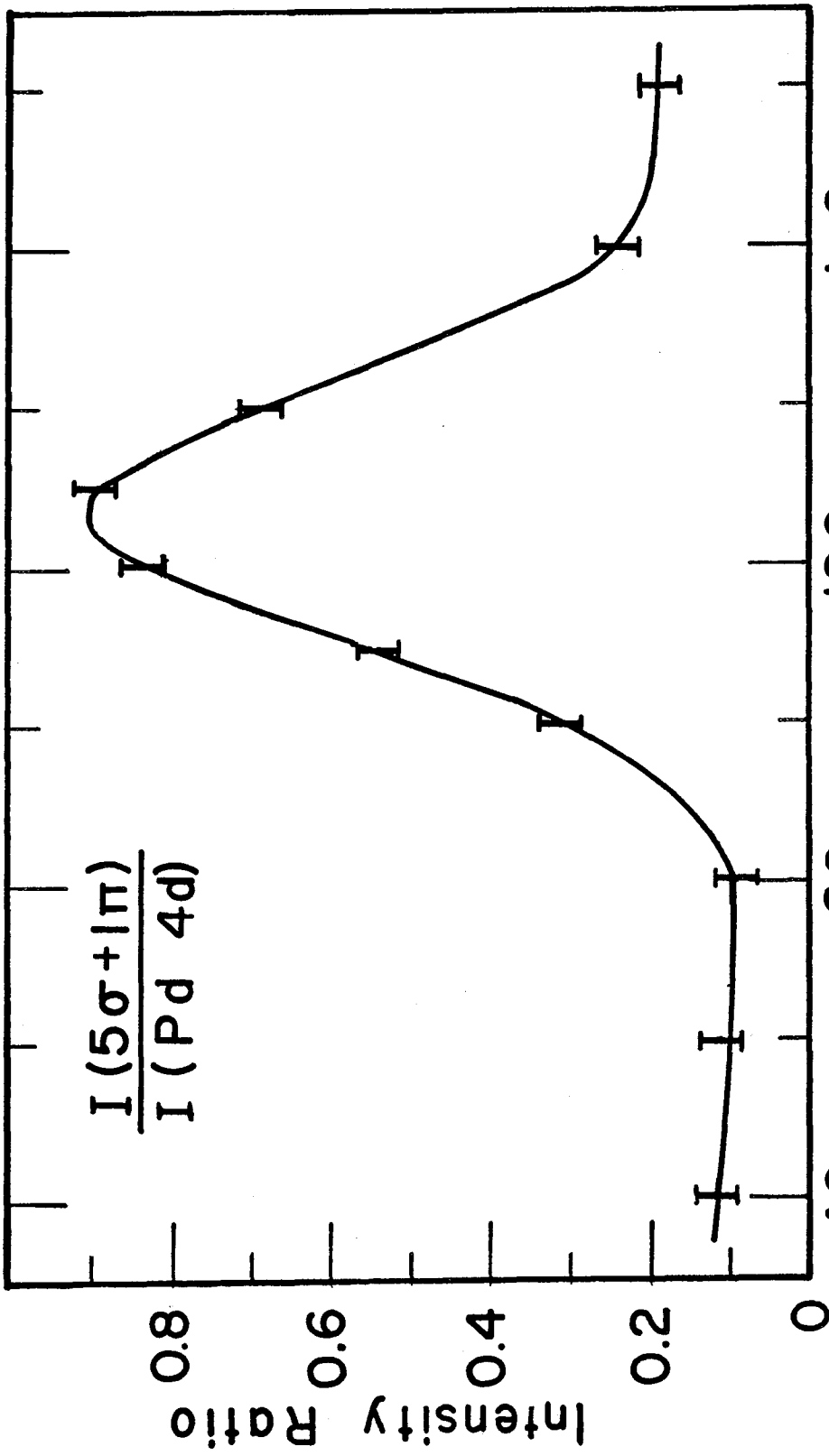
Intensity Ratio
0
0.2
0.4
0.6
0.8
40
80
120
160
Photon Energy (eV)
I(5σ+1π) / I(Pd 4d)
XBL 782-305

Figure 5

PART III.

LOCALIZED EFFECTS IN THE ANGULAR DISTRIBUTION OF VALENCE- AND CORE-LEVEL PHOTOEMISSION

VII. CONDENSED PHASE PHOTOELECTRON ASYMMETRY *

A. Introduction

The preceding chapters have established that (1) ordered condensed phase systems exhibit strong angular distribution effects which have no atomic analogue, but (2) under conditions where total cross sections are probed or ordering effects are unimportant, the photoemission intensities of various subshells including the valence bands show atomic behavior. These are two limiting cases, of course; a given system ought to show both types of effects. In Chapter I, this "dual" nature of photoemission was rationalized: the atomic-core region of the crystal potential governs photoabsorption while the external region governs properties such as band structure effects. In that discussion, we also conjectured the existence of an atomic angular distribution analogue in the condensed phase. Such an effect would be manifestly different from the more traditional picture[1] of condensed phase photoemission, because the latter assumes that angular properties are related to periodicity (or orientation) while only the overall intensity or total cross section can be atomic related. In this chapter, we discuss the experiments which led to the discovery of this new effect which we have termed "condensed phase photoelectron asymmetry."

In the gas phase, photoelectron asymmetry is a well-known effect. Following Yang's theorem,[2] dipole excitation of a photoelectron transition in a randomly-oriented system via a vector potential $\vec{A}$ yields an

angular distribution of intensity given by[2-4]

$$I(E_f,\vec{k}_f) = [\sigma(E_f)/4\pi][1 + \beta(E_f)P_2(\cos \alpha_f)] \quad . \qquad (1)$$

Here E_f and $\vec{k}_f$ are, respectively, the photoelectron kinetic energy and propagation direction, α_f is the angle between $\vec{k}_f$ and $\vec{A}$, $\sigma(E_f)$ is the (total) angle-averaged cross section for the photoelectric transition, P_2 is the second Legendre polynomial [$P_2(x) = (3x^2 - 1)/2$], and $\beta(E_f)$ is the photoelectron asymmetry parameter. Integration of Eq. (1) over all possible $\vec{k}_f$ orientations yields $I = \sigma(E_f)$, and $\beta(E_f)$ has the limits $-1 \leq \beta(E_f) \leq 2$, as required to insure that $I(E_f,\vec{k}_f)$ is nonnegative. The photoemission process in a gaseous system is completely described by σ and β, and the asymmetry in the disordered system arises by virtue of $\vec{A}$; one might say that $\vec{A}$ introduces the asymmetry to the system. Extensive calculations of $\beta(E_f)$ in atoms and molecules are now available, and a number of measurements of $\beta(E_f)$ have been made in recent years (see, e.g., Refs. 5-8). The application of Yang's theorem to atoms and molecules has been quite successful. This has been greatly facilitated by the advent of synchrotron radiation sources, which permit the measurement of energy dependencies of β and σ (Ref. 8).

In condensed phases, however, photoelectron asymmetry from this source was previously either ignored or unknown. In fact, until the present investigations, the question of whether Eq. (1) is even applicable to solids had not been addressed systematically.[9] We have already alluded (Chapter I) to the most likely reasons for this:

ordered solids by nature have asymmetry or anisotropy independent of $\vec{A}$; the crystallographic or molecular axes, rather than the direction of $\vec{A}$, tend to dominate photoelectron angular distributions, and Eq. (1) is no longer directly applicable. Several of the most important effects for ordered systems are $\vec{k}$-conservation (see Part I), photoelectron diffraction,[10] and orbital-directed photoemission,[11] all three of which <u>can</u> be strong (excluding symmetry selection) regardless of the orientation of $\vec{A}$.

In this chapter, order is removed from the condensed phase systems, i.e., disordered systems are studied, and we show that atomic effects can be very strong functions of α_f. We have observed large asymmetries in photoemission from both core and valence levels, at energies well above threshold. Derived $\beta(E_f)$ values show strong qualitative similarities to Manson's calculations[5] on free atoms. It is suggested that these effects have been previously missed because condensed phase photoemission experiments (1) did not incorporate the measurement of peak intensities, and (2) did not include the proper polarization-dependence measurements. The implications of this discovery for condensed-phase photoemission are potentially rather astounding, and we will touch upon this subject below. The remainder of this chapter is organized as follows: In Section B we describe the experimental procedures, Section C contains results and discussion, and in Section D this work is summarized.

B. Experimental

Figure 1 summarizes the important angles and vectors in this experiment (see, also, Section A of Chapter I). We will ignore refraction effects so that $\vec{k}_f$ (internal) and $\vec{p}$ (external) are equivalent as far as photoelectron orientation is concerned. Therefore, α_f is equal to α (angle between $\vec{A}$ and $\vec{p}$) and we need only be concerned with the external distribution of photoelectrons in the description of the internal process. The reasons that we can ignore refraction effects are (1) they are expected to be small for energies well above threshold (see Chapter I), (2) we keep θ_p fixed at a constant value (see below), and (3) we do not know how to treat refraction in a disordered system. The angle-resolved photoemission (ARP) instrument (base pressure $\lesssim 3 \times 10^{-10}$ torr) employed a hemispherical analyzer with two-circle rotation capability and had an angular acceptance cone of 9 millisteradians, as described in Chapter I (Section C) and elsewhere.[12] This analyzer allowed the independent variation of θ_p [the angle between $\vec{p}$ and the sample normal ($\vec{n}$)] and α through the range $0^\circ \leq \alpha, \theta_p \leq 90^\circ$. However, to minimize systematic errors, θ_p was held fixed at 45° in the $\phi_p = 90^\circ$ azimuth.

With reference to Fig. 1, a description of our experimental procedure for obtaining angular distributions is straightforward. The sample was held fixed with $\vec{n}$ in the horizontal plane, which is the x-z plane in Fig. 1, but allowed to rotate about the $\vec{y}$ axis (the manipulator polar-rotation or crystal-rocking axis) thereby achieving θ_A- and concomitantly α-variability. In other words, the x-z plane is the

plane of incidence with the absolute orientation of $\vec{A}$ fixed. Therefore, α-variability is achieved by rotating $\vec{n}$--and thus the coordinate system--about $\vec{y}$, which changes the orientation of $\vec{A}$ in the $\phi_A = 0^\circ$ azimuth. In order for θ_p to remain fixed at 45° in the y-z plane ($\phi_p = 90^\circ$), the analyzer and sample were rotated together. Note that the aspect from which the coordinate system in Fig. 1 is viewed is therefore from underneath and at the back of the instrument (this will help to orient the reader who is familiar with our apparatus). With θ_A variable between 90° (the normal incidence, s-polarization geometry) and 10° (near-grazing incidence of radiation), this procedure thereby covered the range $46^\circ \leq \alpha \leq 90^\circ$ (Ref. 13).

There are other procedures for obtaining α-variability in different ranges of this angle, but this method includes the important combination of s-polarization with $\alpha = 90^\circ$ ($\vec{A}\cdot\vec{p} = 0$). The major difficulty with most procedures is that (unlike the gas phase) condensed phase photoemission is at least a three vector ($\vec{n}$, $\vec{A}$, $\vec{p}$) experiment. Therefore, it is difficult to obtain a reasonable experimental geometry whereby <u>only</u> α-variability is achieved. The procedure detailed above was used because we considered it more important to hold θ_p constant in these measurements rather than θ_A. Another procedure was also investigated which potentially is quite appealing. In this method, the absolute sample orientation is held fixed, thereby keeping θ_A and ϕ_A constant, and α is varied by rotating the analyzer in a cone about the sample normal at a fixed angle θ_p. The only variable in this procedure other than α is ϕ_p,

which for a disordered system is not important. However, we found this technique to be tedious, involving the coupling of both the horizontal and vertical motions of the electron analyzer, and inaccurate because of alignment difficulties. It was therefore abandoned as a viable procedure. Perhaps the best method for future experiments would involve the employment of a multi-dimensional display-type detector[14] which would naturally yield electron intensities in "cones" of constant θ_p about $\vec{n}$ without the necessity of tedious mechanical movements of the analyzer.

Three systems were studied: Pt metal, atomic Se adsorbed on a Pt surface, and polycrystalline Ag. In each case the metal was cleaned of bulk and surface impurities by Ar^+ ion bombardment (beam voltage = 1.5 kV) and annealing cycles, with sample cleanliness monitored by Auger electron spectroscopy (AES). In the case of Pt, the detailed procedure that was followed is outlined in Chapter III. Immediately preceding the ARP measurements with each system, the metal surface was ion-bombarded for an extended period of time (ca. 2 hours) and left in an unannealed state to reduce the local order. AES was again employed to check sample cleanliness. For the atomic Se measurements, the clean (unannealed) Pt surface was exposed to H_2Se gas at room temperature under conditions for which a sub-monolayer coverage of adsorbed Se was obtained.[10]

The experiments were conducted on the 4° branch of Beam Line I at SSRL, with photons in the energy range 40 eV $\leq h\nu \leq$ 252 eV and highly polarized (~ 98 percent[15]) in the horizontal plane. Angular

distributions ($46^\circ \leq \alpha \leq 90^\circ$) were obtained as functions of photon energy for the following levels: Se(3d), Pt(4f), Ag(4s), Ag(4p), and the Ag valence bands (mainly $4d^{10}5s$). Complete photoemission energy distribution curves (EDCs) were collected for each level at each photon energy and α orientation for which data was taken. Relative intensities were obtained as total peak areas normalized to incident photon flux and analyzer efficiency, with the monochromatized photon beam intensity monitored by a gold photoyield detector.[16] The Fresnel equations[17] were used to calculate changes in $\vec{A}$ at vacuum-metal interfaces:[18] the changes, induced by the presence of the conducting surface, were generally small in the energy range covered and only non-negligible below $h\nu \approx 100$ eV and at small-θ_A (10° to 15°) geometries. Typical values of $\Delta\alpha$, the difference between α with and without the corrections, were less than 1°.

C. Results and Discussion

1. The $P_2(\cos\alpha)$ Form.

The trend of the data was very striking. In several levels the peak intensity for $\vec{A} \perp \vec{p}$ was dramatically smaller--by factors up to 25--than for other values of α at a particular photon energy. Selected illustrative spectra are shown in Fig. 2 for Ag(4s) and Ag(4d). This was a major result that we sought to establish, and the experimental geometries were selected with this purpose, rather than covering the whole angular range of α to obtain more precise values of

β. We also chose to emphasize the energy dependence of the asymmetry, rather than the angular dependence of the intensity, which can be assumed to have the general form of Eq. (1), by Yang's theorem.[2] Nevertheless, the data could be used to test this form. The intensity-vs-angle data, also shown in Fig. 2, support the $P_2(\cos \alpha)$ form. We conclude, therefore, that Yang's theorem does indeed apply to condensed phase systems that are disordered.

It is instructive to consider the form of the Yang's-theorem angular distribution for several values of β throughout its possible range; this is shown by the radial plots of photoemission intensity in Fig. 3. Here, we have plotted the intensity from Eq. (1) with $(\sigma/4\pi) = 1$ for $\beta = 2$, 1, 0, and -1. High asymmetries, $\beta \sim 2$, have angular distributions peaked sharply along the direction of $\vec{A}$, i.e., $\alpha = 0^\circ$. In contrast, $\beta = 0$ implies that the distribution is isotropic, and $\beta = -1$ has a distribution that is actually peaked orthogonal to the polarization direction, i.e., $\alpha = 90^\circ$. Therefore, the shape of the distribution for $\beta = -1$ is a torus in three dimensions, as opposed to the "p-orbital-shaped" distribution for $\beta = 2$. For both experimental cases shown in Fig. 2, the β values are large enough that the angular distribution must be peaked along $\vec{A}$; this is a general result for the condensed phase systems we have studied, the consequences of which will be discussed later in this chapter. One immediate result concerns possible experimental difficulties: in a recent review, Manson[19] did not discuss atomic angular distribution effects in solids because he conjectured that the photoelectron should

be subject to strong scattering effects in the bulk and at the surface which would invalidate the $P_2(\cos \alpha)$ form. However, the most elementary theory would suggest that scattering effects in a disordered condensed phase would tend to lower the observed asymmetry (toward $\beta = 0$) from atomic expectations; our measurements are in fact higher than atomic theory predictions in nearly every case. This result implies that condensed phase disordering effects on photoelectron trajectories can be neglected to first order in these studies.

2. Energy Dependence of $\beta(E_f)$ and Comparison with Atomic Theory.

The most interesting result of this work is the detailed manner in which $\beta(E_f)$ qualitatively follows expectations based on atomic calculations. Results for the Se(3d) and Pt(4f) subshells are shown in Fig. 4. The contrasting behavior of these two curves can be understood by comparison with free-atom calculations, also shown in Fig. 4 for nearby elements. Kennedy and Manson[20] have calculated $\beta(E_f)$ for Kr(3d); their Hartree-Fock "length" result is shown in Fig. 4, as are the Hartree-Slater (HS) $\beta(E_f)$ curve for Au(4f) given by Manson[5] and the HS curve for $\sigma(E_f)$ calculated by Combet Farnoux.[21] It happens that the experimental and theoretical $\beta(E_f)$ curves are generically rather similar if considered over the entire range of E_f. The photoemission cross sections $\sigma(E_f)$ also show the behavior expected theoretically, as indicated in Fig. 4, and discussed in Chapter VI. It is clear, however, that our measured $\beta(E_f)$ are systematically higher than the corresponding atomic curves. The shapes

of these curves can be understood by resorting to atomic photoionization theory.[5-7,20,22]

In a single-particle, nonrelativistic, central-field framework, Bethe,[3] and Cooper and Zare[4,23] have shown that the atomic photoelectron angular distribution for a particular initial state ($|n\ell\rangle$) gives the following expression for β:

$$\beta_{n\ell} = \frac{\ell(\ell-1)R_-^2 + (\ell+1)(\ell+2)R_+^2 - 6\ell(\ell+1)R_-R_+ \cos\Delta}{(2\ell+1)\,[\ell R_-^2 + (\ell+1)R_+^2]} \quad . \tag{2}$$

In this expression, the radial dipole matrix elements $R_\pm$ are given by $R_\pm \propto \langle E_f, \ell\pm1|\vec{A}\cdot\vec{P}|n\ell\rangle$, and Δ is the difference between the total continuum phase shifts for the two outgoing channels;

$$\Delta = \xi_{\ell+1} - \xi_{\ell-1} \quad , \text{ and } \quad \xi_\ell = \sigma_\ell + \delta_\ell \quad , \tag{3}$$

with the total phase shift composed of Coulomb (σ) and non-Coulomb (δ) parts. The terms $R_\pm$ and Δ are functions of E_f, therefore $\beta = \beta(E_f)$. With the definition $u \equiv R_+/R_-$, we have for s, p, d, and f initial-state symmetries:

$$\beta_{ns} = 2 \quad , \tag{4a}$$

$$\beta_{np} = (2u^2 - 4u\cos\Delta)/(2u^2 + 1) \quad , \tag{4b}$$

$$\beta_{nd} = (12u^2 + 2 - 36u \cos \Delta)/(15u^2 + 10) \quad , \tag{4c}$$

$$\beta_{nf} = (20u^2 + 6 - 72u \cos \Delta)/(28u^2 + 21) \quad . \tag{4d}$$

Thus, we see that the oscillations in $\beta(E_f)$ arise through an increase in the ratio u with E_f, combined with variation of the total phase shift difference with E_f for the two final-state channels, which affects the interference term between the two channels.

For s-subshells, there is only one photoionization channel ($s \rightarrow p$), so that β equals 2 independent of energy. For all other subshells, β is generally not equal to 2. Near threshold ($E_f \lesssim 2$ Ry), the Coulomb phase shift difference varies rapidly with energy, giving rise to dramatic oscillations (generally downward at threshold) in β.[24] If the initial states are radially nodeless, as are the 1s, 2p, 3d, and 4f levels, then the remaining intermediate-energy structure is characteristic mostly of an increase in u, along with some variations in Δ with E_f.[5,20] At higher energies, Δ and u become essentially constant, therefore β approaches a constant value asymptotically.[20] For 3d and 4f initial states, the variation in u with energy near threshold is somewhat more rapid than 2p because the f and g outgoing channels, respectively, have centrifugal barriers to surmount[25,26] (see Chapter VI). Therefore $\beta_{3d}(E_f)$ and $\beta_{4f}(E_f)$ are more characteristic of $u(E_f)$ than β_{2p} is, and the oscillations are sharper.

The 4f case is different, still,[5,26] from 3d however, in that the ratio u is essentially zero throughout the entire range of energies where the Coulomb phase shifts are varying rapidly, because the 4f → E_f,g dipole matrix element is extremely small near threshold. Therefore, $\beta_{4f}(E_f)$ is not generally characterized by $\Delta(E_f)$ at threshold. However, in the energy region ca. 2 to 4 Ry above threshold, R_+ and R_- are of the same order of magnitude. If we set $R_+ = R_-$, then Eq. (4d) becomes $\beta_{nf} = (26 - 72 \cos \Delta)/49$, and the energy dependence comes entirely from the cos Δ term. As shown in Fig. 4, $\beta_{4f}(E_f)$ goes through a maximum near 3 Ry, because cos Δ is negative in this region.[26] Above this maximum, β_{4f} drops and then approaches an asymptotic value as u becomes much greater than unity at much higher energies.

Figure 4 shows that the experimental curves fulfill these atomic expectations qualitatively: the curves might not extend close enough to threshold for the most dramatic changes to be observed, but the Se(3d)-$\beta(E_f)$ curve is seen to rise with E_f with nearly the identical curvature as that of Kr(3d) above the phase-shift-oscillatory region, and the Pt(4f) curve first has a maximum and then an extended flat minimum, in excellent agreement with the trend discussed above and shown for the free-atom Au(4f) level in Fig. 4. The major differences between experiment and atomic theory are the upward shift in the experimental β curves and in Pt(4f) a decreased amplitude of variation with energy in this intermediate-energy region. These differences are consistent with larger plane-wavelike character in the condensed-phase final state (to be discussed below). We conclude that for the 3d

level of adsorbate Se atoms and the 4f level of Pt metal the $\beta(E_f)$ curves are at least qualitatively predicted by free-atom theory. A more stringent test was desirable, however, because these are both nodeless core levels.

Silver metal provides this test. The 4s, 4p, and valence band ($4d^{10}5s$) wave functions all possess radial nodes, and Cooper minima[27] in $\sigma(E_f)$ are expected above threshold for the 4p and 4d subshells. The energy of the Cooper minimum for Ag(4p) should lie too near threshold[5] for us to detect in this experiment, but the 4d subshell should show the effect at $E_f \approx 10$ Ry (Ref. 28). Indeed, the experimental $\sigma(E_f)$ values shown in Fig. 5 bear out this expectation. The $\beta(E_f)$ results for both 4d and 4s also show a systematic qualitative resemblance to the atomic calculations (Fig. 5), again with a shift to higher values of β. The theoretical $\beta(E_f)$ curves for Xe(4d) and $\sigma(E_f)$ for Xe(4s) and Xe(4d) in Fig. 5 are the Hartree-Fock "length" results of Kennedy and Manson.[20] It is expected that $\beta(E_f) = 2$ for the 4s subshell for all E_f from rather general arguments[22] [i.e., Eq. (4a)] except for correlation and/or relativistic effects very close to threshold. The resemblance between experiment and theory is striking for both the 4s and 4d subshells. The 4p peak was very wide because of final-state effects,[29a] and we were unable to derive precise intensities from our data. Qualitatively, the 4p results tend to support the above conclusions, with $\beta(E_f)$ values being typically in the range 1.1 - 1.5.

It is particularly noteworthy that the Ag(4d) level shows this atomiclike behavior in the angular distribution. This is the same

subshell--the valence band--that gives rise to distinct band structure effects in the UV (Ref. 29b) and (presumably) soft-x-ray range[30] in crystalline Ag. It is a common misconception that an atomic picture is not applicable to photoemission of valence electrons in solids under any circumstances.[19] The atomic picture certainly is not completely applicable, as evidenced by the deviations between experimental and theoretical $\beta(E_f)$ curves, but these deviations are also observed in the core levels of the bulk metal [Pt(4f)] and the adsorbate [Se(3d)], where an atomic picture of the angular distribution would be more generally accepted.

It is again instructive to consider the systematics of the $\beta(E_f)$ curves shown in Fig. 5 within an atomic framework.[5,20,31] The 4s initial state, of course, has a simple angular distribution, because there is only one final-state channel. But the 4d subshell has dramatic oscillatory structure in $\beta(E_f)$. Near threshold (below the energy range shown in Fig. 5) $\beta_{4d}(E_f)$ for Xe experiences a sharp drop with increasing energy, similar to β_{np} and β_{3d}, that once again arises principally from the rapid variation of the Coulomb-phase-shift difference. There is next a sharp upward trend ($10\ \text{eV} \lesssim E_f \lesssim 100\ \text{eV}$) that is produced by a rapid variation of the f-wave non-Coulombic phase shift over a small energy range due to the centrifugal barrier in the effective scattering potential.[31] In this energy region, there is a concomitant increase (or resonance) in the magnitude of the R_+ photoionization matrix element as the f-wave continuum function is "pulled" in toward the nucleus.[27] It will be recalled that this effect, which

is usually termed a shape resonance, was observed in the measured photoemission angle-integrated intensity of 3d, 4d, and 5d valence subshells of metals (Chapter VI); we observe it again here in Ag(4d), both in σ and in β. In the next chapter, we shall see that molecular shape resonance phenomena are quite dramatic in adsorbate molecules. The final oscillation in $\beta(E_f)$ arises as a result of the Cooper minimum[27] in the 4d photoionization cross section, where the f-wave radial matrix element (R_+) changes sign (recall that it is negative at threshold and at the shape-resonance energy). At the Cooper minimum ($u = 0$), Eq. (4c) reduces to $\beta_{4d} = 1/5$, and at higher energies, where u ($= R_+/R_-$) has also changed sign, β_{4d} for Xe actually becomes negative and experiences a minimum. The qualitative aspects of both the shape-resonance- and Cooper-minimum-derived oscillations are easily seen in the Ag(4d) asymmetry curve (Fig. 5). At the time of these measurements, no experimental confirmation was available for the detailed variation of $\beta(E_f)$ for the Xe(4d) level. However, a recent experimental study by Southworth, et al.,[32] of this research group supports the theory of Kennedy and Manson[20] for Xe(4d) photoelectron asymmetry.

3. Nature of the Final-State Wave Function.

In Chapter I, it was stated that these asymmetry measurements would allow us to shed some light on the final-state wave function. In Part I, the plane-wave approximation (PWA) was sufficient to determine the properties of valence-band dispersion relations, but we never addressed the problem of determining peak intensities in the

energy distribution curves--a problem for which the PWA fails (this was also discussed in Chapter I). Additionally, it will be recalled that the PWA yields incorrect atomic angular distributions,[33] except for the trivial case of $\ell = 0$. Simply, the dipole-velocity form of the transition matrix element, in conjunction with a plane-wave final state, always yields an expression for the angle-resolved intensity of the form $I(E_f,\vec{p}) \propto |\Phi_{n\ell}(p)|^2 \cos^2\alpha$, where $|\Phi_{n\ell}(p)|$ is the angle-averaged magnitude of the Fourier transform of the initial state wave function evaluated at p. Substitution of this expression for the intensity into the left-hand side of Eq. (1), which can be assumed to be valid for a plane-wave final-state, yields $\beta = 2$ independent of E_f.

Consideration of the condensed phase asymmetry experiments in light of both this result for the PWA and the free-atom theory suggests that the true final state is correctly described by neither a plane wave nor an atomic-continuum-type wave function: the experimental measurements yield $\beta \approx 2$ only for the Ag(4s) level, whereas the remaining curves have the atomic form <u>but</u> with all β values shifted upward closer to 2 and with an attenuation of oscillatory amplitude in $\beta(E_f)$. However, the final state in the disordered condensed-phase system appears to retain a large plane-wavelike character, especially at energies well above threshold. Perhaps this is somewhat contradictory of the idea expressed previously[34] and in Chapter I that the photoelectron final state is mostly plane-wavelike in an ordered system due to Bloch's theorem and lifetime effects, but atomiclike near the atomic core from which it originates. In these asymmetry studies, Bloch's

theorem is presumably invalid; therefore, plane-wave character may be a general feature of condensed phases. Furthermore, our results imply that there simply do not exist limiting cases of purely-atomiclike and plane-wavelike final states in solids.

However, we have already observed that the cross section can be considered to be "atomiclike" under appropriate circumstances (Chapter VI); the results in this chapter support this conclusion. The somewhat puzzling and contradictory behavior of the cross section and the asymmetry in the condensed phase may be rationalized by considering the simple distinction between the two: cross sections, given by the radial matrix elements, depend on the overlap of wave functions. It is entirely reasonable that in the disordered systems studied here, the overlap is determined largely by the portions of the wave functions that are within the confines of the atomic core where the free-atom and condensed phase environments are similar. However, the asymmetry depends not only on the matrix elements, but critically on the phase shifts [see discussion above and Eq. (2)] which, unlike the matrix elements, must be viewed as asymptotic quantities. Therefore, the condensed phase angular distribution differs from the "atomic" case because the potentials, which govern the phase shifts, must be different outside the core for the two cases <u>even though they are probably similar within the atomic core</u>.

In order to understand the nature of the <u>true</u> condensed-phase final state and its relationship to photoelectron asymmetry, we should compare the asymptotic forms for the "limiting cases" of a plane wave

and an atomic-continuum wave function. It is well known[35] that the plane wave, an eigenfunction of the linear momentum operator, can be expanded in partial-ℓ waves:

$$\exp(i\vec{k}\cdot\vec{r}) = 4\pi \sum_{\ell,m} i^{\ell}\, j_{\ell}(kr)\, Y^{*}_{\ell m}(\hat{k}) Y_{\ell m}(\hat{r}) \quad . \tag{5}$$

The $j_{\ell}(kr)$ terms, which are spherical Bessel functions, solve the one-electron radial Schrodinger equation under the condition that the central field is $V(r) = 0$ (Ref. 36); i.e. (ignoring normalization)

$$\left[-\frac{d^2}{dx^2} + \frac{\ell(\ell+1)}{x^2} - 1\right] x j_{\ell}(x) = 0 \quad ; \quad x \equiv kr \quad . \tag{6}$$

The asymptotic form of $krj_{\ell}(kr)$ is $\sin(kr - \frac{1}{2}\pi\ell)$, compared with the asymptotic form of the sinusoidal part of the correct atomic continuum wave function $[P_{E_f,\ell}(r)]$, which is given by[5]

$$\sin[kr - \tfrac{1}{2}\pi\ell - E_f^{-1/2} \ln(2E_f^{1/2}r) + \sigma_{\ell}(E_f) + \delta_{\ell}(E_f)] \quad .$$

We notice that the phase shift terms are absent from the plane-wave partial-ℓ wave function. Therefore, a large plane-wave character in the true final state would presumably be commensurate with an attenuation of the phase-shift-induced oscillations that are found in the atomic $\beta(E_f)$ curves near threshold. Although this is consistent

with the condensed phase results already at hand, it would be interesting to investigate $\beta(E_f)$ behavior closer to threshold than we have done, because the Coulomb phase shift difference induces the most dramatic free-atom β oscillations in this energy range ($E_f \lesssim 2$ Ry). This experiment could be performed, for example, with the Ag(4d) level at 8°-line photon energies at SSRL.

The PWA yields $\beta = 2$ because it ignores the potential and the phase shifts. The condensed phase results, with near plane-wave behavior in the final state, might best be rationalized by considering the differences between the free-atom Coulombic potential and the condensed-phase field which is quasi-periodic even in a disordered system: in a "muffin tin" potential picture, one would expect the outgoing photoelectron's wave function to show phase shifts characteristic of the atomic potential for about one atomic radius--as compared with the free-atom case of infinity--then to show behavior characteristic of a screened Coulomb potential plus a periodic potential. This "truncation" of the phase shifts might yield the behavior observed in $\beta(E_f)$ curves for condensed-phase systems. This is a problem of considerable theoretical interest because a quantitative development of this picture could add considerably to our understanding of the final state.

4. Further Discussion.

In the preceding subsection, it was suggested that the attenuation of $\beta(E_f)$ oscillatory amplitude in the condensed phase

relative to free atoms is directly related to the differences in the phase shifts between these two cases, which in turn is derived from the distinctly different effective potentials for the condensed and gas phase systems. This is probably only a part of the difference. Consideration of Eq. (2) and the discussion in Section C.2 indicates that the matrix elements ($R_{\pm}$) are also important in determining the form of the angular distributions from free atoms. In the condensed phase, initial- and final-state wave functions which enter explicitly in a calculation of $R_{\pm}$ can be highly perturbed by the crystal potential, or its equivalent for a disordered system. However, it is apparent on inspection of the condensed-phase data in this and the last chapter that the features of the total cross section (σ) are quite similar to atomic expectations. This is probably related to our earlier statements that the cross section is determined primarily by the atomic-core regions of the initial-state and final-state wave functions, where the similarity to the atomic analogue--even for the valence d-band electrons--is strong. It would be expected that the total cross section loses all similarity with the atomic case only near threshold, where the matrix elements are most sensitive to the outer regions of the potential that are far from the nucleus and outside the atomic core. It would be quite interesting therefore, to extend condensed phase asymmetry measurements closer to threshold.

One subtle difference between atomic and solid-state matrix elements can already be identified from the present data. The $\beta(E_f)$ curve for Ag(4d) does not undergo nearly as large an oscillation

around the Cooper minimum as the free-atom Xe(4d) level does. This oscillation in Xe(4d), as we have already discussed, is caused mainly by the Cooper minimum in the matrix element (R_+) for the d ➔ f outgoing channel, rather than the phase shifts, and has been quantitatively verified in recent gas phase experiments with Xe.[32] In the condensed phase, however, the situation may be complicated: the valence band contains an admixture of s and p character (see Part I) that cannot be de-coupled from the d-electron intensity in this type of experiment. Therefore, it is quite reasonable to infer that in an atomic picture the relatively large asymmetry parameter in the vicinity of the Ag(4d) Cooper minimum signals the presence of a finite matrix element for other channels (i.e., s ➔ p, p ➔ d, p ➔ s) of photoemission beside d ➔ p, and that this factor earmarks another important difference between condensed-phase and free-atom angular distribution asymmetries derived from $\vec{A}\cdot\vec{P}$. In fact one need only examine the case of free molecules--one step above atoms--where the loss of spherical symmetry already has an important influence on the photoelectron angular distribution.[37]

5. Implications for Other Experiments.

The final point that we touch upon in this discussion is the influence of photoelectron asymmetry on condensed-phase photoemission in general. At low photon energies (or low E_f values), condensed phase asymmetry effects are not usually very striking. The $\beta(E_f)$ parameter is seldom near either of its limits. Asymmetry effects are

smaller with laboratory sources because they are unpolarized, and even with (polarized) synchrotron radiation, the angle α between $\vec{A}$ and $\vec{p}$ is typically fixed at some value far from 0° or 90° so that dramatic effects that could arise through the $\vec{A}\cdot\vec{P}$ perturbation are minimal. Furthermore, ordered systems tend to yield asymmetries from other sources. Thus the $\beta(E_f)$ effects, which are very large, have gone unnoticed, or at least unremarked. But now we must "back-up" and examine the situation regarding past, present, and future experiments.

The majority of photoemission experiments are performed with unpolarized laboratory sources, for which the asymmetry expression reduces to[38]

$$I(E_f,\vec{p}) = [\sigma(E_f)/4\pi]\,[1 - \tfrac{1}{2}\,\beta(E_f)\,P_2(\cos\alpha_{h\nu})] \quad , \qquad (7)$$

where $\alpha_{h\nu}$ is the angle between $\vec{p}$ and the photon momentum wave vector $\vec{k}_{h\nu}$. We see that the asymmetry effect, although smaller, is still important. The relative importance of β then becomes a function of the particular initial-state symmetries studied, the overall experimental geometry, the type of electron analyzer employed, and the photon energy. The atomic effect will always be smallest for $\alpha_{h\nu}$ angles near the "magic" angle, where $P_2(\cos\alpha_{h\nu})$ vanishes. Furthermore, it will be attenuated by the employment of angle-integration methods which yield $I = \sigma(E_f)$, or at photon energies high enough that $\beta \approx 2$ for all levels. This last detail, however, is subject to considerable question; while β approaching 2 at high energies is evident from some of our

measurements, it is by no means clear that this is the case for all levels. It would be interesting to extend $\beta(E_f)$ measurements to higher energies than those covered by these experiments to investigate the correlation between atomic and condensed phase asymptotic β values. For example, atomic theory suggests that β_p approaches a value of 1.5 asymptotically in nearly every case for rare-gas atoms.[20] Additionally, it should be pointed out that very few electron spectrometers have fully angle-integrating detectors. For example, the cylindrical mirror analyzer (CMA), which is generally considered to be "angle integrating", accepts a range of θ_p that does not include all possible angles. In fact, for the CMA utilized in other experiments in this thesis, the range is $0^\circ \leq \theta_p \leq 42.3^\circ$ for a sample oriented with $\vec{n}$ parallel to the CMA symmetry axis (see Fig. 1 in Chapter VI). Therefore, asymmetry effects could be important even with a CMA although they would tend to be highly attenuated by the partial angular integration. Moreover, it should be pointed out that while the atomic asymmetry effect is most readily observable in disordered condensed phases, it should be considered to be an intrinsic effect that will be present in all photoemission measurements. What we have already shown suggests that its importance in a given experiment will depend heavily on a number of factors, including, for example, the possible existence of band structure effects in the photoemission spectrum.

As an illustration of the possible implications of the $\beta(E_f)$ effect, consider the typical x-ray photoemission (ESCA) experiment, where elemental abundances are analyzed from the intensities of

various core levels.[39] For unpolarized x-rays, a small analyzer angular acceptance cone, and including the effect of β, the expression for the atomic abundance of element A relative to B, based on the measurement of the A(X) and B(Y) intensities (I) in a particular sample, is given by

$$\frac{N_A}{N_B} = \left[\frac{I_A \sigma_{YB} C_B}{I_B \sigma_{XA} C_A}\right]\left[\frac{1 - \frac{1}{2}\beta_{YB}(E_{fB})\, P_2(\cos \alpha_{h\nu})}{1 - \frac{1}{2}\beta_{XA}(E_{fA})\, P_2(\cos \alpha_{h\nu})}\right] . \qquad (8)$$

In this expression, C_A and C_B typically include experimental factors such as electron sampling depth and relative analyzer efficiency at the energies E_{fA} and E_{fB}, respectively, and the σ factors are the total cross sections for the photoemission lines. We have also assumed, as is generally the case, that the angle $\alpha_{h\nu}$ is identical for the two measurements. A common practice in the analysis of ESCA data, where atomic asymmetry is ignored, essentially amounts to the assumption: $\beta_{XA}(E_{fA}) = \beta_{YB}(E_{fB})$. The true situation could be quite different if this equality does not hold. The difference between the two β parameters is likely to depend critically on the identities of X and Y and on the energy difference $E_{fA} - E_{fB}$. For example, consider determination of the abundance ratio, N_A/N_B, from the measurement of A(3p) and B(1s) intensities, where we suppose that $\beta_{3p,A}(E_{fA}) = 1$ and $\beta_{1s,B}(E_{fB}) = 2$. In Fig. 6 we show graphically as a function of $\alpha_{h\nu}$ the correction factor $K_{A/B}$ that would be necessary to obtain the <u>correct</u> abundance

ratio from the incorrect one, i.e., $[N_A/N_B \text{ (correct)}] = [N_A/N_B \text{ (incorrect)}] K_{A/B}$, where the incorrect ratio assumes that the two β's are equal. Clearly, $K_{A/B}$ is a significant correction factor over most of the range of $\alpha_{h\nu}$ except for a region that is ca. 5° on either side of the magic angle (54.7°), for which the correction factor is within ~ 5 percent of unity. Elsewhere, it is seen from the plot that a considerable error in the determination of N_A/N_B is obtained by ignoring the existence of the atomic asymmetry effect in photoemission. For a polarized light source, of course, the effect would be even more dramatic (or serious). The plot shown in Fig. 6 suggests that comparisons of elemental abundance by ESCA will have to be reevaluated, to assess the experimental $\alpha_{h\nu}$ (or α) settings. The extent to which required changes are large will depend largely on the high-energy ($E_f \gtrsim 200$ eV) values of $\beta(E_f)$ for various subshells.

D. Summary and Conclusions

We have reported here the first systematic observation of an important effect, to wit, condensed-phase photoelectron asymmetry arising from the $\vec{A}\cdot\vec{P}$ interaction. The $P_2(\cos\alpha)$ form, expected for a randomly ordered system, was confirmed. Dramatic intensity variations were observed as the angle α between $\vec{A}$ and $\vec{p}$ was varied for three disordered systems: Pt, Ag, and Se-Pt. Additionally, $\beta(E_f)$ was found to vary in a manner similar, but not identical, to free-atom predictions;[5,20] i.e., with a tendency toward higher asymmetry ($\beta = 2$). These experiments encompass adsorbate core levels, metal core levels

and valence bands, s, p, d, and f subshells, and cases with and without Cooper minima.

The deviations between experimental and atomic theoretical $\beta(E_f)$ curves have important implications for the nature of the photoemission final-state wave function, which is found to be more plane-wavelike even in disordered condensed phase systems. This is perhaps largely a result of the dissimilarity of phase shifts between the atomic and condensed phases. Additionally, certain differences between condensed-phase and atomic radial matrix elements have been identified.

This effect has bearing on all condensed phase photoemission--past, present, and future. Because it is an atomic effect, it should always be present. Its phenomenology--especially the $\beta(E_f)$ variation--is itself a challenging theoretical problem. Aside from its intrinsic interest, this phenomenon should be useful in characterizing orbital symmetries and in identifying the origins of photoemission lines; i.e., by controlling α to identify orbital symmetry or to enhance certain peaks. Its implications for x-ray photoemission (ESCA) spectra are considerable. In particular, quantitative comparisons of peak intensities are very sensitive to the angle α (or its equivalent for "unpolarized" x-rays). Finally, photoelectron analyzers intended for use with synchrotron radiation from storage rings should be designed to take advantage of photoelectron angular distribution effects.

There are many additional experiments which would be instrumental in further characterization of condensed phase photoelectron asymmetry. For example, measurements of $\beta(E_f)$ in rare-gas samples implanted in

inert substrates, metallic and nonmetallic, would assess directly the effect of local environment on $\beta(E_f)$. Additionally, a systematic investigation of $\beta(E_f)$ as a function of the degree of system crystallinity would be interesting. Moreover, the extension of $\beta(E_f)$ measurements to higher and lower energies (E_f) would be useful in the verification and quantitative evaluation of several phenomena conjectured in this work as a result of studies in an intermediate-energy range.

Finally, it should be stressed that angular distribution effects in any condensed phase photoemission experiment are non-separable from atomic effects. The angular distribution is derived from both long range ordering phenomena and from localized (i.e., atomic) effects. Therefore, the common and traditional notion that angular-distribution and atomic effects in condensed-phase photoemission have different origins is simply wrong. In any particular experiment, a careful choice of experimental conditions must be made in order for only one of these two traditional approaches to be approximately valid.

REFERENCES

* This chapter is based on experiments performed in collaboration with S. D. Kevan, B.-C. Lu, J. G. Tobin, and D. A. Shirley; published in Chem. Phys. Lett. 71, 448 (1980).

1. Ref. 1 in Chapter I.
2. C. N. Yang, Phys. Rev. 74, 764 (1948).
3. H. A. Bethe, in Handbuch der Physik, Vol. 24/1, edited by H. Geiger and K. Sheel (Springer-Verlag, Berlin, 1933), p. 482.
4. J. Cooper and R. N. Zare, J. Chem. Phys. 48, 942 (1968).
5. S. T. Manson, Adv. Electron. Electron Phys. 44, 1 (1977). This review article also gives a number of useful references to earlier work.
6. J. Berkowitz, Photoabsorption, Photoionization, and Photoelectron Spectroscopy (Academic, New York, 1979), Chapter VII, and references therein.
7. S. T. Manson and D. Dill, in Electron Spectroscopy: Theory, Techniques and Applications, Vol. 2, edited by C. R. Brundle and A. D. Baker (Academic, New York, 1978); J. A. R. Samson, ibid., Vol. 4, edited by C. R. Brundle and A. D. Baker (Academic, New York, 1981).
8. F. J. Wuilleumier, in Atomic Physics, Vol. 7, edited by D. Kleppner and F. M. Pipkin (Plenum, New York, 1981).
9. Some aspects of atomic effects in photoelectron angular distributions from solids have been implicitly included in several recent formulations; e.g., (a) J. Stöhr, F. R. McFeely,

G. Apai, P. S. Wehner, and D. A. Shirley, Phys. Rev. B 14, 4431 (1976); (b) N. J. Shevchik and D. Liebowitz, Phys. Rev. B 18, 1618 (1978); (c) D. Norman, D. P. Woodruff, N. V. Smith, M. M. Traum, and H. H. Farrell, Phys. Rev. B 18, 6789 (1978).

10. S. D. Kevan, D. H. Rosenblatt, D. Denley, B.-C. Lu, and D. A. Shirley, Phys. Rev. Lett. 41, 1565 (1978); Phys. Rev. B 20, 4133 (1979); Refs. 22 and 23 of Chapter I.

11. F. R. McFeely, J. Stöhr, G. Apai, P. S. Wehner, and D. A. Shirley, Phys. Rev. B 14, 3273 (1976).

12. S. D. Kevan and D. A. Shirley, Phys. Rev. B 22, 542 (1980); S. D. Kevan, Ph.D. thesis, University of California, Berkeley, 1980 (LBL-11017, unpublished).

13. The angle α is readily calculated from θ_A using Eq. (2) in Chapter I, with $\theta_p = \pi/4$ and $(\phi_p - \phi_A) = \pi/2$, yielding $\alpha = \cos^{-1}[(\cos \theta_A)/2^{1/2}]$.

14. D. E. Eastman, J. J. Donelon, N. C. Hien, and F. J. Himpsel, Nucl. Instrum. Methods 172, 327 (1980).

15. Estimation based on the very high asymmetry parameter ($\beta = 1.94$) measured for the Ag(4s) photoemission peak, vide infra.

16. D. R. Denley, Ph.D. thesis, University of California, Berkeley, 1979 (LBL-9482, unpublished).

17. See, for example, J. A. Stratton, Electromagnetic Theory (McGraw-Hill, New York, 1941), Chapter IX.

18. The method we used is given by S. P. Weeks and E. W. Plummer, Solid State Commun. 21, 695 (1977). Optical data were obtained

from H.-J. Hagemann, W. Gudat, and C. Kunz, J. Opt. Soc. Am. 65, 742 (1975), and Ref. 1, therein.

19. S. T. Manson, in Photoemission in Solids I, edited by M. Cardona and L. Ley (Springer-Verlag, New York, 1978).
20. D. J. Kennedy and S. T. Manson, Phys. Rev. A 5, 227 (1972).
21. F. Combet Farnoux, J. Phys. (Paris) 32 (C4), 7 (1971).
22. S. T. Manson, Adv. Electron. Electron Phys. 41, 73 (1976).
23. J. Cooper and R. N. Zare, in Lectures in Theoretical Physics, Vol. IIC, edited by S. Geltman, K. Mahanthappa, and W. Brittin (Gordon and Breach, New York, 1969), p. 317.
24. S. T. Manson, J. Electron Spectrosc. Relat. Phenom. 1, 413 (1973); ibid. 2, 206 (1973).
25. S. T. Manson and J. W. Cooper, Phys. Rev. 165, 126 (1968).
26. J. S. Shyu and S. T. Manson, Phys. Rev. A 11, 166 (1975).
27. J. W. Cooper, Phys. Rev. Lett. 13, 762 (1964); U. Fano and J. W. Cooper, Rev. Mod. Phys. 40, 441 (1968).
28. P. S. Wehner, J. Stöhr, G. Apai, F. R. McFeely, R. S. Williams, and D. A. Shirley, Phys. Rev. B 14, 2411 (1976).
29. (a) S. P. Kowalczyk, L. Ley, R. L. Martin, F. R. McFeely, and D. A. Shirley, Faraday Discussions Chem. Soc. 60, 7 (1975); (b) Refs. 5-7 in Chapter IV.
30. Ref. 3 in Chapter IV.
31. S. T. Manson, Phys. Rev. 182, 97 (1969); Phys. Rev. Lett. 26, 219 (1971).

32. S. H. Southworth, P. H. Kobrin, C. M. Truesdale, D. Lindle, S. Owaki, and D. A. Shirley, Phys. Rev. A 24, 2257 (1981).

33. Ref. 53 in Chapter I.

34. Ref. 9b.

35. A. R. Edmonds, Angular Momentum in Quantum Mechanics (Princeton University, Princeton, 1960), p. 80.

36. R. A. Buckingham, in Quantum Theory I. Elements, edited by D. R. Bates (Academic, New York, 1961), Chapter 4.

37. D. Loomba, S. Wallace, D. Dill, and J. L. Dehmer, J. Chem. Phys. 75, 4546 (1981), and references therein.

38. J. W. Cooper and S. T. Manson, Phys. Rev. 177, 157 (1969).

39. W. J. Carter, G. K. Schweitzer, and T. A. Carlson, J. Electron Spectrosc. Relat. Phenom. 5, 827 (1974).

FIGURE CAPTIONS

Fig. 1. General coordinate scheme utilized in condensed-phase angle-resolved photoemission studies, with the $\vec{z}$ axis parallel to the surface normal ($\vec{n}$). Thus, the radiation polarization angle is $\theta_A = \angle(\vec{n},\vec{A})$ and the photoemission angle is $\theta_p = \angle(\vec{n},\vec{p})$, with $\vec{A}$ and $\vec{p}$ the radiation vector potential and photoelectron momentum vector, respectively, and with the azimuthal angles (ϕ_A, ϕ_p) defined relative to the $\vec{x}$ axis. Condensed phase photoelectron asymmetry is a strong function of the angle α, between $\vec{A}$ and $\vec{p}$.

Fig. 2. Upper panels: the Ag(4s) photoemission peak at $h\nu$ = 225 eV, from polycrystalline silver, with $\alpha = \angle(\vec{A}, \vec{p}) = 48^\circ$ and 90° (left); peak intensity for $48^\circ \leq \alpha \leq 90^\circ$, fitted to Eq. (1) with $\beta = 1.92$ (right). Lower panels: similar results for the silver valence-band peak [nominally Ag(4d)], with $h\nu$ = 100 eV and $\beta = 1.72$.

Fig. 3. Radial plots (I, α) of the expression $I = 1 + \beta P_2(\cos\alpha)$ as functions of α for various values of β (2, 1, 0, and -1), showing widely different shapes. The angle $\alpha = 0^\circ$ ($\vec{p} \parallel \vec{A}$) is indicated by the vertical axis with an arrowhead for $\vec{A}$, and $\alpha = 90^\circ$ ($\vec{p} \perp \vec{A}$) is designated by the horizontal axis. With $\alpha = 0^\circ$, we have I = 3, 2, 1, and 0 for β = 2, 1, 0, and -1, respectively. High asymmetry (β close to 2) implies that the angular distribution is peaked along the direction of $\vec{A}$.

Fig. 4. Variations of photoemission cross sections (σ) and asymmetry parameters (β) with photoelectron kinetic energy. Data are

denoted by circles and connected by curves in experimental (left) panels, for Se (Z = 34) as adsorbate atoms and Pt (Z = 78) as metal. Theoretical curves for Kr (Z = 36) and Au (Z = 79) as free atoms were taken from Refs. 20, and 5 and 21, respectively. The experimental σ values are only on a relative scale. The σ variations are close to theory, while β shows an upward shift and in Pt a decreased amplitude of variation with energy.

Fig. 5. Comparison of σ and β results for silver (Z = 47) metal with theoretical values for atomic Xe (Z = 54), from Ref. 20, with format similar to Fig. 4. The Ag(4s) peak shows $\beta \approx 2$, while for the Ag(4d) peak both the Cooper minimum in σ and the modulation of β are qualitatively reproduced, though the latter is attenuated, perhaps in part by admixture of s and p character in the valence band.

Fig. 6. Factor ($K_{A/B}$) required to correct the ESCA-derived atomic abundance ratio (N_A/N_B), plotted as a function of the angle ($\alpha_{h\nu}$) between incident photon and outgoing photoelectron momentum vectors, for a hypothetical case (see text) where $\beta_{3p,A} = 1$ and $\beta_{1s,B} = 2$. $K_{A/B}$ differs notably from unity over most of the range of $\alpha_{h\nu}$, except for angles within ca. 5° of the magic angle (54.7°) where the deviation from unity is only about 5 percent. This example demonstrates the importance of accounting for condensed phase asymmetry effects in the analysis of ESCA data.

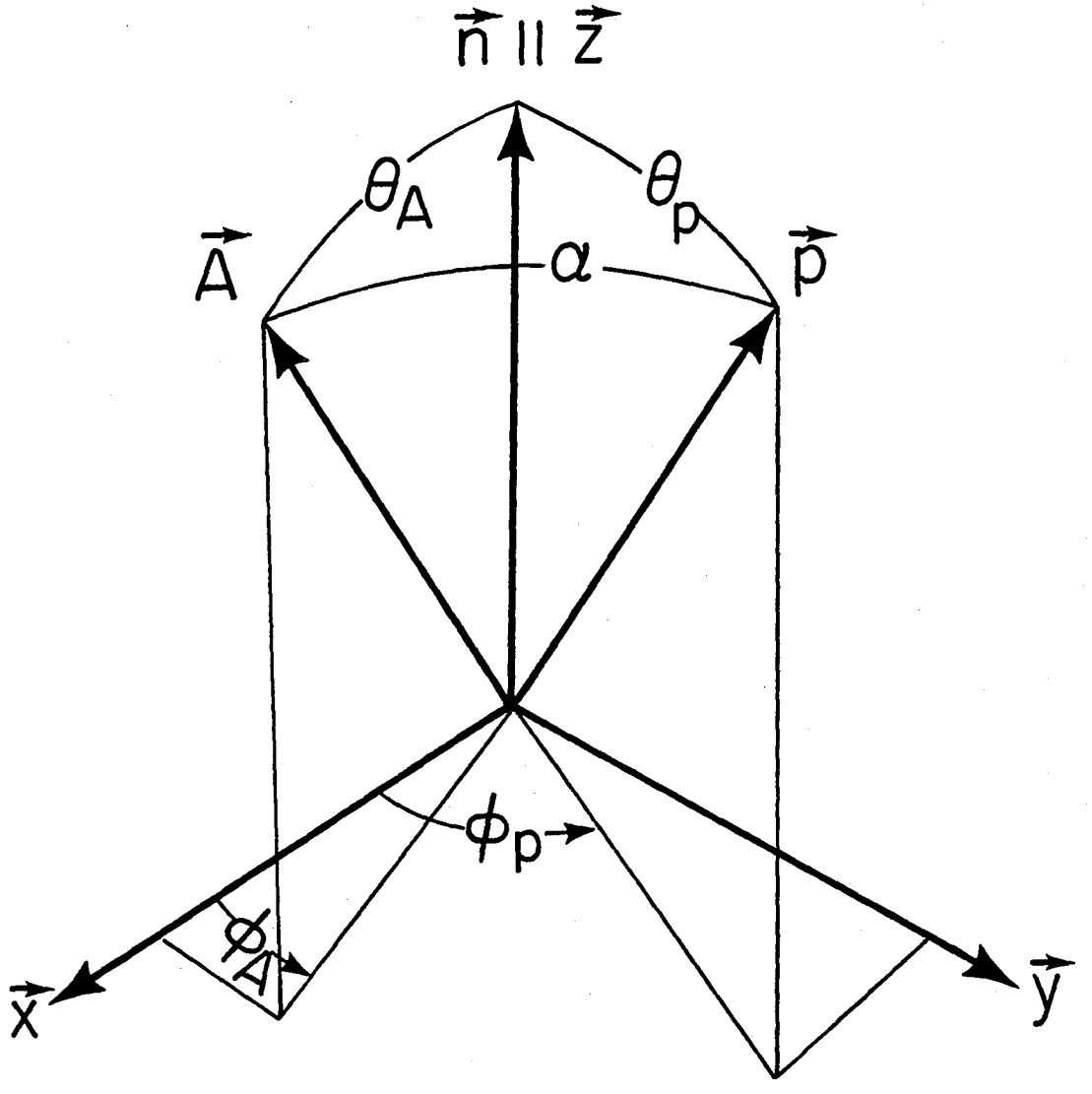

XBL8111-12052

Figure 1

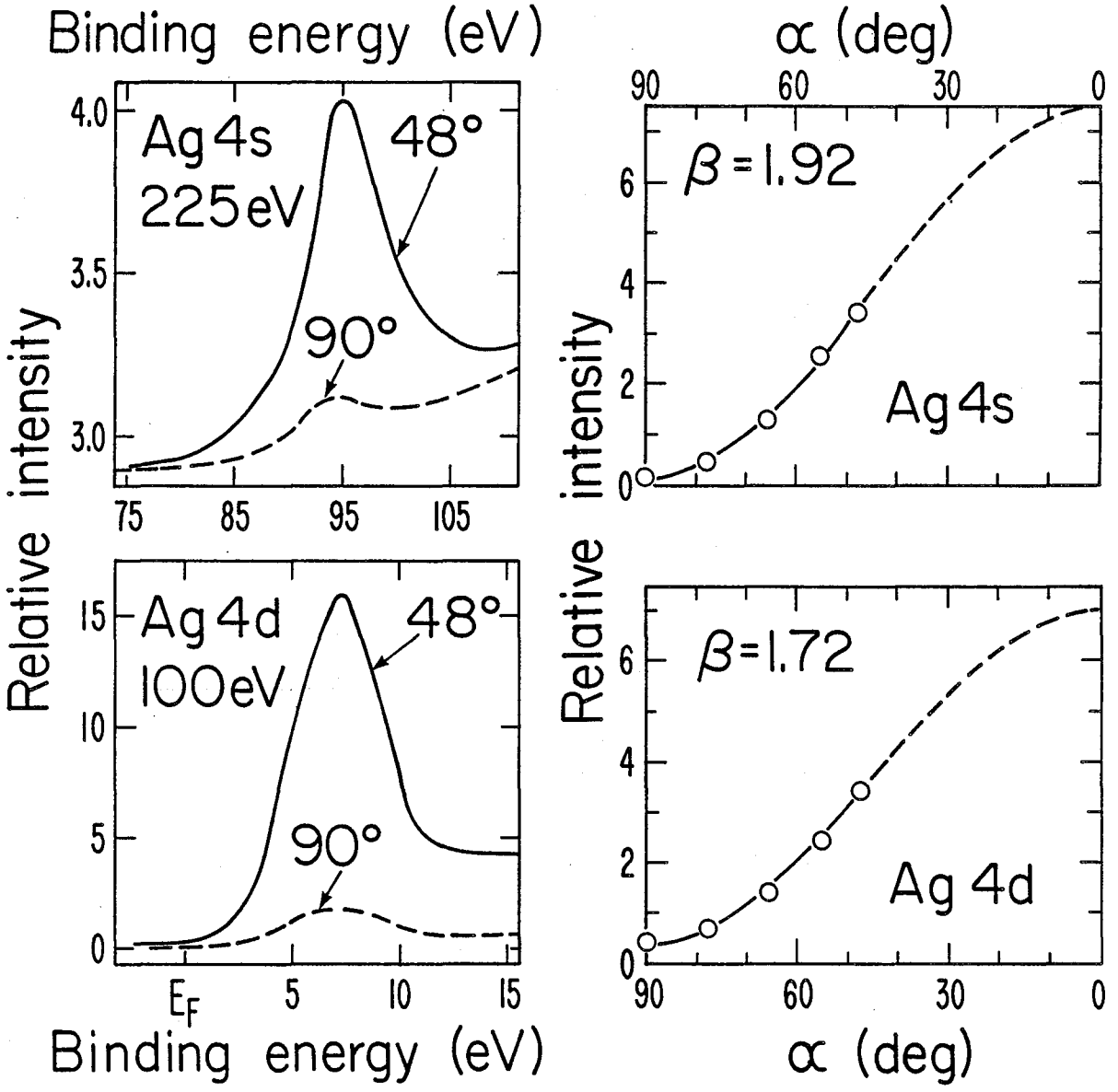

XBL 797-2103

Figure 2

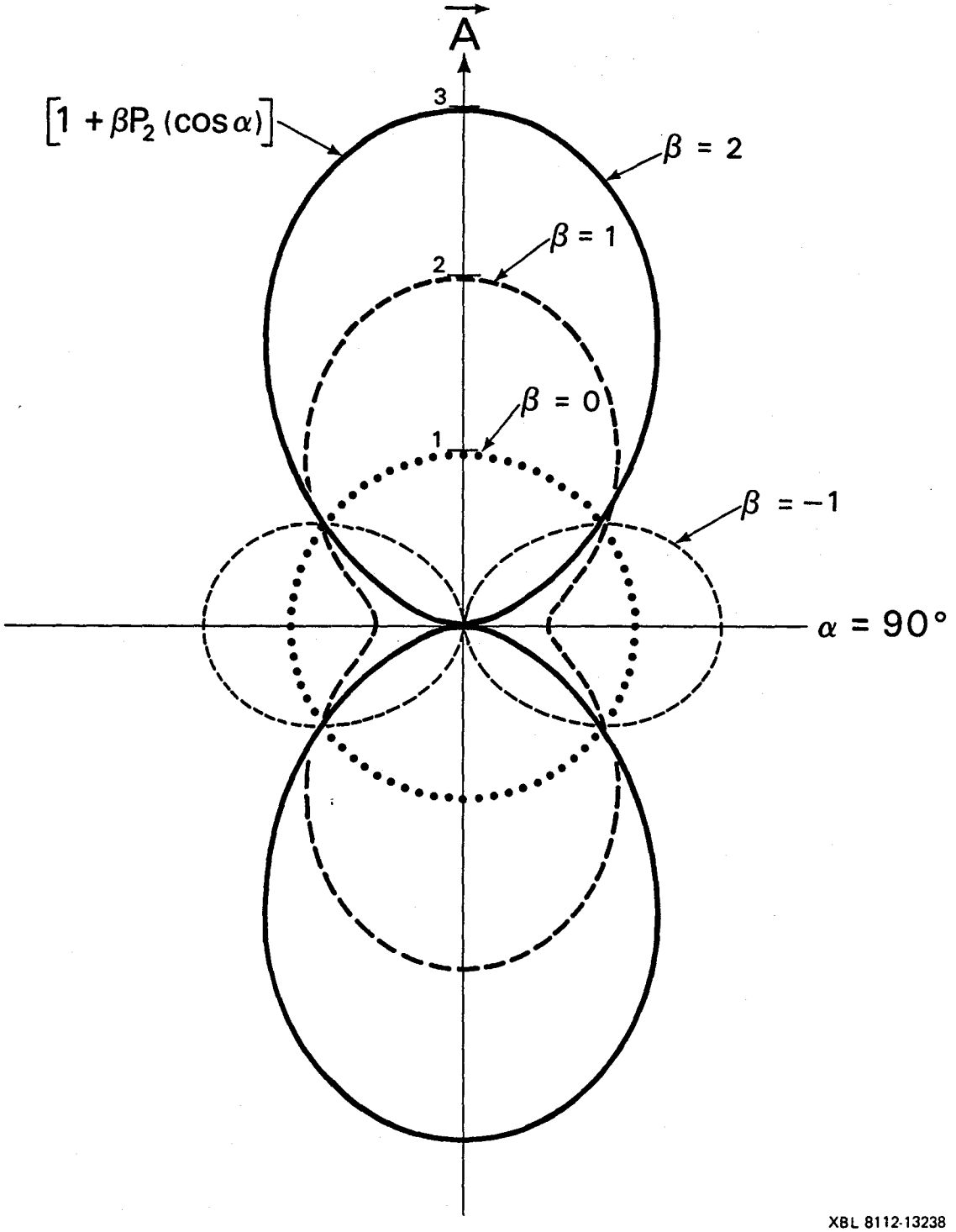
$\alpha = L(\vec{A},\vec{p}) = 0°$
$\vec{A}$
$[1 + \beta P_2(\cos\alpha)]$
3
2
1
$\beta = 2$
$\beta = 1$
$\beta = 0$
$\beta = -1$
$\alpha = 90°$
XBL 8112-13238

Figure 3

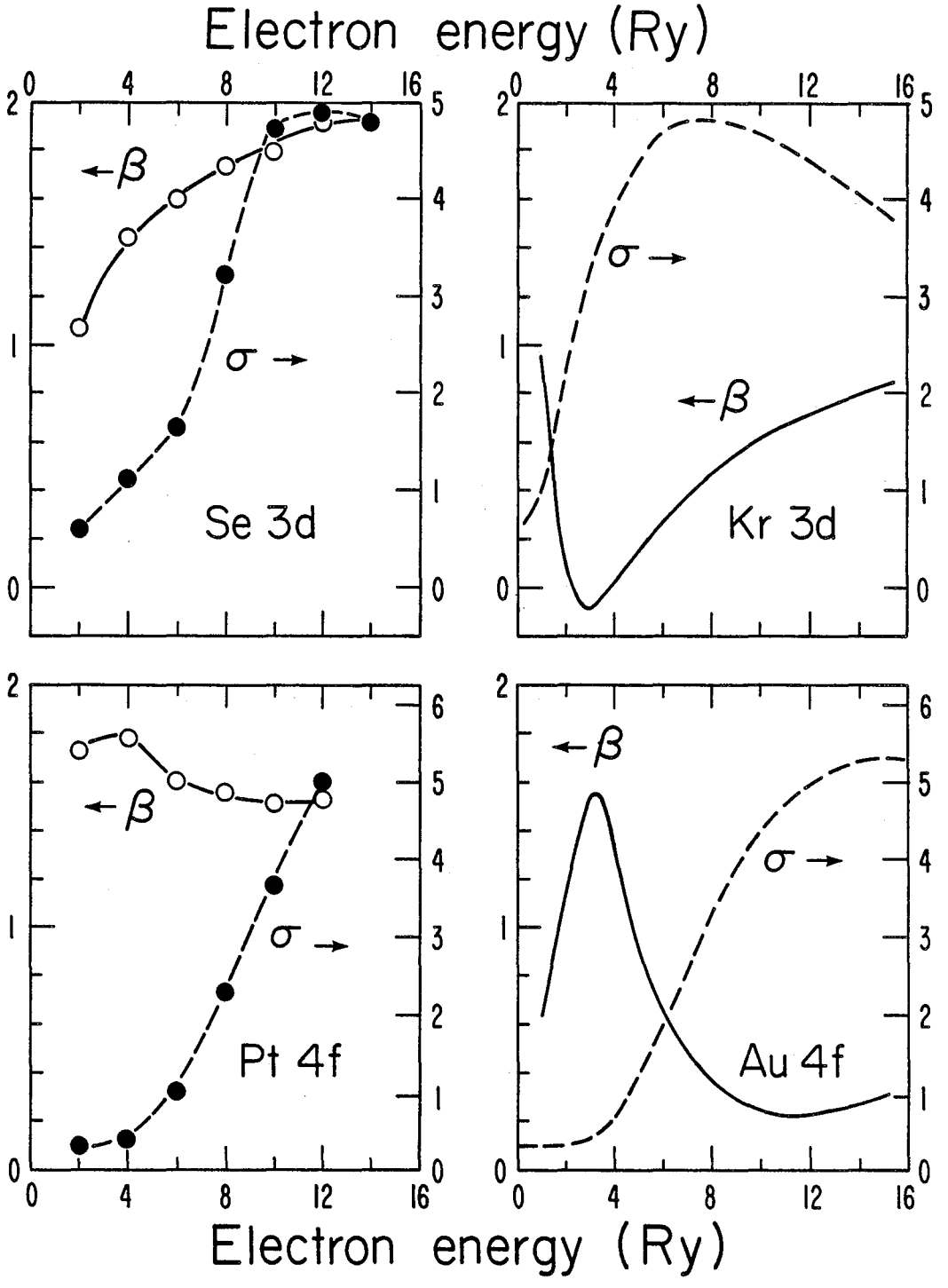

XBL 797-2102

Figure 4

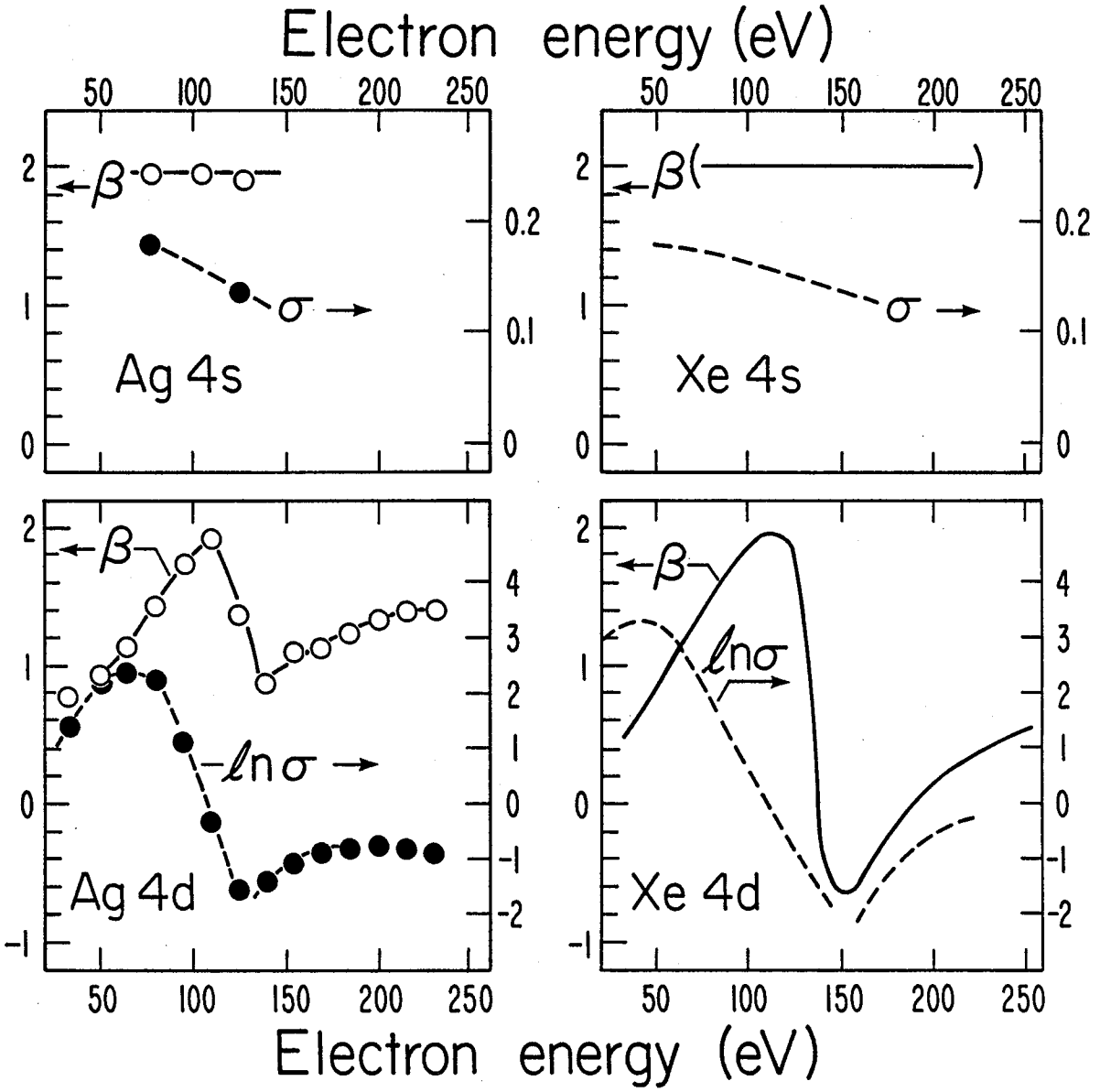

XBL 797-2104

Figure 5

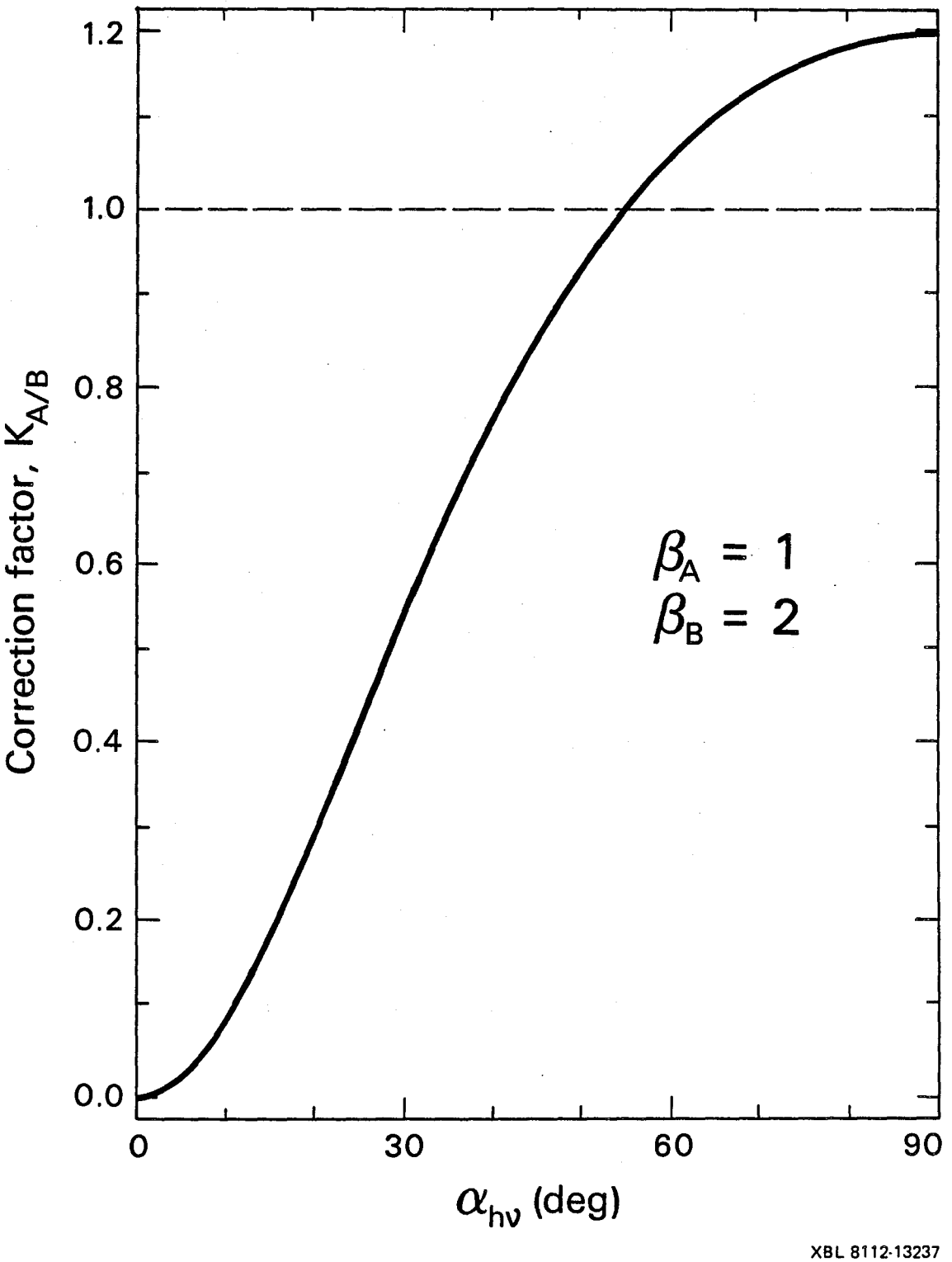

XBL 8112-13237

Figure 6

VIII. SUBSTRATE-DEPENDENT C(1s) SHAPE RESONANCE IN CO OVERLAYERS ON Ni(111) AND Ni(001) *

A. Introduction

In the previous chapter, the existence of a condensed phase analogue to atomic photoelectron asymmetry was clearly established through angle-resolved photoemission (ARP) studies of photoelectron angular distributions. A logical extension of the concepts underlying that work is the study of angular distributions in molecular overlayers. Disordered overlayers would be expected to exhibit condensed phase photoelectron asymmetry much like the atomic systems. However, in this chapter we discuss experiments with ordered molecular overlayers, for which the experimental situation is different: the ordered system shows angular distribution properties indicative of both the $\vec{A}\cdot\vec{P}$ interaction (Chapter VII) and molecular orbital orientation. We have already alluded (previous chapters) to the fact that ordered systems should be characterized by both types of effects. However, it is important to keep in mind that the angular distribution effects discussed in this chapter are fundamentally different from band structure effects (see Part I) because they are derived from the localized properties of molecular photoemission. In Chapter I, an angular distribution expression for an "oriented" atomic orbital is given by Eq. (20), but it will become apparent that the case of molecular orbital angular distributions is much more interesting than that suggested by this equation. Once again, as in the case of atomic

asymmetry, there are significant differences between the experimental results and gas-phase predictions.

The study of the structure of molecular overlayers on metal surfaces by valence-band angle-resolved photoemission is an important problem that has recently received considerable attention.[1] The primary result has usually been the determination of molecular axis ($\vec{M}$) orientation with respect to the crystal normal ($\vec{n}$), as inferred from comparison of experimental ARP intensities with gas-phase data and theory. Examples include the prototype systems CO-Ni(111) (Ref. 2) and CO-Ni(001) (Refs. 3 and 4). In the latter system, an intensity resonance in the overlayer level derived from the 4σ molecular orbital[4] has been assigned to the adsorbed-molecule analogue of the well-known gaseous CO valence-shell shape resonance.[5-7] It has been pointed out that the angular peaking of photoelectrons along the molecular axis at the shape resonance energy could serve as a direct "beacon" identifying the molecular adsorbate orientation,[6,8] provided that adsorbed molecules possess resonances similar to those predicted for free molecules.[6,9] In this connection, adsorbate core levels[9] possess distinct advantages for orientation studies, because their spatial localization eliminates ambiguities due to initial-state substrate effects.[10] Recently, the advantages of core levels have been exploited in ARP studies of CO-Ni(001) with use of Al Kα radiation.[11] In this chapter, we report the first observation of adsorbate core-level ARP resonances, for the C(1s) level in CO-Ni(111) and CO-Ni(001). Although these resonances are similar to the predicted

oriented-molecule shape resonance,[8] there is strong evidence for both substrate perturbations and substrate specificity. However, the sharp angular- and energy-dependence structures of these core-level resonances, which are expected to be general features of small molecules,[9] should facilitate interesting experiments on other adsorbates concerning molecular bond axis orientation.

The remainder of this chapter is organized as follows: Experimental procedures are discussed in Section B, results and discussion are given in Section C, and Section D contains a summary.

B. Experimental

The ARP experiments employed soft x-rays from Beam line I-1 at the Stanford Synchrotron Radiation Laboratory, in the energy range 300 eV $\leq h\nu \leq$ 360 eV, and highly polarized (~ 98 percent[12]) in the horizontal plane. By using a grazing-incidence "grasshopper" monochromator equipped with a 1200-lines/mm holographic grating during dedicated operation of the storage ring, we obtained photon flux and resolution sufficient to measure the adsorbate C(1s) core level in this near-threshold energy range. These experiments, together with our recent C(1s) and O(1s) normal photoelectron diffraction measurements for CO-Ni(111) and CO-Ni(001) (Ref. 13) in the energy range 300 eV $\leq h\nu \leq$ 650 eV, are the first systematic ARP studies of these light-element core levels with intermediate-energy x-rays.

Our photoemission spectrometer, described elsewhere,[14] employs a 5.40-cm mean radius hemispherical analyzer with independent two-circle

rotation. In these experiments, the relative orientations of the radiation vector potential ($\vec{A}$), the outgoing photoelectron direction ($\vec{p}$), and the crystal normal ($\vec{n}$) were independently varied in the plane of incidence. In this way, as shown in Fig. 1(a), the emission angle $\theta_p = \angle(\vec{n},\vec{p})$ could be varied between 0° and 45° in the $\phi_p = 0°$ azimuth (toward the photon beam direction) and between 0° and 90° in the ϕ_p = 180° azimuth. The polarization angle $\theta_A = \angle(\vec{n},\vec{A})$ could be varied from 0° to 45° in the $\phi_A = 180°$ azimuth.

The Ni(111) and Ni(001) crystals were cut and polished to within ± 1/4° of the [111] and [001] directions, respectively, with a mean surface roughness of 0.05 μm. After etching in a solution of 30 percent nitric acid, 50 percent glacial acetic acid, and 10 percent each of sulfuric and orthophosphoric acids[15] (ca. 45 sec at 363 ± 5K), the crystals were installed in the photoemission instrument (base pressure $\lesssim 3 \times 10^{-10}$ torr) and cleaned of bulk and surface impurities <u>in situ</u> by cycles of Ar^+ ion bombardment (beam voltage = 1 kV) and annealing (ca. 975K). The resulting surfaces were monitored by Auger electron spectroscopy (AES) for cleanliness and low energy electron diffraction (LEED) for crystallographic order, yielding an absence of impurity (C, O, and S) AES signals and LEED patterns with sharp and intense spots characteristic of the normal (1x1) clean surface structures. Carbon, usually the most tenacious surface impurity, could not be detected on either surface using AES, but a small C(1s) peak was visible for Ni(001) using photoemission at $h\nu$ = 360 eV, a photon energy where the C(1s) level has a reasonably large

photoemission cross section. It appears that, at least in our apparatus, the C(1s) sensitivity by photoemission is significantly better than by AES. We suspect from this experience that minor carbon contamination (< 0.05 monolayers) is more prevalent in studies of this surface than the literature tends to imply. A subsequent, more extensive ion etching and annealing procedure followed by a post-anneal rapid cooling method (from 930K to 120K in ca. 5 min) similar to the one employed by Passler, et al.,[16] was found to produce a contaminant-free and well-ordered Ni(001) surface.

The 2 L (1 L = 10^{-6} torr sec) CO exposures and subsequent ARP measurements were made with the Ni(001) crystal cooled to 120K and the Ni(111) sample at 295K. LEED was not performed on the overlayer systems prior to the ARP experiments, to avoid the usual primary-beam damage.[16-18] No time-dependent degradation of the overlayers (as determined by photoemission) was apparent over several hours of ARP experimentation. In addition, LEED measurements after the ARP studies yielded patterns that were typically faint and diffuse, but showed $(\sqrt{3} \times \sqrt{3})R30^\circ$ and c(2x2) structures for the (111) (see Refs. 19 and 20) and (001) (see Refs. 16-18) faces, respectively. Normal-emission C(1s) and O(1s) photoelectron diffraction studies of the same overlayers further characterized these systems:[13,21] the atop-bonded CO structure for c(2x2) CO-Ni(001) was found, confirming recent detailed LEED investigations,[16-18] while the adsorbate was determined to occupy the twofold bridge site in $(\sqrt{3} \times \sqrt{3})R30^\circ$ CO-Ni(111).

As a further comment on the Ni(001) surface, we should point out that the rapid-quenching procedure discussed above presumably lowers

the migration rate of carbon from the bulk sufficiently that the surface remains carbon-free for the period of time required to prepare the CO overlayer, after which bulk diffusion of C to the surface is no longer a problem. Because the bulk-impurity- and CO-derived peak structures could be differentiated in the C(1s) photoemission spectrum, this hypothesis was tested by monitoring the C(1s) spectrum over a relatively long period of time (ca. 8 to 12 hours) after the quenching procedure and subsequent CO overlayer preparation: no bulk impurity structure was observed. Additionally, we found that the clean surface remained carbon-free at 120K for at least several hours after the quenching procedure, and the CO-Ni(001) system could be warmed to room temperature without causing the introduction of the impurity-derived structure to the C(1s) spectrum. However, to avoid possible systematic errors, all CO-Ni(001) measurements reported below were obtained with the sample remaining cooled at 120K.

Complete photoemission energy distribution curves (EDCs) were collected at various photon energies, and relative C(1s) intensities were obtained as peak areas normalized to analyzer efficiency and continuously monitored incident photon flux, with the azimuthal crystal orientations, shown in Fig. 1(b), held fixed throughout the experiments. Polar and azimuthal crystal orientations on the sample manipulator, which had previously been determined by the back-reflection Laue method, were checked with laser autocollimation and LEED. We estimate the uncertainty in these orientations [Fig. 1(b)] to be less than $\pm 1^{\circ}$ (polar) and about ± 1 to $\pm 2^{\circ}$ (azimuthal). It

should be pointed out that $\vec{A}$-vector variations at the vacuum-metal interface should not be important in the energy range employed, and were not considered in the analysis of the data presented below. The possibility of a problem being associated with $\vec{A}$-variation at vacuum-metal interfaces in the soft x-ray region is a misconception often held by spectroscopists familiar with a problem that does exist in the VUV region[22] (see, e.g., Chapter II). $\vec{A}$-variation effects are small or negligible above 100 eV, and certainly can be neglected above 300 eV, where our photoemission measurements were made. To quantify this, the ratio n/κ (for metals) is typically 1-2 in the VUV, while it is 200-500 near $h\nu$ = 300 eV, more than two orders of magnitude higher[23] (n and κ are the real and imaginary parts of the dielectric function). It follows from the Fresnel equations[24] that $\vec{A}$ is not significantly affected at these energies.

C. Results and Discussion

1. Energy Dependence of the Near-Resonance C(1s) Intensity.

The C(1s) resonance is clearly seen in Fig. 1(c) for normal emission from CO-Ni(111), where some of the normalized EDCs are plotted for a range of photon energies, sweeping through the resonance maximum at $h\nu$ = 311 eV. The total experimental C(1s) linewidth (FWHM) for photon energies in this region was 1.5 eV, consistent with photon energy and analyzer resolutions of approximately 1.45 eV and 0.25 eV (FWHM), respectively. This near-threshold ARP experiment was

complicated by the large inelastic background structure characteristic of condensed-phase photoemission spectra. However, by collecting digital data with good statistical accuracy over a large energy range for each spectrum, and careful least-squares fitting, we were able to derive very accurate peak intensities.

In Fig. 2, we show a region of the energy-dependent photoemission cross section curve for CO-Ni(111) obtained from the EDC peak areas, along with similar results for CO-Ni(001). The non-atomiclike behavior and sharp peak structures of these cross section curves are striking. To facilitate a comparison of the two curves, they have been normalized at the minimum region around $h\nu$ = 335 eV. This procedure is justified because this region is the only portion of the total C(1s) cross section curve obtained that is relatively free of photoelectron diffraction modulations.[13] It thus approximates the "atomiclike" background near 335 eV. As a further test of this point, the resonance peak intensity was also normalized to an "average" curve drawn through the ARP results at higher photon energies, thereby averaging over the modulations arising from photoelectron diffraction. The results were consistent. The resonance maximum for both curves in Fig. 2 is shown to lie at $h\nu$ = 311 eV. Additionally, the curves are seen to be nearly identical in shape, but the intensity maximum relative to the "atomic" value is attenuated by a factor of two for CO-Ni(001) relative to CO-Ni(111).

2. Angular Distribution of the Resonance and Similarities with the Gaseous CO Shape Resonance.

The characterization of this resonant behavior is aided by the previous orientation studies discussed above,[2-4,11] which yielded $\vec{M}$ parallel to $\vec{n}$ for CO overlayers on both substrates.[25] Consequently, we have determined that the resonance has properties very similar to those for the shape resonance predicted in the C(1s) cross section in gaseous CO. For an oriented molecule, the shape-resonant photoemission intensity should be sharply maximized in θ when the three vectors $\vec{A}$, $\vec{p}$, and $\vec{M}$ (or equivalently $\vec{n}$ in the present case) are aligned.[8] Figures 3(a) and 3(b) show that the adsorbate resonance has this property. In Fig. 3(a), we show the θ_A dependence of the near-resonance cross section for CO-Ni(111) [similar measurements have not yet been made with CO-Ni(001)]. In these measurements, $\vec{p}$ is fixed along $\vec{n}$, and the intensity is seen to increase as $\vec{A}$ is brought into near alignment with these two vectors. The θ_p dependence of the C(1s) intensity at $h\nu$ = 311 eV is shown in Fig. 3(b) for both systems. As $\vec{p}$ is brought to near alignment with fixed $\vec{n}$ and $\vec{A}$, the intensity reaches a maximum for CO on both substrates. Changes in θ_p by 20° bring about intensity modulations by factors of 2 or more.

The general properties of this shape resonance can be understood by considering first the photoionization process in the gaseous CO molecule, and subsequently, the oriented molecule. Dehmer and Dill[9,26] suggested that the molecular core-level photoionization process can be conceptualized in two steps: (1) photoexcitation of a

K-shell electron via the electric dipole interaction, producing a photoelectron within the atomic core with $\ell = 1$; and (2) scattering of this p-wave electron off the anisotropic molecular field, yielding amplitude in the entire range of allowed partial ℓ-wave outgoing components of the electron's final state as it propagates away from the molecule in either the σ or π ($\Delta\lambda = 0, \pm 1$, respectively) ionization channel. A shape resonance occurs in the $\ell = 3$ component of the σ channel because the spatial extent of the molecular field and the large f-wave centrifugal barrier in the effective scattering potential allow this component to penetrate its barrier at the resonant final-state energy and form a quasi-bound state with dramatically enhanced overlap with the initial-state 1s wave function (thus producing a resonance in the photoionization cross section).[9,26] Analogous to the barrier-penetration problem in elementary quantum mechanics,[27] the resonance exists over a very small range of photoelectron kinetic energies as determined, to first order, by the internuclear separation in the diatomic molecule;[28] in CO-Ni, the resonance width is about 10 eV (FWHM) as evidenced by the cross section curves in Fig. 2.

Dehmer and Dill[9] pointed out that the $\sigma \rightarrow \pi$ channel does not undergo a resonance in the continuum, indicating that the quasibound f wave is oriented only along the molecular axis. This has dramatic consequences for the oriented-molecule angular distributions, as evidenced by the θ_p-dependence curves in Fig. 3(b) and as we will consider in more detail shortly. Shape resonances appear to be general phenomena of small molecules[26] and various initial-state

levels in addition to the K shells, having been predicted and/or observed in valence- and/or core-level photoemission in systems such as CO, N_2, NO, O_2, NO_2, OCS, CS_2, CO_2, N_2O, and H_2O (Ref. 29). Prior to the measurements discussed here, shape resonances in the 4σ photoemission cross section had been observed in gaseous CO (Ref. 7) and in CO overlayers on Ni(001) and Cu(001) substrates (Refs. 4 and 37, respectively), but no measurements had been performed on the C(1s) or O(1s) levels for which resonances are expected to lie about 11 eV above threshold[8,38] in gaseous CO. The results reported here represent the first measurements of K-shell molecular shape resonances by photoemission.

The σ-channel shape resonance has interesting photoemission properties in oriented (i.e., adsorbed) molecules, thus establishing its connection with molecular adsorbate orientation studies. This connection can be understood within the framework of the angular distribution of oriented-molecule photoemission for an isolated system. For a cylindrically-symmetric, oriented molecule and linearly-polarized light, Dill[39] has shown that the angular distribution with $\vec{A}$ either parallel or perpendicular to $\vec{M}$ has the form

$$I(E_f,\vec{p}) = \sum_{\ell=0}^{2\ell_{max}} B_\ell(E_f)\, P_\ell[\cos \angle(\vec{p},\vec{M})] \quad , \qquad (1)$$

where $I(E_f,\vec{p})$ is the angle-resolved photoemission intensity, ℓ_{max} is the maximum orbital angular momentum component of the final-state

wave function, the P_ℓ terms are Legendre polynomials, and the angle between $\vec{p}$ and $\vec{M}$ is equal to θ_p in the present case of CO-Ni. This expression for the angular distribution is quite different from the Yang's[40] theorem form [see Eq. (1) in Chapter VII] for a randomly-oriented system. First of all, the angular dependence reflects the "built-in" spatial asymmetry of the oriented system, rather than only that of the $\vec{A}$ vector which enters explicitly into the expression for the B_ℓ coefficients. Furthermore, the Yang expression[40] can be cast into a form similar to Eq. (1), but with only $\ell = 0, 2$ terms in the summation over orbital momentum,[39] whereas the expression for the oriented molecule allows the complete range of ℓ in the final-state wave function to contribute to the angular distribution. In particular, the component of $\vec{A}$ along $\vec{M}$ excites the σ photoionization channel, which contains the shape resonance in the $\ell = 3$ final-state partial-wave component. Equation (1) predicts the angular distribution for an oriented CO molecule to be characteristic of an f wave at the shape resonance energy: at this energy, the B_3 coefficient dominates the sum in Eq. (1), so that (neglecting all other terms) the angular distribution with $\vec{A} \parallel \vec{M}$ is given simply by $I(\vec{p}) \sim P_3(\cos \theta_p)$. In other words, the f-wave component is so much larger than the other components at the σ shape resonance--the B_ℓ terms are proportional to the partial ℓ-wave photoemission matrix elements[39]--that the angular distribution essentially has the form of $P_3(\cos \theta_p)$, which is sharply peaked along $\theta_p = 0°$. In fact, with $x \equiv \cos \theta_p$, it is straightforward to show that $P_3(x) = (5x^3 - 3x)/2$ is a more sharply peaked function of θ_p along the

$\theta_p = 0°$ direction than $P_2(x) = (3x^2 - 1)/2$. This is why the shape resonance phenomenon should generally be quite readily exploited in molecular adsorbate orientation studies: because the final-state wave function has mainly f-wave character at the shape resonance energy, the angular distribution should be a "beacon" of the orientation of $\vec{M}$. Although the general intensity expression for arbitrary orientations of $\vec{A}$ and $\vec{p}$ with respect to $\vec{M}$ (θ_A and θ_p) is more complicated[8] than Eq. (1), it is expected that orientation of $\vec{p}$ along $\vec{M}$ yields a θ_A dependence of photoemission intensity [Fig. 3(a)] characteristic of the $\vec{A}\cdot\vec{P}$ dipole interaction, while the θ_p dependence with near alignment of $\vec{A}$ and $\vec{M}$ [Fig. 3(b)] probes mainly the f-wave angular symmetry of the shape resonance.[8,41] The curves in Fig. 3 are qualitatively in excellent agreement with these expectations. Actually, the adsorbate angular distributions are even more sharply peaked (although not exactly along $\vec{M}$) than P_3. It would be interesting in future studies to extend angular dependence measurements to larger values of θ_p to look for the second, much smaller intensity maximum in $P_3(\cos\theta_p)$ near $\theta_p = 65°$. This other lobe, which by its existence verifies the f-wave character of the shape resonance, can be seen in calculated oriented molecule angular distribution curves.[38]

3. Condensed-Phase Effects.

Comparison of the resonant behavior for CO-Ni(111) and CO-Ni(001) allows us to identify several important differences between the predicted gas-phase and observed adsorbed-molecule shape resonances.

These constitute substrate or condensed-phase effects, and are summarized below:

(1) The resonance intensity difference of a factor of two between the two nickel faces obviously cannot be accounted for by any isolated molecule theory,[8] and must indicate a strong substrate effect. A difficulty in this interpretation is that a substrate-induced attenuation of the shape resonance intensity might also shift the energy of the resonance, contrary to our observation. Additionally, the intensity difference is probably not indicative of a difference[42] in C-O bond distances (d_{CO}) between the two systems: Our O(1s) normal photoelectron diffraction (NPD) measurements[13] show excellent agreement with theory for d_{CO} = 1.13 Å, which is the isolated molecule bond distance, in both adsorbate-substrate systems. As discussed in our recent Letter,[13] O(1s) NPD is a quite sensitive probe of this bond distance. A likely contribution to the intensity difference between the two nickel faces is the difference in adsorption-site geometries. Based on our photoelectron diffraction studies,[13] and LEED,[16,18] electron energy loss,[19] and infrared[20] measurements by other workers, CO is known to occupy the atop site on Ni(001) whereas the twofold bridge site is occupied on Ni(111).

(2) For CO-Ni(001), the θ_p angular distribution shown in Fig. 3(b) is peaked at 5° in the ϕ_p = 180° azimuthal direction, exactly between the orientations of $\vec{A}$ and $\vec{M}$. Under the assumption that the dipole nature of the $\sigma \rightarrow \sigma$ photoemission transition and the angular symmetry of the shape resonance are equally important in determining

the resonant intensity maximum for the oriented molecule, this is exactly in agreement with theoretical predictions for isolated CO.[8] However, the CO-Ni(111) distribution in Fig. 3(b) is peaked at 5° in the $\phi_p = 0°$ azimuth, and the entire curve is shifted by 10° in θ_p relative to CO-Ni(001), in a direction away from $\vec{A}$. This unexpected result for CO-Ni(111) is consistent with a substrate-induced shift of the ARP intensity maximum away from the molecular axis $\vec{M}$ (and thus from $\vec{n}$). We note that rotations of $\vec{p}$ by 180° about $\vec{n}$ are crystallographically equivalent for Ni(001) but not for the threefold symmetric [111] axis on Ni(111). Hence, a substrate-induced shift of the angular distribution could be "symmetry masked" in the ensemble for Ni(001) but not for Ni(111). It should also be pointed out that the overall angular behavior of the θ_p-dependence curve for both systems, being more sharply peaked than $P_3(\cos\theta)$, is additional evidence for condensed-phase effects.

(3) For the adsorbate resonance, the vacuum-referenced resonance kinetic energy is shifted upward by 10 eV to 21 eV and the photon energy by 4 eV to 311 eV relative to gas-phase predictions.[8,9,38] Loubriel and Plummer[43] have shown that shifts such as these are caused by potential changes upon bonding to the substrate. A differential shift of the resonance level with respect to C(1s) induces changes in both the kinetic and photon energy at resonance, relative to the gas phase. The shift in resonance kinetic energy can be understood qualitatively with the aid of simple potential plots as shown in Fig. 4 (Ref. 44). The one-electron effective scattering

potential in the gas phase is given by the sum of centrifugal (r^{-2}) and attractive ($-r^{-n}$) parts, shown as one of the solid lines ($r^{-2} - r^{-n}$) in Fig. 4. If we ignore the details of the electronic structure of the substrate, we can consider a major effect of the adsorbate-substrate interaction to be a simple relaxation of all levels, bound and unbound, induced by screening charge from the substrate.[4a] The screened attractive part of the potential for the adsorbed molecule is then given by the dashed curve in Fig. 4 corresponding to ($-e^{-r}r^{-n}$). Combined with r^{-2}, the relaxed scattering potential is the solid line given by ($r^{-2} - e^{-r}r^{-n}$), which has an interior centrifugal wall much closer to r = 0 than that of the unscreened potential for the isolated molecule. By analogy with the barrier-penetration problem,[27,28] this shift raises the kinetic energy of the resonance which is dependent on the "width" of the effective potential well for the molecule. Since the resonance energy position is highly sensitive to the upper part of V(r) (> 0), a differential shift of the resonance level is not unexpected.[4a] In Fig. 5, we summarize the relaxation process for the C(1s) shape resonance in CO-Ni by an energy level diagram. The measured gaseous C(1s) binding energy[45] is equal to 296 eV, with the predicted shape resonance kinetic energy at 11 eV and a photon energy at the resonance given by $h\nu$ = 307 eV. In the condensed phase, we can view the relaxation process schematically in two steps: the first (static) relaxes both levels equally by about 6 eV relative to the vacuum level, E_v (ΔE_B = 6 eV), leaving the photon energy at resonance unchanged; a

(differential) shift of the resonance level in the second step changes the photon energy by 4 eV to 311 eV. This value of the shift ($\Delta h\nu$) is identical to the corresponding value for the 4σ shape resonance in CO-Ni(001) (Ref. 4). At the time of these condensed-phase core-level measurements, no gas phase data was available for the C(1s) resonance. However, very recent experiments[31] suggest that the gaseous shape resonance in the C(1s) level occurs at a photon energy of about 306 eV, somewhat lower than the theoretical value, implying that the differential relaxation is slightly larger for the C(1s) level than for the 4σ level. We should note that the arguments presented here would also suggest that the resonance kinetic energy is dependent on the value of d_{CO}. The fact that we observe the resonances for both CO-Ni systems at the same photon energy can be construed as additional evidence against any C-O bond length variations.

Finally, we did not observe a resonance in the O(1s) cross section for CO on either substrate. This result is in agreement with the oriented-molecule theory of Wallace, et al.,[8] after phase errors in their original work are accounted for:[46] The core-level resonance intensity is predicted to be sharply peaked along $\vec{M}$ with the electron intensity maximum in the direction opposite to the photoemitting atom. Because the adsorbed CO molecule is oriented with the C end toward the substrate on both Ni surfaces,[2-4] only the C(1s) level should give rise to a resonance in our experiment; i.e., the O(1s) resonance should have its intensity directed toward the substrate rather than in the direction of the electron detector, rendering it unobservable.

D. Summary and Conclusions

We have observed large resonances in the near threshold C(1s) photoemission cross section for CO-Ni(111) and CO-Ni(001). These resonances appear to be closely related to the so-called "shape resonances" observed in gaseous[7] and adsorbate[4] CO valence levels, and predicted for the core levels.[9] As expected,[8] the C(1s) core-level resonances appear to be highly sensitive to molecular orientation and photon energy. This should facilitate interesting molecular orientation experiments with different adsorbate molecules. An analogous resonance, for example, has more recently been found above the N K-edge for the NO-Ni(001) system.[47] Also, we have initiated studies of other carbon-containing molecular adsorbates. As an example of the wealth of structure that exists in the near-threshold region of the C K-edge for these molecules, Fig. 6 shows the relative C(1s) cross section obtained for C_2H_4 adsorbed on Ni(111) (Ref. 48) with the experimental geometry identical to the CO-Ni(111) case shown in Fig. 2. The three sharp structures seen in Fig. 6 are clearly <u>not</u> atomiclike; however, any or all three might be shape-resonance related.[49] At the time of this writing, detailed calculations of the C(1s) cross-section curve in gaseous C_2H_4 have not been performed, but it appears that our gas-phase group at LBL will be able to make analogous measurements in the near future. If the origin of the three structures in the C_2H_4-Ni(111) cross-section curve can be understood at least qualitatively in terms of molecular processes, detailed angular distribution studies at the corresponding peak photon energies might add considerable information

to the understanding of this adsorption system and adsorbate molecular phenomena in general.

An important unanticipated result of this research is the pronounced difference in the C(1s) resonance between Ni(001) and Ni(111). This result, which is probably due to rather complicated final-state effects such as multiple scattering processes at the relatively low resonance kinetic energy, implies that future theoretical treatments of adsorbate shape-resonance phenomena must take into account the position of substrate atoms to facilitate a meaningful comparison with theory.

REFERENCES

* This chapter is based on experiments performed in collaboration with S. D. Kevan, D. H. Rosenblatt, M. G. Mason, J. G. Tobin, and D. A. Shirley; published in Phys. Rev. Lett. 45, 1877 (1980).

1. See, for example, T. Gustafsson and E. W. Plummer, and A. Liebsch, in Photoemission and the Electronic Properties of Surfaces, edited by B. Feuerbacher, B. Fitton, and R. F. Willis (Wiley, New York, 1978).
2. G. Apai, P. S. Wehner, R. S. Williams, J. Stöhr, and D. A. Shirley, Phys. Rev. Lett. 37, 1497 (1976); P. M. Williams, P. Butcher, J. Wood, and K. Jacobi, Phys. Rev. B 14, 3215 (1976).
3. R. J. Smith, J. Anderson, and G. J. Lapeyre, Phys. Rev. Lett. 37, 1081 (1976).
4. (a) C. L. Allyn, T. Gustafsson, and E. W. Plummer, Chem. Phys. Lett. 47, 127 (1977); (b) Solid State Commun. 28, 85 (1978), and references therein.
5. S. Wallace, D. Dill, and J. L. Dehmer, J. Phys. B 12, L417 (1979), and references therein.
6. J. W. Davenport, Phys. Rev. Lett. 36, 945 (1976).
7. E. W. Plummer, T. Gustafsson, W. Gudat, and D. E. Eastman, Phys. Rev. A 15, 2339 (1977).
8. S. Wallace, D. Dill, and J. L. Dehmer, Phys. Rev. B 17, 2004 (1978).
9. J. L. Dehmer and D. Dill, Phys. Rev. Lett. 35, 213 (1975).
10. (a) A. Liebsch, Phys. Rev. B 13, 544 (1976); (b) R. S. Wallace, Ph.D. thesis, Boston University, 1980 (unpublished).

11. L.-G. Petersson, S. Kono, N. F. T. Hall, C. S. Fadley, and J. B. Pendry, Phys. Rev. Lett. 42, 1545 (1979).

12. Estimation based on the very high condensed-phase photoelectron asymmetry parameter ($\beta = 1.94$) measured for the Ag(4s) photoemission peak; see R. F. Davis, S. D. Kevan, B.-C. Lu, J. G. Tobin, and D. A. Shirley, Chem. Phys. Lett. 71, 448 (1980); see, also, Chapter VII of this thesis.

13. S. D. Kevan, R. F. Davis, D. H. Rosenblatt, J. G. Tobin, M. G. Mason, D. A. Shirley, C. H. Li, and S. Y. Tong, Phys. Rev. Lett. 46, 1629 (1981).

14. S. D. Kevan and D. A. Shirley, Phys. Rev. B 22, 542 (1980); S. D. Kevan, Ph.D. thesis, University of California, Berkeley, 1980 (LBL-11017, unpublished).

15. W. J. McG. Tegart, The Electrolytic and Chemical Polishing of Metals (Pergamon, New York, 1959), p. 102.

16. M. Passler, A. Ignatiev, F. Jona, D. W. Jepsen, and P. M. Marcus, Phys. Rev. Lett. 43, 360 (1979).

17. S. Andersson and J. B. Pendry, Surf. Sci. 71, 75 (1978).

18. S. Andersson and J. B. Pendry, Phys. Rev. Lett. 43, 363 (1979).

19. W. Erley, H. Wagner, and H. Ibach, Surf. Sci. 80, 612 (1979).

20. J. C. Compuzano and R. G. Greenler, J. Vac. Sci. Technol. 16, 445 (1979).

21. For discussion of the normal photoelectron diffraction technique, see S. D. Kevan, D. H. Rosenblatt, D. Denley, B.-C. Lu, and D. A. Shirley, Phys. Rev. Lett. 41, 1565 (1978); Phys. Rev. B 20, 4133 (1979); S. D. Kevan, Appl. Opt. 19, 3974 (1980); Ph.D. thesis,

University of California, Berkeley, 1980 (LBL-11017, unpublished); S. D. Kevan, J. G. Tobin, D. H. Rosenblatt, R. F. Davis, and D. A. Shirley, Phys. Rev. B 23, 493 (1981); D. H. Rosenblatt, J. G. Tobin, M. G. Mason, R. F. Davis, S. D. Kevan, D. A. Shirley, C. H. Li, and S. Y. Tong, ibid. 23, 3828 (1981).

22. S. P. Weeks and E. W. Plummer, Solid State Commun. 21, 695 (1977).

23. H.-J. Hagemann, W. Gudat, and C. Kunz, J. Opt. Soc. Am. 65, 742 (1975), and Ref. 1 therein.

24. See, for example, J. A. Stratton, Electromagnetic Theory (McGraw-Hill, New York, 1941), Chapter IX.

25. The experimental accuracy of these ARP CO orientation measurements has typically been quoted to be ±5 to ±15°. Much of this uncertainty arises from vibrationally-induced angular broadening (Ref. 4b). The orientation of CO on Ni(001) has undergone some controversy, more recently. Original LEED work (Ref. 17) suggested a CO tilt of 34° ± 10° with respect to the normal; however, a reexamination showed that the molecule was oriented along the normal (Ref. 18), and recent angle-resolved XPS (Ref. 11) and UPS (Ref. 4b) experiments have determined the orientation to be within 12° of the normal, and along the normal ± 15°, respectively.

26. J. L. Dehmer and D. Dill, J. Chem. Phys. 65, 5327 (1976).

27. See, for example, E. Merzbacher, Quantum Mechanics, 2nd ed. (Wiley, New York, 1970), Chapter 6.

28. T. Gustafsson and H. J. Levinson, Chem. Phys. Lett. 78, 28 (1981), and references therein.

29. See, for example, Refs. 5-9, 10b, 26, 28, and 30-36.

30. D. Loomba, S. Wallace, D. Dill, and J. L. Dehmer, J. Chem. Phys. 75, 4546 (1981), and references therein.

31. C. M. Truesdale, S. Southworth, P. H. Kobrin, U. E. Becker, D. W. Lindle, H. G. Kerkhoff, and D. A. Shirley, to be published. This work includes core-level measurements for CO, N_2, and CO_2, and valence-band measurements for NO_2, OCS, CS_2, CO_2, and N_2O.

32. C. M. Truesdale, S. Southworth, P. H. Kobrin, D. W. Lindle, G. Thornton, and D. A. Shirley, J. Chem. Phys., to be published (in press) (LBL-11822).

33. S. H. Southworth, C. M. Truesdale, P. H. Kobrin, D. W. Lindle, W. D. Brewer, and D. A. Shirley, J. Chem. Phys., to be published (in press) (LBL-12907).

34. F. A. Grimm, Chem. Phys. 53, 71 (1980).

35. N. Padial, G. Csanak, B. V. McKoy, and P. W. Langhoff, J. Chem. Phys. 69, 2992 (1978); P. W. Langhoff, S. R. Langhoff, T. N. Rescigno, J. Schirmer, L. S. Cederbaum, W. Domcke, and W. Von Niessen, Chem. Phys. 58, 71 (1981).

36. F. A. Grimm, T. A. Carlson, W. B. Dress, P. Agron, J. O. Thomson, and J. W. Davenport, J. Chem. Phys. 72, 3041 (1980); T. A. Carlson, M. O. Krause, F. A. Grimm, J. D. Allen Jr., D. Mehaffy, P. R. Keller, and J. W. Taylor, ibid. 75, 3288 (1981).

37. C. L. Allyn, T. Gustafsson, and E. W. Plummer, Solid State Commun. 24, 531 (1977).

38. D. Dill, J. Siegel, and J. L. Dehmer, J. Chem. Phys. 65, 3158 (1976).

39. D. Dill, J. Chem. Phys. 65, 1130 (1976).

40. C. N. Yang, Phys. Rev. 74, 764 (1948).

41. S. Wallace and D. Dill, Phys. Rev. B 17, 1692 (1978).

42. J. K. Nørskov, Solid State Commun. 28, 899 (1978).

43. G. Loubriel and E. W. Plummer, Chem. Phys. Lett. 64, 234 (1979).

44. General aspects of effective scattering potentials and their relationship to shape-resonance phenomena have been reviewed recently. See V. Schmidt, Appl. Opt. 19, 4080 (1980).

45. K. Siegbahn, et al., ESCA Applied to Free Molecules (North-Holland, London, 1969), Chapter 5.

46. D. Dill, S. Wallace, J. Siegel, and J. L. Dehmer, Phys. Rev. Lett. 42, 411 (1979); D. Dill and S. Wallace, private communications, 1980.

47. J. Stöhr, K. Baberschke, R. Jaeger, R. Treichler, and S. Brennan, Phys. Rev. Lett. 47, 381 (1981).

48. Based on the interpretation of recent electron energy loss measurements for C_2H_4-Ni(111), a "flat"-bonded geometry with the C-C bond axis nearly perpendicular to the Ni(111) surface normal has been proposed for this adsorption system. See J. C. Bertolini and J. Rousseau, Surf. Sci. 83, 531 (1979); S. Lehwald and H. Ibach, ibid. 89, 425 (1979).

49. Several shape-resonance related final states (σ and π) are expected to lie in the continuum for the free C_2H_4 molecule; S. Wallace, private communication, 1980.

FIGURE CAPTIONS

Fig. 1. (a) Experimental arrangement, showing typical plane-of-incidence orientations of the vector potential $\vec{A}$, the outgoing photoelectron direction $\vec{p}$, the crystal surface normal $\vec{n}$, and the incident photon beam direction $h\nu$. The photoemission angle θ_p is varied in either the $\phi = 0^\circ$ (toward the photon beam) or 180° azimuth, while the polarization angle θ_A is confined to the $\phi = 180^\circ$ azimuth. (b) Experimental orientation of the crystals. In addition to the normal vector, the plane of incidence contains the [100] and $[\bar{2}11]$ direction for the (001) and (111) face, respectively, in the $\phi = 0^\circ$ azimuth. (c) C(1s) photoemission energy distribution curves for Ni(111) + 2 L of CO, with photons in the energy region near the resonance at $h\nu$ = 311 eV. The spectra are normalized to incident radiation flux and analyzer transmission. θ_p and θ_A are defined in (a).

Fig. 2. Relative C(1s) photoemission cross section for CO-Ni(111) (solid line) and CO-Ni(001) (dashed line) in the energy region 300 eV $\leq h\nu \leq$ 356 eV. The two curves are normalized to each other at $h\nu$ = 335 eV, and the resonance maximum for both curves is shown to lie at $h\nu$ = 311 eV. θ_p and θ_A are defined in Fig. 1(a).

Fig. 3. Relative C(1s) cross section: (a) θ_A dependence in the energy region near the resonance maximum for CO-Ni(111) and various values of the polarization angle. (b) θ_p dependence

at $h\nu = 311$ eV, with the polar orientation of $\vec{p}$ varied in both the 0° and 180° azimuths about the crystal normal in the plane of incidence. Data are shown for both CO-Ni(111) (closed circles, solid line) and CO-Ni(001) (open circles, dashed line), where the CO-Ni(001) curve has been normalized so that its value at $\theta_p = 0°$ equals the corresponding value for CO-Ni(111). θ_p, θ_A, and ϕ_p are defined in Fig. 1(a).

Fig. 4. A simple schematic representation of the effect of relaxation on the shape resonance energy position. The dashed curves for $V(r) < 0$, $-r^{-n}$ and $-e^{-r}r^{-n}$, correspond to unscreened (gaseous) and screened (condensed phase) attractive parts of the effective scattering potential, respectively, and the upper dashed curve, r^{-2}, is the centrifugal barrier potential. The two solid curves, $(r^{-2} - r^{-n})$ and $(r^{-2} - e^{-r}r^{-n})$, are the unscreened and screened total scattering potentials. It is clear from these two solid curves that relaxation in the condensed phase causes a net reduction in the spatial extent of the centrifugal barrier [$V(r) \sim 0$], raising the kinetic energy of the resonance. Because the resonance-level energy position is more sensitive to the exact form of the attractive part of the potential than is C(1s), screening charge from the substrate induces a <u>differential</u> shift in the resonance level (see Refs. 4a and 43).

Fig. 5. Correlation of the resonance and C(1s) energy levels between the gas and condensed phases. Energies are referenced to the vacuum level (E_v) and the gas-phase resonance level is

given by theory (Refs. 8, 9, and 38). The effect of relaxation is shown schematically in two steps: (1) a (static) relaxation shifts both levels upward relative to E_v by an amount equal to the change in the C(1s) binding energy (ΔE_B = 6 eV); (2) a (differential) shift occurs in the resonance level by an amount given by the change in the resonance photon energy ($\Delta h\nu$ = 4 eV). The resulting resonance kinetic energy, KE^V = 21 eV, is exactly equal to our measured value.

Fig. 6. Relative C(1s) photoemission cross section for Ni(111) + 1 L of C_2H_4 in the energy region 298 eV $\leq h\nu \leq$ 355 eV. The experimental geometry, $\theta_A = 10^\circ$ and $\theta_p = 0^\circ$ in the plane of incidence, and the azimuthal crystal orientation, are identical to the corresponding arrangement for CO-Ni(111) (see Figs. 1-3). The ethylene overlayer gave rise to a (2x2) C_2H_4-Ni(111) surface structure as determined by LEED, and the EDCs from which the C(1s) intensities are derived were recorded at room temperature. The overlayer was prepared with the Ni(111) substrate cooled to 120K, then warmed to 295K afterward.

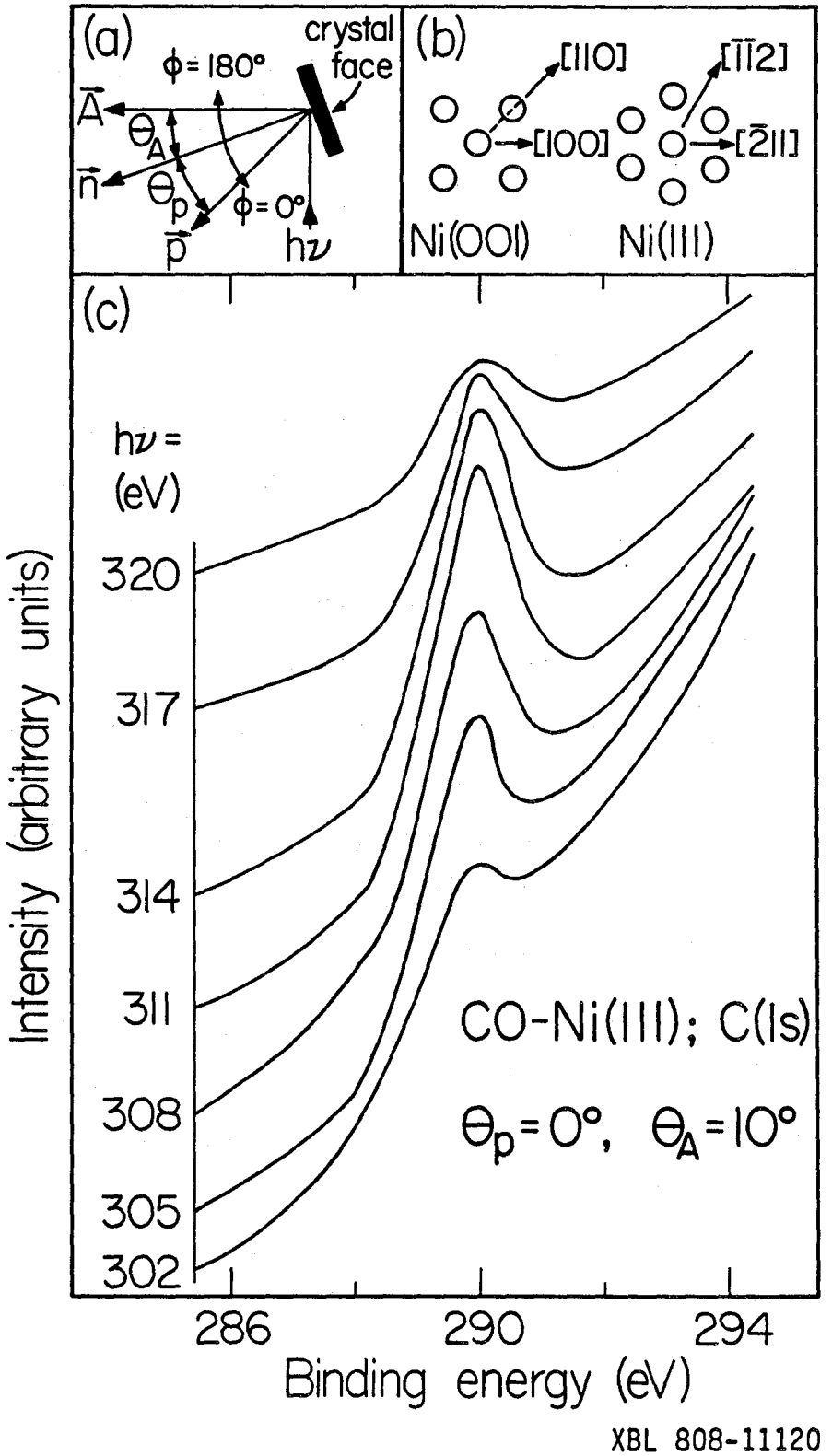

XBL 808-11120

Figure 1

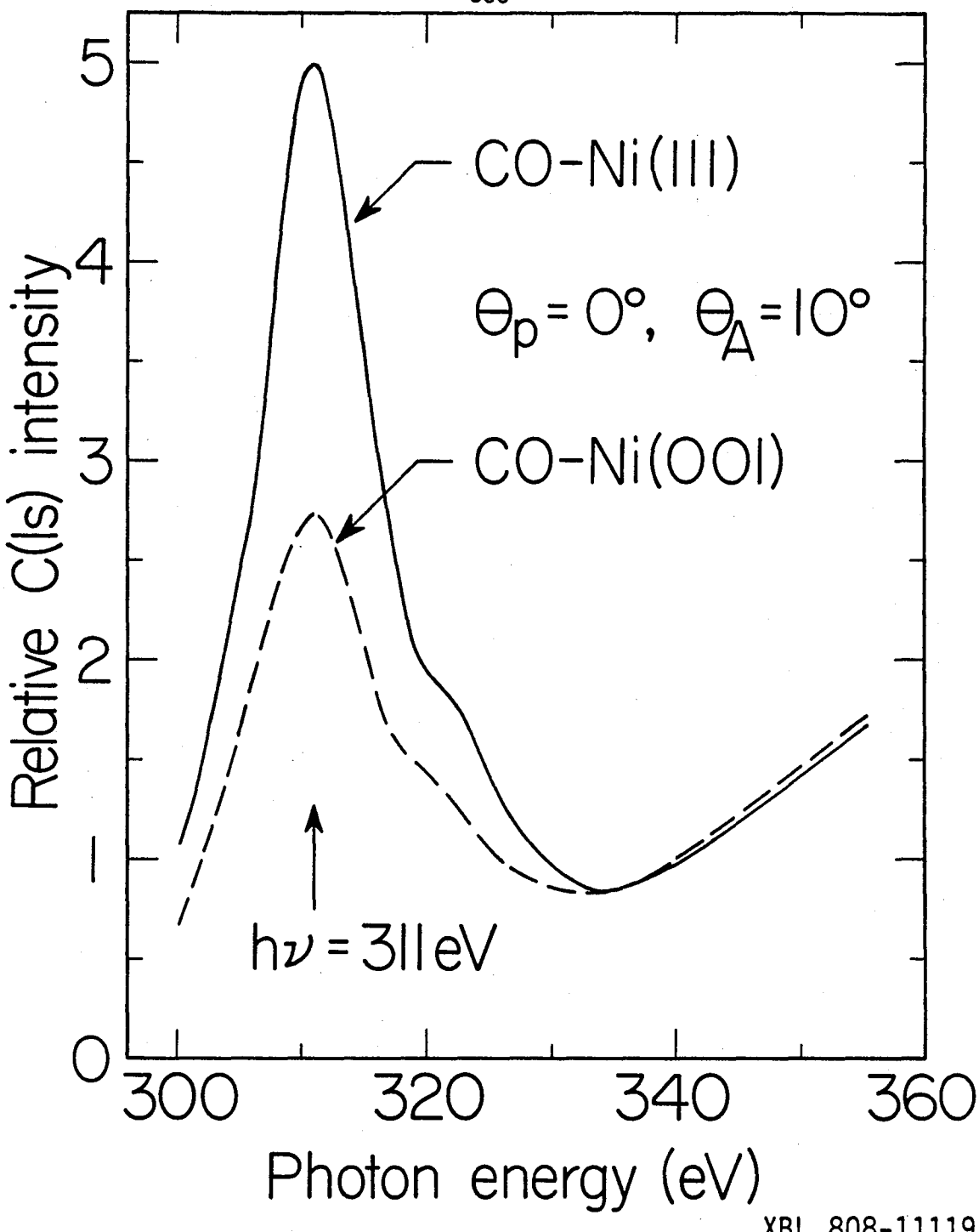

XBL 808-11119

Figure 2

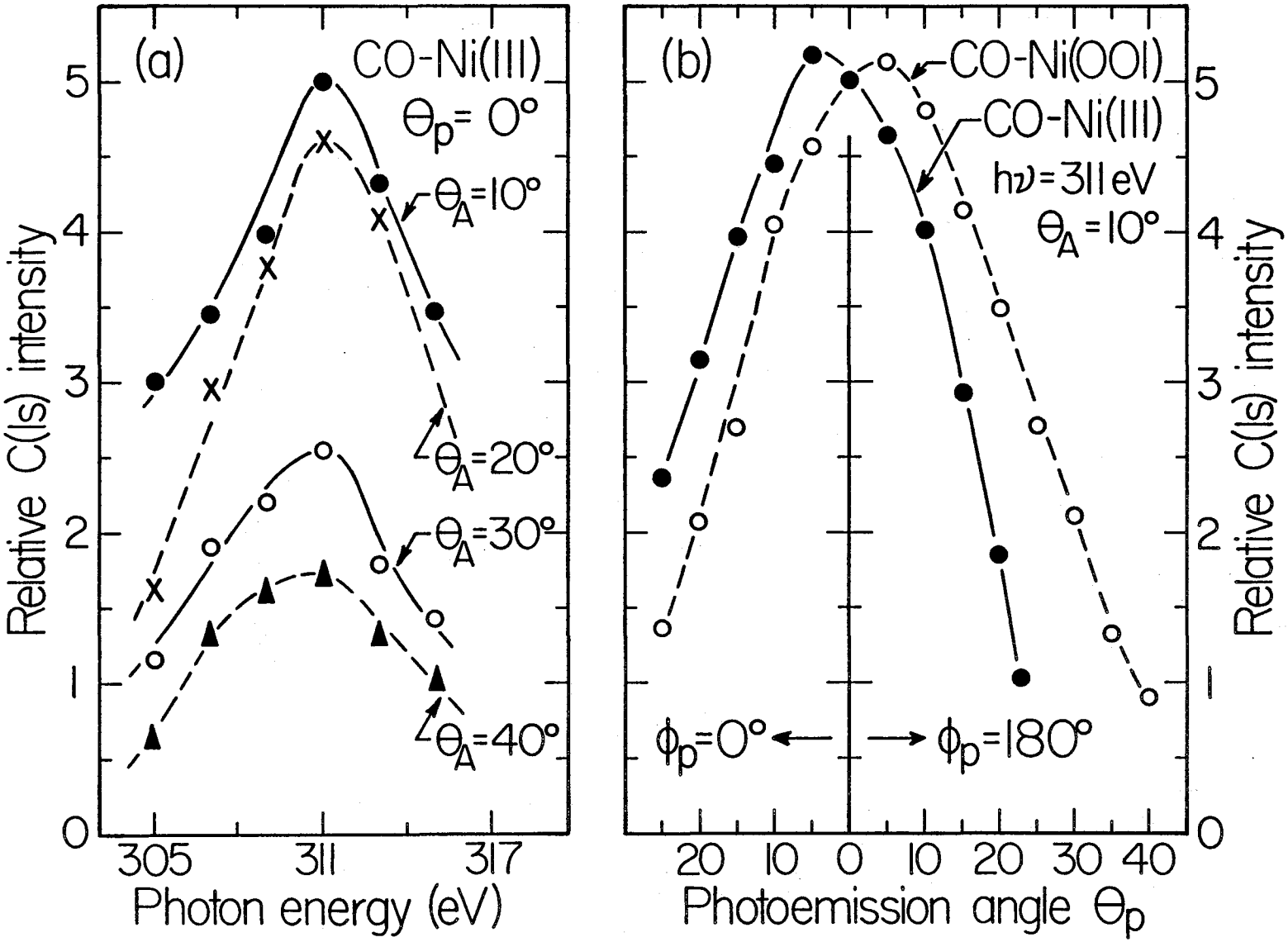

XBL 808-11118

Figure 3

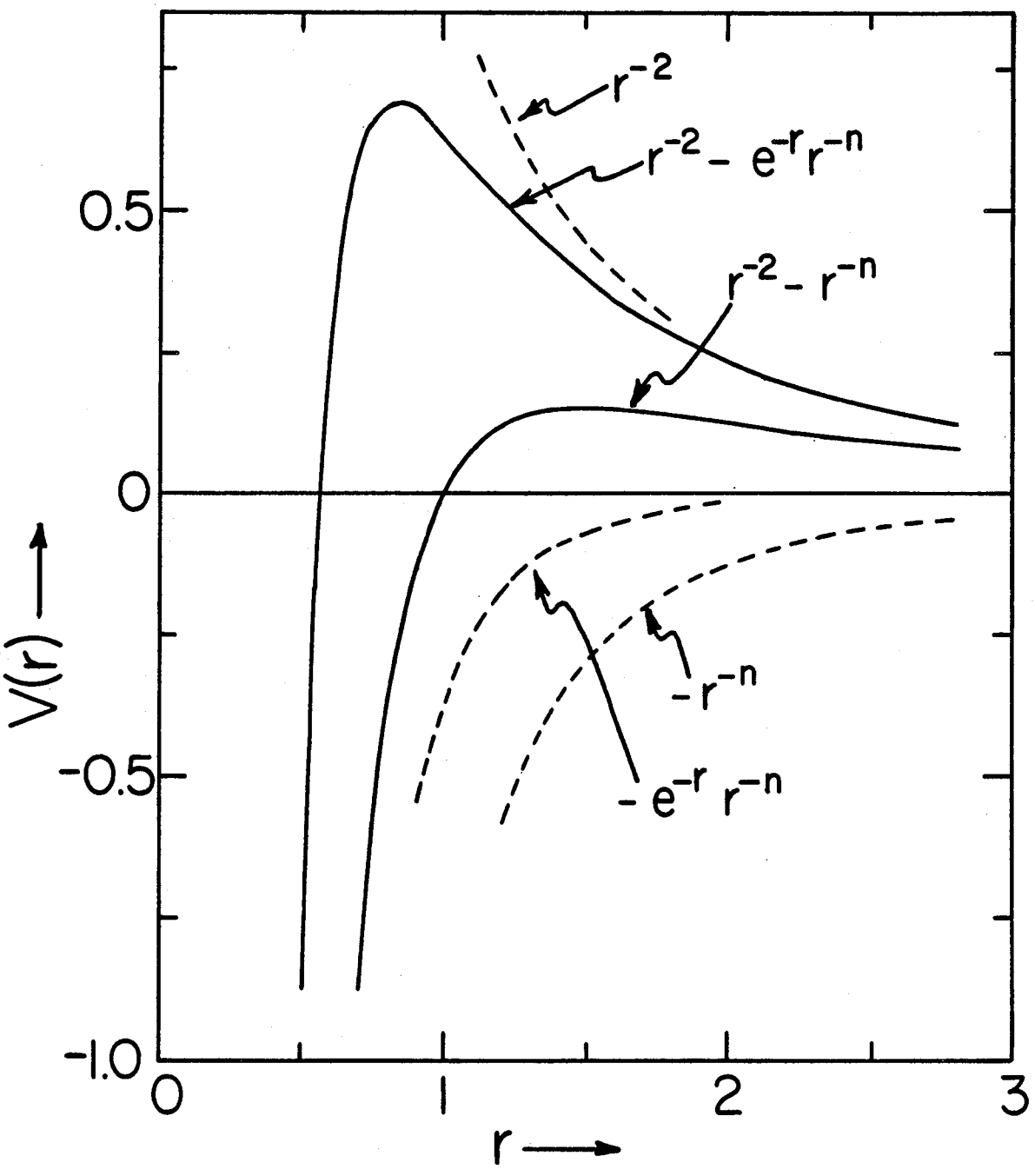

Figure 4

XBL 817-10705

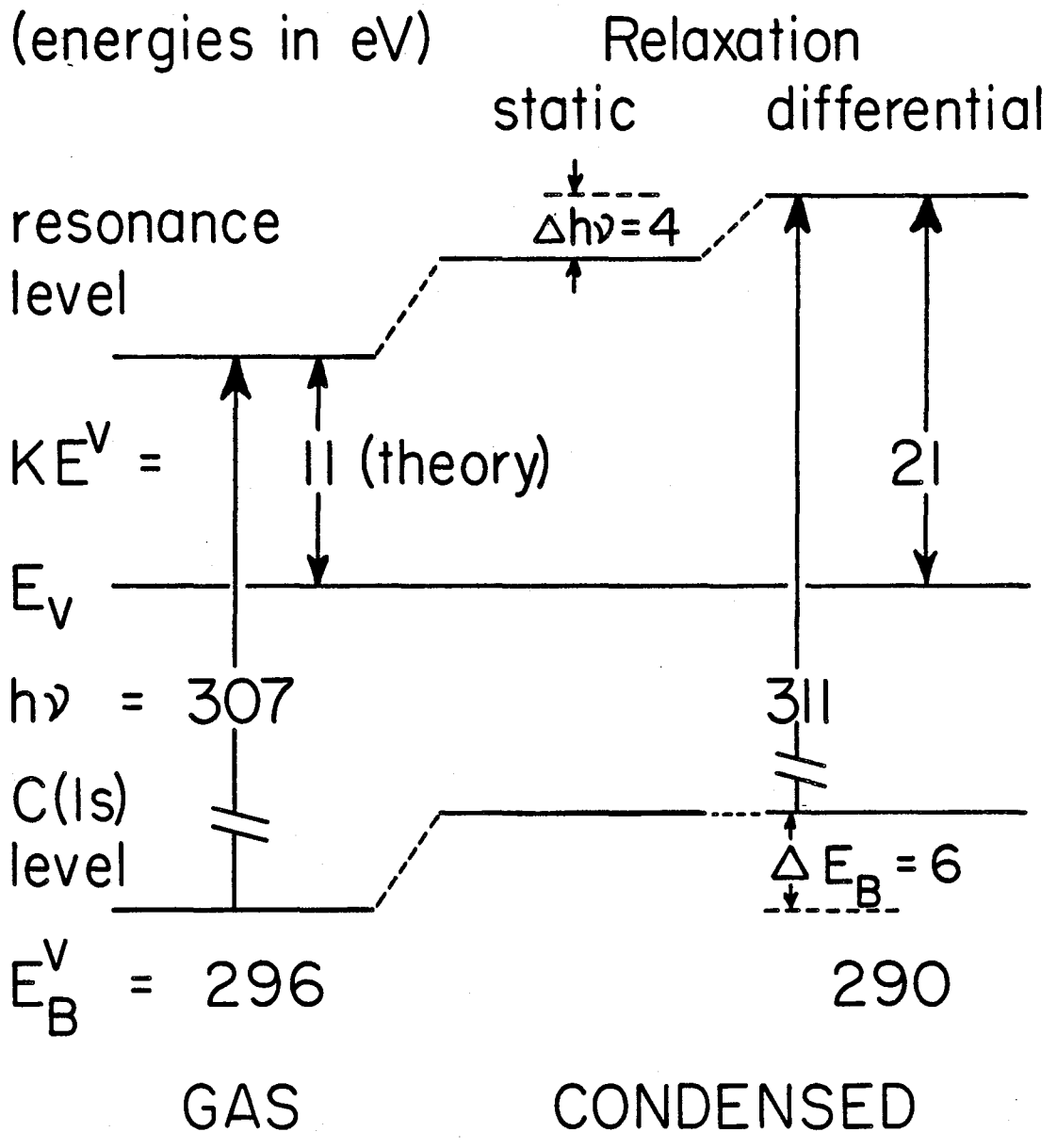

Figure 5

XBL 817-10702

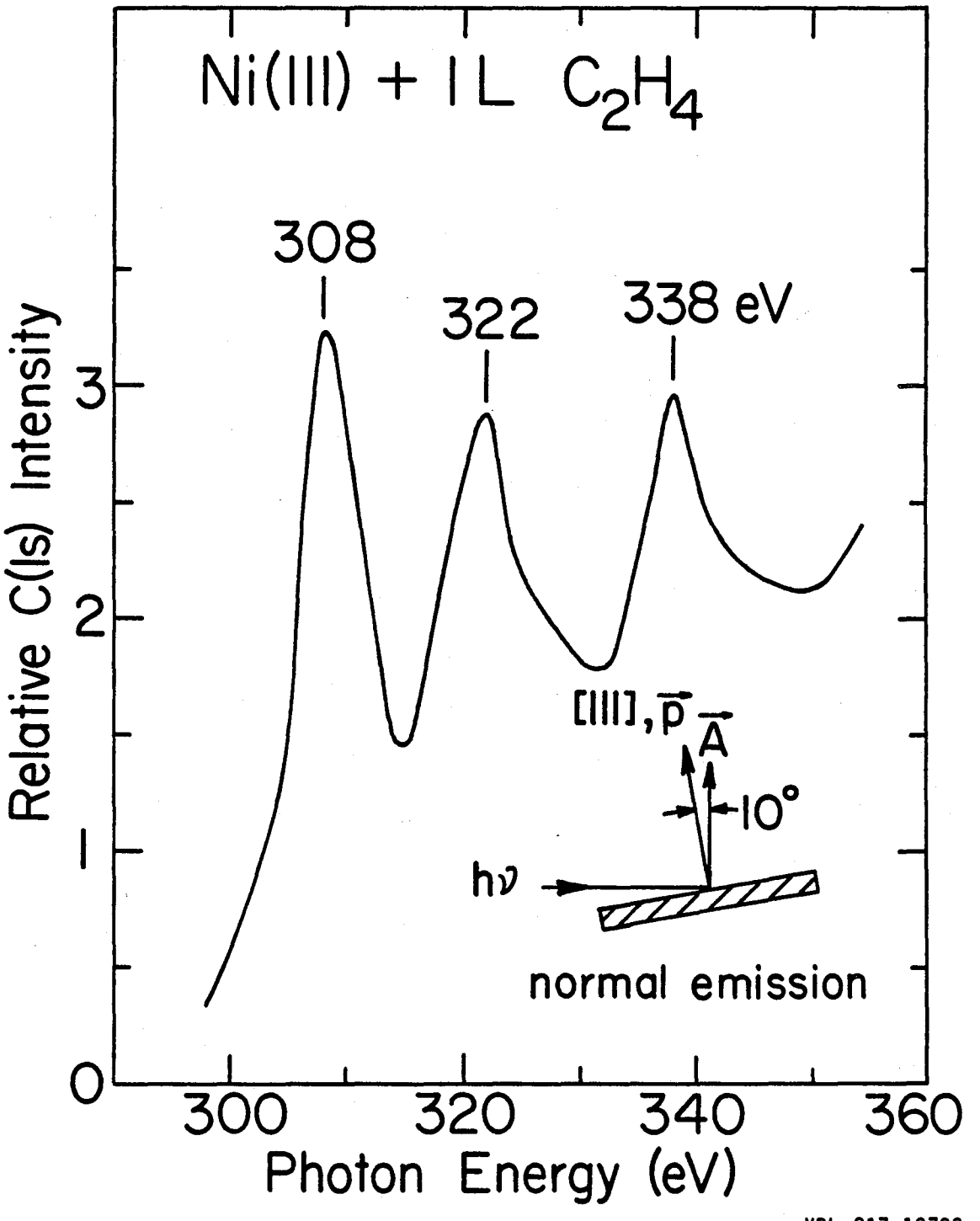

XBL 817-10703

Figure 6

ACKNOWLEDGMENTS

The culmination of one's graduate career is naturally a time of reflection upon those people whose efforts have made this achievement possible. Unfortunately, a proper expression of my gratitude to all those concerned would require an acknowledgment the magnitude of which would equal the remainder of this thesis. Therefore, I must apologize for my incompleteness, below, in this regard.

I have had the privilege of being guided as a student by two superb research directors. During my undergraduate years, Prof. R. H. Herber was responsible for instilling in me a love of scientific research in physical chemistry. As a graduate student, I have matured as a scientist under the direction of Prof. D. A. Shirley, whose great knowledge, keen insight, and scientific enthusiasm has been essential to my achievements. Both men deserve more credit than these pages can give. I hope that my future accomplishments will serve as an example of their ability and inspiration to mold successful members of the scientific community.

I have benefited greatly, both personally and scientifically, from my association and friendship with many students, post-docs, and visitors in our research group at Berkeley, past and present. All of my research has been a collaborative effort. Prof. R. S. Williams and Dr. P. S. Wehner taught me a great deal about angle-resolved photo-emission near the beginning of my graduate career. I have also

collaborated with and learned from Dr. S. D. Kevan, Dr. M. G. Mason, Dr. K. A. Mills, Dr. G. Thornton, Dr. Z. Hussain, Dr. E. Umbach, Dr. B.-C. Lu, Mr. D. H. Rosenblatt, Mr. J. G. Tobin, Mr. C. C. Parks, and Mr. L. E. Klebanoff. In particular, I thank Steve Kevan, who was the instrumental collaborator in much of my research, and Danny Rosenblatt, Jim Tobin, Gary Mason, and Chris Parks, who have served as close friends over the past several years in addition to their roles as important scientific collaborators. Additionally, I extend my gratitude to Dr. D. Denley, Dr. D. J. Trevor, Mr. J. E. Pollard, Dr. J. Stöhr, and many other members of our group, past and present, for their roles as scientific colleagues and/or friends. It has been a pleasure to work with and learn from all the above people, and they are gratefully acknowledged.

The support of the staff at LBL is gratefully acknowledged. In particular, I take great pleasure in thanking Ms. Wini Heppler and Ms. Barbara Moriguchi for their friendship and cheerful technical assistance throughout the course of this work. Mr. Joseph Katz, Mr. Richard Strudwick, Mr. Richard Escobales, and Mr. Donald Malone have assisted with electrical and mechanical engineering problems on numerous occasions. Additionally, many thanks go to Mrs. Connie Silva, Ms. June DeLaVergne, and Ms. Jean Wolslegel for their expert and patient job of typing this manuscript, and Mrs. Mirriam Schwartz for her beautiful and expert illustrative work in producing many of the figures.

Finally, and most importantly, I have been blessed with great parents--the best--whose constant source of inspiration, love, and encouragement throughout my life has always been tremendously important to me. My gratitude to them exceeds words.

This work was supported by the Director, Office of Energy Research, Office of Basic Energy Sciences, Chemical Sciences Division of the U.S. Department of Energy under Contract No. W-7405-ENG-48. It was performed in part at the Stanford Synchrotron Radiation Laboratory, which is supported by the NSF through the Division of Materials Research.

This report was done with support from the Department of Energy. Any conclusions or opinions expressed in this report represent solely those of the author(s) and not necessarily those of The Regents of the University of California, the Lawrence Berkeley Laboratory or the Department of Energy.

Reference to a company or product name does not imply approval or recommendation of the product by the University of California or the U.S. Department of Energy to the exclusion of others that may be suitable.

TECHNICAL INFORMATION DEPARTMENT
LAWRENCE BERKELEY LABORATORY
UNIVERSITY OF CALIFORNIA
BERKELEY, CALIFORNIA 94720